Resolving the properties of massive, high–redshift starbursts

James Matthew Simpson

Abstract

Sub-millimeter galaxies (SMGs) are a population of dusty, obscured sources that represent some of the most extreme sites of star-formation in the Universe. These galaxies have total far–infrared (FIR) luminosities of 10^{12}–$10^{13}\,\mathrm{L}_{\odot}$ and colossal star formation rates (SFRs) of ~ 100–$1000\,\mathrm{M}_{\odot}\mathrm{yr}^{-1}$, with the FIR–emission arising due to the reprocessing of ultraviolet radiation from massive, young stars by dust. Despite their discovery nearly 20 years ago, our understanding of the SMG population has been hampered by the coarse resolution (FWHM = 15–30″) of single-dish sub-millimeter surveys. In this thesis I present observations of FIR–bright ($S_{870} \gtrsim 1\,\mathrm{mJy}$) galaxies that have precise identifications from high-resolution imaging taken with sub–mm / mm interferometers. I present a multi-wavelength study of 96 SMGs that have unambiguous identifications from observations with Atacama Large Millimeter sub–millimeter Array (ALMA) and determine that the photometric redshift distribution for the SMG population has a median of $z_{phot} = 2.5 \pm 0.2$. I show that if the star formation activity in SMGs has a timescale of $\sim 100\,\mathrm{Myr}$ then their descendants at $z \sim 0$ would have a space density and absolute H–band magnitude distribution that are in good agreement with a volume limited sample of local ellipticals. The low resolution of single-dish surveys has led to concerns about the blending of multiple individual galaxies into a single sub–millimeter source. I present ALMA observations of a sample of 30 bright, single–dish–identified sub-mm sources and show that $61^{+19}_{-15}\,\%$ are comprised of a blend of multiple SMGs brighter than $\gtrsim 1\,\mathrm{mJy}$. Furthermore, I show that source blending boosts the apparent single-dish number counts by 20 % at $S_{870} > 7.5\,\mathrm{mJy}$. A morphological analysis of the far-infrared emission from a subset of 23 of the brightest sources detected in the ALMA maps shows that the intense starburst in SMGs occurs in a compact region with a median physical half–light diameter of $2.4 \pm 0.2\,\mathrm{kpc}$. Finally, I present observations of two far–infrared–bright quasars, a potential transition stage in the evolution of SMGs. By considering the gas and black hole properties of these sources I show that they are consistent with the evolutionary scenario where far-infrared bright quasars represent a short phase in the transformation of a starburst dominated SMGs into an unobscured quasar.

Resolving the properties of massive, high–redshift starbursts

James Matthew Simpson

A Thesis presented for the degree of

Doctor of Philosophy

Department of Physics
University of Durham

June 26, 2015

Contents

List of Figures

List of Tables

Declaration

The work in this thesis is based on research carried out while the author was a research student, under the supervision of Professor Ian Smail, in the Department of Physics at Durham University. No part of this thesis has been submitted elsewhere for any other degree or qualification and it is all the author's own work, unless referenced to the contrary in the text.

Portions of this work have appeared in the following articles:

1. **The evolutionary connection between QSOs and SMGs: molecular gas in far-infrared luminous QSOs at $z \sim 2.5$** Simpson, J. M.; Smail, I.; Swinbank, A. M.; Alexander, D. M.; Auld, R.; Baes, M.; Bonfield, D. G.; Clements, D. L.; Cooray, A.; Coppin, K. E. K.; Danielson, A. L. R.; Dariush, A.; Dunne, L.; de Zotti, G.; Harrison, C. M.; Hopwood, R., Hoyos, C.; Ibar, E.; Ivison, R. J.; Jarvis, M. J.; Lapi, A.; Maddox, S. J.; Page, M. J.; Riechers, D. A.; Valiante, E. and van der Werf, P. P., 2012, *MNRAS*, 426, 3201 (Chapter 5)

2. **An ALMA Survey of Submillimeter Galaxies in the Extended Chandra Deep Field South: The Redshift Distribution and Evolution of Submillimeter Galaxies** Simpson, J. M.; Swinbank, A. M.; Smail, I.; Alexander, D. M.; Brandt, W. N.; Bertoldi, F.; de Breuck, C.; Chapman, S. C.; Coppin, K. E. K.; da Cunha, E.; Danielson, A. L. R.; Dannerbauer, H.; Greve, T. R.; Hodge, J. A.; Ivison, R. J.; Karim, A.; Knudsen, K. K.; Poggianti, B. M.; Schinnerer, E.; Thomson, A. P.; Walter, F.; Wardlow, J. L.; Wei, A. and van der Werf, P. P., 2014, *ApJ*, 788, 125 (Chapter 2)

3. **The SCUBA-2 Cosmology Legacy Survey: ALMA Resolves the Rest-frame Far-infrared Emission of Sub-millimeter Galaxies** Simpson, J. M.; Smail, I.; Swinbank, A. M.; Almaini, O.; Blain, A. W.; Bremer, M. N.; Chapman, S. C.; Chen, C.-C.; Conselice, C.; Coppin, K. E. K.; Danielson, A. L. R.; Dunlop,

J. S.; Edge, A. C.; Farrah, D.; Geach, J. E.; Hartley, W. G.; Ivison, R. J.; Karim, A.; Lani, C.; Ma, C.-J.; Meijerink, R.; Michałowski, M. J.; Mortlock, A.; Scott, D.; Simpson, C. J.; Spaans, M.; Thomson, A. P.; van Kampen, E. and van der Werf, P. P., 2015, *ApJ*, 799, 81 (Chapter 3)

4. **The SCUBA-2 Cosmology Legacy Survey: ALMA Resolves the Bright End of the Sub-millimeter Number Counts** Simpson, J. M.; Smail, I.; Swinbank, A. M.; Chapman, S. C.; Geach, J. E.; Ivison, R. J.; Thomson, A. P.; Aretxaga, I.; Cowley, W. I.; Chen, C.-C.; Coppin, K. E. K.; Dunlop, J. S.; Edge, A. C.; Farrah, D.; Ibar, E.; Knudsen, K. K.; Meijerink, R.; Michałowski, M. J.; Scott, D.; Spaans, M. and van der Werf, P. P., 2015, *ApJ*, submitted (Chapter 4)

The author has conducted all of the data reduction and analysis presented in this thesis, with the following exceptions: the deblended *Herschel* / SPIRE fluxes and FIR–luminosities that are presented in chapters 2, 4 and 5 were calculated by A. M. Swinbank; B. M. Poggianti provided the sample of local ellipticals used in chapter 2, and calculated their mass–weighted ages; the PdBI data used in chapter 5 was reduced by A. M. Swinbank.

The author has also contributed to the following work over the course of this thesis:

1. **An ALMA survey of submillimetre galaxies in the Extended Chandra Deep Field-South: detection of [C II] at z = 4.4** Swinbank, A. M.; Karim, A.; Smail, I.; Hodge, J.; Walter, F.; Bertoldi, F.; Biggs, A. D.; de Breuck, C.; Chapman, S. C.; Coppin, K. E. K.; Cox, P.; Danielson, A. L. R.; Dannerbauer, H.; Ivison, R. J.; Greve, T. R.; Knudsen, K. K.; Menten, K. M.; **Simpson, J. M.**; Schinnerer, E.; Wardlow, J. L.; Weiß, A. and van der Werf, P. P., 2012, *MNRAS*, 427, 1066

2. **An ALMA Survey of Submillimeter Galaxies in the Extended Chandra Deep Field South: Source Catalog and Multiplicity** Hodge, J. A.; Karim, A.; Smail, I.; Swinbank, A. M.; Walter, F.; Biggs, A. D.; Ivison, R. J.; Weiss, A.; Alexander, D. M.; Bertoldi, F.; Brandt, W. N.; Chapman, S. C.; Coppin, K. E. K.; Cox, P.; Danielson, A. L. R.; Dannerbauer, H.; De Breuck, C.; Decarli, R.; Edge, A. C.; Greve, T. R.; Knudsen, K. K.; Menten, K. M.; Rix, H.-W.; Schinnerer, E.; **Simpson, J. M.**; Wardlow, J. L. and van der Werf, P. P.,2013, *ApJ*, 768, 91

3. **An ALMA survey of submillimetre galaxies in the Extended Chandra Deep Field South: high-resolution 870 μm source counts** Karim, A.; Swin-

bank, A. M.; Hodge, J. A.; Smail, I. R.; Walter, F.; Biggs, A. D.; **Simpson, J. M.** and 16 additional co-authors, 2013, *MNRAS*, 432, 2

4. **The SCUBA-2 Cosmology Legacy Survey: blank-field number counts of 450-μm-selected galaxies and their contribution to the cosmic infrared background** Geach, J. E.; Chapin, E. L.; Coppin, K. E. K.; Dunlop, J. S.; Halpern, M.; Smail, I.; van der Werf, P. P.; Serjeant, S.; Farrah, D.; Roseboom, I.; Targett, T.; Arumugam, V.; Asboth, V.; Blain, A.; Chrysostomou, A.; Clarke, C.; Ivison, R. J.; Jones, S. L.; Karim, A.; Mackenzie, T.; Meijerink, R.; Michałowski, M. J.; Scott, D.; **Simpson, J. M.** and 29 additional co-authors, 2013, 432, 53

5. **The SCUBA-2 Cosmology Legacy Survey: demographics of the 450-μm population** Rosebooom, I. G.; Dunlop, J. S.; Cirasuolo, M.; Geach, J. E.; Smail, I.; Halpern, M.; van der Werf, P. P.; Almaini, O.; Arumugam, V.; Asboth, V.; Auld, R.; Blain, A.; Bremer, M. N.; Bock, J.; Bowler, R. A. A.; Buitrago, F.; Chapin, E.; Chapman, S.; Chrysostomou, A.; Clarke, C.; Conley, A.; Coppin, K. E. K.; Danielson, A. L. R.; Farrah, D.; Glenn, J.; Hatziminaoglou, E.; Ibar, E.; Ivison, R. J.; Jenness, T.; van Kampen, E.; Karim, A.;Mackenzie, T.; Marsden, G.; Meijerink, R.; Michałowski, M. J.; Oliver, S. J.; Page, M. J.; Pearson, E.; Scott, D.; **Simpson, J. M.** and ten additional co-authors, 2013, *MNRAS*, 430

6. **An ALMA Survey of Submillimeter Galaxies in the Extended Chandra Deep Field-South: The AGN Fraction and X-Ray Properties of Submillimeter Galaxies** Wang, S. X.; Brandt, W. N.; Luo, B.; Smail, I.; Alexander, D. M.; Danielson, A. L. R.; Hodge, J. A.; Karim, A.; Lehmer, B. D.; **Simpson, J. M.** and ten additional co-authors, 2013, *Apj*, 778, 179

7. **Star formation histories, extinction, and dust properties of strongly lensed $z \sim$ 1.5–3 star-forming galaxies from the Herschel Lensing Survey** Sklias, P.; Zamojski, M.; Schaerer, D.; Dessauges-Zavadsky, M.; Egami, E.; Rex, M.; Rawle, T.; Richard, J.; Boone, F.; **Simpson, J. M.**; Smail, I.; van der Werf, P. P.; Altieri, B. and Kneib, J. P., 2014, *A & A*, 561, A149

8. **An ALMA Survey of Sub-millimeter Galaxies in the Extended Chandra Deep Field South: Sub-millimeter Properties of Color-selected Galaxies** Decarli, R.; Smail, I.; Walter, F.; Swinbank, A. M.; Chapman, S.; Coppin, K. E. K.;

Cox, P.; Dannerbauer, H.; Greve, T. R.; Hodge, J. A.; Ivison, R.; Karim, A.; Knudsen, K. K.; Lindroos, L.; Rix, H.-W.; Schinnerer, E.; **Simpson, J. M.**; van der Werf, P. P. and Weiß, A., 2014, *ApJ*, 780, 115

9. **The SCUBA-2 Cosmology Legacy Survey: Ultraluminous Star-forming Galaxies in a z = 1.6 Cluster** Smail, I.; Geach, J. E.; Swinbank, A. M.; Tadaki, K.; Arumugam, V.; Hartley, W.; Almaini, O.; Bremer, M. N.; Chapin, E.; Chapman, S. C.; Danielson, A. L. R.; Edge, A. C.; Scott, D.; Simpson, C. J.; **Simpson, J. M.** and eleven additional co-authors, 2014, *ApJ*, 782, 19

10. **An ALMA survey of sub-millimetre Galaxies in the Extended Chandra Deep Field South: the far-infrared properties of SMGs** Swinbank, A. M.; **Simpson, J. M.** and 23 additional co-authors, 2014, *MNRAS*, 438, 1267

11. **An ALMA survey of submillimetre galaxies in the Extended Chandra Deep Field South: radio properties and the far-infrared/radio correlation** Thomson, A. P.; Ivison, R. J.; **Simpson, J. M.** and 18 additional co-authors, 2014, *MNRAS*, 442, 577

12. **Lens Models of Herschel-selected Galaxies from High-resolution Near-IR Observations** Calanog, J. A.; Fu, H.; Cooray, A.; Wardlow, J.; Ma, B.; Amber, S.; Baker, A. J; Baes, M.; Bock, J.; Bourne, N.;Bussmann, R. S.; Casey, C. M.; Chapman, S. C.; Clements, D. L.; Conley, A.; Dannerbauer, H.; De Zotti, G.; Dunne, L.; Dye, S.; Eales, S.; Farrah, D.; Furlanetto, C.; Harris, A. I.; Ivison, R. J.; Kim, S.; Maddox, S. J.; Magdis, G.; Messias, H.; Michałowski, M. J.; Negrello, M.; Nightingale, J.; O'Bryan, J. M.; Oliver, S. J.; Riechers, D.; Scott, D.; Serjeant, S.; **Simpson, J. M.** and five additional co-authors, 2014, *ApJ*, 797, 138

13. **An ALMA Survey of Submillimeter Galaxies in the Extended Chandra Deep Field South: Near-infrared Morphologies and Stellar Sizes** Chen, C.-C.; Smail, I.; Swinbank, A. M.; **Simpson, J. M.** and 18 additional co-authors, 2015, *ApJ*, 799, 194

be published without the author's prior written consent and information derived from it should be acknowledged".

Acknowledgements

It is a pleasure to thank both Ian Smail and Mark Swinbank for their supervision throughout my Ph. D. The guidance and advice that they have provided to me for the past three and a half years has been invaluable. During my time at Durham University it has been a pleasure to work as part of a great group and I'd like to thank Alice Danielson, Alastair Edge, Alex Karim, Chian-Chou Chen, Alasdair Thomson and Cheng–Juin Ma for all of their help and advice. Finally, I need to say big thank you to Caroline. You have supported me throughout my Ph. D. and always reminded me of what is important in life.

Dedicated to

my mum, for everything

Chapter 1

Introduction

1.1 Overview

The detection of the cosmic infrared background (Puget et al., 1996) showed that the energy density of the Universe is comparable at ultraviolet / optical and infrared wavelengths. The balance of the optical and infrared energy density of the Universe indicates that a large fraction of the light that is emitted by stars is reprocessed by dust and emitted in the infrared. An important consequence of this is that traditional surveys at optical wavelengths miss a large fraction of the obscured activity, and hence star-formation, that occurs in the Universe. Recent advances in instrumentation have made it possible to conduct sensitive surveys for extragalactic sources at infrared wavelengths. Conducted at a range of facilities, these surveys have uncovered large number densities of dusty, obscured galaxies that have extremely high levels of star formation. An important subset of the dusty galaxy population are sub-millimetre galaxies (SMGs), named purely due to their detection at sub-millimetre wavelengths. These SMGs are forming stars at colossal rates, dwarfing the amount of star formation within our own Galaxy by up to three orders of magnitude.

In this thesis I study the properties of SMGs and, using observational techniques, try to address the following key questions:

- How many of these intense starbursts exist, and at what epoch where they most prevalent?
- What is the spatial distribution of the ongoing star-formation, and how does this impact the host galaxy?

- How do far-infrared detected galaxies fit into our understanding of galaxy evolution?

At the start of each chapter of this thesis I give a detailed introduction that is relevant to the work presented. However, the following chapter gives a broad introduction to the field of galaxies, infrared emission and sub-millimetre astronomy.

1.2 Galaxies

The Copernican revolution, around 500 years ago, established the heliocentric model, placing the sun at the centre of our solar system. Nearly 250 years later observations of distant "nebulae" were made that would instigate a similar revolution in our understanding of the Universe. In the late 18th century both Messier (1781) and Herschel (1786) presented large catalogues of "nebulae" in which they unwittingly catalogued extragalactic sources; it would take a further 150 years from the publishing of these catalogues for the existence of other galaxies to be accepted. The first detailed study of the many known "nebulae" was conducted by William Parsons, the third Earl of Rosse, using the 1.8 m "Leviathan of Parsonstown" telescope. With the unique ability to resolve many of these "nebulae", Lord Rosse identified the spiral structure that is present in a subset of these sources. Early spectroscopy built upon the observations of Lord Rosse, and showed that these "spiral nebulae" are indeed conglomerations of stars (Huggins, 1864; Scheiner, 1899) with radial velocities far exceeding any other known astronomical object (Slipher, 1914). However, it was observations of pulsating stars, Cepheid variables, that proved irrefutably that "spiral nebulae" are indeed galaxies in their own right. By exploiting the period-luminosity relation for Cepheid's, Hubble demonstrated in 1925 that these galaxies lie at distances far beyond the known extent of the Milky-Way (Hubble, 1926, 1929).

The Universe is now known to contain a vast number of galaxies with a wide-range of masses, colours and morphologies. In 1926, Hubble presented a morphological classification for galaxies, using the visual appearance of their stellar distribution, that is still in use today. Hubble placed galaxies into three broad classes: ellipticals that have a smooth, spheroidal distribution of stars; lenticulars, which appear similar to ellipticals but have an additional smooth disc of stars; and spiral galaxies that have both a central concentration of stars and a disc of stars that is either barred / un-barred, and has spiral arm features. Moving along the Hubble sequence, galaxies are referred to as either "early-types" (ellipticals and lenticulars) or "late-types" (spiral galaxies). Frequently,

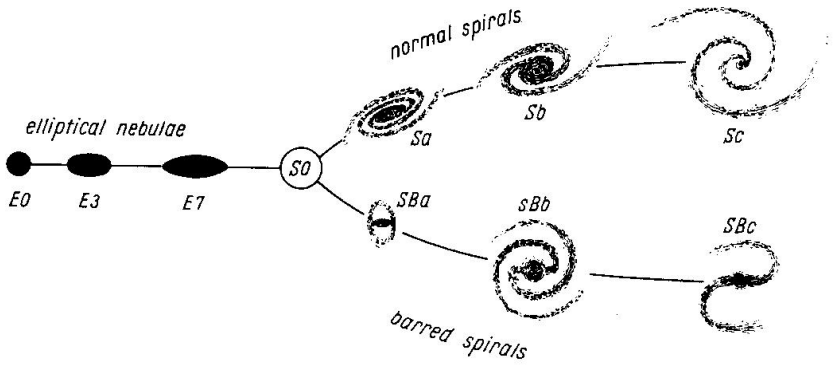

Figure 1.1: The traditional "tuning fork" classification of galaxies, presented by Hubble in 1936.

the nomenclature of "early-" and "late-type" galaxies adopted by Hubble is interpreted, incorrectly, as representing an evolutionary sequence. In fact, such a temporal connection was never intended by Hubble, who choose the notation to describe the increasing complexity of spiral galaxies (see the footnotes of Hubble (1926) in which the temporal connection is disregarded.). Indeed, spectroscopy has shown that early-type galaxies have old, quiescent, stellar populations, whereas late-type galaxies are actively star-forming, and have a younger stellar population. Hence, in an evolutionary context, the arrow of time generally points from late-type to early-type galaxies on the Hubble sequence.

Understanding how galaxies evolve into their classifications along the Hubble sequence is one the fundamental challenges of extragalactic astronomy. A powerful method to investigate galaxy evolution, amongst the many techniques that are available, is to observe the progenitors of local galaxies. In this thesis I use observations of dusty, obscured, star-forming galaxies selected at around the peak of the cosmic star-formation rate of the Universe. By studying such galaxies we can gain an insight into galaxy formation at a period when the Universe was most active, and before it settled into the relatively inert place that it is today.

1.3 Growth of Galaxies

Fundamentally, galaxies are comprised of three main components: stars; an interstellar medium of dust and gas; and dark matter. To understand how galaxies form, and evolve, we therefore need to study galaxies when they are most actively forming stars. By tracing the total star formation of the Universe, as a function of its age, we can determine when the stellar mass that we see in galaxies today was formed. If we observe galaxies when they are forming stars then we can gain insights in to their properties, and thereby understand

how they evolved into the galaxies that we observe locally.

The star formation rate (SFR) of a galaxy can be measured using a number of different methods. However, nearly all of the methods to measure the SFR of a galaxy are driven by ultraviolet (UV) emission from the youngest, most massive stars. When stars form in a galaxy they do so from dense regions of molecular gas clouds, and with a distribution of masses known as an initial mass function (IMF). The most massive stars that form dominate the UV emission from the stellar population, but have a short lifetime. Hence the integrated UV emission from a galaxy fades rapidly after an initial burst of star formation. If a galaxy has been forming stars for longer than ~ 30 Myrs (see Madau & Dickinson 2014) the amount of UV emission reaches a limiting value. As such, by observing the UV emission from a galaxy it is possible to infer the instantaneous SFR, although this estimate may be sensitive to fluctuation in the SFR on small timescales.

By tracing the evolution of the star formation rate density (SFRD) of the Universe with time we can understand when galaxies were most actively forming stellar mass. Arguably the first major study of the cosmic SFRD of field galaxies, using UV emission, was presented by Lilly et al. (1995), who combined spectroscopic redshifts from the Canada-France Redshift Survey (CFRS) with the available $BVIK$ photometry. Lilly et al. (1995) measured the UV luminosity density of galaxies out to a redshift of $z \sim 1$, and showed that this was around an order of magnitude higher than is seen locally, inferring a rapid rise in cosmic star formation. Madau et al. (1996) built upon the results presented by Lilly et al. (1995) and extended the redshift range surveyed to $z \sim 4$, using Lyman Break Galaxies (LBGs). However, the analysis by Madau et al. (1996) only placed lower limits on the SFRD at high redshift. More recent studies placed further constraints on the SFRD of the Universe and established that the cosmic star formation rate density appears to peak at $z \sim 1$–2 (Connolly et al., 1997; Pascarelle et al., 1998; Steidel et al., 1999), and then declines again out to higher redshifts.

When discussing how to trace the SFRD of the Universe, using emission at UV wavelengths, I have neglected to mention a significant complication: dust. The effect of dust is to extinct UV and optical emission, and this must be corrected for in studies that measure SFRs through UV emission (see Section 1.4). Indeed, the extinction of UV light due to dust is so strong that even a small amount of dust can lead to orders of magnitude correction to the UV light. The issue of dust is exacerbated in the most rapidly star-forming galaxies, since it is produced via supernovae and asymptotic giant branch (AGB)

stars. The most rapidly star-forming galaxies produce the largest number of supernovae and AGB stars, and hence may be expected to contain the most dust. Thus, studies that use UV light to trace star formation require a significant correction to measure the unattenuated UV emission, and may miss the most actively star forming systems altogether (see Figure 1.3).

1.4 Importance of Obscured Activity

The term dust covers a large number of complex molecules, whose size and composition we still do not fully understand. Currently, the best model is that dust is comprised of a mixture of amorphous silicates and carbonaceous grain, with typical sizes of $\lesssim 1\,\mu$m. The carbonaceous grains represent dust that is dominated in mass by carbon atoms, the smallest of which are polycyclic aromatic hydrocarbons (PAHs). The size of the dust grains is vitally important as incident light preferentially interacts with grains of comparable size to the wavelength of the light. It is for this reason that the extinction is so significant at UV wavelengths. Photons that are incident upon a dust grain can be affected in two ways: scattered, resulting in a "reddening" of the observed light, as the size distribution of the grains results in a preferential scattering of "bluer" light; or absorbed, which heats the dust grains. The heated dust grains cool via thermal emission and emit in the infrared in the form of a modified blackbody

$$S_\nu \propto e_\nu B_\nu, \tag{1.4.1}$$

where B_v represents the planck function, and e_ν, the emissivity function, is $\propto \nu^\beta$. The value of β is dependant on the properties of the dust, but is typically assumed to take a value of 1–2 (Dunne & Eales, 2001; Chakrabarti & McKee, 2008; Magnelli et al., 2012). The peak wavelength of the infrared emission is sensitive to the temperature of the dust (T_d), and is at $\sim 100\,\mu$m for $T_d \sim 30\,$K. Around 99 % of the infrared emission from a galaxy arises from thermal dust emission, with the remaining energy emitted by molecular and atomic emission line transitions.

As dust is inherently linked to the process of star formation, we may expect that a significant proportion of the UV emission from young stellar populations is reprocessed, and emitted as infrared light. To get a complete picture of star formation we thus need to observe galaxies in both UV and infrared emission. Ground based observations in

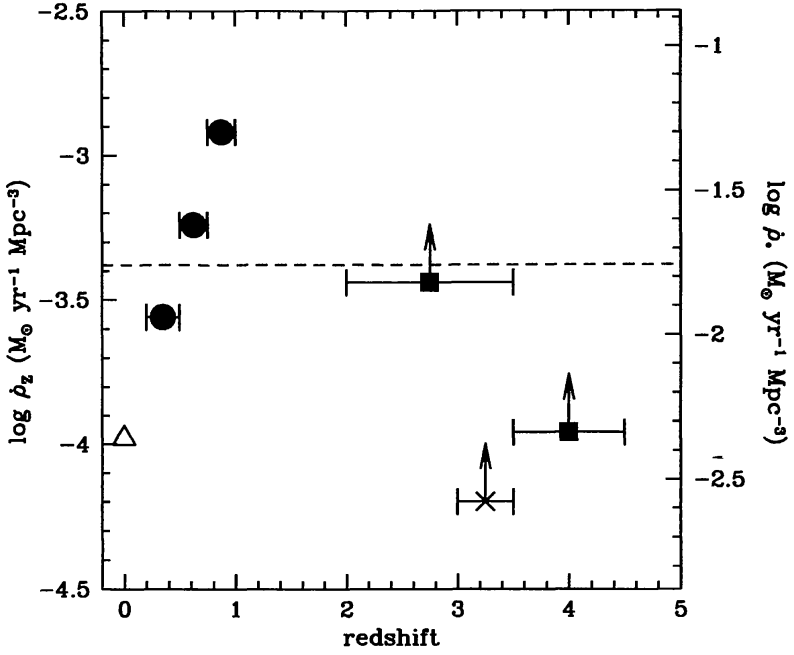

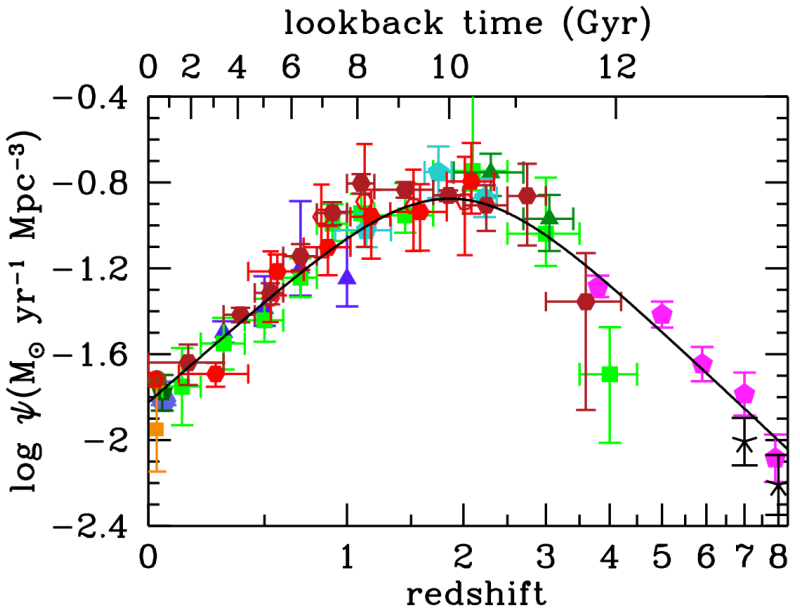

Figure 1.2: Left: The cosmic star formation rate density of the Universe, measured from UV emission. The figure is taken from Madau et al. (1996). The filled circles are taken from Lilly et al. (1995), and are measured using of sample of spectroscopically confirmed galaxies with ground based $BVIK$-photometry. Madau et al. (1996) built upon this result using LBGs detected in *HST* imaging, and placed lower limits on the UV SFRD of the Universe at z 2–4 (see also Steidel et al. 1996). The observations helped establish that the amount of star formation in the Universe rises rapidly out to $z \sim 1$, but they do not account for the effects of dust extinction. **Right:** The current, best measurement of the cosmic SFRD from a combination of UV and infrared studies (see Madau & Dickinson 2014). The combined studies show that star formation activity in the Universe peaked at around $z \sim 2$, at around 25% of the current age of the Universe.

the infrared are inherently challenging as molecules in the Earth's atmosphere (primarily H_2O) render the atmosphere opaque at all but a few near- / mid-infrared wavelengths (the atmospheric transmission improves at far-infrared / sub-millimetre wavelengths). Small atmospheric windows with high transmission mean that ground based observations are feasible at carefully selected near- / mid-infrared wavelengths, but these are further complicated by the variability of the sky brightness, and the thermal emission of the both the Earth and the telescope, which must be carefully subtracted. The first, large infrared survey was conducted with the *Infrared Astronomy Satellite* (*IRAS*). Launched in 1983, *IRAS* was used to survey 96 % of the sky at 12, 25, 60 and 100 μm, and at a resolution of 30–120″. In total over a quarter of a million sources were detected, primarily at low redshift. The vast majority of *IRAS* sources correspond to "normal" galaxies, but a small number of very high luminosity sources were detected. These bright sources correspond to Luminous InfraRed Galaxies (LIRGs) with total infrared luminosities (integrated 8–1000 μm) of $10^{11}\,\mathrm{L}_\odot < L_{IR} < 10^{12}\,\mathrm{L}_\odot$, or UltraLuminous Infrared Galaxies (ULIRGs) with $L_{IR} > 10^{12}\,\mathrm{L}_\odot$, and high SFRs of $\gtrsim 100\,\mathrm{M}_\odot\mathrm{yr}^{-1}$. Follow-up observations determined that these "starburst" galaxies are primarily major-mergers, establishing the view that merger activity leads to high star-formation rates (Lonsdale et al., 1984; Sanders et al., 1988; Murphy et al., 1996; Veilleux et al., 2002). Recently, high-resolution imaging has shown that the star-formation in these local U / LIRGs occurs on scales of 1–2 kpc, with compact knots of star-formation on scales of 100 pc (Condon et al., 1991b; Downes & Solomon, 1998; Soifer et al., 1999; Sakamoto et al., 2008; Rujopakarn et al., 2011; Ueda et al., 2014). In contrast, "normal" star-forming disc galaxies have low-level star-formation on scales of ~ 10 kpc.

Determining the total amount of light emitted in the infrared, from all galaxies at all redshifts, is crucial to understanding the importance of obscured star formation for galaxy evolution. Although *IRAS* mapped almost the entire sky, the uncertainty on the absolute zero point for brightness measurements was too large to robustly detect the cosmic infrared background (CIB). The CIB was first detected by the Far-InfraRed Absolute Spectrophotometer (FIRAS) and Diffuse InfraRed Background Experiment (DIRBE) instruments onboard the *Cosmic Background Explorer* satellite (*COBE*). The instruments onboard *COBE* were designed to limit stray light contamination and reduce systematic uncertainties, both of which must be minimised to robustly detect the CIB. Puget et al. (1996) presented the first, robust, detection of the CIB with observations taken with

Figure 1.3: A composite image of the Antennae galaxies, an intense starburst triggered by the merger of two spiral galaxies. The image was created by overlaying a composite ALMA image of the carbon monoxide emission (Band 3 & 7) from the galaxy on to a *HST* image taken at visible wavelengths. The young, unobscured stars in the galaxy are traced by visible light (blue), whereas the ALMA observations (yellow,pink,red) trace the cold, dense gas in which new stars are forming. The image highlights that large areas of the ongoing star formation in this galaxy are not visible in the *HST* imaging. Credit: ALMA (ESO/NAOJ/NRAO). Visible light image: the NASA/ESA Hubble Space Telescope.

the FIRAS instrument at $\lambda > 200\,\mu$m. Subsequent analysis of data taken with DIRBE confirmed this across a range of wavelengths from 2.2–240 μm (see Hauser & Dwek 2001).

The detection of the CIB confirmed the importance of observing galaxies at infrared wavelengths. Importantly, the energy density of the infrared background was found to be comparable in magnitude to the UV / optical background (see Figure 1.4). In the local Universe the infrared background is only around a third of the optical background (Soifer & Neugebauer, 1991), and hence the balance across all epochs indicates that obscured activity must become more important at higher redshifts. However, in order to understand the importance of the CIB for galaxy formation it must first be resolved it into discrete sources. Once the CIB has been resolved, it is then possible to determine the redshifts of the sources and so determine the epoch of stellar mass growth in obscured galaxies.

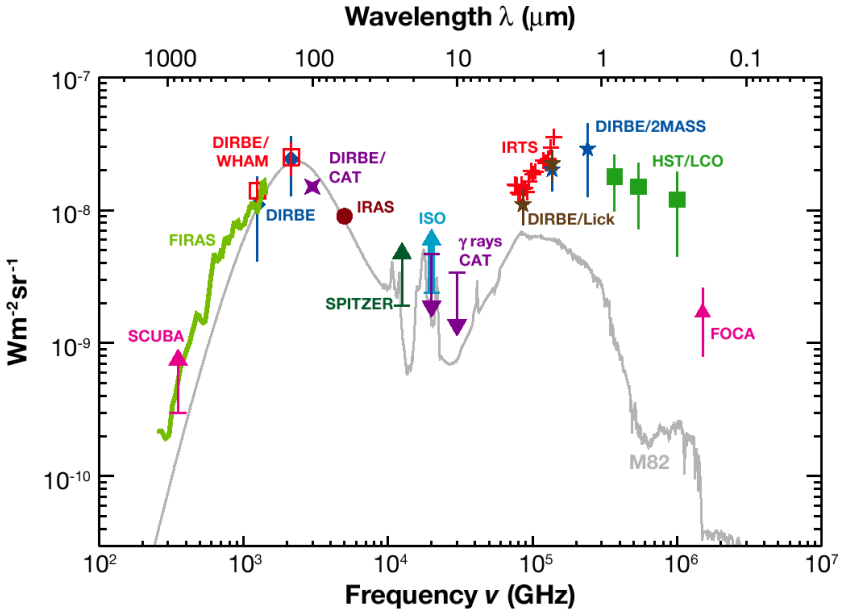

Figure 1.4: The energy density of the Universe, from UV to millimetre wavelengths. The figure is taken from Lagache et al. (2005), and references for individual data points are given therein. Observations with instruments onboard *COBE* showed for the first time that the energy density of the cosmic infrared background is comparable to that in UV / optical, indicating that a significant proportion of stellar emission is reprocessed by dust.

1.5 Sub-millimetre Galaxies

Resolving the infrared background into individually detected galaxies is a non-trivial task, especially out to high redshift. Ideally, a survey for infrared galaxies would target sources at the peak of the infrared spectral energy distribution (SED); the peak is at around $\sim 100\,\mu$m ($T_d \sim 30\,$K), and is shifted to higher wavelengths with increasing redshift. The brightness of the sky, as well as absorption in the Earth's atmosphere, means that ground based observations are not feasible at these wavelengths until atmospheric windows begin to open up at $\sim 350\,\mu$m (see Figure 1.5). At far-infrared wavelengths it also becomes necessary to build telescopes with larger primary mirrors in order to resolve individual galaxies. The resolution of a telescope is set by $1.22\lambda\,/\,D$, where D is the diameter of the primary mirror. At redshifts $\gtrsim 0.5$, an angular resolution of around an arcsecond is required to resolve individual galaxies: a telescope designed to operate at $100\,\mu$m with a resolution of $\sim 1.5''$ requires a primary mirror with a diameter of 20 m. The technical challenge of putting a reasonable resolution, sensitive, far-infrared telescope in space meant that initial searches for far-infrared galaxies were conducted at ground based facilities

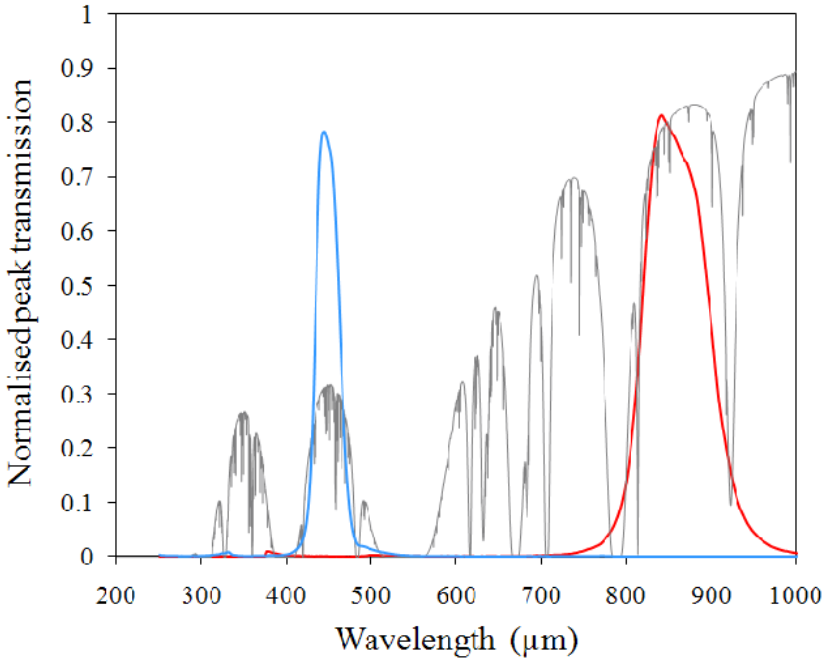

Figure 1.5: The atmospheric transmission at the summit of Mauna Kea, for 1 mm of precipitable water vapour (τ_{225}=0.06). Overlaid on the atmospheric transmission are the filter bandpasses for the SCUBA-2 instrument at the JCMT. SCUBA-2 is a bolometer camera that observes simultaneously at 450 μm (blue) and 850 μm (red). Even at the summit of Mauna Kea (13796 ft) sensitive observations at 450 μm are only possible in the best weather conditions. The figure is taken from Holland et al. (2013).

(although recently this changed with the launch of the *Herschel Space Observatory* in 2009). The transmission of the Earth's atmosphere towards sub-millimetre wavelengths and, other than the local *IRAS* samples, observations of infrared galaxies initially focused on two key atmospheric windows, at $\sim$450 and $\sim$850 μm.

At sub-millimetre wavelengths the Rayleigh-Jeans limit applies and the infrared emission from a modified black-body (Equation 1.4.1) can be approximated as

$$S_\nu \propto e_\nu \nu^2 \propto \nu^{2+\beta}, \tag{1.5.2}$$

where β is assumed to take a value between 1–2. The emitted frequency of the observed light increases with redshift. Hence, for observations at a fixed sub-millimetre wavelength, the peak of the infrared emission from a redshifted source moves towards the observed frequency. The effect of the increasing emitted frequency is that the *observed* flux from a source increases rapidly until the peak of the infrared emission is redshifted out of the

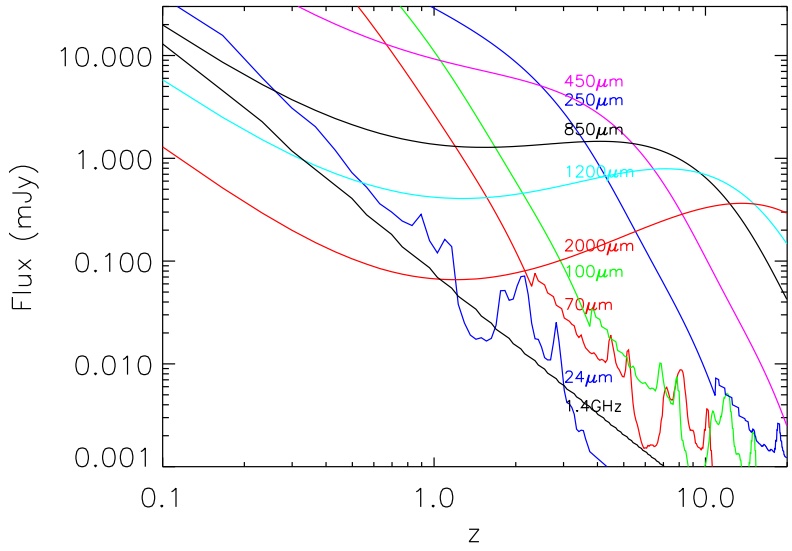

Figure 1.6: The observed flux from the well-studied SMG, SMM J2135−0102 , across a wide redshift range, and at a range of observed wavelengths. For observations at sub-millimetre wavelengths the "negative K correction" counters the apparent dimming of a source due to its increased distance with increasing redshift. At 850 μm the observed flux from the source is roughly constant over the redshift range $z \sim 1$–7. For sources with the same infrared SED the "negative K-correction" means that a $\sim 850\,\mu$m selection yields an almost uniform selection of star-forming galaxies at high redshift.

sub-millimetre band, countering the dimming of the source due to increasing distance. The effect of increasing *observed* flux with redshift is known as the "negative K-correction", and is one of the key advantages of observing at sub-millimetre wavelengths. In Figure 1.6 the *observed* flux at a range of sub- / mm wavelengths, and as a function of redshift, is shown for a dusty, star-forming galaxy. For observations at $\sim$850 μm the "negative K-correction" means that a source with a fixed infrared luminosity has the same *observed* flux across a redshift range of $z \sim 1$–7. The consequence of the "negative K-correction" at $\sim$850 μm is hugely important: for sources with the same intrinsic infrared spectral energy distribution (SED), observations at $\sim$850 μm provide a uniform selection in infrared luminosity (a proxy for star formation) back to a time when the Universe was < 1 Gyr old.

1.5.1 Sub-millimetre surveys

The commissioning of the Sub-millimetre Common User Bolometer Array (SCUBA) at the James Clerk Maxwell Telescope (JCMT) kick-started the field of extragalactic sub-mm astronomy. The combination of advances in bolometer technology, and a location at one of the worlds driest observing sites, meant that SCUBA had unparalleled sensitivity at 450 and 850 μm along with a substantial field-of-view ($\sim 2'$). The first SCUBA-detected sub-mm sources were presented by Smail et al. (1997) in observations of two, massive galaxy clusters. The observations exploited the effect of gravitational lensing by the foreground clusters, to search for sub-mm emission from background, lensed sources. In total, six 850 μm sources were detected in the ~ 2 mJy rms imaging. After correcting the measured fluxes of the sources for the effect of lensing, Smail et al. (1997) showed that the surface density of 850 μm sources was approximately three orders of magnitude higher than expected from a non-evolving model of the local IRAS 60 μm luminosity function. Furthermore, it was demonstrated that strong evolution of the luminosity density to $z \gtrsim 2$ was required to explain the large surface density of sub-mm sources, indicating that the SFRD of the Universe continued to increase beyond the redshift probed by surveys of UV emission (see Figure 4.8). The first observations of SCUBA-detected sub-mm sources by Smail et al. (1997) were rapidly complemented by small, blank field surveys with SCUBA that confirmed the strong evolution with redshift of the sub-mm population (Barger et al., 1998; Hughes et al., 1998).

Over the following decade a number of sub-mm surveys with increasing area and sensitivity were conducted, primarily with either SCUBA or the MAx-planck Millimetre BOlometer (MAMBO) camera, operating at 1.2 mm on the Institut de RadioAstronomie Millimétrique (IRAM) 30 m telescope (see Blain et al. 2002; Casey et al. 2014 for a review of the early sub-mm surveys). The culmination of surveys with SCUBA at the JCMT was the SCUBA HAlf-DEgree Extragalactic Survey (SHADES; Coppin et al. 2006), which obtained deep sub-mm imaging of two extragalactic fields: Lockman Hole (LH) and the Subaru-XMM Deep Field (SXDF). The SHADES observations mapped an area of 720 arcmin^2 to a depth of ~ 2 mJy, and detected 120 850 μm, sub-mm sources.

At the start of this project, the LABOCA survey of the Extended *Chandra* Deep Field South (LESS; Weiß et al. 2009) was the largest, contiguous survey at 870 μm. The LESS observations imaged an area of 0.25 deg^2 to a uniform depth of 1.2 mJy, and detected 126 sub-mm sources with 870-μm flux densities of $S_{870} > 4.4$ mJy. Surveys conducted

with the AzTEC camera, located at both the JCMT and the Atacama Sub-millimetre Telescope Experiment (ASTE), provided similar, large-area, uniform-noise, imaging, but at a longer wavelength of 1.1 mm. The number of dusty, obscured starbursts detected at sub-millimetre wavelengths increased dramatically with the launch of the *Herschel Space Observatory* (*Herschel*; Pilbratt et al. 2010) in 2009. The H-ATLAS (Eales et al., 2010) and HERMES (Oliver et al., 2012) legacy surveys observed large areas of the sky (∼570 and $\sim 370\,\mathrm{deg}^2$, respectively) at 250–500 μm with the Spectral and Photometric Imaging Receiver (SPIRE; Griffin et al. 2010) onboard *Herschel*, at a wide range of 1–σ depths from ∼5–50 mJy RMS. The effect of the K-correction (see Figure 1.6) means that these SPIRE-selected sources are not uniformly selected in redshift, while the large beam size ($\sim 36''$ at 500 μm) means that source blending is a serious concern. However, the observations taken with the instruments onboard *Herschel* have been invaluable for constraining properties of dusty starbursts, and provide data with sufficient sampling in wavelength to accurately model the far-infrared SED of sub-mm sources.

In 2011 the SCUBA-2 instrument was installed at the JCMT, providing significantly increased mapping speed and sensitivity relative to SCUBA. The SCUBA-2 Cosmology Legacy Survey (S2CLS) is the largest of the legacy surveys to be allocated guaranteed time with SCUBA-2, and had the initial aim of surveying $\sim 30\,\mathrm{deg}^2$ to ∼1mJy RMS, at 850 μm. The S2CLS project was descoped due to the transfer of ownership of the JCMT, but it will still provide a sample of many thousands of 850 μm sources, selected across seven key extragalactic fields.

1.5.2 Number Counts

The 850 μm number counts were one of the most fundamental properties of the infrared Universe that was unveiled in the first sub-mm surveys. The number counts are a crucial property of the sub-mm population, as they represent both the total amount of the CIB that has been resolved into discrete sources, and the distribution of the CIB (and hence SFR) amongst the detected galaxies. Perhaps the key use of the number counts is to place strict observational constraints on theoretical models of galaxy formation. It quickly became apparent that the number density of sub-mm sources detected by SCUBA was significantly higher than those predicted by models of galaxy formation that attempt to reproduce observations of the far-infrared Universe (Blain et al., 1999a; Devriendt & Guiderdoni, 2000; Granato et al., 2000). To account for the high surface density of sub-mm

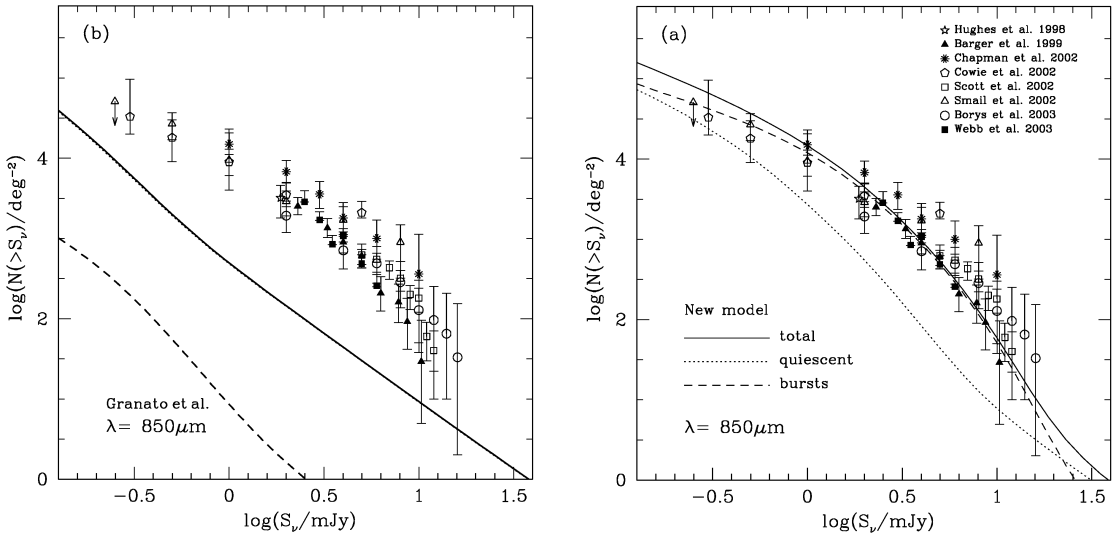

Figure 1.7: Left: The observed 850 μm cumulative number counts from a combination of surveys with SCUBA at the JCMT (see right panel for key). Overlaid on the figure are the predicted total counts (solid line) from using the semi-analytic model of galaxy formation GALFORM in conjunction with GRASIL (Granato et al., 2000). The theoretical cumulative counts under-predict the observations by over an order of magnitude at $S_{850} \sim 1$–15 mJy **Right:** The 850 μm number counts (solid line) from the Baugh et al. (2005) version of GALFORM. The new version of GALFORM reproduced the observed sub-mm number counts, but required a significant change to the treatment of starbursts in the model. A top heavy IMF was introduced for starburst galaxies, increasing the dust production and hence the observed sub-mm flux density from these sources. Both panels of the figure are taken from Baugh et al. (2005).

sources a number of significant changes to galaxy formation models were required. For example, to correct the mis-match between the observed counts, and the sub-mm number counts predicted by the Durham semi-analytic model of galaxy formation GALFORM and observations, Baugh et al. (2005) made controversial changes to the treatment of the most active starbursts. A top heavy IMF was adopted in starbursts, which results in a larger fraction of massive stars and hence an increase in both the amount of UV emission per stellar mass formed, and the total dust mass. The overall effect is an increase in the sub-mm flux from starburst galaxies, and Baugh et al. (2005) demonstrated that the change to the model results in number counts that are in agreement with observations (see Figure 1.7). As well as semi-analytic models, numerical simulations have also been used to model the properties of sub-mm sources. These simulations have reproduced the sub-mm number counts, typically at the expense of a mis-match with other observational constraints, but are not restricted by the requirement to reproduce the properties of

galaxies in the local Universe (e.g. Davé et al. 2010; Narayanan et al. 2010; Hayward et al. 2013b).

It is clear from the changes that were required to early theoretical models of the far-infrared Universe that the number counts of sub-mm sources have the potential to place powerful constraints on galaxy evolution. The impact of SMGs is perhaps unsurprising since they represent some of the most extreme sites of star-formation in the Universe and, as with all extreme events, these are most challenging to reproduce. However, it is important to note that the impact of the sub-mm number counts on galaxy formation models is dependant upon their accuracy. As I discuss in the Section 1.5.3, the coarse resolution (FWHM = 15–30″) of sub-mm observations at single-dish facilities, combined with the large volume probed due to the "negative K-correction", means that there is significant potential for the blending of multiple sub-millimetre galaxies (SMGs) into a single sub-mm source. In such a scenario the shape of the sub-mm number counts would appear distorted in single-dish observations, with bright sources created artificially due to blending.

1.5.3 Multi-wavelength Identifications

Initial attempts to understand the properties of sub-mm sources were significantly hampered by the coarse resolution provided by single-dish facilities. The JCMT and SCUBA represented an ideal combination of a high-altitude site, sensitive sub-mm detector, and a 15 m diameter telescope. However, despite the JCMT being one of the largest telescopes operating at sub-mm wavelengths, the resolution of observations at 850 μm is only 14.5″. As such, although the CIB has been resolved in to discrete sources, the resolution is not sufficient to resolve it into individual, precisely located galaxies. Identifying the correct counterpart to the sub-mm emission allows fundamental properties such as the redshift or far-infrared luminosity of the source to be determined, and hence is a vital step towards understanding the sub-mm galaxy population. The surface density of optical sources is such that multiple potential counterparts exist within the beam of the sub-mm observations ($\gtrsim$5–10; see Figure 1.8). Optical identifications are made even more challenging by the dusty nature of sub-mm sources, which means that they are expected to be faint at optical wavelengths (Smail et al., 2002).

A breakthrough in identifying sub-mm sources came with the realisation that the far-infrared–radio correlation, along with high-resolution ($\sim$arcsecond) radio imaging, could

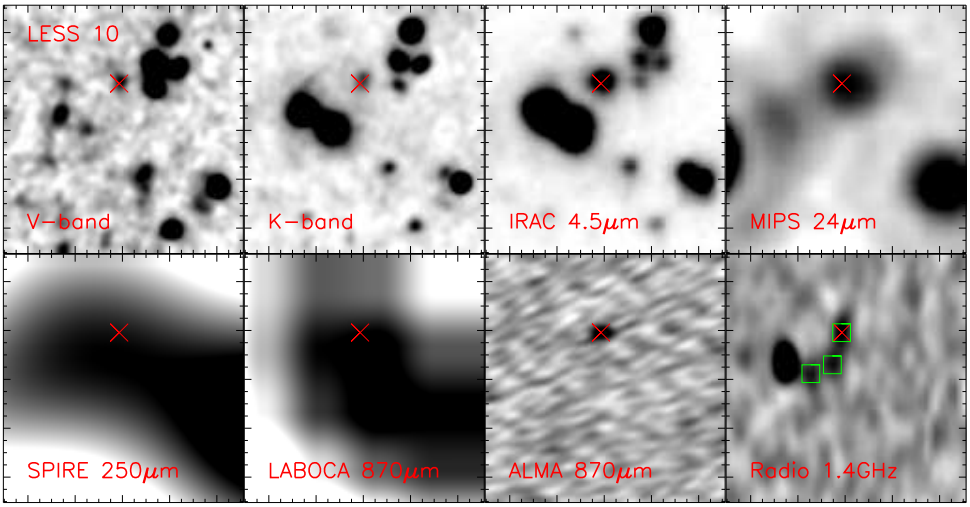

Figure 1.8: $13'' \times 13''$ thumbnails of the optical-to-radio emission from LESS 10, an example single-dish-detected, 870 μm source. The resolution of the LABOCA 870 μm imaging (FWHM = 19.2″) is too coarse to identify the individual galaxies responsible for the sub-mm emission. Prior to high-resolution interferometric follow-up at sub-mm wavelengths, the optical counterparts were typically identified using correlations with emission at other wavelengths. High-resolution ALMA imaging, taken as part of the ALESS survey, confirms that one of the radio identifications (square; Biggs et al. 2011) for LESS 10 is correct (cross), but demonstrates that two of the robust identifications are incorrect (Hodge et al., 2013b).

be exploited to accurately pinpoint counterparts to sub-mm sources. The far-infrared–radio correlation is a well-studied relation between the infrared emission and radio emission from galaxies at both low and high redshift (de Jong et al., 1985; Helou et al., 1985; Condon et al., 1991a; Yun et al., 2001; Vlahakis et al., 2007; Ivison et al., 2010a). The relation is believed to be due to the emission at both wavelengths sharing a common source: massive stars. The UV emission from massive stars heats dust grains that cool thermally and produce the majority of the infrared emission from a galaxy. When the same stars go through a supernova phase they produce the relativistic electrons responsible for the synchrotron emission that dominates the radio spectrum of a galaxy at frequencies $\lesssim 20$ GHz (see Condon 1992) resulting in the observed relation between FIR and radio fluxes.

Deep, panoramic radio imaging obtained primarily with the Very Large Array (VLA) at 1.4 GHz, has been used to try and locate the counterparts to sub-mm sources (e.g. Ivison et al. 2002, 2004, 2007; Bertoldi et al. 2007; Biggs et al. 2011; Lindner et al. 2011). However, the reliability of the identified counterparts is probabilistic, and is typically determined

using the *corrected poissonian probability*, or p-stat, which determines the probability that a radio source is detected by chance within the error circle of the sub-mm emission. A value of $p \leq 0.05$ is usually taken to represent a *robust* counterpart. Recently, attempts have been made to extended the identification methods to both $24\,\mu$m and $3.6\,\mu$m (e.g. Biggs et al. 2011). While the emission at these wavelengths does have a correlation with the emission at sub-mm wavelengths the surface density of sources is much higher than at radio wavelengths. The effect of the higher surface density is to increase the number of potential counterparts and, as I discuss in Chapter 2, identifications at $24\,\mu$m and $3.6\,\mu$m have been found to be less reliable than identifications at radio frequencies.

Although the technique of identifying sub-mm sources via emission at different wavelengths (primarily at 1.4 GHz) is powerful it has significant drawbacks. The technique is inherently probabilistic, and makes assumptions about the multiwavelength properties of sub-mm sources. In the case of radio identifications it depends on the form of the far-infrared–radio correlation at high redshift and its applicability to sub-mm galaxies, both of which had not been accurately determined at the start of this thesis. The more immediate concern is that observations at alternative wavelengths do not benefit from the "negative K-correction" that makes observations at sub-mm wavelengths so appealing. Indeed, the radio emission from a galaxy suffers a "positive K-correction", and at the current depth of radio imaging it becomes increasingly challenging to detect sub-mm sources at $z \gtrsim 2.5$ (see Figure 1.6).

A further complication to the multi-wavelength identification procedure is caused by the potential blending of multiple individual SMGs into a single sub-mm source. Such source blending is somewhat expected given the coarse resolution of single-dish surveys but the issue is exacerbated by the negative K-correction. The negative K-correction means that a sub-mm selection probes a large redshift range ($z \sim 1$–8), and hence provides a large path length for line-of-sight projections. The first tentative evidence for source blending came from studies of sub-mm sources that employ radio identifications, and which often identify multiple *robust* counterparts to a single sub-mm source (e.g. Ivison et al. 2007). However, these radio identifications cannot unambiguously confirm the prevalence of source blending, and similarly cannot determine the distribution of sub-mm flux amongst the individual components.

The multiwavelength identification procedure typically provides *robust* counterparts to only 50–60 % of sub-mm sources. Hence, while the identification procedure is clearly

useful for investigating a subset of the sub-mm population it imprints additional selection effects onto the initial sub-mm selection, which is otherwise broadly uniform with redshift. Ideally, we would like to identify sub-mm sources through high-resolution imaging at their initial selection wavelength. Such observations would allow us to confirm the reliability of the multiwavelength identifications, and identify the large subset of the sub-mm population that remains unidentified.

With current technology it is not feasible to build an operational telescope with a sufficiently large, filled aperture to resolve sub-mm sources into individual galaxies. Instead, observations with dedicated sub-mm / mm interferometers are required, which provide the 1–2″ resolution needed to resolve these sources. A number of individual sub-mm sources have been followed-up at high-resolution with both the IRAM Plateau de Bure Interferometer (PdBI) and the Sub-Millimetre Array (SMA). However, while these facilities offer the only definitive route to pinpoint the SMGs contributing to a single-dish detected sub-mm source, their sensitivity has meant that follow-up observations have only been conducted for an inhomogenously selected subset of the brightest sub-mm sources, and often at different wavelengths to the initial single-dish selection. (e.g. Gear et al. 2000; Iono et al. 2006; Wang et al. 2007; Younger et al. 2007, 2009; Dannerbauer et al. 2008; Cowie et al. 2009; Aravena et al. 2010; Wang et al. 2011).

A particularly interesting follow-up study was presented by Wang et al. (2011), who used observations with the SMA to show that two bright sub-mm sources were comprised of blends of two-or-three individual SMGs, with flux densities of $S_{850} = 3$–$5\,\mathrm{mJy}$. The result confirmed the earlier tentative evidence that source blending may be significant, and cast serious doubts on the validity of the brightest sources that are detected in single-dish surveys. As discussed earlier, source blending has a significant impact on the number counts of SMGs, and biases the form of the number counts that have been used to constrain theoretical models of galaxy formation. In order to use the number counts of SMGs as a constraint on these models it is imperative to determine the *intrinsic* sub-mm number counts.

The recent commissioning, and start of operations, at the Atacama Large Millimetre / sub-millimetre Array (ALMA), promises to revolutionise our understanding of SMGs. When completed ALMA will consists of a main array of fifty four 12 m, and twelve 7 m, diameter antennae, and will be capable of observing on baselines of up to $\sim$16km. In comparison, the PdBI and SMA are comprised of six 15 m, and eight 6 m antennae,

respectively. The start of operations at ALMA means that it is now possible to obtain sensitive, high-resolution images of large samples of single-dish sub-mm sources. It is studies of uniformly selected sub-mm sources with ALMA that form the majority of the work presented in this thesis.

1.5.4 Properties of sub-millimetre galaxies

In order to characterise, and study, the sub-mm population it is crucial to determine the redshifts of individual sources. At the start of this thesis, the radio-identified subset of the 850 μm population were the best-studied to date. In 2005, Chapman et al. presented observations with the Low Resolution Imaging Spectrograph (LRIS), located at the Keck 10 m telescopes on Mauna Kea, of 104 radio-identified sub-mm sources (out of a complete sample of 150 sources). In total, spectroscopic redshifts were determined for 73 radio-identified SMGs ($\sim$50% of the total sample), and this subset of the SMG population was shown to have a median redshift of $z = 2.2 \pm 0.1$. By necessity the Chapman et al. (2005) sample is an amalgamation of sub-mm sources detected in SCUBA observations of seven well-studied extragalactic fields. Although the sample does not have a uniform selection function the Chapman et al. (2005) sample remain the best studied SMGs to date. The observations confirmed that these dusty, obscured sources lie at high-redshifts, and that they have FIR-luminosities of $\gtrsim 10^{12}\,L_{\odot}$, comparable to local ULIRGs. Importantly, the observations demonstrated that the space density of ULIRGs at $z \sim 2$ is $\sim 1000\times$ higher than at $z = 0$. Guided by the spectroscopic redshifts presented by Chapman et al. (2005), numerous studies have now characterised the physical properties of the radio-identified SMG population, such as their stellar masses, far-infrared SEDs, kinematics, gas masses, clustering and stellar morphologies (e.g. Blain et al. 2004; Chapman et al. 2005; Swinbank et al. 2006, 2010a; Hainline et al. 2011; Magnelli et al. 2012; Bothwell et al. 2013). In particular, studies of the kinematics of SMGs have broadly concluded that the intense starburst is triggered through merger activity, strengthening the apparent similarity of SMGs to local ULIRGs (Frayer et al., 1998; Blain et al., 2002; Swinbank et al., 2006, 2010a; Tacconi et al., 2006, 2008; Engel et al., 2010).

Ideally, spectroscopic redshifts are required to perform a detailed analysis of individual SMGs. However, obtaining spectroscopic redshifts for SMGs requires many hours of integration on 8–10 m class telescopes, making them expensive to obtain for large samples of sub-mm sources. Spectroscopic surveys also suffer from selection biases due to the

absence of bright emission lines in the wavelength coverage of the spectrograph used. For example, the Chapman et al. (2005) sample is incomplete at $1.2 \lesssim z \lesssim 1.8$ as key emission lines such as [OII], [OIII] and Hα are redshifted out of the wavelength coverage of LRIS.

Despite their lower reliability, photometric redshifts can be used to constrain global properties of the sub-mm population. Wardlow et al. (2011) exploited the wealth of photometric imaging available in the ECDFS to study the multi-wavelength properties of the 126 sub-mm sources detected in the LESS survey (Weiß et al., 2009). At the start of this thesis this was one of the most representative studies of the 870 μm population due to the uniformity and wide area coverage of the LESS imaging. Wardlow et al. (2011) determined photometric redshifts for 78 SMGs, which were identified as *robust* counterparts to 75 of the 126 LESS sub-mm sources (Biggs et al., 2011). These sources were shown to lie at a median redshift of $z_{phot} = 2.2 \pm 0.1$, and it was suggested that $S_{870} > 1$ mJy SMGs may account for up to 50 % of the cosmic SFRD at $z \sim 2$.

Fundamentally the studies by Wardlow et al. (2011) and Chapman et al. (2005) are both limited by the requirement for identifications to the sub-mm emission at different wavelengths. In the study by Wardlow et al. (2011), 51 / 126 of the LESS sub-mm sources ($\sim$ 40 % of the sample) do not have a *robust* counterpart. Wardlow et al. (2011) tentatively claim that these sources lie at higher redshifts, increasing the median redshift of the population to $z_{phot} = 2.5 \pm 0.2$. However, it is clear from the analysis that identifications at sub-mm wavelengths are required to both confirm the validity of the multi-wavelength identifications, pinpoint the unidentified sources and allow an unbiased view of the sub-mm population.

1.6 Evolutionary Pathways

The low volume density, but high star-formation rates of SMGs means that they are an important population for studies of galaxy formation and evolution. Studies of the kinematics of SMGs appear to show that they are mainly merger-driven and, in combination with studies of the gas masses of SMGs, indicate that they have gas-to-total mass fractions of $\sim$ 40 % (Swinbank et al., 2004; Alaghband-Zadeh et al., 2012; Bothwell et al., 2013). The large gas reservoirs of SMGs ($\sim 5 \times 10^{11}$ M$_\odot$; Bothwell et al. 2013), combined with their high star-formation rates, mean that they have the potential to form a significant proportion of the stars in a $\sim 10^{11}$ M$_\odot$ galaxy in only 100 Myr. In the following section I discuss the proposed evolutionary links between SMGs and FIR-bright QSOs; compact,

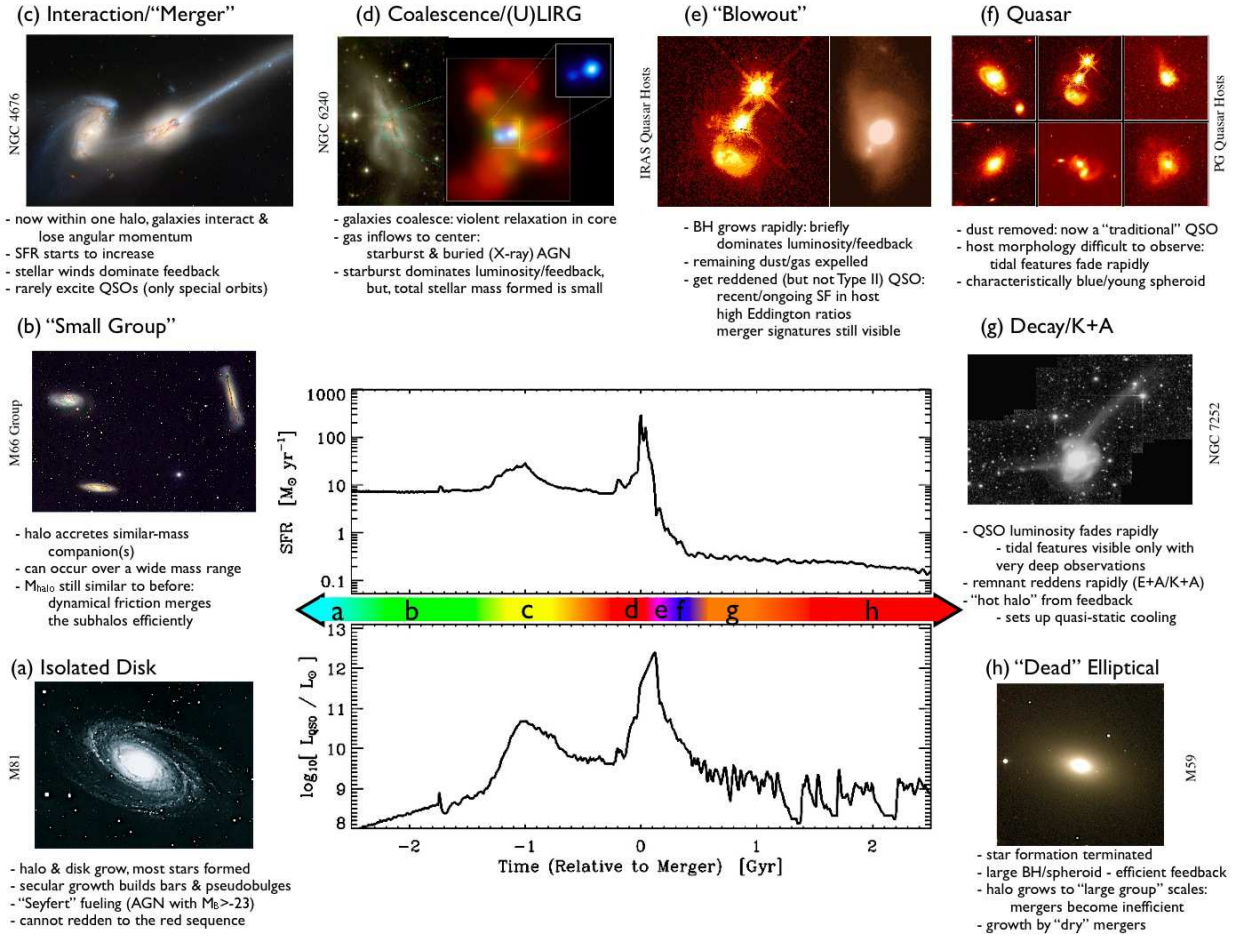

Figure 1.9: A schematic outline of a suggested evolutionary pathway for a local elliptical galaxy (Hopkins et al., 2008). In this scenario a merger of two gas rich discs triggers an intense, obscured starburst (an SMG phase). During the starburst phase gas is accreted on to the central SMBH leading to first an obscured, and then an unobscured QSO as the remaining dust is expelled. After the QSO phase the galaxy fades into a massive, "red-and-dead" elliptical galaxy.

quiescent galaxies at $z \sim 1.5-2$; and local elliptical galaxies.

1.6.1 Link between SMGs and local ellipticals

In the local Universe, stellar archaeology indicates that low-redshift ellipticals tend to be dominated by old stellar populations that formed at $z \gtrsim 1$ (Nelan et al., 2005), with the most massive systems formed when the Universe was only a few Gyrs old. Furthermore, studies of the ratio of so called α elements (O, Ne, Mg, Si, S, Ar, Ca, and Ti) to Fe abundance in ellipticals indicates that the majority of the stellar population formed in a compact burst with a duration <1 Gyr (e.g. Thomas et al. 2005). These factors have led a number of authors to suggest that SMGs may have the properties expected of the progenitors of local elliptical galaxies (e.g. Lilly et al. 1999; Genzel et al. 2003; Blain et al. 2004; Swinbank et al. 2006; Tacconi et al. 2008; Swinbank et al. 2010a). One of the methods to test whether SMGs are the progenitors of elliptical galaxies is to measure the clustering of the population, and use this to infer mass of the dark matter haloes in which these galaxies reside. In a study of the LESS SMGs, Hickox et al. (2012) find that SMGs have similar clustering to $\sim 2-3\,L_\star$ elliptical galaxies, suggesting that SMGs are indeed the progenitors of massive, elliptical galaxies. However, the conclusions are limited by the lack of robust identifications and redshifts for the LESS SMGs. A different route to test the proposed evolutionary link is to study the physical properties of SMGs and investigate whether it is feasible that they evolve into local elliptical galaxies.

1.6.2 Link between SMGs and compact, quiescent galaxies at $z \sim 1.5-2$

In the last decade high redshift surveys have also uncovered a population of massive galaxies at $z \sim 1.5-2$ that have well-established, quiescent stellar populations. Spectroscopy at NIR wavelengths suggests that the stellar populations in these quiescent galaxies formed in a compact burst at $z \sim 2.5$ (Bedregal et al., 2013; Whitaker et al., 2013). Are these high-redshift, quiescent galaxies one stage in evolutionary sequence where an intense starburst at high redshift (an SMG) fades into first a quiescent spheroid at $z \sim 1.5-2$, and then into a local elliptical galaxy? One of the most surprising features of the $z \sim 1.5-2$ quiescent galaxies is that they appear to have very compact stellar populations (half-light radii [R_e] of ~ 1 kpc; e.g. Daddi et al. 2005; Zirm et al. 2007; Toft et al. 2007; Buitrago et al. 2008; van Dokkum et al. 2008; Newman et al. 2012; Patel et al. 2013; Krogager et al. 2013). In contrast, the pre-existing stellar distribution in SMGs has been shown to be

more extended ($R_e \sim 4-5\,\mathrm{kpc}$; Swinbank et al. 2010a; Chen et al. 2013), suggesting that a significant transformation of the stellar mass profile is required if SMGs are the progenitors of these compact, quiescent galaxies.

1.6.3 Link between SMGs and FIR-bright QSOs

Finally, Sanders et al. (1988) first suggested that an evolutionary connection exists between ULIRGs and Quasars (QSOs) due to the prevalence of AGN activity within IRAS selected ULIRGs, and the similarity in the space density of both populations (Soifer et al., 1987). The connection between the ULIRG and QSO populations was strengthened by the discovery of the Magorrian relation between the mass of the Super Massive Black Hole (SMBH) at the centre of a galaxy and the stellar mass of the bulge (e.g. Magorrian et al. 1998; Gebhardt et al. 2000; Ferrarese & Merritt 2000), which suggests that the SMBH must be growing at a rate roughly proportional to the stellar mass. As ULIRGs are forming stars at prodigious rates, it follows naturally that the SMBH must go through a similar phase of rapid growth: an AGN dominated, QSO-phase. Intriguingly, the ULIRG / SMG and QSO populations evolve very rapidly with redshift and both populations appear to reach a broad peak in their activity at $z \sim 2.5$ (Shaver, 1988; Chapman et al., 2005; Wardlow et al., 2011).

Further support for an evolutionary connection between SMGs and QSOs came from studies to measure the SMBH masses of SMGs. Alexander et al. (2008) measured the Hα and Hβ line widths for a sample of SMGs and showed that the population have a typical black hole mass of $\sim 6 \times 10^7\,\mathrm{M}_\odot$. By comparing the SMBH and host galaxy masses, Alexander et al. (2008) showed that the SMBHs in SMGs must grow by a factor of $\gtrsim 3$ to match the local Magorrian relation, indicating that they must undergo an extended period of growth. Finally, numerical simulations have provided additional weight to the proposed evolutionary sequence (e.g. Hopkins et al. 2008). These simulations have shown that mergers of gas rich discs initially results in an intense, obscured starburst (an SMG). As the starburst progresses the large reservoir of gas and dust falls onto the SMBH resulting in high levels of accretion and an obscured QSO-phase where the AGN heats the surrounding dust. Finally, either star-formation, or AGN-driven winds deplete the reservoir of gas and dust, resulting in a unobscured QSO (see Figure 1.9). If this proposed evolution sequence between QSOs and SMGs is correct then the populations should have the same clustering strength (e.g Hickox et al. 2012), and we would expect to detect a small surface density of

high-redshift, FIR-bright QSOs as SMGs transition from a starburst to AGN-dominated phase (e.g. Coppin et al. 2008)

Understanding how SMGs fit into the evolution of massive galaxies is one of the key steps towards understanding the growth of stellar mass in the Universe, and hence galaxy evolution.

1.7 Overview of this Thesis

In this thesis I use observational techniques to place constraints on the multi-wavelength properties of FIR-bright galaxies, primarily SMGs. The SMGs studied in this thesis have been identified using interferometric observations that directly pinpoint the galaxies that contribute to the original sub-mm sources that were selected for follow-up, high-resolution observations. The work presented in chapter 3 has been submitted for publication, whereas chapters 2,4 & 5 are comprised of published work. A brief outline of each of these chapters is given below. Finally, I present my conclusions in chapter 6, along with a discussion of the future direction of the work presented in this thesis.

- In chapter 2 I present a multi-wavelength study of a sample of 96 ALMA-identified SMGs. The SMGs were detected in high-resolution follow-up imaging of the 126 sub-mm sources detected in the LESS survey. The ALMA observations provide the first, large sample of SMGs with unambiguous identifications at the same wavelength as their initial single-dish selection. Using the extensive optical-to-NIR imaging of the ECDFS I measure the photometry of the SMGs and use this to determine their photometric redshift. Finally, I present an investigation into the expected descendants of SMGs, and compare these to a local sample of elliptical galaxies.

- Chapter 3 presents an ALMA study of 30 bright sub-mm sources, selected from wide-field imaging with SCUBA-2 taken as part of S2CLS. The work builds on an interesting result from chapter 2, that all of the single-dish selected sub-mm sources above a certain flux limit are comprised of a blend of multiple, fainter SMGs. The effect of blending biases the shape of the sub-mm number counts as determined from surveys with sub-mm detectors at single-dish facilities. I constructed the intrinsic sub-mm number counts from our ALMA observations and compare them to recent theoretical predictions.

- In chapter 4 I present a morphological study of the FIR emission from a subset of the sources presented in chapter 3. The ALMA imaging is taken at 0.3″ resolution, and resolves the FIR-emission from the SMGs. A subset of 23 of the brightest SMGs are detected at a sufficiently high signal-to-noise to robustly determine the physical size of the star-forming region. The work presented in this chapter provided the first measurement of the size distribution of the star-forming region in a large sample of SMGs, as measured directly at sub-mm wavelengths. I compared the sizes of the SMGs resolved in the ALMA imaging to other sample of SMGs with sizes measured at different wavelengths. Finally, I discuss the consequences of the compact starburst in SMGs on their proposed evolution into compact, quiescent galaxies at $z \sim 2$.

- In chapter 5 I present an observational study of two FIR-bright QSOs. An advantage of the work presented in this thesis is that the QSOs were selected to have supermassive black holes with masses similar to those thought to reside in SMGs. The sample is thus well suited to test a proposed evolutionary connection between SMGs and QSOs. I measure the properties of the gas and black holes in these QSO and determine whether it is feasible that they have recently transitioned from a starburst-dominated SMG-phase.

Chapter 2

An ALMA Survey of Sub-millimetre Galaxies in the Extended Chandra Deep Field South: The Redshift Distribution and Evolution of Sub-millimetre Galaxies

2.1 Motivation

The LESS survey represents one of the largest, contiguous, 870 μm surveys of extragalactic sources that has been published to date. Undertaken with the LABOCA instrument on the APEX 12 m telescope in 2009, the survey reaches a uniform depth of $\sigma_{870} = 1.2\,\mathrm{mJy\,beam^{-1}}$ across 900 $\mathrm{arcmin^2}$ of the Extended *Chandra* Deep Field South (ECDFS). Weiß et al. (2009) present the source catalogue for the LESS survey, which comprises 126 sub-mm sources detected at $> 3.7\,\sigma$, and studies have used this catalogue to constrain the properties of the SMG population (e.g. Wardlow et al. 2011; Hickox et al. 2012). However, these studies are fundamentally limited by the coarse resolution of the LABOCA observations (FWHM $= 19.2''$), which, as discussed in Section 1.5.3, means that significant assumptions are required to identify the correct counterpart to the sub-mm emission. To characterize

the SMG population in an unbiased manner we undertook an ALMA Cycle-0 program to observe all 126 SMGs from the LESS survey at 1.5″ resolution. These ALMA observations resolved the sub-mm sources in their constituent SMGs and showed the previous "robust" identifications were only $\sim 70\,\%$ reliable, and $\sim 50\,\%$ complete (Hodge et al., 2013b). In the following chapter I exploit the precise identifications that are provided by our ALMA observations, along with the excellent multi-wavelength coverage of the ECDFS, to study the properties of an unbiased sample of SMGs. In particular I present the photometric redshift distribution for these ALMA-identified SMGs, and discuss their potential evolution into local Elliptical galaxies. The following chapter was presented in part in Simpson et al. (2014), ApJ, 788, 125.

2.2 Abstract

We present the first photometric redshift distribution for a large sample of 870 μm SMGs with robust identifications based on observations with ALMA. In our analysis we consider 96 SMGs in the ECDFS, 77 of which have 4–19 band photometry. We model the SEDs for these 77 SMGs, deriving a median photometric redshift of $z_{phot} = 2.3 \pm 0.1$. The remaining 19 SMGs have insufficient photometry to derive photometric redshifts, but a stacking analysis of *Herschel* observations confirms they are not spurious. Assuming that these SMGs have an absolute H-band magnitude distribution comparable to that of a complete sample of $z \sim 1$–2 SMGs, we demonstrate that they lie at slightly higher redshifts, raising the median redshift for SMGs to $z_{phot} = 2.5 \pm 0.2$. Critically we show that the proportion of galaxies undergoing an SMG-like phase at $z \geq 3$ is at most 35 ± 5 per cent of the total population. We derive a median stellar mass of $M_\star = (8 \pm 1) \times 10^{10}\,\mathrm{M}_\odot$, although there are systematic uncertainties of up to $5\times$ for individual sources. Assuming that the star formation activity in SMGs has a timescale of $\sim 100\,\mathrm{Myr}$ we show that their descendants at $z \sim 0$ would have a space density and M_H distribution which are in good agreement with those of local ellipticals. In addition the inferred mass-weighted ages of the local ellipticals broadly agree with the look-back times of the SMG events. Taken together, these results are consistent with a simple model that identifies SMGs as events that form most of the stars seen in the majority of luminous elliptical galaxies at the present day.

2.3 Introduction

In the local Universe ~ 60 per cent of the total stellar mass is in early-type and elliptical galaxies (Bell et al., 2003). These galaxies lie on a tight "red sequence" (Sandage & Visvanathan, 1978; Bower et al., 1992; Blanton et al., 2003); follow well-defined scaling relations (the fundamental plane); and show correlations between the age, and velocity dispersion (σ) of their stellar population. Typically, the most massive ellipticals have velocity dispersions of $\sigma \sim 200$–$400\,\mathrm{km\,s^{-1}}$, with estimated luminosity-weighted stellar ages of $\sim 10 - 13\,\mathrm{Gyr}$ (Nelan et al., 2005). Recently, near-infrared spectroscopy of quiescent, red, galaxies at $z \sim 1.5$–2, the potential progenitors of elliptical galaxies (see van Dokkum et al. 2004), has suggested the stellar populations in these galaxies have a typical age of ~ 1–$2\,\mathrm{Gyr}$ (e.g. Whitaker et al. 2013; Bedregal et al. 2013). Taken together, these results suggest that the bulk of the stellar mass in elliptical galaxies formed early in the history of the Universe, at redshifts $z > 2$. However it has proved challenging to study the progenitors of these galaxies as the most massive, star-forming galaxies at $z > 2$ are also the most dust obscured (Dole et al., 2004; LeFloc'h et al., 2009). One route to uncovering these dusty starbursts is to search at sub-millimetre (sub-mm) wavelengths, where the shape of the spectral energy distribution (SED) of the far-infrared (FIR) dust emission means that cosmological fading is negated by the strongly increasing flux density of the SED. For sources at a fixed luminosity, this "negative k-correction" results in an almost constant apparent flux density in the sub-mm over the redshift range $z = 0.5$–7 (see the review by Blain et al. 2002).

The earliest surveys aimed at searching for distant sub-millimetre galaxies (SMGs), particularly with the SCUBA camera on the James Clerk Maxwell Telescope (JCMT), uncovered moderate numbers of sub-mm sources with 850-μm flux densities of $S_\nu = 5$–$15\,\mathrm{mJy}$ (e.g. Smail et al. 1997; Hughes et al. 1998; Barger et al. 1998; Eales et al. 1999; Coppin et al. 2006). However, the coarse beam size of single dish sub-mm telescopes ($\sim 15''$ for the JCMT at 850μm) meant that resolving these sub-mm sources into their constituent SMGs (and so determining their basic properties, such as redshift and luminosity) was impossible without significant assumptions about the properties of their multi-wavelength counterparts. For example, the correlation between the far-infrared and radio flux density of star-forming galaxies could be employed (e.g. Ivison et al. 1998, 2000), as deep $1.4\,\mathrm{GHz}$ radio imaging with the Very Large Array (VLA) provides the sub-arcsecond resolution required to accurately locate the counterpart to the sub-mm

emission (Ivison et al., 2002, 2004, 2007; Bertoldi et al., 2007; Biggs et al., 2011; Lindner et al., 2011). However in typical surveys, radio imaging only identifies $\sim$50–60 per cent of the SMGs brighter than $S_{850\mu\mathrm{m}} > 5\,\mathrm{mJy}$ and furthermore is expected to miss the counterparts of the most distant SMGs due to the disadvantageous radio k-correction. Despite this low identification rate, this technique has facilitated extensive follow-up of the counterparts of SMGs, and spectroscopy has shown that the radio-identified subset of the population have a redshift distribution which peaks at $z \sim 2.3$ (Chapman et al., 2005). These observations confirmed that SMGs have luminosities comparable to local ultra luminous infrared galaxies (ULIRGs), but crucially demonstrated that the space density of ULIRGs at $z \sim 2$ is $\sim$1000$\times$ higher than at $z = 0$. With implied star formation rates of 100–1000 $\mathrm{M_\odot\,yr^{-1}}$, SMGs brighter than 1 mJy may contribute up to half of the co-moving star-formation rate density at $z \sim 2$ (Hughes et al., 1998; Blain et al., 1999b; Smail et al., 2002; Wardlow et al., 2011; Casey et al., 2013).

Extensive multi-wavelength follow-up of the radio-identified subset of the SMG population, particularly with the Plateau de Bure Interferometer, measured the kinematic and structural properties of high-redshift SMGs, suggesting that SMGs have morphologies and gas kinematics consistent with merging systems (e.g. Tacconi et al. 2008; Engel et al. 2010; Swinbank et al. 2010a; Alaghband-Zadeh et al. 2012; Menéndez-Delmestre et al. 2013). Moreover, their large molecular gas reservoirs (which comprise $\sim$50 per cent of the dynamical mass in the central few kpc; Greve et al. 2005; Riechers et al. 2010; Carilli et al. 2010; Bothwell et al. 2013) and star-formation rates mean they have the potential to form a significant proportion of the stars in a $\sim 10^{11}\,\mathrm{M_\odot}$ galaxy in only 10^8 yr. Taken with their space densities ($\sim 10^{-5}\,\mathrm{Mpc^{-3}}$; Chapman et al. 2005; Wardlow et al. 2011), large black hole masses ($\sim 10^8\,\mathrm{M_\odot}$; Alexander et al. 2005, 2008) and clustering (e.g. Hickox et al. 2012) it appears likely that, like local ULIRGs, the luminous starbursts in SMGs are frequently triggered by major mergers of gas-rich galaxies (e.g. Ivison et al. 2012).

Comparison with numerical simulations (e.g. Granato et al. 2004; Di Matteo et al. 2005; Hopkins et al. 2006) also suggests that the starburst SMG phase will be followed by a dust enshrouded AGN phase, which evolves through an optically bright QSO phase before evolving passively into an elliptical galaxy. Moreover, assuming the timescales for the AGN and QSO phases are short and that SMGs do not undergo significant gas accretion at much lower redshift, it has been shown via simple dynamical arguments that the SMGs can evolve onto the scaling relations observed for local, early-type galaxies at

$z = 0$ (e.g. Nelan et al. 2005; Swinbank et al. 2006). It has thus been speculated that SMGs are the progenitors of local elliptical galaxies (Lilly et al., 1999; Genzel et al., 2003; Blain et al., 2004; Swinbank et al., 2006; Tacconi et al., 2008; Hainline et al., 2011; Hickox et al., 2012).

These 850 μm-selected samples remain the best-studied SMGs. However, by necessity, the samples from which most of the follow-up has so far concentrated have been biased to the radio-identified and UV-bright subset of the population where their counterparts and redshifts could be measured. In 2009 we undertook a 310 hr survey of the 0.5×0.5 degree Extended *Chandra* Deep Field South (ECDFS) at 870μm, with the LABOCA camera on APEX. This "LESS" survey (Weiß et al., 2009) detected 126 sub-mm sources with 870–μm fluxes $S_{870} > 4.4$ mJy, but still relied on radio and mid-infrared imaging (Biggs et al., 2011) to statistically identify probable counterparts to $\sim$60 per cent of the sources, with the remaining $\sim$40 per cent remaining unidentified (Wardlow et al., 2011).

To characterize the *whole* population of bright SMGs in an unbiased manner, we have subsequently undertaken an ALMA survey of these 126 LESS sub-mm sources. The ALMA data resolve the sub-mm emission into its constituent SMGs, *directly* pinpointing the source(s) responsible for the sub-mm emission to within $< 0.3''$ (Hodge et al., 2013b), removing the requirement for statistical radio / mid-IR associations. Crucially, one of the first results from our survey demonstrated that just $\sim$70 per cent of the "robust" counterparts from Biggs et al. (2011) were correct and that the radio and 24 μm identifications only provide $\sim$50 per cent completeness (Hodge et al., 2013b), highlighting the potential biases in previous surveys (see also Younger et al. 2009; Barger et al. 2012; Smolčić et al. 2012). These ALMA identifications allow us for the first time to make basic measurements, such as the redshift distribution, for a complete and unbiased sample of SMGs.

In this chapter, we exploit the extensive optical and near-infrared imaging of the ECDFS to derive the photometric redshift distribution, stellar mass distribution, and evolution of the ALMA-LESS (ALESS) SMGs. The chapter is structured as follows. In § 2.4 we present the multi-wavelength data used in our analysis, followed by a description of our method for measuring aperture photometry for the ALESS SMGs, and sources in the field. In § 2.5 we discuss the technique of SED fitting to determine photometric redshifts for the ALESS SMGs. Finally, in § 2.6 we discuss the derived properties of the ALESS SMGs, such as redshift and stellar mass, and their comparison to similar high-redshift

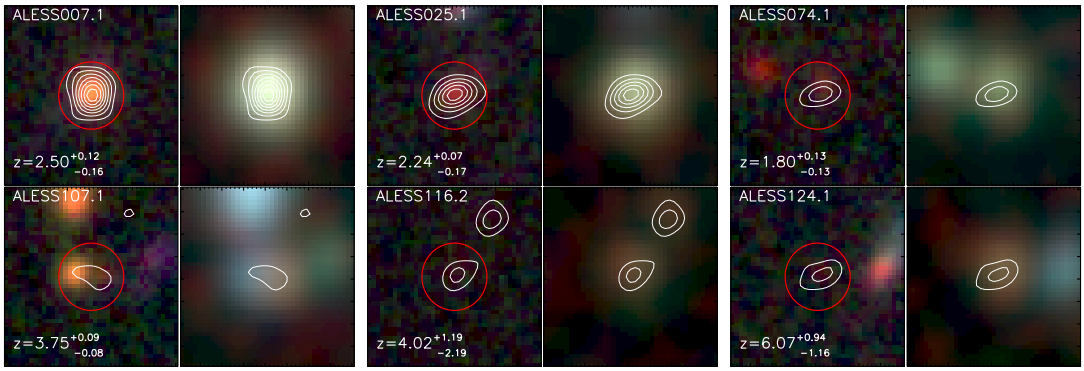

Figure 2.1: In our analysis we make use of extensive archival imaging of the ECDFS, covering 19 optical through near-infrared wavebands (see Table 2.2). Here we present $8'' \times 8''$ optical (coadded B, I and K_S; left) and near-infrared (coadded 3.6, 4.5 and 8.0 μm; right) false colour images for six example SMGs, from our sample of 96 SMGs, which span the full range of 870 μm flux (thumbnails of all sources are shown in Figure 2.17). Contours represent ALMA 870 μm detections at 3, 5, 7 .... $\times\sigma$. The ALMA observations pinpoint the 870 μm emission to $< 0.3''$ precision, identifying the optical/near-infrared counterpart without the requirement for indirect statistical associations. Using the precise locations we measure aperture photometry for each SMG (the size of the aperture is indicated with a red circle) and derive photometric redshifts using the SED-fitting code HYPERZ (Bolzonella et al., 2000), see § 2.5.

studies, concluding with remarks on their comparison to low redshift populations. We give our conclusions in § 2.7. Throughout the chapter, we adopt a cosmology with $\Omega_\Lambda = 0.73$, $\Omega_\mathrm{m} = 0.27$, and $H_0 = 71\,\mathrm{km\,s^{-1}\,Mpc^{-1}}$ and unless otherwise stated, error estimates are from a bootstrap analysis. All magnitudes quoted in this chapter are given in the AB magnitude system.

2.4 Observations & Analysis

2.4.1 Sample Selection

In this study we undertake a multi-wavelength analysis of the ALMA detected sub-mm galaxies from the catalogue presented by Hodge et al. (2013b) [see also Karim et al. 2013]. To briefly summarize the observations, we obtained 120s integrations of 122 of the original 126 LESS sub-mm sources, initially identified using the LABOCA camera on the APEX telescope (Weiß et al., 2009). These Cycle 0 observations used the compact configuration, yielding a median synthesized beam of $\sim 1.6'' \times 1.2''$. The observing frequency was matched to the original LESS survey, 344 GHz (Band 7), and we reach a typical RMS across our

velocity-integrated maps of $0.4\,\mathrm{mJy\,beam^{-1}}$. The observations are a factor of $3\times$ deeper than LESS, but crucially the angular resolution is increased from $\sim 19''$ to $\sim 1.5''$. The primary beam of ALMA is $\sim 17''$, which encompasses the original LESS error circles of $\lesssim 5''$. For full details of the data reduction and source extraction we refer the reader to Hodge et al. (2013b). From the observations Hodge et al. (2013b) construct a MAIN source catalogue consisting of all detected SMGs obeying the following criteria; primary-beam-corrected map RMS $< 0.6\,\mathrm{mJy\,beam^{-1}}$, S/N > 3.5, beam axial ratio < 2.0 and lying within the ALMA primary beam. The resulting catalogue contains 99 SMGs, extracted from 88 ALMA maps, which form the basis of the sample used in this chapter. The positional uncertainty on each SMG is $< 0.3''$. Karim et al. (2013) demonstrate that the MAIN catalogue is expected to contain one spurious source, and to have missed one SMG. We remove three SMGs from our sample which lie on the edge of the ECDFS and so only have photometric coverage in two IRAC bands. Our final sample thus consists of 96 SMGs with precise interferometrically-identified positions.

A supplementary catalogue is also provided comprising sources extracted from outside the ALMA primary beam, or in lower quality maps (i.e. primary-beam-corrected map RMS $> 0.6\,\mathrm{mJy\,beam^{-1}}$ or axial ratio > 2.0; see Hodge et al. 2013b). In contrast to the MAIN catalogue Karim et al. (2013) demonstrate that up to ~ 30 per cent of the supplementary sources are likely to be spurious, and as such we do not consider them in the main body of this work. However, we present the photometry of these supplementary sources with detections in more than three wavebands (14 out of 31 sources) in Figure 2.18, along with their photometric redshifts and derived properties in Table 2.7.

2.4.2 Optical & NIR Imaging

The majority of our optical – near-infrared data comes from the MUltiwavelength Survey by Yale-Chile (MUSYC; Gawiser et al. 2006), which provides U–K-band imaging (Taylor et al., 2009) of the entire 0.5×0.5 degree ECDFS region (detection limits are given in Table 2.2). We supplement this with U-band data from the GOODS/VIMOS imaging survey (Nonino et al., 2009), covering $\sim 0.17\,\mathrm{deg^2}$ of the ECDFS. Although the additional U-band imaging only covers ~ 60 per cent of the ALESS SMGs, it is ~ 2 magnitudes deeper than the MUSYC U-band imaging, and provides a valuable constraint on SMGs undetected in the shallower imaging.

In addition, we include deep near-infrared J and K_S imaging from both the ESO-

Filter	$\lambda_{\rm effective}$ (μm)	Detection limit ($3\,\sigma$; AB mag)	Reference
MUSYC WFI U	0.35	26.2	Taylor et al. (2009)
MUSYC WFI U_{38}	0.37	25.3	Taylor et al. (2009)
VIMOS U	0.38	28.1	Nonino et al. (2009)
MUSYC WFI B	0.46	26.5	Taylor et al. (2009)
MUSYC WFI V	0.54	26.3	Taylor et al. (2009)
MUSYC WFI R	0.66	25.5	Taylor et al. (2009)
MUSYC WFI I	0.87	24.7	Taylor et al. (2009)
MUSYC Mosaic-II z	0.91	24.3	Taylor et al. (2009)
MUSYC ISPI J	1.25	23.2	Taylor et al. (2009)
HAWK-I J	1.26	24.6	Zibetti et al. (in prep)
TENIS WIRCam J	1.26	24.9	Hsieh et al. (2012)
MUSYC Sofi H	1.66	23.0	Taylor et al. (2009)
MUSYC ISPI K	2.13	22.4	Taylor et al. (2009)
HAWK-I K_s	2.15	24.0	Zibetti et al. (in prep)
TENIS WIRCam K_s	2.15	24.4	Hsieh et al. (2012)
SIMPLE IRAC 3.6 μm	3.58	24.5	Damen et al. (2011)
SIMPLE IRAC 4.5 μm	4.53	24.1	Damen et al. (2011)
SIMPLE IRAC 5.8 μm	5.79	22.4	Damen et al. (2011)
SIMPLE IRAC 8.0 μm	8.05	23.4	Damen et al. (2011)

Table 2.1: Summary of Photometry

VLT/HAWK-I survey by Zibetti et al. (in prep) and the Taiwan ECDFS NIR Survey (TENIS; Hsieh et al. 2012), taken using CFHT/WIRCAM. Both surveys are $\sim$1.5–2.0 magnitudes deeper than the MUSYC J or K_S imaging (Table 2.2). We include all three sets of J and K_S imaging in our analysis, however where multiple observations exist we quote, or plot, a single value in order of the detection limit of the original imaging.

Finally, we include data taken as part of the *Spitzer* IRAC/MUSYC Public Legacy in ECDFS (SIMPLE; Damen et al. 2011) survey, which provides imaging at 3.6, 4.5, 5.8 and 8.0 μm over the entire field. We note that the 5.8 μm imaging is $\sim$2 magnitudes shallower than the other IRAC imaging.

To highlight the optical – near-infrared imaging, in Figure 2.1 we show BIK_S and 3.6/4.5/8.0 μm false colour images for six example ALESS SMGs, spanning the full range of ALMA 870 μm flux. Figure 2.1 demonstrates that the SMGs typically have counterparts

in the near-infrared, and where detected appear red in the BIK_S colour images. The full sample of 96 sources are shown in Figure 2.17.

2.4.2.1 Photometry

To derive photometric redshifts we need to measure seeing- and aperture-matched multi-band aperture photometry across all 19 filters available (see Table 2.2). First, we align all imaging to the ALMA astrometry. We use SExtractor (Bertin & Arnouts, 1996) to create a source catalogue for each image, and match this catalogue to the ALESS SMGs. The measured offsets in R.A. and Dec. are $< 0.3''$ in all cases, and correspond to approximately a single pixel shift in the optical imaging, and a sub-pixel shift in the near-infrared imaging.

After aligning all data to a common astrometric frame, we next seeing match the optical – near-infrared images. The resolution of the U–K_S imaging is $\leq 1.5''$, and we convolve each image to the lowest resolution. We then measure photometry in a $3''$-diameter aperture using the IRAF package APPHOT. We initially center the aperture at the ALMA identified position, but allow APPHOT to re-center the aperture up to a shift of $< 0.5''$ from the original position. To correct for residual resolution differences in the U–K_S imaging we aperture correct our measurements to total magnitudes. We create a composite PSF, from 15 unsaturated point sources in each image, and derive the aperture correction as the ratio of the total flux in the composite PSF, to the flux in the original $3''$ diameter aperture. The derived aperture corrections range from $f_{\rm tot}(\lambda) \,/\, f_{\rm ap}(\lambda) = 1.18$ – 1.27. We assume sky noise is the dominant source of uncertainty for these faint galaxies, and estimate photometric errors by measuring the uncertainty in the flux in $3''$ apertures placed randomly on blank patches of sky in each image.

The resolution of the IRAC imaging is considerably poorer than the U–K_S data, $2.2''$ at $8.0\,\mu$m. We therefore match the resolution of all the IRAC imaging to $2.2''$ FWHM, and measure photometry in the same manner as the U–K_S, using a $3.8''$-diameter aperture. To correct for the resolution difference between the IRAC and U–K_S imaging, we again convert the IRAC photometry to total magnitudes. Following the same procedure as above, we measure the aperture correction from a composite PSF of 15 unsaturated point sources in each IRAC image. We measure aperture corrections of $f_{\rm tot}(\lambda) \,/\, f_{\rm ap}(\lambda) = 1.49$ – 1.89, in the 3.6–8.0 μm wavebands, which are consistent with those estimated by the SWIRE team (Surace et al., 2005).

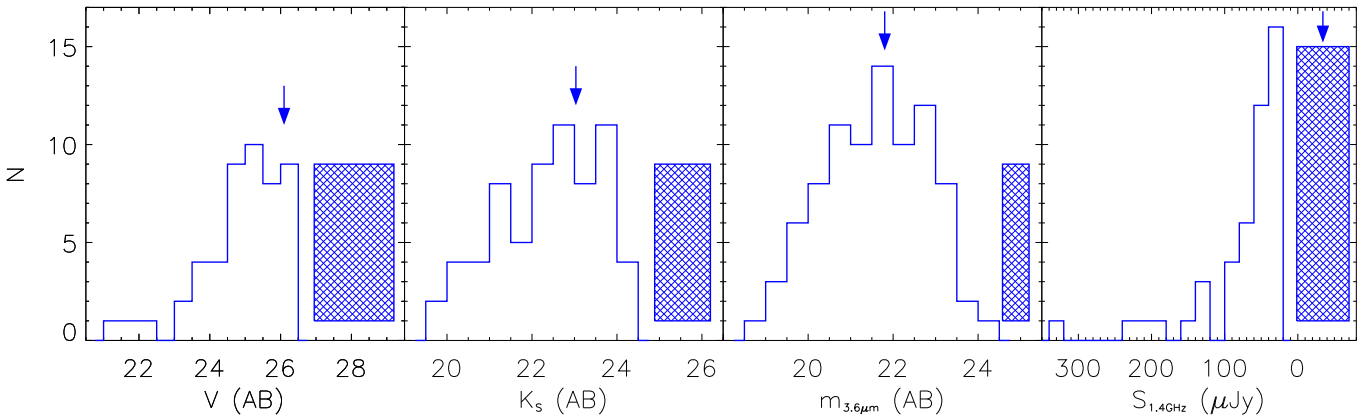

Figure 2.2: The apparent magnitude distributions of ALESS SMGs in the V, K_s and IRAC 3.6 μm bands, along with the flux density distribution at 1.4 GHz. On each panel a checked region indicates the undetected sources (see Table 1 for magnitude limits). The median SMG V, K_S & 3.6 μm-band magnitudes, including non-detections, are $V = 26.09 \pm 0.19$, $K_S = 23.0 \pm 0.3$ and $m_{3.6} = 21.80 \pm 0.17$ and we mark these on each panel with an arrow. The radio data reaches a depth of 19.5 μJy at its deepest (3 σ detection limit), however only 45 per cent of the ALESS SMGs are detected at this level, and the median 1.4 GHz flux for SMGs is thus constrained at $\lesssim 19.5\,\mu$Jy.

In all of the following analysis, we define detections if the flux is $3\,\sigma$ above the background noise. The median number of filters covering each SMG is 14, and of the 96 SMGs in our sample, 77 are detected in $\geq$ 4 wavebands. Of the remaining 19 sources, 10 are detected in 2 or 3 wavebands, and 9 are detected in $\leq$ 1 waveband. We discuss these 19 sources in § 2.5.2.3, where we show that a stacking analysis of IRAC & *Herschel* fluxes confirms that they correspond to far-infrared luminous sources, on average. We note that we do not perform any deblending of our photometry, and that we derive redshifts for 12 SMGs which are within $4''$ of a 3.6-μm source of comparable, or greater, flux. In Table 2.1 we highlight sources which suffer significant blending, and discuss the effects of blending in § 2.5.2.1.

The photometry for the ALESS SMGs is given in Table 2.1, and in Figure 2.2 we show the V, K_S and 3.6 μm magnitude histograms. The ALESS SMGs have median magnitudes of $V = 26.09 \pm 0.19$, $K_s = 23.0 \pm 0.3$ and $m_{3.6} = 21.80 \pm 0.17$ (58, 76 and 90 per cent detection rates in each band). We note that at 3.6 μm the Chapman et al. (2005) sample of radio-detected SMG are a magnitude brighter than the ALESS SMGs ($m_{3.6} = 20.63 \pm 0.18$; Hainline et al. 2009)

2.4.3 Herschel/SPIRE

In this work we make use of observations at 250, 350 and 500 μm using the Spectral and Photometric Imaging Receiver (SPIRE; Griffin et al. 2010), onboard the *Herschel Space Observatory* (Pilbratt et al., 2010). The ECDFS was observed for 32.4 ks at 250, 350 and 500 μm in $\sim$1.8 ks blocks as part of the Herschel Multi-tiered Extragalactic Survey (HerMES; Oliver et al. 2012). These data are described in Swinbank et al. (2014), the companion paper to this work studying the far-infrared properties of the ALESS SMGs. The final co-added maps reach a 1-σ noise level of 1.6, 1.3 and 1.9 mJy at 250, 350 and 500 μm (see also Oliver et al. 2012), although source confusion means that the effective depth of these data is shallower than these noise levels imply. Deblended 250, 350 and 500 μm fluxes for each ALESS SMG, along with the FIR-properties, are presented in Swinbank et al. (2014).

2.4.4 VLA/1.4 GHz

To study the radio properties of the ALESS SMGs, we utilize the VLA 1.4-GHz imaging of the ECDFS. The observations come from Miller et al. (2008) and we use the catalogue

described in Biggs et al. (2011). These data reach an rms of 6.5 μJy in the central regions, and a median rms of 8.3 μJy across the entire map. Biggs et al. (2011) extract a source catalogue, complete to 3σ, and we obtain radio fluxes for the ALESS SMGs by cross-correlating the catalogues with a matching radius of $1''$. In our 1.4 GHz stacking analysis we use the 1.4 GHz map from Miller et al. (2013), a re-reduction of the original data achieving an improved typical map rms of 7.4 μJy. We note that the 5 σ catalogue from Miller et al. (2013) does not match any more SMGs than the catalogue from Biggs et al. (2011), and that the 1.4 GHz fluxes for individual sources all agree within their 1–σ errors.

2.5 Photometric redshifts

The first step in our analysis is to derive photometric redshifts for the ALESS SMGs in our sample, and so determine the first photometric distribution for a large sub-mm-identified population of SMGs. To derive photometric redshifts, we use the SED fitting code HYPERZ (Bolzonella et al., 2000), which computes the χ^2 statistic for a set of model SEDs to the observed photometry. In the case of non-detections we adopt a flux of zero during the SED fitting, but with an uncertainty equal to the 1-σ limiting magnitude in that filter. The model SEDs are characterized by a star formation history (SFH), and parametrized by age, reddening and redshift. HYPERZ returns the best-fit parameters for the model SED corresponding to the lowest χ^2. We use the spectral templates of Bruzual & Charlot (2003), with solar metalicities, and consider four SFHs; a single burst (B), constant star formation (C) and two exponentially decaying SFHs with timescales of 1 Gyr (E) and 5 Gyr (Sb). Redshifts from $z = 0$–7 are considered and we allow reddening (A_V) in the range 0–5, in steps of 0.1, following the Calzetti et al. (2000) dust law. We also include the constraint that the age of the galaxy must be less than the age of Universe. Finally we follow the same prescription as Wardlow et al. (2011) for handling of Lyman–α absorption in HYPERZ; the strength of the intergalactic absorption is increased, but we also allow a wider range of possible optical depths (see Wardlow et al. 2011).

ID	MUSYC U	MUSYC U_{38}	VIMOS U	B	V	R	I	z	J^b	H	K^b	3.6 μm	4.5 μm	5.8 μm	8.0 μm
ALESS 1.1[a]	>26.18	>25.29	>28.14	>26.53	>26.32	>25.53	>24.68	>24.29	>24.88	>23.06	$23.68 \pm 0.19^*$	22.81 ± 0.06	22.72 ± 0.07	22.28 ± 0.19	21.87 ± 0.06
ALESS 1.2	>26.18	>25.29	>28.14	>26.53	>26.32	>25.53	>24.68	>24.29	>24.88	>23.06	24.27 ± 0.25	22.81 ± 0.06	22.84 ± 0.08	21.99 ± 0.15	22.11 ± 0.07
ALESS 1.3[a]	>26.18	>25.29	27.52 ± 0.16	>26.53	>26.32	>25.53	>24.68	>24.29	>24.88	>23.06	23.98 ± 0.20	23.05 ± 0.07	22.92 ± 0.09	>22.44	22.19 ± 0.08
ALESS 2.1[a]	>26.18	>25.29	28.05 ± 0.25	>26.53	26.30 ± 0.26	>25.53	>24.68	>24.29	24.45 ± 0.18	...	23.03 ± 0.09	21.92 ± 0.03	21.66 ± 0.03	21.35 ± 0.08	21.83 ± 0.06
ALESS 2.2	>26.18	>25.29	>28.14	>26.53	>26.32	>25.53	>24.68	>24.29	>24.88	...	>24.35	23.32 ± 0.09	23.00 ± 0.10	>22.44	22.12 ± 0.07
ALESS 3.1	>26.18	>25.29	...	>26.53	>26.32	>25.53	>24.68	>24.29	$>24.56^*$	>23.06	23.24 ± 0.10	22.34 ± 0.04	21.71 ± 0.03	21.33 ± 0.08	21.03 ± 0.03
ALESS 5.1[a]	24.83 ± 0.08	24.75 ± 0.17	...	23.15 ± 0.01	22.11 ± 0.01	21.33 ± 0.01	20.70 ± 0.01	20.60 ± 0.01	20.26 ± 0.00	...	19.79 ± 0.00	19.35 ± 0.00	19.50 ± 0.00	19.87 ± 0.02	20.09 ± 0.01
ALESS 6.1	24.58 ± 0.07	24.48 ± 0.13	24.52 ± 0.01	22.51 ± 0.01	21.70 ± 0.00	20.88 ± 0.00	19.90 ± 0.00	19.83 ± 0.00	19.73 ± 0.00	19.32 ± 0.01	19.81 ± 0.00	20.07 ± 0.00	20.36 ± 0.01	20.45 ± 0.04	20.81 ± 0.02
ALESS 7.1	25.97 ± 0.22	>25.29	26.09 ± 0.04	24.63 ± 0.05	23.81 ± 0.03	23.06 ± 0.03	21.89 ± 0.02	21.81 ± 0.03	21.13 ± 0.01	20.68 ± 0.03	20.16 ± 0.01	19.65 ± 0.00	19.54 ± 0.00	19.47 ± 0.02	19.76 ± 0.01
ALESS 9.1	>26.18	>25.29	>28.14	>26.53	>26.32	>25.53	>24.68	>24.29	>24.88	...	23.57 ± 0.14	21.76 ± 0.02	21.35 ± 0.02	21.03 ± 0.06	20.85 ± 0.02
ALESS 10.1	25.80 ± 0.19	...	25.58 ± 0.03	25.28 ± 0.09	25.35 ± 0.17	24.77 ± 0.14	24.36 ± 0.20	>24.29	23.70 ± 0.10	...	22.74 ± 0.07	21.82 ± 0.03	21.39 ± 0.03	21.28 ± 0.09	21.06 ± 0.04
ALESS 11.1	>26.18	>25.29	28.06 ± 0.25	>26.53	>26.32	>25.53	>24.68	>24.29	>24.88	>23.06	23.03 ± 0.09	21.78 ± 0.02	21.26 ± 0.02	20.89 ± 0.06	20.75 ± 0.02
ALESS 13.1	>26.18	>25.29	>28.14	>26.53	26.09 ± 0.22	25.35 ± 0.23	>24.68	>24.29	24.11 ± 0.14	>23.06	22.54 ± 0.06	21.78 ± 0.02	21.51 ± 0.02	21.30 ± 0.08	21.14 ± 0.03
ALESS 14.1[a]	>26.18	>25.29	...	>26.53	>26.32	>25.53	>24.68	>24.29	24.00 ± 0.13	...	23.15 ± 0.10	22.14 ± 0.03	21.50 ± 0.02	21.16 ± 0.07	20.74 ± 0.02
ALESS 15.1	>26.18	>25.29	...	>26.53	>26.32	>25.53	>24.68	>24.29	$>23.22^{**}$	...	$>22.41^{**}$	21.54 ± 0.02	20.93 ± 0.01	20.72 ± 0.05	20.64 ± 0.02
ALESS 15.3	>26.18	>25.29	...	>26.53	>26.32	>25.53	>24.68	>24.29	$>23.22^{**}$	...	$>22.41^{**}$	22.76 ± 0.06	22.93 ± 0.09	>22.44	>23.38
ALESS 17.1	24.80 ± 0.08	25.02 ± 0.21	24.84 ± 0.01	24.20 ± 0.03	24.14 ± 0.04	23.72 ± 0.06	23.00 ± 0.06	22.83 ± 0.08	21.70 ± 0.02	21.14 ± 0.05	20.77 ± 0.01	19.98 ± 0.00	19.77 ± 0.01	19.96 ± 0.02	20.35 ± 0.01
ALESS 18.1	25.62 ± 0.17	>25.29	25.54 ± 0.03	25.24 ± 0.09	25.06 ± 0.09	24.99 ± 0.17	24.31 ± 0.20	24.15 ± 0.24	22.64 ± 0.04	21.66 ± 0.08	21.13 ± 0.02	20.01 ± 0.00	19.68 ± 0.00	19.61 ± 0.02	20.28 ± 0.01
ALESS 19.1	>26.18	>25.29	26.81 ± 0.09	>26.53	26.12 ± 0.23	>25.53	>24.68	>24.29	>24.88	...	23.60 ± 0.14	22.35 ± 0.04	21.85 ± 0.03	21.43 ± 0.09	21.58 ± 0.04
ALESS 19.2	26.04 ± 0.24	>25.29	25.81 ± 0.03	25.05 ± 0.07	24.71 ± 0.07	24.48 ± 0.11	23.97 ± 0.15	24.02 ± 0.21	23.15 ± 0.06	...	22.29 ± 0.04	21.62 ± 0.02	21.68 ± 0.03	21.46 ± 0.09	21.60 ± 0.05
ALESS 22.1	>26.18	>25.29	...	>26.53	25.96 ± 0.20	25.29 ± 0.22	>24.68	>24.29	...	...	...	20.11 ± 0.00	19.79 ± 0.01	19.64 ± 0.02	20.15 ± 0.01
ALESS 23.1	...	...	...	...	...	...	...	...	>24.20	...	>23.74	23.11 ± 0.08	22.55 ± 0.06	21.78 ± 0.12	21.43 ± 0.04
ALESS 23.7	...	...	...	...	...	...	...	...	...	...	...	22.90 ± 0.06	22.70 ± 0.07	>22.44	>23.38
ALESS 25.1	>26.18	>25.29	26.66 ± 0.07	25.74 ± 0.14	25.19 ± 0.10	24.73 ± 0.14	24.12 ± 0.17	23.95 ± 0.20	23.01 ± 0.05	...	21.52 ± 0.02	20.66 ± 0.01	20.35 ± 0.01	20.19 ± 0.03	20.44 ± 0.02
ALESS 29.1	>26.18	>25.29	...	>26.53	>26.32	>25.53	>24.68	>24.29	$>23.22^{**}$	...	$>22.41^{**}$	21.85 ± 0.02	21.33 ± 0.02	20.86 ± 0.05	20.79 ± 0.02
ALESS 31.1	>26.18	>25.29	...	>26.53	>26.32	>25.53	>24.68	>24.29	>24.88	...	23.58 ± 0.14	22.30 ± 0.04	21.76 ± 0.03	21.27 ± 0.08	21.25 ± 0.03
ALESS 37.1	>26.18	>25.29	...	>26.53	25.55 ± 0.14	24.29 ± 0.09	23.50 ± 0.10	...	$23.07 \pm 0.24^{**}$	...	$21.43 \pm 0.12^{**}$	20.56 ± 0.01	20.30 ± 0.01	20.46 ± 0.04	20.60 ± 0.02
ALESS 37.2	>26.18	>25.29	...	>26.53	26.10 ± 0.22	24.62 ± 0.12	...	...	$>23.22^{**}$	>23.06	$>22.41^{**}$	22.33 ± 0.04	22.13 ± 0.04	21.73 ± 0.12	21.72 ± 0.05
ALESS 39.1	25.08 ± 0.10	>25.29	...	25.06 ± 0.07	24.65 ± 0.06	23.98 ± 0.07	23.75 ± 0.12	23.20 ± 0.10	$>23.22^{**}$	...	22.04 ± 0.04	21.24 ± 0.01	20.90 ± 0.01	20.66 ± 0.05	20.67 ± 0.02
ALESS 41.1	...	...	...	...	...	...	...	...	...	...	...	20.12 ± 0.01	19.83 ± 0.01	19.55 ± 0.02	19.51 ± 0.01
ALESS 41.3	...	...	...	...	...	...	...	...	...	...	...	22.39 ± 0.04	22.95 ± 0.09	>22.44	22.45 ± 0.10
ALESS 43.1	>26.18	>25.29	28.10 ± 0.26	>26.53	>26.32	>25.53	>24.68	>24.29	24.10 ± 0.14	...	22.48 ± 0.05	21.10 ± 0.01	20.67 ± 0.01	20.69 ± 0.05	21.33 ± 0.04
ALESS 45.1	>26.18	>25.29	>28.14	>26.53	>26.32	>25.53	>24.68	>24.29	>24.88	...	22.67 ± 0.06	21.24 ± 0.01	20.80 ± 0.01	20.55 ± 0.04	20.75 ± 0.02
ALESS 49.1	>26.18	>25.29	...	24.61 ± 0.05	24.35 ± 0.05	24.10 ± 0.08	23.80 ± 0.13	24.07 ± 0.22	23.32 ± 0.07	...	22.63 ± 0.06	21.77 ± 0.02	21.49 ± 0.02	21.26 ± 0.08	21.27 ± 0.03
ALESS 49.2	26.11 ± 0.25	>25.29	...	25.25 ± 0.09	25.23 ± 0.10	24.53 ± 0.11	23.98 ± 0.15	24.25 ± 0.26	23.60 ± 0.09	...	21.94 ± 0.03	20.88 ± 0.01	20.59 ± 0.01	21.01 ± 0.06	21.32 ± 0.03
ALESS 51.1	>26.18	>25.29	25.63 ± 0.03	24.97 ± 0.07	24.63 ± 0.06	23.65 ± 0.05	22.29 ± 0.03	22.09 ± 0.04	21.15 ± 0.01	20.73 ± 0.03	20.38 ± 0.01	19.47 ± 0.00	19.61 ± 0.00	19.80 ± 0.02	20.17 ± 0.01
ALESS 55.1	24.66 ± 0.07	24.60 ± 0.15	24.49 ± 0.01	24.25 ± 0.04	24.20 ± 0.04	24.05 ± 0.07	23.74 ± 0.12	...	23.26 ± 0.07	>23.06	22.72 ± 0.11	22.25 ± 0.04	22.07 ± 0.04	21.82 ± 0.13	21.56 ± 0.07

Table 2.2: $3\,\sigma$ upper limits are presented for non-detections, and the entry is left blank where a source is not covered by available imaging. [a] Source is within $4''$ of a 3.6-μm source of comparable, or greater, flux [b] We measure J and K_S photometry from three imaging surveys, but quote a single value, in order of $3\,\sigma$ detection limit (see Table 2.2). * Photometry measured from HAWK-I imaging. ** Photometry measured from MUSYC imaging, otherwise photometry measured from TENIS imaging.

ID	MUSYC U	MUSYC U_{38}	VIMOS U	B	V	R	I	z	J^b	H	K^b	3.6 μm	4.5 μm	5.8 μm	8.0 μm
ALESS 55.2	>26.18	>25.29	>28.14	>26.53	>26.32	>25.53	>24.68	>24.29	>24.88	>23.06	>24.35	>24.45	>24.09	>22.44	>23.38
ALESS 55.5	25.31 ± 0.13	25.15 ± 0.24	25.21 ± 0.02	24.74 ± 0.06	24.77 ± 0.07	24.75 ± 0.14	>24.68	...	24.42 ± 0.18	>23.06	23.64 ± 0.15	22.70 ± 0.05	22.50 ± 0.06	22.35 ± 0.20	22.04 ± 0.07
ALESS 57.1	>26.18	>25.29	26.38 ± 0.06	24.86 ± 0.06	25.10 ± 0.09	24.65 ± 0.13	>24.68	>24.29	23.99 ± 0.12	22.66 ± 0.19	22.55 ± 0.06	21.64 ± 0.02	21.26 ± 0.02	20.95 ± 0.06	20.15 ± 0.01
ALESS 59.2	>26.18	>25.29	26.90 ± 0.09	26.21 ± 0.20	26.29 ± 0.26	>25.53	>24.68	>24.29	24.24 ± 0.15	...	23.51 ± 0.13	22.92 ± 0.06	22.54 ± 0.06	>22.44	22.31 ± 0.09
ALESS 61.1[a]	>26.18	>25.29	...	>26.53	>26.32	>25.53	24.39 ± 0.21	23.94 ± 0.20	23.00 ± 0.05	-	22.56 ± 0.06	22.83 ± 0.06	22.45 ± 0.06	>22.44	22.02 ± 0.07
ALESS 63.1	>26.18	>25.29	...	25.96 ± 0.17	25.52 ± 0.14	24.79 ± 0.14	23.64 ± 0.11	23.23 ± 0.11	22.14 ± 0.02	...	21.26 ± 0.02	20.51 ± 0.01	20.29 ± 0.01	20.38 ± 0.04	20.63 ± 0.02
ALESS 65.1	>26.18	>25.29	...	>26.53	>26.32	>25.53	>24.68	>24.29	>24.88	...	>24.35	23.33 ± 0.09	23.77 ± 0.19	>22.44	22.88 ± 0.14
ALESS 66.1	20.91 ± 0.00	20.85 ± 0.01	...	21.27 ± 0.00	21.22 ± 0.00	20.82 ± 0.00	20.66 ± 0.01	20.08 ± 0.01	21.21 ± 0.05**	...	20.28 ± 0.04**	19.41 ± 0.00	19.26 ± 0.00	19.08 ± 0.01	19.10 ± 0.00
ALESS 67.1	25.69 ± 0.18	>25.29	25.24 ± 0.02	24.65 ± 0.05	24.30 ± 0.05	24.17 ± 0.08	23.52 ± 0.10	23.50 ± 0.14	22.41 ± 0.03	...	21.09 ± 0.01	20.26 ± 0.01	19.93 ± 0.01	19.80 ± 0.02	20.36 ± 0.01
ALESS 67.2	>26.18	>25.29	26.09 ± 0.04	25.57 ± 0.12	25.43 ± 0.13	25.10 ± 0.19	24.59 ± 0.25	24.12 ± 0.23	24.09 ± 0.14	...	22.98 ± 0.08	21.36 ± 0.02	21.13 ± 0.02	20.82 ± 0.05	21.48 ± 0.04
ALESS 68.1	>26.18	>25.29	>28.14	>26.53	>26.32	>25.53	>24.68	>24.29	>24.88	...	>24.35	23.34 ± 0.09	22.77 ± 0.08	>22.44	22.09 ± 0.07
ALESS 69.1	>26.18	>25.29	...	>26.53	>26.32	>25.53	>24.68	>24.29	>24.88	...	22.74 ± 0.07	21.49 ± 0.02	21.08 ± 0.02	20.72 ± 0.05	21.02 ± 0.03
ALESS 69.2	>26.18	>25.29	...	>26.53	>26.32	>25.53	>24.68	>24.29	>24.88	...	24.29 ± 0.25	>24.45	>24.09	>22.44	>23.38
ALESS 69.3	>26.18	>25.29	...	>26.53	>26.32	>25.53	>24.68	>24.29	>24.88	...	>24.35	>24.45	>24.09	>22.44	>23.38
ALESS 70.1[a]	24.86 ± 0.09	24.37 ± 0.12	24.49 ± 0.01	23.72 ± 0.02	23.61 ± 0.02	23.47 ± 0.04	23.33 ± 0.08	23.34 ± 0.12	22.27 ± 0.03	...	21.16 ± 0.02	20.25 ± 0.01	20.03 ± 0.01	19.87 ± 0.02	20.21 ± 0.01
ALESS 71.1	>26.18	>25.29	...	25.36 ± 0.10	25.23 ± 0.10	24.28 ± 0.09	23.10 ± 0.07	23.03 ± 0.09	21.81 ± 0.08**	...	20.73 ± 0.06**	18.76 ± 0.00	18.08 ± 0.00	17.66 ± 0.00	17.79 ± 0.00
ALESS 71.3	26.18 ± 0.27	>25.29	...	25.03 ± 0.07	25.13 ± 0.10	25.10 ± 0.19	>24.68	>24.29	>23.22**	...	>22.41**	23.40 ± 0.10	23.34 ± 0.13	>22.44	>23.38
ALESS 72.1	>26.18	>25.29	>28.14	>26.53	>26.32	>25.53	>24.68	>24.29	>24.88	>23.06	>24.35	22.80 ± 0.06	22.91 ± 0.09	>22.44	22.93 ± 0.15
ALESS 73.1	>26.18	>25.29	>28.14	>26.53	>26.32	25.73 ± 0.13	24.00 ± 0.15	>24.29	24.04 ± 0.13	...	23.57 ± 0.14	22.53 ± 0.05	22.41 ± 0.06	21.92 ± 0.14	21.59 ± 0.04
ALESS 74.1[a]	>26.18	>25.29	27.55 ± 0.16	>26.53	>26.32	>25.53	>24.68	>24.29	23.51 ± 0.08	...	22.36 ± 0.05	21.17 ± 0.01	20.77 ± 0.01	20.61 ± 0.04	21.18 ± 0.03
ALESS 75.1	24.65 ± 0.07	24.44 ± 0.13	...	23.58 ± 0.02	23.32 ± 0.02	23.11 ± 0.03	23.05 ± 0.07	23.22 ± 0.11	22.38 ± 0.03	...	22.01 ± 0.03	20.71 ± 0.01	20.06 ± 0.01	19.39 ± 0.01	18.68 ± 0.00
ALESS 75.4[a]	26.09 ± 0.25	>25.29	...	25.41 ± 0.10	25.21 ± 0.10	24.94 ± 0.16	>24.68	>24.29	24.43 ± 0.18	...	>24.35	24.01 ± 0.17	>24.09	...	...
ALESS 76.1	>26.18	>25.29	...	>26.53	>26.32	>25.53	>24.68	>24.29	>23.22**	...	>22.41**	23.49 ± 0.11	23.06 ± 0.10	>22.44	22.68 ± 0.12
ALESS 79.1	>26.18	>25.29	>28.14	>26.53	>26.32	>25.53	>24.68	>24.29	>24.88	...	23.03 ± 0.09	21.70 ± 0.02	21.21 ± 0.02	20.90 ± 0.06	21.11 ± 0.03
ALESS 79.2	26.08 ± 0.25	>25.29	25.65 ± 0.03	24.97 ± 0.07	24.64 ± 0.06	24.31 ± 0.09	23.39 ± 0.09	23.31 ± 0.12	22.05 ± 0.02	...	20.89 ± 0.01	19.95 ± 0.00	19.75 ± 0.00	19.91 ± 0.02	20.45 ± 0.02
ALESS 79.4	>26.18	>25.29	27.73 ± 0.19	>26.53	>26.32	>25.53	>24.68	>24.29	>24.88	...	>24.35	>24.45	>24.09	>22.44	>23.38
ALESS 80.1	>26.18	>25.29	27.68 ± 0.18	>26.53	26.30 ± 0.26	>25.53	24.66 ± 0.26	>24.29	23.88 ± 0.11	...	22.28 ± 0.04	21.45 ± 0.02	21.12 ± 0.02	20.81 ± 0.05	21.34 ± 0.04
ALESS 80.2	>26.18	>25.29	27.00 ± 0.10	26.31 ± 0.22	25.83 ± 0.18	>25.53	>24.68	>24.29	23.90 ± 0.12	...	22.51 ± 0.05	21.39 ± 0.02	21.14 ± 0.02	21.25 ± 0.08	21.94 ± 0.06
ALESS 82.1	>26.18	>25.29	>28.14	>26.53	>26.32	>25.53	>24.68	>24.29	24.56 ± 0.27*	...	23.48 ± 0.13	22.19 ± 0.03	21.79 ± 0.03	21.61 ± 0.11	21.71 ± 0.05
ALESS 83.4[a]	...	...	...	...	...	...	...	...	...	...	...	20.79 ± 0.01	21.01 ± 0.02	21.35 ± 0.09	22.06 ± 0.07
ALESS 84.1	25.81 ± 0.20	25.27 ± 0.26	25.30 ± 0.02	24.71 ± 0.05	24.60 ± 0.06	24.40 ± 0.10	24.03 ± 0.15	...	23.24 ± 0.06	22.45 ± 0.16	21.95 ± 0.03	21.06 ± 0.01	20.71 ± 0.01	20.50 ± 0.04	20.70 ± 0.02
ALESS 84.2	>26.18	>25.29	26.56 ± 0.07	25.83 ± 0.15	25.33 ± 0.11	25.08 ± 0.18	24.71 ± 0.27	24.28 ± 0.26	22.83 ± 0.04	22.48 ± 0.16	21.65 ± 0.02	21.00 ± 0.01	20.81 ± 0.01	20.77 ± 0.05	21.33 ± 0.04
ALESS 87.1	...	...	25.33 ± 0.02	...	...	...	...	...	...	...	...	20.92 ± 0.01	20.68 ± 0.01	20.62 ± 0.04	20.50 ± 0.02
ALESS 87.3	...	...	>28.14	...	...	...	...	...	...	...	...	>24.45	>24.09	>22.44	>23.38
ALESS 88.1	25.65 ± 0.17	>25.29	25.51 ± 0.03	24.93 ± 0.07	24.65 ± 0.06	24.46 ± 0.11	23.75 ± 0.12	23.78 ± 0.17	22.91 ± 0.05	22.98 ± 0.25	21.83 ± 0.03	20.93 ± 0.01	20.64 ± 0.01	20.48 ± 0.04	20.82 ± 0.02
ALESS 88.2	>26.18	>25.29	>28.14	>26.53	>26.32	>25.53	>24.68	>24.29	>24.88	>23.06	>24.35	>24.45	>24.09	>22.44	>23.38
ALESS 88.5	>26.18	>25.29	28.11 ± 0.26	>26.53	26.07 ± 0.22	>25.53	>24.68	>24.29	23.77 ± 0.10	22.12 ± 0.12	22.31 ± 0.04	21.52 ± 0.02	21.17 ± 0.02	20.93 ± 0.06	21.27 ± 0.03
ALESS 88.11	25.03 ± 0.10	24.92 ± 0.20	25.17 ± 0.02	24.06 ± 0.03	23.65 ± 0.03	23.50 ± 0.05	23.19 ± 0.07	23.08 ± 0.09	22.99 ± 0.05	>23.06	22.06 ± 0.04	21.37 ± 0.02	21.21 ± 0.02	21.18 ± 0.07	21.50 ± 0.04
ALESS 92.2	25.56 ± 0.16	>25.29	25.55 ± 0.03	25.28 ± 0.09	24.82 ± 0.07	24.42 ± 0.10	24.48 ± 0.23	23.63 ± 0.15	23.83 ± 0.11	...	23.75 ± 0.16	23.48 ± 0.11	23.52 ± 0.15	>22.44	>23.38
ALESS 94.1	>26.18	>25.29	...	26.03 ± 0.18	25.92 ± 0.19	>25.53	>24.68	>24.29	>24.88	>23.06	23.33 ± 0.11	22.06 ± 0.03	21.66 ± 0.03	21.33 ± 0.08	21.47 ± 0.04
ALESS 98.1	>26.18	>25.29	...	>26.53	>26.32	>25.53	24.28 ± 0.19	...	22.71 ± 0.04	...	21.22 ± 0.02	19.86 ± 0.00	19.47 ± 0.00	19.59 ± 0.02	19.91 ± 0.01
ALESS 99.1	>26.18	>25.29	28.10 ± 0.26	>26.53	>26.32	>25.53	>24.68	>24.29	>24.88	>23.06	>24.35	>24.45	>24.09	>22.44	>23.38
ALESS 102.1	>26.18	>25.29	...	>26.53	26.27 ± 0.22	>25.53	>24.68	>24.29	22.79 ± 0.19**	...	21.07 ± 0.08**	20.07 ± 0.00	19.78 ± 0.01	19.77 ± 0.02	20.56 ± 0.02
ALESS 103.3	>26.18	>25.29	...	>26.53	>26.32	>25.53	>24.68	>24.29	>23.22**	...	>22.41**	>24.45	>24.09	>22.44	>23.38

Table 2.2: continued

ID	MUSYC U	MUSYC U_{38}	VIMOS U	B	V	R	I	z	J^b	H	K^b	3.6 μm	4.5 μm	5.8 μm	8.0 μm
ALESS 107.1	>26.18	>25.29	...	25.63 ± 0.12	24.62 ± 0.06	23.66 ± 0.05	22.61 ± 0.04	22.61 ± 0.06	21.83 ± 0.02	...	21.08 ± 0.01	20.49 ± 0.01	20.71 ± 0.01	20.77 ± 0.05	20.89 ± 0.02
ALESS 107.3	>26.18	>25.29	...	25.82 ± 0.15	25.52 ± 0.14	25.52 ± 0.26	>24.68	>24.29	24.44 ± 0.18	...	24.17 ± 0.23	>24.45	>24.09	>22.44	>23.38
ALESS 110.1	...	...	...	...	...	...	...	...	>24.88	...	>24.35	22.72 ± 0.05	22.04 ± 0.04	21.53 ± 0.10	21.32 ± 0.04
ALESS 110.5	...	...	...	...	...	...	...	...	>24.88	...	>24.35	22.49 ± 0.04	23.01 ± 0.10	>22.44	>23.38
ALESS 112.1	...	...	26.79 ± 0.08	...	...	...	...	...	...	...	...	20.56 ± 0.01	20.22 ± 0.01	20.03 ± 0.03	20.66 ± 0.02
ALESS 114.1	>26.18	>25.29	>28.14	>26.53	>26.32	>25.53	>24.68	>24.29	>24.88	>23.06	>24.35	23.99 ± 0.16	23.21 ± 0.11	>22.44	>23.38
ALESS 114.2	24.83 ± 0.08	24.87 ± 0.19	24.78 ± 0.01	24.24 ± 0.04	23.93 ± 0.03	23.56 ± 0.05	22.73 ± 0.05	22.61 ± 0.06	21.21 ± 0.01	20.58 ± 0.03	20.37 ± 0.01	19.56 ± 0.00	19.26 ± 0.00	19.46 ± 0.02	19.70 ± 0.01
ALESS 116.1[a]	>26.18	>25.29	>28.14	>26.53	>26.32	>25.53	>24.68	>24.29	>24.88	>23.06	24.01 ± 0.20	23.52 ± 0.11	22.83 ± 0.08	>22.44	22.49 ± 0.10
ALESS 116.2	>26.18	>25.29	>28.14	>26.53	>26.32	>25.53	>24.68	>24.29	>24.88	>23.06	23.85 ± 0.17	22.86 ± 0.06	22.22 ± 0.05	21.92 ± 0.14	21.87 ± 0.06
ALESS 118.1	...	...	...	...	...	...	...	...	23.42 ± 0.08	...	22.67 ± 0.06	21.84 ± 0.02	21.29 ± 0.02	21.07 ± 0.07	21.35 ± 0.04
ALESS 119.1	>26.18	>25.29	...	>26.53	25.82 ± 0.18	25.17 ± 0.20	>24.68	24.04 ± 0.22	24.20 ± 0.20*	...	23.41 ± 0.15*	22.78 ± 0.06	22.19 ± 0.05	21.66 ± 0.11	21.89 ± 0.06
ALESS 122.1	24.34 ± 0.05	24.31 ± 0.12	24.22 ± 0.01	23.49 ± 0.02	23.16 ± 0.02	22.96 ± 0.03	22.62 ± 0.04	22.55 ± 0.06	21.49 ± 0.01	...	20.68 ± 0.01	19.88 ± 0.00	19.51 ± 0.00	19.19 ± 0.01	19.27 ± 0.01
ALESS 124.1[a]	>26.18	>25.29	>28.14	>26.53	>26.32	>25.53	>24.68	>24.29	24.63 ± 0.22	>23.06	23.73 ± 0.16	21.92 ± 0.03	21.49 ± 0.02	21.44 ± 0.09	21.18 ± 0.03
ALESS 124.4	>26.18	>25.29	>28.14	>26.53	>26.32	>25.53	>24.68	...	>24.88	>23.06	>24.35	>24.45	>24.09	>22.44	>23.38
ALESS 126.1	>26.18	>25.29	26.68 ± 0.08	26.11 ± 0.19	26.31 ± 0.26	>25.53	>24.68	...	23.79 ± 0.10	22.33 ± 0.14	22.28 ± 0.04	20.95 ± 0.01	20.74 ± 0.01	20.86 ± 0.06	21.42 ± 0.04

Table 2.2: continued

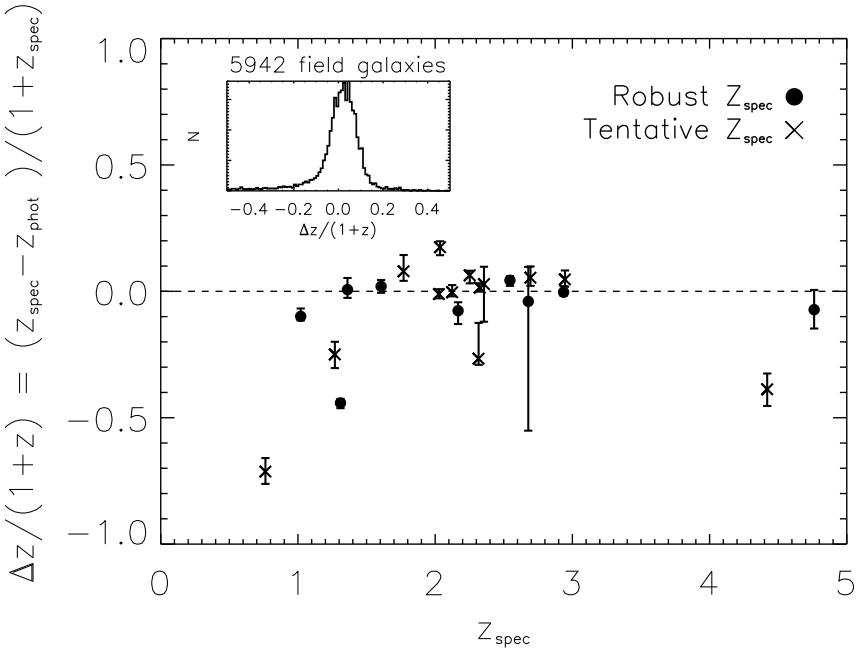

Figure 2.3: A comparison of the photometric redshifts derived in this work, to spectroscopically confirmed redshifts drawn from the literature and from our redshift follow-up of the original LESS sources (zLESS; Danielson et al. in prep). The inset shows the distribution of $\Delta z\,/\,(1+z_{\rm spec})$ for a 3.6 μm selected training sample with spectroscopic redshifts. For the field sample we find good agreement between the photometric and spectroscopic redshifts, with a median $\Delta z\,/\,(1+z_{\rm spec})$ of 0.011 ± 0.002, and a 1-σ dispersion of 0.06. In the main panel we compare the photometric redshifts for 22 ALESS SMGs with confirmed spectroscopic redshifts. We again find good agreement, with a median $\Delta z\,/\,(1+z_{\rm spec})$ of -0.004 ± 0.026. We identify spectroscopic redshifts as robust where they are calculated from multiple strong emission lines, and tentative where multiple weak lines, or single line IDs are used. We identify three outliers, at $|\,\Delta z\,/\,(1+z_{\rm spec})\,| > 0.3$. Of the three sources only one, ALESS 66.1, has a robust spectroscopic redshift, and is an optically bright QSO. The remaining two sources have spectroscopic redshifts drawn from single line identifications.

2.5.1 Training sample

Before deriving photometric redshifts for the ALESS SMGs, we first calibrate our photometry to the template SEDs used in the photometric redshift calculation. To do so, we use SExtractor to create a 3.6-μm selected catalogue designed to test the reliability of our photometric redshifts against archival spectroscopic surveys. The spectroscopic sample is collated from a wide range of sources (Cristiani et al. 2000; Croom et al. 2001; Cimatti et al. 2002; Teplitz et al. 2003; Bunker et al. 2003; Le Fèvre et al. 2004; Zheng et al. 2004; Szokoly et al. 2004; Strolger et al. 2004; Stanway et al. 2004; van der Wel et al. 2005; Mignoli et al. 2005; Daddi et al. 2005; Doherty et al. 2005; Ravikumar et al. 2007;

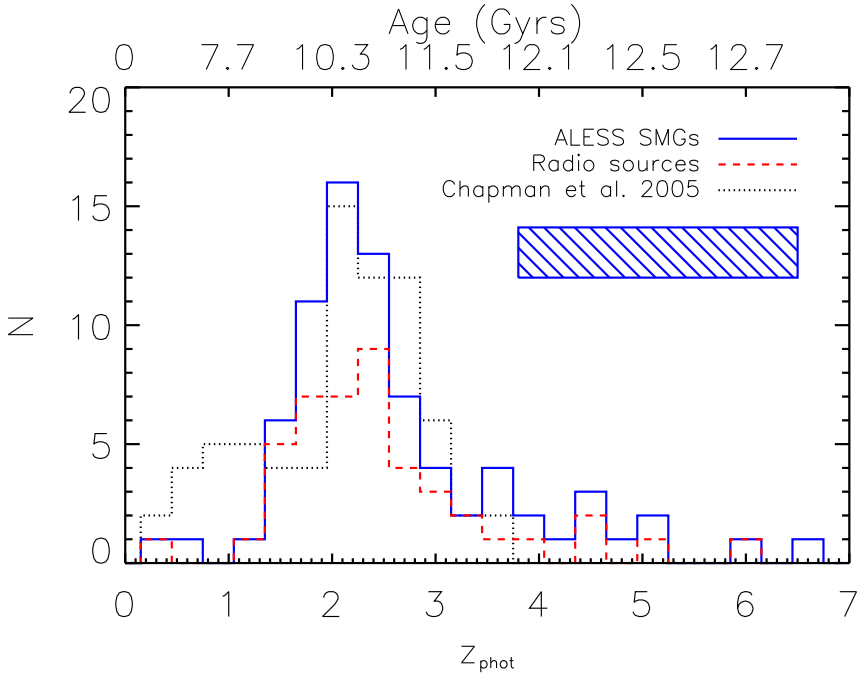

Figure 2.4: The photometric redshift distribution of ALESS SMGs with individually derived photometric redshifts. For comparison we show the spectroscopic redshift distribution from Chapman et al. (2005), a radio-selected sample of SMGs. We find the ALESS SMGs lie at a median redshift of $z = 2.3 \pm 0.1$, consistent with the result from Chapman et al. (2005). In contrast to Chapman et al. (2005) we do not find a significant number of SMGs at $z \lesssim 1$, and we identify a high redshift tail at $z \gtrsim 3.5$, not seen in Chapman et al. (2005). The hatched box represents the area missing from the ALESS histogram due to 19 SMGs with insufficient photometry to derive photometric redshifts. In § 2.5.2.3 we identify these sources as belonging to the high-redshift tail of the distribution (i.e. $z \gtrsim 3$). Including these 19 SMGs raises the median redshift to $z = 2.5 \pm 0.2$, see Figure 2.12.

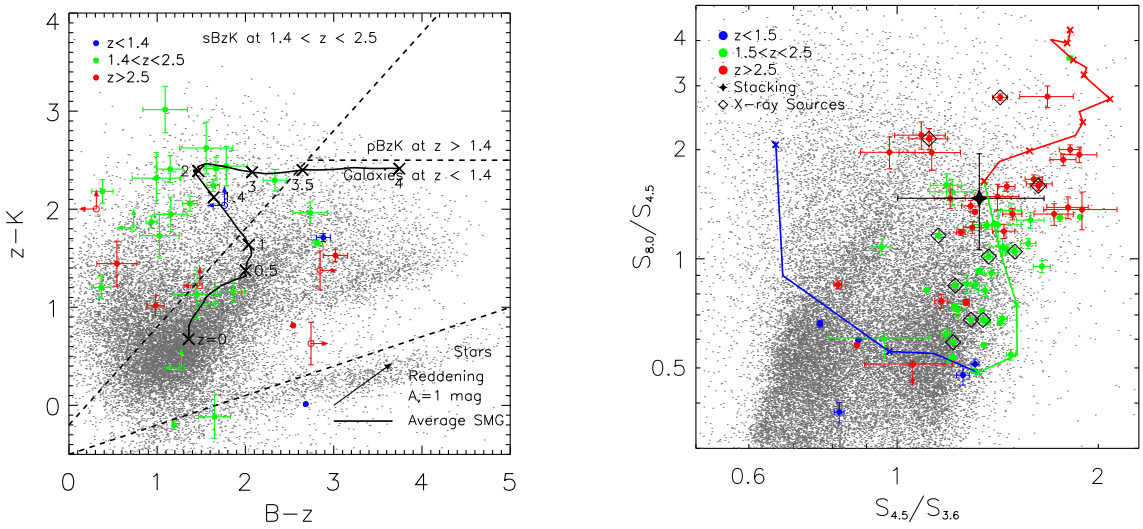

Figure 2.5: *Left:* The $(B-z)$ - $(z-K_S)$ colours for the ALESS SMGs, colour-coded by photometric redshift. The regions where star-forming and passive BzK galaxies at $z = 1.4$–2.5 are expected to lie (sBzK and pBzK respectively) are shown, and we plot the distribution of field galaxies in grey. We find that ~ 70 per cent of SMGs have photometric redshifts which are consistent with the predictions from the BzK diagram. The solid line shows the track of the average ALESS SMG, derived by de-redshifting the observed photometry (see Figure 2.11). From this track we expect the BzK diagnostic to fail for SMGs at $z \gtrsim 3.5$. In the lower right we plot the reddening vector for one magnitude of extinction. *Right:* The ratio of the IRAC fluxes for the ALESS SMGs, colour-coded by redshift. For comparison we plot the track of SMM J2135–0102, a $z = 2.3$ SMG (Swinbank et al., 2010b), colour-coded in the same manner as the data points. Similar to the BzK analysis we find our photometric redshifts provide a good match to the expected colours of the ALESS SMGs. We also plot the average IRAC colour from a stacking analysis of SMGs detected in only 2 or 3 wavebands (the error represents the variance in the measured flux). The measured flux from our stacking is clearly noisy, and although we cannot derive photometric redshifts for these SMGs, their colours appear consistent with the bulk of the SMG population at $z \sim 2.5$. We highlight ALESS SMG detected in X-ray emission (Wang et al., 2013). We find that one X-ray detected SMG, ALESS 57.1, and six SMGs in the complete sample show evidence of an 8 μm excess suggestive of AGN emission.

Vanzella et al. 2008; Kriek et al. 2008b; Popesso et al. 2009; Treister et al. 2009; Balestra et al. 2010; Silverman et al. 2010; Casey et al. 2011; Cooper et al. 2012; Bonzini et al. 2012; Swinbank et al. 2012; Koposov et al. in prep; Danielson et al. in prep), yielding 5942 spectroscopic redshifts with a median $z_{\rm spec} = 0.67$, an interquartile range of 0.45–0.85 and 1077 galaxies at $z > 1$. We measure photometry for these sources in the same manner as the ALESS SMGs (see § 2.4.2.1). For reference, the spectroscopic sample has 10 – 90 percentile magnitude ranges of $V = 21.6 - 24.4$, and $m_{3.6} = 19.3 - 22.8$.

To test for small discrepancies between the observed photometry and the template SEDs we run HYPERZ on our training set of 5942 galaxies with spectroscopic redshifts, fixing the redshift to the spectroscopic value. We then measure the offset between the observed photometry and that predicted from the best-fit model SED. We apply the measured offset to the observed photometry and then repeat the procedure for three iterations. After the final iteration we derive, and apply, significant offsets in the MUSYC U (-0.16), U_{38} (-0.12), MUSYC J (-0.10), H (-0.14), HAWK K_S (-0.10), TENIS K (0.10), 5.8 μm (0.19) and 8.0 μm (0.40) photometry. Offsets in the remaining bands are < 0.06, and the typical uncertainty is ± 0.02. The largest offset is an excess in the IRAC 8.0 μm, which may be due to a hot dust component in the SEDs which is not included in the HYPERZ templates. We test whether the 8.0 μm data drives systematic offsets at other wavelengths by omitting the IRAC 5.8 and 8.0 μm data and repeating the procedure, but find the magnitude offsets are consistent with those determined when these wavebands are included.

To determine the accuracy of our photometric redshifts we initially compare the results for the 5942 galaxies in the ECDFS with spectroscopic redshifts. We calculate $\Delta z = z_{\rm spec} - z_{\rm phot}$ for each galaxy and plot the histogram of $\Delta z \,/\, 1 + z_{\rm spec}$ in Figure 2.3. We find excellent agreement between the photometric and spectroscopic redshifts, measuring a median $\Delta\, z \,/\, (1 + z_{\rm spec}) = 0.011 \pm 0.002$, with a $1\,\sigma$ dispersion of 0.057 and a Normalized Median Absolute Deviation (NMAD) of $\sigma_{\rm NMAD} = 1.48 \times {\rm median}(|\Delta {\rm z} - {\rm median}(\Delta {\rm z})|/1 + {\rm z_{spec}}) = 0.073$ [1].

Previous studies indicate that the majority of the ALESS SMGs lie at $z > 1.0$ (see

[1] We also derived photometric redshifts for our training sample using the SED fitting code EAZY (Brammer et al., 2008). We find the photometric redshifts derived by EAZY are comparable with those from HYPERZ, with a median $\Delta z \,/\, 1 + z_{\rm spec} = 0.020 \pm 0.006$; consistent with Dahlen et al. (2013) who find comparable performance between photometric redshift estimation codes.

Wardlow et al. 2011), and so we also investigate the accuracy of our photometric redshifts limiting just to this redshift range. For the $z > 1.0$ sources in the training sample the median $\Delta z / (1 + z_{\rm spec})$ is 0.033 $\pm$ 0.005, marginally higher than for the training sample as a whole. We define catastrophic failures as sources with $\Delta z / (1 + z_{\rm spec}) > 0.3$, and we find the failure rate for the 1077 sources at $z > 1.0$ is 4 per cent. Importantly the $z > 1.0$ training sample has a median 3.6 μm magnitude of $m_{3.6} = 21.2 \pm 0.1$, which is similar to the median 3.6 μm magnitude of the ALESS sample, $m_{3.6} = 21.8 \pm 0.2$.

Although HYPERZ returns a best-fit model and 1 σ error, for our sample of field galaxies we determine that the HYPERZ "99 per cent" confidence intervals provide the best estimate of the redshift error; yielding $\sim$68% agreement between the photometric and spectroscopic redshifts at 1σ and so we adopt these as our 1-σ error estimates (see also Luo et al. 2010; Wardlow et al. 2011).

2.5.2 ALESS Photometric Redshifts

Before deriving the redshift distribution for all ALESS SMGs, we next make use of the existing spectroscopy of ALESS sources to test the reliability of our photometric redshifts for SMGs. Combining our results with a small number from the literature we have spectroscopic redshifts for 22 ALESS SMGs (Zheng et al. 2004; Kriek et al. 2008b; Coppin et al. 2009; Silverman et al. 2010; Casey et al. 2011; Bonzini et al. 2012; Swinbank et al. 2012; Danielson et al. in prep). We run HYPERZ on these SMGs to derive their photometric redshifts, and in Figure 2.3 we compare the spectroscopic results to our photometric redshifts (Figure 2.3) and find a median $\Delta z / (1+z_{\rm spec}) = -0.004 \pm 0.026$, and $\sigma_{\rm NMAD} = 0.099$. The spectroscopically confirmed ALESS SMGs have a median redshift $z_{\rm spec} = 2.2 \pm 0.2$ and a median 3.6 μm magnitude of $m_{3.6} = 20.5 \pm 0.5$. Together with the results for the 5924 galaxies in the spectroscopic training sample we can therefore be confident that the photometric redshifts we derive provide a reliable estimate of the SMG population.

2.5.2.1 Reliability of SMG redshifts

Running HYPERZ on the photometry catalogue of 77 ALESS SMGs, with detections in > 3 wavebands, we derive a median photometric redshift of $z_{\rm phot} = 2.3 \pm 0.1$, with a tail to $z \sim 6$ (Figure 2.4) and a 1-σ spread of $z_{phot} = 1.8$–3.5. In Table 2.3 we provide the redshifts for individual sources. We note that we will return to discuss the 19 SMGs detected in

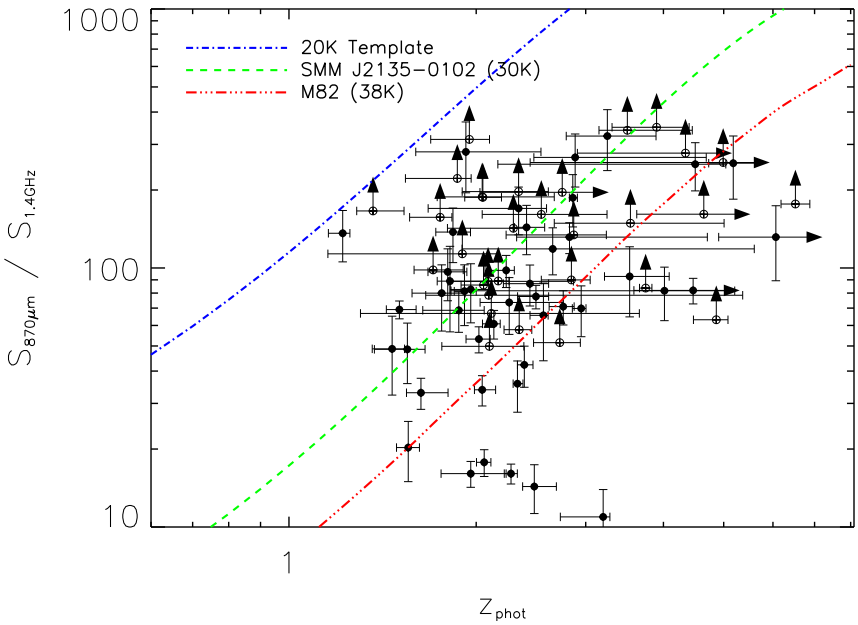

Figure 2.6: The variation in $S_{870\mu m}\,/\,S_{1.4\mathrm{GHz}}$ as a function of redshift for the 77 SMGs with photometric redshifts. We overlay tracks for the local star-forming galaxy M 82 (T_d = 38 K), SMM J2135–0102 a $z\sim2.3$ SMG ($T_\mathrm{d}\sim30$ K) and a cool dust template (T_d = 20 K; Chary & Elbaz 2001). The tracks for M 82 and SMM J2135–0102 pass through the bulk of the population, however we find a large dispersion in $\mathrm{S}_{870\mu m}\,/\,\mathrm{S}_{1.4\mathrm{GHz}}$; around 1.5 dex at a fixed redshift. For the 32 SMGs which are not detected at 1.4 GHz we adopt a 3-σ upper limit (open symbols with arrows), corresponding to 3 × the VLA map rms at the SMG position. The 32 ALESS SMGs which are not detected in available radio data have a range of photometric redshifts from $z_{phot} > 1$. We note that the $S_{870\mu m}\,/\,S_{1.4\mathrm{GHz}}$ flux ratios of these undetected, low redshift ($z \lesssim 2.5$), SMGs can be adequately reproduced using a "cool" dust template (T_d = 20–30 K) consistent with previous studies (Magnelli et al., 2012; Weiß et al., 2013).

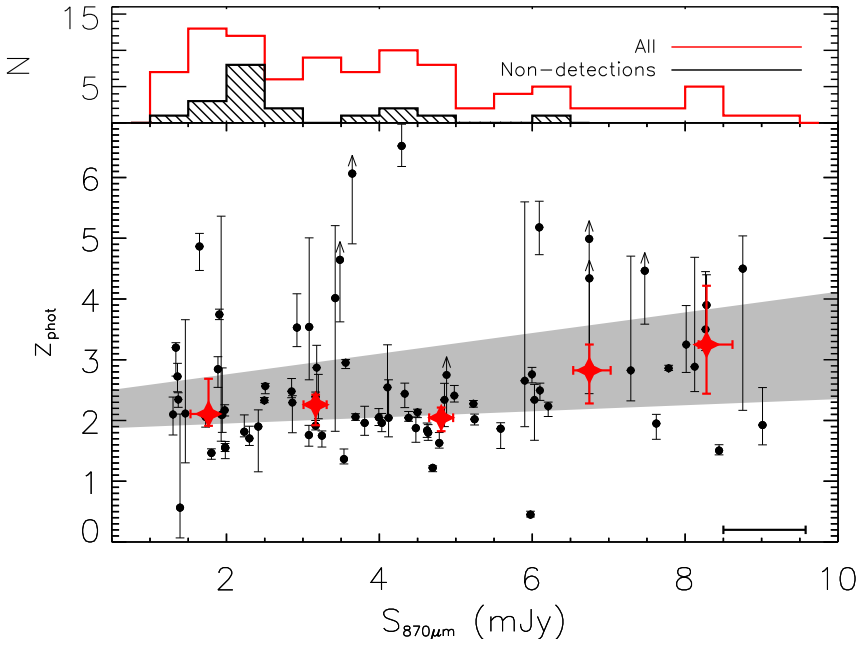

Figure 2.7: The photometric redshifts of the ALESS SMGs versus their 870 μm flux density. We also split the data into 2-mJy bins and plot the median $S_{870\mu m}$ and redshift for each bin, with 1-σ error bars. We test for a trend of higher $S_{870\mu m}$ sources lying at higher redshift, but a linear fit to the data shows the deviation from a constant with redshift is not significant, at $< 1.5\,\sigma$. A grey region shows the linear fit and associated 1-σ uncertainty. In the upper panel we highlight the 870-μm flux distribution of those SMGs for which we cannot derive photometric redshifts. As we show in § 2.5.2.3 these SMGs are likely to lie at $z \gtrsim 3$, and the weak trend we see with redshift is therefore likely driven by incompleteness in our results: including these photometrically-faint SMGs would further weaken any trend. The error bar on the median flux density is shown in the lower right.

fewer than four wavebands in § 2.5.2.3. We caution that five SMGs (ALESS 5.1, 6.1, 57.1, 66.1 and 75.1) have best-fit solutions with anomalously high values of $\chi^2_{\rm red}$ (> 10). We inspect the photometry for each of these and find ALESS 57.1, 66.1 and 75.1 have an 8.0 μm excess consistent with obscured AGN activity (ALESS 66.1 is an optically identified QSO, ALESS 57.1 is an X-ray detected SMG and ALESS 75.1 has excess radio emission consistent with AGN activity, Wang et al. 2013). As we do not include AGN templates in our model SEDs it is unsurprising that we find poor agreement for these sources. For the remaining two sources, the photometry of ALESS 5.1 is dominated by a large nearby galaxy, while ALESS 6.1 is a potential lensed source; the 870 μm emission is offset by $\sim 1.5''$ from a bright optical source at $z_{\rm phot} \sim 0.4$. We therefore advise that the photometric redshifts for ALESS 5.1 and 6.1 are treated with caution and we highlight these SMGs in Table 2.3.

For six ALESS SMGs we derive photometric redshifts from detections in only four wavebands, our enforced minimum (although we note the SED fit is constrained by sensitive upper limits in the remaining wavebands). To test if this introduces a bias in our following analysis we take the photometry for 37 SMGs in our sample detected in > 8 wavebands and make each source intrinsically fainter until only four of the photometry points remain above our detection limits. We then repeat the SED fitting procedure on these "faded" SMGs. We find a median offset in $(z_4 - z_{\rm All}) \,/\, (1 + z_{\rm All}) = -0.098 \pm 0.050$, and agreement at $3\,\sigma$ for all sources. Crucially, whilst we find increased scatter between the original and faded photometric redshifts, and larger associated uncertainties, we do not find any bias towards higher, or lower, redshifts [2].

Five SMGs in our sample are covered by IRAC imaging alone. To test the reliability of redshifts for ALESS SMGs derived from such photometry, we take the same sub-sample of 37 SMGs, remove *all* other photometric data, including upper limits, and repeat the SED fitting. We find a median offset in $(z_{\rm IRAC} - z_{\rm All}) \,/\, (1 + z_{\rm All}) = 0.015 \pm 0.031$, and agreement at $3\,\sigma$ for 36/37 SMGs. If we restrict our comparison to the ALESS

[2] We also test the likely effect of emission lines on the SED fitting using a young/blue template, with emission lines of similar equivalent width to SMGs (Swinbank et al., 2004), provided with the EAZY SED fitting code (Brammer et al., 2008). We run HYPERZ on the ALESS SMGs, using both the emission line template, and the same template with all emission lines removed. The resulting photometric redshifts are in agreement to within $\Delta\, z \,/\, (1 + z) = 0.000 \pm 0.001$. We observe a small increase in scatter at $z \sim 2.5$, which we attribute to Hα falling in/out of the K_s-band. The effect is small and over the redshift range $z = 2.2$–2.8 and we measure $\Delta\, z \,/\, (1 + z) = 0.009 \pm 0.009$. Due to the modest magnitude of the effect of Hα on the photometric redshifts we do not make any attempt to correct for it in our SED fitting.

SMGs with spectroscopic redshifts then we find $(z_{\rm IRAC} - z_{\rm spec}) \ / (1 + z_{\rm spec}) = -0.09 \pm 0.13$, with a median error on each photometric redshift of $\sigma_{\rm z} = 0.6$. We note that if we only use 3 photometric data points in the SED fitting then the photometric redshifts are unconstrained, with a median 1-σ error of $\sigma_{\rm z} = 2.0$. We therefore can be confident in the reliability of photometric redshifts derived from detections in four photometric bands, and adopt this limit throughout our analysis.

Finally we investigate the effect of source blending on our results. We re-measure aperture photometry for all of the ALESS SMGs, in the same manner described in § 2.4.2.1, but with a $2''$ diameter aperture across all wavelengths. A smaller aperture means the effects of blending are reduced, especially in the IRAC data. We repeat the SED fitting procedure described in § 2.5, to derive photometric redshifts from the new, small aperture, photometry. Considering all ALESS SMGs we find good agreement between the photometric redshifts, with $(z_{\rm Original} - z_{\rm SmallAperture}) \, / \, (1 + z_{\rm All}) = -0.012 \pm 0.009$. Of the 12 SMGs we flag as blended with a nearby bright IRAC source (see Table 2.1), nine have a photometric redshift derived from photometry measured in a smaller aperture which is consistent with the original redshift to within 1-σ. Of the remaining three SMGs, ALESS 5.1 has been discussed already as a possible lens system, and two other sources ALESS 75.4 & 83.4 are not detected in > 3 wavebands in the smaller apertures. We highlight these SMGs in Table 2.3 and note that their redshifts should be treated with caution. In Figure 2.9 we highlight these three SMGs, along with ALESS 6.1, another potential lens system, as having suspicious photometry. We conclude that blending of sources does not have a significant effect on the bulk of the redshifts we derive.

2.5.2.2 Redshift indicators

A number of colour-colour diagnostics have been suggested to identify star-forming galaxies. We consider three of these as simple tests of the reliability of our photometric redshifts. The first we consider is the BzK diagram, which has been proposed as a tool to separate star-forming and passive galaxies at $z \sim 1.4$–2.5, by means of identifying the Balmer/4000Å break. In Figure 2.5 we show the BzK diagram for the ALESS SMGs with suitable photometric detections. We find that within the photometric errors 65 per cent are correctly identified as star-forming at $z > 1.4$ and 25 per cent are incorrectly classed as lying at $z < 1.4$. One ALESS SMG is correctly classified as a galaxy at $z < 1.4$, and no ALESS SMGs are classed as passive galaxies at $z > 1.4$. Three ALESS SMGs have BzK

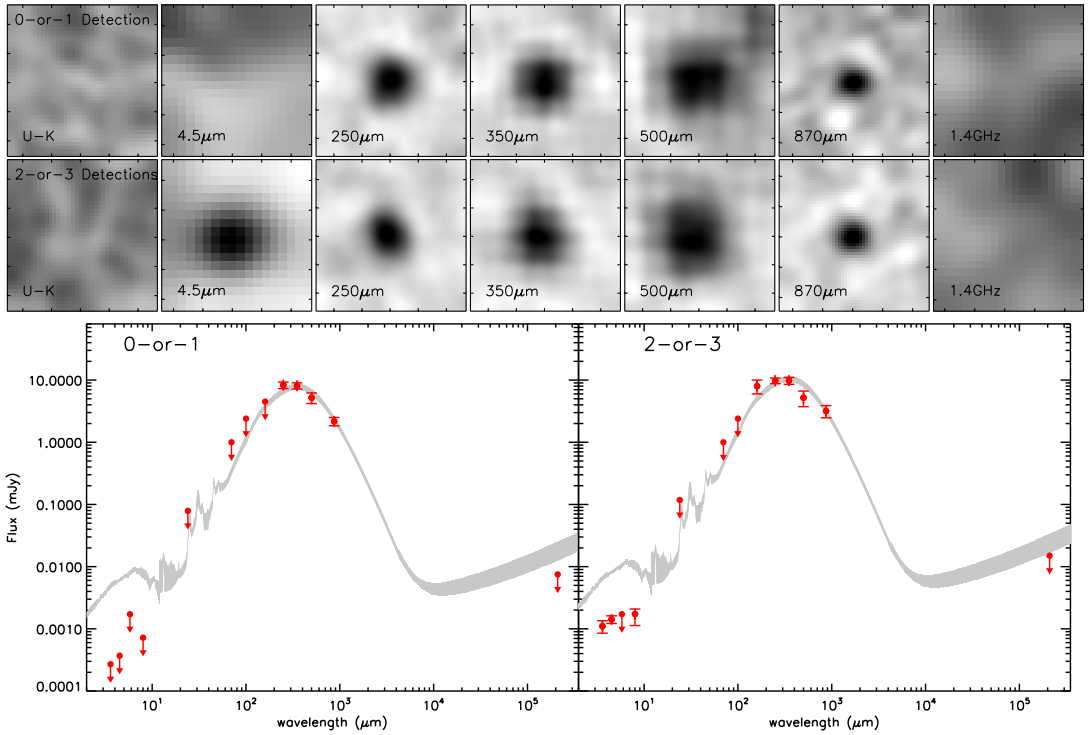

Figure 2.8: 19 SMGs from our sample are detected in fewer than four optical – near-infrared wavebands (see Table 2.1). We sub-divide these 19 sources into those detected in either 0-or-1 (9) or 2-or-3 (10) wavebands and stack the available imaging at the ALMA position to test if they are real or spurious. In particular we stack the *Herschel* 250, 350, and 500 μm imaging, and the 1.4 GHz VLA data. The *Herschel* 250, 350, and 500 μm greyscale images are $80'' \times 80''$, and the other greyscale images are $10'' \times 10''$. Both subsets are detected in stacks of all three *Herschel* bands, confirming, on average, that they do represent far-infrared sources. We do not find a detection for either subset in a stack of the U - K_s imaging, or the 1.4 GHz data. The subset of SMGs with 2-or-3 detections does yield a detection in the IRAC 3.6, 4.5 and 8.0 μm bands, however this is unsurprising as their 2-or-3 photometric detections are usually in the IRAC bands. In the lower panel we show the far-infrared properties of these 19 SMGs. We also show the results of stacking the MIPS 24 μm and PACS 70, 100 and 160 μm imaging, for details of this data see Swinbank et al. (2014). The stacked FIR emission for both subsets appears to peak between 250–350 μm, suggesting that these SMGs do not lie, on average, at very high redshifts ($z \gtrsim 5$). On each panel the grey line represents the average ALESS SMG SED, plotted at a redshift of $z = 2.5$ and 2.0, for the 0-or-1 and 2-or-3 subsets respectively (see also Swinbank et al. 2014). We note that the line is not a fit to the data points, but is simply scaled to match the peak of the far-infrared SED. We highlight that the shape of the SED appears well matched to the stacked FIR emission, but that the NIR properties of these SMGs are an order of magnitude fainter than the average SED. Similarly, at the nominal redshift plotted the composite SED over-predicts the radio emission from both subsets of SMGs.

colours consistent with stars, one of which, ALESS 66.1, is an optically identified QSO. We caution that half of the ALESS SMGs incorrectly classified as galaxies at $z < 1.4$ have photometric redshifts greater than the upper range of the BzK diagnostic, i.e. $z > 2.5$. We plot the SED for the composite ALESS SMG in Figure 2.5, which shows that we expect the BzK diagram to classify SMGs at redshifts from $z \sim 1$–4, as star-forming BzKs at $z \sim 1.4$–2.5, and SMGs at redshifts greater than $z > 3.5$ as galaxies at $z < 1.4$.

We find that the ALESS SMGs display a clear trend with redshift in $S_{8.0} \,/\, S_{4.5}$ versus $S_{4.5} \,/\, S_{3.6}$ colour (Figure 2.5), with sources at high redshift tending to have higher ratios of $S_{8.0} \,/\, S_{4.5}$. As a further test of our photometric redshifts we overlay the predicted colours of SMM J2135–0102 (a well-studied SMG at $z = 2.3$; Swinbank et al. 2010b) as a function of redshift on Figure 2.5. We find that the derived photometric redshifts for the ALESS SMGs are in good agreement with the predictions from this SED track.

Ten ALESS SMGs are detected in data taken with the *Chandra* X-ray Observatory (see Wang et al. 2013). This X-ray emission is often indicative of an AGN component in the host galaxy, which can affect the SED shape. As such, we now investigate whether the X-ray detected SMGs (Wang et al., 2013) are distinguishable from the parent sample of SMGs in terms of their IRAC fluxes. We identify one X-ray detected SMG, ALESS 57.1, which has a high $S_{8.0} \,/\, S_{4.5}$ ratio, relative to $S_{4.5} \,/\, S_{3.6}$, suggestive of a power-law AGN component in the SED. A further inspection of the SED fits in Figure 2.16 shows that only two SMGs display a clear enhancement in IRAC flux (ALESS 57.1 & 75.1), which is often attributed to AGN heated dust emission [3]. The remaining X-ray sources appear well-matched to the complete SMG sample. We perform a two-sided Kolmogorov-Smirnov (KS) test between the X-ray detected SMGs, and the parent sample, in terms of both $S_{8.0} \,/\, S_{4.5}$ and $S_{4.5} \,/\, S_{3.6}$. The KS test returns a probability of 85 per cent that the samples are drawn from the same parent distribution, in terms of both $S_{8.0} \,/\, S_{4.5}$ and $S_{4.5} \,/\, S_{3.6}$. This suggests that in terms of IRAC colour the X-ray detected SMGs do not represent a distinct subset of SMGs.

Finally we consider the link between 870 μm and 1.4 GHz emission, which has been used

[3] The low rate of near-infrared excess in the ALESS SEDs is in stark contrast to the SEDs seen in previous SMG samples, where a large fraction show restframe near-infrared excesses whose amplitude appears to correlate with AGN luminosity (Hainline et al., 2011). This may reflect differences in the sample selection between the predominantly radio-pre-selected, spectroscopically confirmed, SMGs in Hainline et al. (2011) and the purely sub-mm-flux-limited sample analysed here.

to identify the optical – near-infrared counterpart to sub-mm emission. We first stress that we see an order of magnitude of scatter in $S_{870\mu m}$ / $S_{1.4GHz}$ at a fixed redshift (Figure 2.6). We now compare the ALESS SMGs to three template SEDs with varying characteristic dust temperatures. We use templates for two well-studied dusty galaxies, SMM J2135–0102[4] ($\sim$30 K) and M 82 (38 K). In addition we also use a 20 K template drawn from the Chary & Elbaz (2001) template SED library. These templates span typical dust temperatures for SMGs (Magnelli et al., 2012; Weiß et al., 2013), and we find they are sufficient to describe the majority of ALESS SMGs. Previous studies have suggested redshift solutions below $z \lesssim 2.5$ are incorrect for radio-non-detected SMGs (Smolčić et al., 2012). We find templates with a characteristic temperature of 20–30 K are a plausible explanation for similar ALESS SMGs, and we therefore do not discard redshift solutions at $z \lesssim 2.5$ (see also Swinbank et al. 2014).

2.5.2.3 Undetected or Faint Counterparts

For the 77 ALESS SMGs which have counterparts in at least four optical or near-infrared bands, we are able to estimate reliable photometric redshifts. However, this leaves 19 ALESS SMGs ($\sim$20 per cent of the sample) which do not have sufficient detections to derive a photometric redshift. To test whether these sources are spurious or simply fainter than the rest of the population, we divide the SMGs into subsets compromising 0-or-1 and 2-or-3 detections in both the optical ($U-K_S$) and IRAC wavebands, and stack their emission in these wavebands using a clipped mean algorithm. Fig. 2.8 shows that only the 2-or-3 waveband subset yields a stacked detection in the IRAC wavebands at the 7σ level, whereas the optical stacks of both subsets, and the IRAC stack of the 0-or-1 subset, all yield non-detections at the $< 3\sigma$ level.

Next, we stack the emission from these SMGs in the far-infrared *Herschel* / SPIRE maps at 250, 350 and 500 μm and show these in Figure 2.8. The SMGs are clearly detected at $> 4\sigma$ in all SPIRE bands in both the 0-or-1 and 2-or-3 subsets, with 250, 350 and 500 μm flux densities between 4–16 mJy [5]. We note that four of the SMGs are detected individually

[4]The best-fit far-infrared SED to the photometry of SMM J2135–0102 is a two component dust model at 30 K and 60 K. The dust masses of each component are $M_{\rm d}^{\rm warm} = 10^6\,{\rm M}_\odot$ and $M_{\rm d}^{\rm cold} = 4\times10^8\,{\rm M}_\odot$ (Ivison et al., 2010c)

[5]We use the deblended SPIRE maps described in Swinbank et al. (2014) but to account for the clustering, we use a deblended map where the ALESS SMGs are not included in the a-priori catalogue.

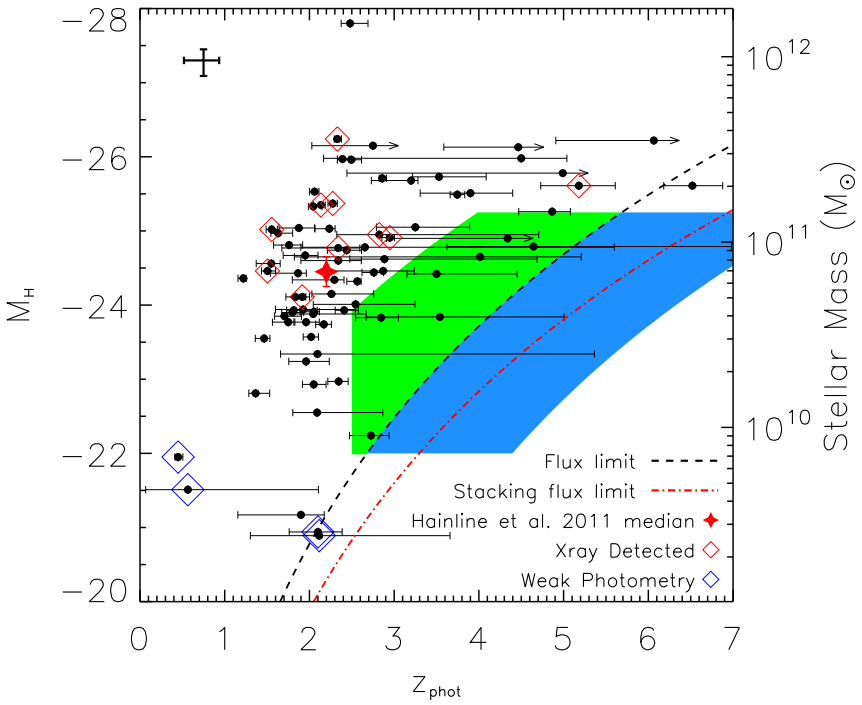

Figure 2.9: The absolute H-band magnitude distribution of the ALESS SMGs, derived from SED fits to the observed photometry. The median M_H of the ALESS SMGs is -24.56 ± 0.15, which agrees with that derived for the SMG sample presented by Hainline et al. (2011), $M_H = -24.45 \pm 0.20$. The dashed line illustrates the flux limited nature of our survey, and the red line the limit in our IRAC stacking (flux limit taken from the IRAC 4.5 μm limiting magnitude). By requiring that the M_H distribution is not bimodal, and using the IRAC selection limits we can estimate the redshift distribution for those ALESS SMGs without sufficient photometry to derive photometric redshifts. Shaded regions represent the area populated by ALESS sources detected in 0-or-1 (blue) or 2-or-3 (green) wavebands. For each source we determine a mass-to-light ratio, $M\,/\,L_H$, from the SFH returned in the SED fitting, and estimate a median stellar mass for the complete sample of 96 SMGs of $M_\star = (8 \pm 1) \times 10^{10}\,\mathrm{M}_\odot$, for a Salpeter IMF. We caution that due to the unknown SFHs, the stellar masses of the ALESS SMGs are very poorly constrained (see § 2.6.3). Sources which are possible gravitational lenses, or with questionable photometry, are highlighted with blue diamonds.

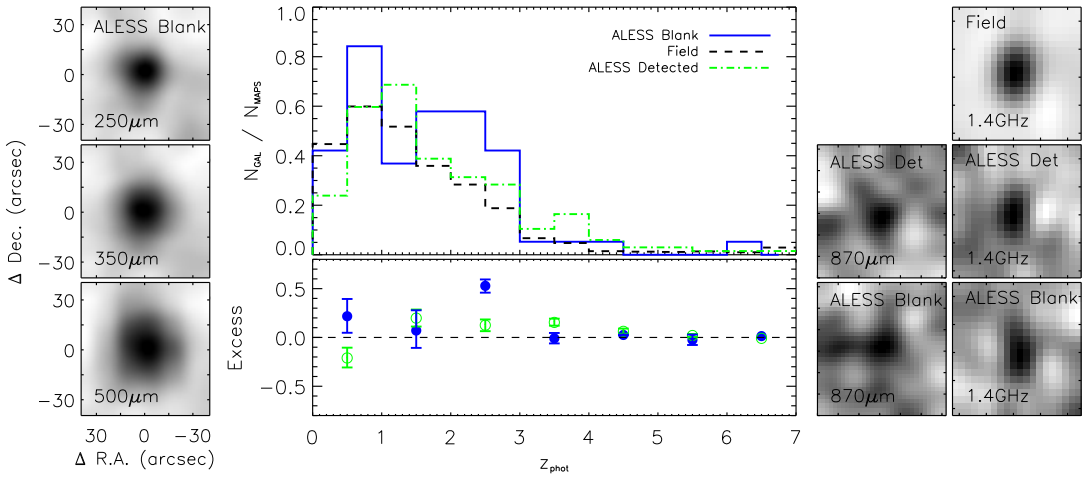

Figure 2.10: *Left:* 19 of the 86 ALMA maps of LESS sub-mm sources do not contain an SMG brighter than our 870-μm detection threshold of $\sim$1.4 mJy, within the ALMA primary beam. We show the results of stacking the *Herschel* / SPIRE 250, 350 and 500 μm maps at the position of these 19 LABOCA detections in the left hand column. We detect emission at $> 8\,\sigma$ at all three SPIRE wavelengths, confirming that on average these sources are real. *Middle:* We compare the redshift distribution of IRAC sources in ALMA maps without SMGs to the field, and to those in areas covered by ALMA maps containing detected SMGs. The field sample is drawn from random apertures with the same size as the ALMA primary beam, and any ALESS SMGs are removed from all samples. In the maps with detections we find that the redshift distribution is consistent with the field, but in the blank ALMA maps we find an excess of sources at $z \sim 2.5$. This suggests that the LESS SMGs have fragmented into multiple components below our detection threshold, and that they have a redshift distribution consistent with the $S_{870\mu\mathrm{m}}$-brighter ALESS sample. *Right:* Stacked maps of 3.6 μm-selected galaxies with photometric redshifts between $z = 1$–3. We stack the 870 μm emission for sources covered by our ALMA observations, and the 1.4 GHz emission for all galaxies. We again split the sample into subsets based on whether they are in an ALMA map or not, and furthermore into ALMA blank maps and ALMA maps containing SMGs. We obtain a $\sim 4\,\sigma$ detection of the IRAC samples in both 870 μm stacks. The ALMA maps lacking SMGs have a primary-beam corrected flux of $S_{870} = 0.36 \pm 0.09$ mJy, and a number density of sources $\sim 2\times$ higher than the field over the range $z = 1$–3. We detect all subsets at 1.4 GHz, and we find the IRAC sources in the ALMA maps are $\sim 2.5\times$ brighter at 1.4 GHz than those in the general field population at $2.8\,\sigma$. This tentative result suggests that IRAC-selected sources are typically brighter at 870 μm when in the vicinity of a sub-mm source.

at 250 μm, two of which are detected at 350 and 500 μm. The SEDs for these stacks peak between 250 and 350 μm for both the 0-or-1 and 2-or-3 subsets, as shown in Figure 2.8. In this figure we also overlay the composite ALESS SMG SED, see § 2.5.3, redshifted to $z = 2.5$ and $z = 2.0$ for the 0-or-1 and 2-or-3 subsets respectively, to match the peak of the far-infrared SED. The redshifted template appears to roughly reproduce the far-infrared properties of these SMGs, although we note that their near-infrared properties are approximately an order of magnitude fainter than the composite ALESS SMG SED. We caution that variation in the dust temperature or redshift of the SMGs in the 0-or-1 and 2-or-3 subsets would smear the peak wavelength of the stacked far-infrared SED. Indeed, there is evidence that average dust temperature of the ALESS SMGs increases with redshift (Swinbank et al., 2014). As such, we may expect the composite SED to have a lower dust temperature than the SMGs detected in 0-or-1 and 2-or-3 subsets, and the degeneracy between the dust temperature and redshift of the FIR SED means that a simple scaling of the composite SED to the peak of the stacked emission may underestimate the redshift of these sources. A full discussion of the far-infrared properties of these SMGs is presented in Swinbank et al. (2014).

In Figure 2.9 we plot the H-band absolute magnitude (M_H) versus redshift for the 77 ALESS SMGs for which we have derived a photometric redshift. We also highlight the survey selection limits, which show that between $z = 0$ and $z \sim 2.5$ the near-infrared survey limits should be complete at magnitudes brighter than $M_H = -22$ (equivalent to a stellar mass of $\mathrm{M}_\star \sim 10^{10}\,\mathrm{M}_\odot$ for a light-to-mass ratio of $\mathrm{L}_H\,/\,\mathrm{M}_\star \sim 3.8$; Hainline et al. 2011). However, above $z \sim 2.5$, the optical – near-infrared survey limits mean that only the brightest SMGs are detected, despite the 870 μm selection ensuring we have an unbiased sample of SMGs from $0 < z \lesssim 6$. We make the assumption that the absolute H-band magnitude distribution of the ALESS SMGs is complete at $z < 2.5$ and that incompleteness in the distribution at $z > 2.5$ is due to our near-infrared selection limits, i.e. that the 19 SMGs detected in < 4 wavebands lie at $z > 2.5$ and that the absolute H-band magnitude distribution is not bimodal. Our assumption is in agreement with Fig. 2.8, which shows the stacked far-infrared SED of these SMGs peaks at longer wavelengths, and indeed one of the SMGs detected in < 4 wavebands, ALESS 65.1, has been spectroscopically confirmed to be at $z = 4.4$ (Swinbank et al., 2012). We caution that an alternative explanation is that the SMGs detected in 0-or-1 and 2-or-3 wavebands are either significantly more dust obscured ($A_V > 4$) or lower stellar mass ($\mathrm{M}_\star < 10^{10}\,\mathrm{M}_\odot$) than the optical–near-infrared

detected ALESS SMGs, but note that this would mean both properties have a bimodal distribution.

To estimate the likely redshift distribution of the 19 ALESS SMGs which are detected in <4-bands, we first assume that the survey is complete in M_H at $z<2.5$ (Figure 2.9). To determine incompleteness in the magnitude distribution at $z>2.5$, we construct $\sim$1000 realizations of the ALESS SMG H-band absolute magnitude distribution over the range $z=0$–2.5 and compare this to the H-band absolute magnitude at $z>2.5$. We then assign values of M_H to the ten ALESS SMGs detected in 2-or-3 wavebands to minimize the incompleteness in the H-band absolute magnitude above $z>2.5$. These ten sources have a stacked flux close to our photometric selection limit, and hence are assigned redshifts based on the selection limit at the corresponding value of their M_H. We repeat this procedure for the remaining nine ALESS SMGs detected in the 0-or-1 wavebands. Since these SMGs are not detected in our optical or near-infrared stacking, we assume these SMGs must lie below (or close to) the detection limit in our stacked IRAC maps. We caution that, in both cases, this may underestimate the redshift of these SMGs, although since both subsets peak at $\sim$350μm in the *Herschel* stacks in Figure 2.8 it appears on average they do not lie at very high redshifts ($z\gtrsim5$). Using this approach, the median redshift of the ALESS SMGs is $z\sim3.5$ and $z\sim4.5$ for sources detected in 2-or-3 and 0-or-1 wavebands respectively, similar to the redshifts derived from the composite SMG SED (Figure 2.8). Including these redshifts in our redshift distribution, the median photometric redshift for our complete sample of 96 ALESS SMGs is then $z_{phot}=2.5\pm0.2$ (Figure 2.12). The distribution has a tail to high redshift, and 35 ± 5 per cent of the ALESS SMGs lie at $z_{phot}>3$.

2.5.2.4 ALMA Blank Maps

We have now discussed the redshift distribution of *all* SMGs in the ALESS MAIN catalogue. Before continuing it is important to consider the ALMA maps in which we do not detect any SMGs. In total we obtained high quality ALMA observations of 88 LABOCA sub-mm sources. Of these 88 ALMA observations, 19 are blank maps and do not contain an SMG above a $S/N>3.5$ within the primary beam (Hodge et al., 2013b). The ALMA blank maps are predominantly faint LABOCA detections, and comprise 14 out of 24 LABOCA detections with $S_{870}<5.5$ mJy. To verify the reliability of the original LABOCA detections we stack the FIR-emission from all 19 sources in the far-infrared

Herschel / SPIRE maps at 250, 350 and 500 μm. We detect emission at $>8\,\sigma$ in our stacks of all three SPIRE wavebands, and show the images of each stack in Figure 2.10. Furthermore, we split the sample at a detection significance of $4.2\,\sigma$ in the original LABOCA map, yielding subsets containing 10 and 9 sources respectively. We again stack the FIR-emission for both subsets and detect emission at $>6\,\sigma$ at 250, 350 and 500 μm in both subsets, again confirming that on average both subsets contain real sources. The results of our stacking analysis are consistent with Weiß et al. (2009), who state that only ~ 3 of the 88 LESS sub-mm sources are expected to be false detections [6].

Our ALMA observations have demonstrated that single-dish-detected sub-mm sources often fragment into multiple SMGs in interferometric observations (Karim et al. 2013; Hodge et al. 2013b; see also Barger et al. 2012). We now test if it is possible that the ALMA blank maps similarly contain multiple SMGs, each below the 870-μm flux limit of the ALESS survey, but which together appear as a single, blended, source in the LABOCA observations. First, we use the photometric redshifts derived for the 3.6 μm training set to search for an excess of 3.6 μm sources in the ALMA blank maps, when compared to the field (see Figure 2.10). We construct the redshift distribution for the field by placing 1000 random apertures of equal size to the ALMA primary beam across the ECDFS. We compare the redshift distribution in these random fields to that of sources in the ALMA blank maps, and identify an excess of 0.61 ± 0.07 sources per ALMA blank map across the redshift range $z = 2$–3. There is also a small excess of 0.15 ± 0.06 of 3.6 μm-selected sources in the ALMA maps containing an SMG, over the same redshift range $z = 2$–3, compared to the field, where we have removed the ALESS SMG counterparts from the comparison. The existence of a small excess suggests that the ALMA blank maps contain multiple faint SMGs, and crucially that they have a redshift distribution broadly similar to the ALESS SMGs.

We assess the 870 μm flux contribution of these IRAC sources by stacking the primary beam corrected ALMA maps at the position of the 3.6 μm sources, again removing all ALESS SMGs in the MAIN catalogue from the sample. In Figure 2.10 we show 870 μm stacks for 3.6 μm sources, over the redshift range $z = 1$–3, in both ALMA blank maps

[6] Weiß et al. (2009) predict that the complete LESS sample of 126 sub-mm sources contains five false detections. In addition Weiß et al. (2009) consider the effects of map noise on measured source fluxes, which boosts otherwise faint sources above the nominal flux limit of their catalogue. However, they do not account for source clustering in their analysis, which may result in a higher flux boost.

("Blank"), and ALMA maps containing at least one SMG ("Detected"). We choose to stack over the redshift range $z = 1$–3 as it covers the observed excess in IRAC sources, and the expected range of redshifts for the bulk of the SMGs. Both "Blank" and "Detected" subsets are detected at a significance of $\sim 4\sigma$ in the 870 μm stacks, and the ALMA blank maps have an average primary beam corrected peak flux of $S_{870} = 0.36 \pm 0.09$ mJy (the sources in maps with detected SMGs yield $S_{870} = 0.29 \pm 0.08$ mJy). Using the number density of the 3.6 μm sources we calculate that these contribute a total 870 μm flux per ALMA blank map of $S_{870} = 0.76 \pm 0.19$ mJy.

However, we also need to confirm that these 3.6 μm sources in the ALMA maps are brighter in the sub-mm than the IRAC population outside the ALMA fields. This is difficult as we only have ALMA coverage of the LABOCA source positions, but we can take advantage of the radio coverage of the whole field to use this as a proxy to estimate the relative brightness of these two samples. We therefore stack the 1.4 GHz VLA map at the positions of the 3.6 μm sources, at $z = 1$–3, in the ALMA blank maps and the surrounding field. We note that we do not account for resolved radio emission in our stacking, but at $z = 2$ the resolution of the 1.4 GHz map is $\sim 25 \times 14$ kpc and we do not expect SMGs to be significantly resolved on these scales (Biggs & Ivison, 2008). We measure $\sim 2.5\times$ higher radio fluxes, at a significance of 2.8 σ, for 3.6 μm sources at $z = 1$–3 in the ALMA "Blank" and "Detected" maps compared to the field. We note that this analysis is limited by the small number of 3.6 μm sources considered in the ALMA maps and the depth of the radio map combined with the expected faint 1.4 GHz flux distribution of SMGs (Figure 2.2). If we instead only consider the ALMA "Blank" maps we measure $\sim 3.5\times$ higher radio fluxes, at a decreased significance of 2.0 σ, compared to the field. The significance of these results means they only provide tentative evidence that the ALMA maps contain 3.6 μm sources, at $z = 1$–3, which are typically brighter in the sub-mm, compared to the field.

The flux limit of the original LESS survey was 4.4 mJy beam^{-1}, and hence our results are insufficient to fully explain the ALMA blank maps. There are two important caveats with this result. The first is that we expect at least three of the LABOCA sources to be spurious detections, which will downweight our stacking results to lower values of S_{870}. The second is that although we selected sources at 3.6 μm, the requirement for a photometric redshift means each source must be detected in > 4 wavebands. If we have the same proportion of sources detected in < 4 wavebands as the MAIN sample, i.e. 20 per cent, this would explain a further fraction of the missing flux. Although we cannot explain all

of the missing flux, these results do indicate that the ALMA blank maps contain multiple faint SMGs, below the detection limit of the ALESS survey. Crucially we find that there is an excess of sources at $z \sim 2.5$ in these maps, which suggests the redshift distribution of faint SMGs appears to match the ALMA-detected SMGs.

2.5.3 Constraints on SFH

The primary use of HYPERZ is to derive photometric redshifts, but in the SED fitting procedure HYPERZ also determines the best fit star formation history (SFH) for each source. We now investigate the reliability of the returned SFH parameters. We find that 52 (68 per cent), 15 (19 per cent), 6 (8 per cent) and 4 (5 per cent) of the ALESS SMGs have SFHs corresponding to the burst, 1 Gyr, 5 Gyr and constant templates, respectively. While this appears to indicate a strong preference for the instantaneous burst SFH, we test for degeneracy in our results by re-running HYPERZ allowing just the constant or just the burst SFHs. The SED fits, for the two SFHs, are indistinguishable, with a median $\Delta\chi^2_{\rm red}$ between the constant and burst SFH of $0.34^{+0.16}_{-0.09}$. The SED fits return a median age of 35 ± 15 Myr and 1.0 ± 0.4 Gyr for the burst and constant SFHs respectively. In § 2.6.3 we discuss the uncertainties introduced into stellar mass estimates for SMGs from these unconstrained SFHs.

To investigate whether we can extract any further information about the SFHs from the ALESS photometry we construct the SED for the "average" ALESS SMG. In Figure 2.11, we present the de-redshifted photometry for the ALESS SMGs normalized by restframe H-band luminosity. The composite SED shows a steep red spectrum consistent with strong dust reddening, as expected for SMGs. However, there may also be a hint of a break at ~ 4000 Å. If this feature is indeed real it is most likely from a Balmer break, which would suggest the presence of stars with ages $\geq 10^8$ yr. We also present the median best-fit SEDs from re-running HYPERZ allowing just the burst and just the constant SFH, and as expected these appear consistent with the average SMG. However, the median best-fit templates are clearly indistinguishable, and we conclude that even for the limited selection of SFHs we consider for the ALESS SMGs it is not possible to distinguish between each SFH. This is in agreement with previous work which demonstrates the difficulty in constraining the individual SFHs of high-redshift SMGs with SED fitting (Hainline et al., 2011; Michałowski et al., 2012).

Although we find it is not possible to distinguish between the SFHs of the ALESS

SMGs, the reddening correction returned by HYPERZ appears consistent. Considering all SFHs we find a median reddening correction of $A_V^{\rm all} = 1.7 \pm 0.1$, and $A_V^{\rm const} = 2.0 \pm 0.1$ for the constant SFH alone. The reddening correction is an average correction across the entire galaxy, however, the dust in SMGs is likely to be clumpy (Swinbank et al., 2010b; Danielson et al., 2011; Hodge et al., 2012; Menéndez-Delmestre et al., 2013), and as such it is likely to be considerably higher in the star-forming regions. To confirm this we derive SFRs from the dust-corrected restframe UV emission, at 1500 Å, of each ALESS SMG, following Kennicutt (1998), and compare these values to the far-infrared SFRs derived by Swinbank et al. (2014). To bring the UV-derived SFR into agreement with $\rm SFR_{FIR}$, requires a median reddening correction of $A_V = 2.4 \pm 0.1$, or an additional ~ 0.7 mag to the A_V derived from SED fitting, indicating that star formation in the SMGs is occurring in highly obscured regions. We note that the UV-derived SFR indicator is only likely to be reliable for a constant SFR SFH at ages of > 100 Myr, and as such it is likely that our UV-derived SFR is overestimated, and that the reddening correction is higher than $A_V \sim 2.4$.

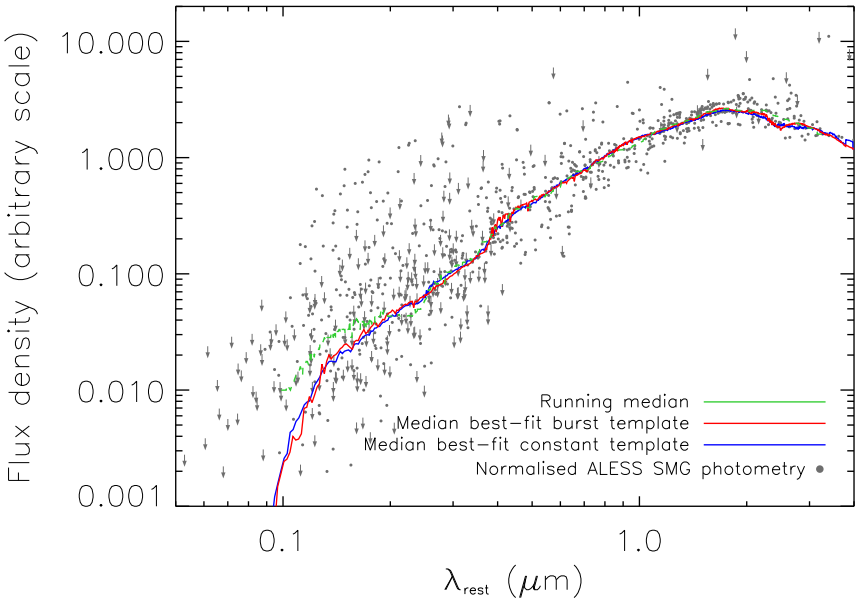

Figure 2.11: The photometry for the ALESS SMGs, de-redshifted and normalized by their median H-band absolute magnitude. We show the running median (dashed line), which represents the SED of an average SMG, and exhibits a steep red spectrum indicative of strong reddening but with a hint of a break at 0.4 μm due to a Balmer or 4000 Å break. We indicate non-detections with arrows, and set the flux for these values to 1-σ when calculating the running median. To test whether we can distinguish between different SFHs for the ALESS SMGs, we re-run HYPERZ allowing just a burst, or just a constant, SFH. We find the two SFHs are indistinguishable with a median $\Delta\chi^2_{\rm red} = 0.34^{+0.16}_{-0.09}$. We combine the median best-fit optical – near-infrared SED and the median best-fit FIR SED of the ALESS SMGs, presented in Swinbank et al. (2014), to create an average optical – far-infrared SMG template.

ID	RA (J2000)	Dec (J2000)	z_{phot}	z_{spec}	χ^2_{red}	Filters (Det [Obs])	M_H (AB)	$M\,/\,L_H$ ($M_\odot L_\odot^{-1}$)
ALESS 001.1	03:33:14.46	−27:56:14.5	$4.34^{+2.66}_{-1.43}$		0.91	5 [15]	−24.90	0.14
ALESS 001.2	03:33:14.41	−27:56:11.6	$4.65^{+2.34}_{-1.02}$		1.04	5 [15]	−24.79	0.29
ALESS 001.3	03:33:14.18	−27:56:12.3	$2.85^{+0.20}_{-0.30}$		3.78	5 [15]	−23.83	0.29
ALESS 002.1	03:33:02.69	−27:56:42.8	$1.96^{+0.27}_{-0.20}$		1.39	8 [14]	−23.24	0.17
ALESS 003.1	03:33:21.50	−27:55:20.3	$3.90^{+0.50}_{-0.59}$		0.68	5 [14]	−25.51	0.20
ALESS 005.1[a]	03:31:28.91	−27:59:09.0	$2.86^{+0.05}_{-0.04}$		14.76	13 [13]	−25.71	0.04
ALESS 006.1[a]	03:32:56.96	−28:01:00.7	$0.45^{+0.06}_{-0.04}$		17.54	15 [15]	−21.95	0.25
ALESS 007.1	03:33:15.42	−27:45:24.3	$2.50^{+0.12}_{-0.16}$		8.32	14 [15]	−25.96	0.04
ALESS 009.1	03:32:11.34	−27:52:11.9	$4.50^{+0.54}_{-2.33}$		0.22	5 [14]	−25.98	0.25
ALESS 010.1	03:32:19.06	−27:52:14.8	$2.02^{+0.09}_{-0.09}$		9.89	12 [13]	−23.57	0.15
ALESS 011.1	03:32:13.85	−27:56:00.3	$2.83^{+1.88}_{-0.50}$		2.02	6 [15]	−24.95	0.36
ALESS 013.1	03:32:48.99	−27:42:51.8	$3.25^{+0.64}_{-0.46}$		2.12	8 [15]	−25.05	0.11
ALESS 014.1	03:31:52.49	−28:03:19.1	$4.47^{+2.54}_{-0.88}$		1.46	6 [13]	−26.13	0.06
ALESS 015.1	03:33:33.37	−27:59:29.6	$1.93^{+0.62}_{-0.33}$		0.43	4 [13]	−23.94	0.21
ALESS 017.1	03:32:07.30	−27:51:20.8	$1.51^{+0.10}_{-0.07}$		1.95	15 [15]	−24.46	0.18
ALESS 018.1	03:32:04.88	−27:46:47.7	$2.04^{+0.10}_{-0.06}$	2.25[b]	5.44	14 [15]	−25.33	0.15
ALESS 019.1	03:32:08.26	−27:58:14.2	$2.41^{+0.17}_{-0.11}$		8.40	7 [14]	−23.93	0.15
ALESS 019.2	03:32:07.89	−27:58:24.1	$2.17^{+0.09}_{-0.10}$		2.04	13 [14]	−23.74	0.14
ALESS 022.1	03:31:46.92	−27:32:39.3	$1.88^{+0.18}_{-0.23}$		3.50	6 [11]	−25.04	0.22
ALESS 023.1	03:32:12.01	−28:05:06.5	$4.99^{+2.01}_{-2.55}$		0.35	4 [6]	−25.78	0.09
ALESS 025.1	03:31:56.88	−27:59:39.3	$2.24^{+0.07}_{-0.17}$		1.65	12 [14]	−25.03	0.17
ALESS 029.1	03:33:36.90	−27:58:09.3	$2.66^{+2.94}_{-0.76}$		0.10	4 [13]	−24.78	0.36
ALESS 031.1	03:31:49.79	−27:57:40.8	$2.89^{+1.80}_{-0.41}$		1.09	5 [13]	−24.62	0.12
ALESS 037.1	03:33:36.14	−27:53:50.6	$3.53^{+0.56}_{-0.31}$		2.07	9 [12]	−25.73	0.04
ALESS 037.2	03:33:36.36	−27:53:48.3	$4.87^{+0.22}_{-0.40}$		0.95	6 [12]	−25.26	0.17
ALESS 039.1	03:31:45.03	−27:34:36.7	$2.44^{+0.17}_{-0.23}$		9.14	11 [13]	−24.74	0.04
ALESS 041.1	03:31:10.07	−27:52:36.7	$2.75^{+4.25}_{-0.72}$		0.00	4 [4]	−26.15	0.17
ALESS 043.1	03:33:06.64	−27:48:02.4	$1.71^{+0.20}_{-0.12}$		4.33	7 [14]	−23.85	0.22
ALESS 045.1	03:32:25.26	−27:52:30.5	$2.34^{+0.26}_{-0.67}$		0.32	5 [14]	−24.77	0.36
ALESS 049.1	03:31:24.72	−27:50:47.1	$2.76^{+0.11}_{-0.14}$		1.56	11 [13]	−24.44	0.05
ALESS 049.2	03:31:24.47	−27:50:38.1	$1.47^{+0.07}_{-0.10}$		3.99	12 [13]	−23.55	0.04
ALESS 051.1	03:31:45.06	−27:44:27.3	$1.22^{+0.03}_{-0.06}$		7.76	13 [15]	−24.36	0.25

Table 2.4: [a] As discussed in § 2.5.2.1 these SMGs are potential gravitational lenses, or have significantly contaminated photometry. We advise that the photometric redshifts for these SMGs are treated with extreme caution. [b] Casey et al. (2011) [c] Zheng et al. (2004) [d] Swinbank et al. (2012) [e] Silverman et al. (2010) [f] Kriek et al. (2008b) [g] Coppin et al. (2009) [h] Coppin et al. (2012); Danielson et al. in prep [i] Bonzini et al. (2012)

ID	RA (J2000)	Dec (J2000)	z_{phot}	z_{spec}	χ^2_{red}	Filters (Det [Obs])	M_H (AB)	$M\,/\,L_H$ ($M_\odot L_\odot^{-1}$)
ALESS 055.1	03:33:02.22	−27:40:35.4	$2.05^{+0.15}_{-0.13}$		7.04	13 [14]	−22.93	0.15
ALESS 055.5	03:33:02.35	−27:40:35.4	$2.35^{+0.11}_{-0.13}$		6.89	12 [14]	−22.97	0.15
ALESS 057.1	03:31:51.92	−27:53:27.1	$2.95^{+0.05}_{-0.10}$	2.94^{c}	17.28	11 [15]	−24.91	0.15
ALESS 059.2	03:33:03.82	−27:44:18.2	$2.09^{+0.78}_{-0.29}$		3.88	8 [14]	−22.55	0.15
ALESS 061.1	03:32:45.87	−28:00:23.4	$6.52^{+0.36}_{-0.34}$	4.44^{d}	3.97	7 [13]	−25.61	0.05
ALESS 063.1	03:33:08.45	−28:00:43.8	$1.87^{+0.10}_{-0.33}$		3.07	11 [13]	−24.43	0.14
ALESS 066.1	03:33:31.93	−27:54:09.5	$2.33^{+0.05}_{-0.04}$	1.31^{e}	46.79	13 [13]	−26.24	0.15
ALESS 067.1	03:32:43.20	−27:55:14.3	$2.14^{+0.05}_{-0.09}$	2.12^{f}	3.31	13 [14]	−25.35	0.15
ALESS 067.2	03:32:43.02	−27:55:14.7	$2.05^{+0.06}_{-0.16}$		7.42	12 [14]	−23.91	0.05
ALESS 069.1	03:31:33.78	−27:59:32.4	$2.34^{+0.27}_{-0.44}$		0.51	5 [13]	−24.60	0.36
ALESS 070.1	03:31:44.02	−27:38:35.5	$2.28^{+0.05}_{-0.06}$		2.47	14 [14]	−25.37	0.15
ALESS 071.1	03:33:05.65	−27:33:28.2	$2.48^{+0.21}_{-0.11}$		7.65	11 [13]	−27.80	0.04
ALESS 071.3	03:33:06.14	−27:33:23.1	$2.73^{+0.22}_{-0.25}$		2.87	6 [13]	−22.24	0.15
ALESS 073.1	03:32:29.29	−27:56:19.7	$5.18^{+0.43}_{-0.45}$	4.76^{g}	2.00	8 [14]	−25.61	0.07
ALESS 074.1	03:33:09.15	−27:48:17.2	$1.80^{+0.13}_{-0.13}$		4.95	7 [14]	−23.90	0.19
ALESS 075.1	03:31:27.19	−27:55:51.3	$2.39^{+0.08}_{-0.06}$		41.20	13 [13]	−25.97	0.05
ALESS 075.4[a]	03:31:26.57	−27:55:55.7	$2.10^{+0.29}_{-0.34}$		3.14	6 [11]	−20.94	0.09
ALESS 079.1	03:32:21.14	−27:56:27.0	$2.04^{+0.63}_{-0.31}$		0.29	5 [14]	−23.88	0.36
ALESS 079.2	03:32:21.60	−27:56:24.0	$1.55^{+0.11}_{-0.18}$		2.42	13 [14]	−24.56	0.18
ALESS 080.1	03:31:42.80	−27:48:36.9	$1.96^{+0.16}_{-0.14}$		3.24	9 [14]	−23.77	0.15
ALESS 080.2	03:31:42.62	−27:48:41.0	$1.37^{+0.17}_{-0.08}$		4.06	9 [14]	−22.81	0.15
ALESS 082.1	03:32:54.00	−27:38:14.9	$2.10^{+3.27}_{-0.44}$		0.38	6 [14]	−23.34	0.14
ALESS 083.4[a]	03:33:08.71	−28:05:18.5	$0.57^{+1.54}_{-0.50}$		0.07	4 [4]	−21.51	0.11
ALESS 084.1	03:31:54.50	−27:51:05.6	$1.92^{+0.09}_{-0.07}$		3.71	14 [14]	−24.11	0.15
ALESS 084.2	03:31:53.85	−27:51:04.3	$1.75^{+0.08}_{-0.19}$		1.70	13 [15]	−23.77	0.20
ALESS 087.1	03:32:50.88	−27:31:41.5	$3.20^{+0.08}_{-0.47}$		0.22	5 [5]	−25.68	0.04
ALESS 088.1	03:31:54.76	−27:53:41.5	$1.84^{+0.12}_{-0.11}$	1.27^{h}	3.04	14 [15]	−24.11	0.15
ALESS 088.5	03:31:55.81	−27:53:47.2	$2.30^{+0.11}_{-0.50}$		3.69	9 [15]	−24.34	0.25
ALESS 088.11	03:31:54.95	−27:53:37.6	$2.57^{+0.04}_{-0.12}$		8.73	14 [15]	−24.32	0.07
ALESS 092.2	03:31:38.14	−27:43:43.4	$1.90^{+0.28}_{-0.75}$		2.66	11 [14]	−21.17	0.04
ALESS 094.1	03:33:07.59	−27:58:05.8	$2.87^{+0.37}_{-0.64}$		3.98	7 [14]	−24.46	0.15
ALESS 098.1	03:31:29.92	−27:57:22.7	$1.63^{+0.17}_{-0.09}$	1.48^{b}	2.65	7 [12]	−24.97	0.20
ALESS 102.1	03:33:35.60	−27:40:23.0	$1.76^{+0.16}_{-0.18}$		4.42	7 [13]	−24.81	0.27
ALESS 107.1	03:31:30.50	−27:51:49.1	$3.75^{+0.09}_{-0.08}$		3.55	11 [13]	−25.49	0.04
ALESS 107.3	03:31:30.72	−27:51:55.7	$2.12^{+1.54}_{-0.81}$		1.91	5 [13]	−20.89	0.11
ALESS 110.1	03:31:22.66	−27:54:17.2	$2.55^{+0.70}_{-0.50}$		0.78	4 [6]	−24.01	0.36
ALESS 112.1	03:32:48.86	−27:31:13.3	$1.95^{+0.15}_{-0.26}$		2.73	5 [5]	−24.67	0.22
ALESS 114.2	03:31:51.11	−27:44:37.3	$1.56^{+0.07}_{-0.07}$	1.61^{h}	3.12	15 [15]	−25.02	0.17

Table 2.4: continued

ID	RA (J2000)	Dec (J2000)	z_{phot}	z_{spec}	χ^2_{red}	Filters (Det [Obs])	M_H (AB)	$M\,/\,L_H$ ($M_\odot L_\odot^{-1}$)
ALESS 116.1	03:31:54.32	−27:45:28.9	$3.54^{+1.47}_{-0.87}$		0.82	4 [15]	−23.84	0.25
ALESS 116.2	03:31:54.44	−27:45:31.4	$4.02^{+1.19}_{-2.19}$		0.50	5 [15]	−24.65	0.04
ALESS 118.1	03:31:21.92	−27:49:41.4	$2.26^{+0.50}_{-0.23}$		3.85	6 [6]	−24.15	0.04
ALESS 119.1	03:32:56.64	−28:03:25.2	$3.50^{+0.95}_{-0.35}$		3.41	9 [13]	−24.42	0.05
ALESS 122.1	03:31:39.54	−27:41:19.7	$2.06^{+0.05}_{-0.06}$	2.03^{i}	6.08	14 [14]	−25.53	0.15
ALESS 124.1	03:32:04.04	−27:36:06.4	$6.07^{+0.94}_{-1.16}$		0.80	6 [15]	−26.22	0.16
ALESS 126.1	03:32:09.61	−27:41:07.7	$1.82^{+0.28}_{-0.08}$		7.42	10 [14]	−23.93	0.15

Table 2.4: Continued

2.6 Discussion

2.6.1 Redshift Distribution

The complete redshift distribution of the 96 ALESS SMGs in our sample has a median redshift of $z_{phot} = 2.5 \pm 0.2$ and a tail to high redshift, with 35 ± 5 per cent of sources lying at $z > 3$. As an initial comparison to the ALESS SMGs we use the spectroscopically confirmed, radio-identified, SMG sample from Chapman et al. (2005; C05). The C05 sample has a median redshift of $z = 2.2 \pm 0.1$, in agreement with our results, however there are notable discrepancies between the samples. The C05 sources are radio-selected, which due to the positive K-correction is likely to bias their results to lower redshifts. Indeed the highest redshift SMG in the C05 sample is $z = 3.6$, and the distribution does not show such a pronounced tail to high redshifts as we observe in the ALESS SMG distribution. We also note differences between the samples at $z < 1.5$. The C05 sample contains a significant number of SMGs at these redshifts (25 per cent), but only five ALESS SMG, or 6 per cent, lie at $z < 1.5$. A two-sided Kolmogorov-Smirnov (KS) test between the ALESS SMGs and C05 indicates that there is a 13 per cent probability that the samples are drawn from the same parent distribution. A fairer comparison is to only consider the ALESS SMGs with radio fluxes $S_{1.4} > 40\,\mu$Jy, roughly the selection limit of the C05 sample. Here, the median redshift of $S_{1.4} > 40\,\mu$Jy ALESS SMGs is $z_{phot} = 2.3 \pm 0.1$, and the above analysis remains unchanged. We note the median redshift of the radio-detected ALESS SMGs is $z_{phot} = 2.3 \pm 0.1$, and is lower than the radio-non-detections which have a median redshift of $z_{phot} = 3.0 \pm 0.3$.

We caution that the ALESS sample is selected from the original LABOCA survey, which had a detection threshold of 4.4 mJy. Our ALMA observations reach a typical depth of 1.4 mJy ($3.5\,\sigma$) and so we have SMGs in our sample below the original LABOCA limit. These SMGs are biased in their selection, and are only in our SMG sample due to their on-sky clustering with other SMGs. It is difficult to quantify the effect of these SMGs on our redshift distribution, but we note that we do not see any significant trend between redshift and 870 μm flux density (see Figure 2.7). If we split the ALESS SMGs into sub-samples based on the LABOCA detection limit, we find the median redshift for SMGs above 4.4 mJy is $z_{phot} = 2.5 \pm 0.2$, and $z_{phot} = 2.6 \pm 0.3$ below 4.4 mJy. However, we should also consider the ALMA maps where the original LABOCA source has not fragmented into multiple components. The median redshift of these 45 "isolated" SMGs

is $z_{phot} = 2.3 \pm 0.2$, consistent with the complete sample of 96 SMGs.

A number of SMGs in our sample have secondary redshift solutions (which correspond to secondary minima in χ^2, e.g. Figure 2.16) or have large uncertainties in their photometric redshifts. To investigate whether these could significantly affect the shape of the redshift distribution we calculate the redshift probability distribution for each SMG, and normalize the integral of the distribution. For the SMGs detected in < 3 wavebands we assign a uniform probability distribution between the detection limits described in § 2.5.2.3. We combine the redshift probability distributions for each SMG and show the combined redshift distribution in Figure 2.12. We find that the redshift distribution derived from the combined probability distributions is in excellent agreement with the "best-fit" redshift distribution, indicating that while secondary minima and large redshift uncertainties are important for individual sources, they do not significantly affect the shape of the redshift distribution.

In Figure 2.12 we show the redshift distribution of the ALESS SMGs as a function of look-back time. The distribution is well-described by a Gaussian ($\chi^2_r = 0.99$) of the form

$$N(T) = A\, e[\,-(T - T_0)^2 \,/\, 2\sigma_{\rm T}^2\,], \tag{2.6.1}$$

where $A = 14.10 \pm 0.55$, $T_0 = 11.10 \pm 0.05$ and $\sigma_{\rm T} = 1.07 \pm 0.05$, (of course, this function extends beyond the Hubble time and hence must be truncated at 13.7 Gyr). We note that the high redshift tail to the distribution is a less pronounced feature when the distribution is parametrized, linearly, by age[7].

One of the main results from our ALESS survey is that the "robust" radio/1.4 Ghz and MIPS/24 μm identifications for the multiwavelength counterpart to the original LABOCA detection were only 80 per cent correct, and 45 per cent complete (Hodge et al. 2013b). As such, we do not compare our results to redshift distributions derived from single-dish sub-mm/mm surveys (i.e. Aretxaga et al. 2007; Chapin et al. 2009; Wardlow et al. 2011; Yun et al. 2012; Casey et al. 2013). Instead, we restrict the comparison to recent millimetre interferometric observations of other, albeit small, samples of SMGs. First we compare to the 28 SMGs from Smolčić et al. (2012), which can be split into two distinct subsets: 1)

[7]We note that the ALESS SMG redshift distribution is well described by a log-normal distribution of the form:

$$\frac{dN}{dz} = \frac{B}{(z-1)\sigma_{\rm z}} e^{-[(\ln(z-1)-\mu)^2/2\sigma_z^2]}, \tag{2.6.2}$$

where $B = 89.2 \pm 1.7$, $\mu = 1.53 \pm 0.02$ and $\sigma_{\rm z} = 0.59 \pm 0.01$ (see also Yun et al. 2012)

17 1.1 mm-selected sources, with follow-up observations at 890 μm with the sub-mm Array (SMA) and 2) 16 870 μm-selected sources, with follow-up observations at 1.3 mm with the Plateau de Bure Interferometer (PdBI). Five sources are duplicated in both samples.

The 1.1 mm selected sample from Smolčić et al. (2012) has a median redshift of $z = 2.8 \pm 0.4$, which is comprised of a mixture of seven spectroscopic redshifts, seven photometric redshifts and three redshifts derived from the mm - radio relation (see Figure 2.6). Due to the shape of the FIR SED we might expect samples selected at longer wavelength to lie at higher redshift, and indeed we observe this for the ALESS SMGs when the sample is split into detections which peak at 250, 350 and 500 μm (Swinbank et al., 2014). As such it is unsurprising that the 1.1 mm selected sample from Smolčić et al. (2012) has a marginally higher median redshift, although we note that within the errors it is in agreement with the median of the ALESS SMGs. The second sample consists of 870 μm selected galaxies, with interferometric observations at 1.3 mm. The initial selection criteria at 870 μm means the sample is a closer match to the ALESS SMGs (although they must still be brighter than ~ 1.5 mJy at 1.3 mm) and indeed the median redshift is $z = 2.6 \pm 0.6$ (five spectroscopic/eight photometric/three mm-radio redshifts), in good agreement with the results presented here.

Overall the combined mm and sub-mm samples from Smolčić et al. (2012) contains 28 SMGs with a median redshift of $z = 2.6 \pm 0.4$, in agreement with the ALESS SMGs. We note that redshifts for five SMGs from the Smolčić et al. (2012) sample, are derived from the mm - radio relation and are claimed to lie at $z > 2.6$. As we have noted, this relation displays an order of magnitude scatter at a fixed redshift (Figure 2.6), however these sources are not detected in the photometry employed by Smolčić et al. (2012) and hence are indeed likely to lie at high redshifts. We note two interesting features of the Smolčić et al. (2012) redshift distribution: firstly there is a deficit of SMGs at $z \sim 2$ which lies close to the peak of the ALESS SMG redshift distribution (see Figure 2.13). Secondly, a further possible discrepancy between the samples is the shape of the distribution from $z = 2.5$–4.5, where the ALESS SMG redshift distribution declines whereas the Smolčić et al. (2012) distribution remains relatively flat. However, given the limited number of sources in the comparison we caution against strong conclusions.

We can also compare to another ALMA sample. Weiß et al. (2013) recently used ALMA to search for molecular emission lines from a sample of 28 strongly lensed SMGs (see also Vieira et al. 2013), selected from observations at 1.4 mm with the South Pole Telescope

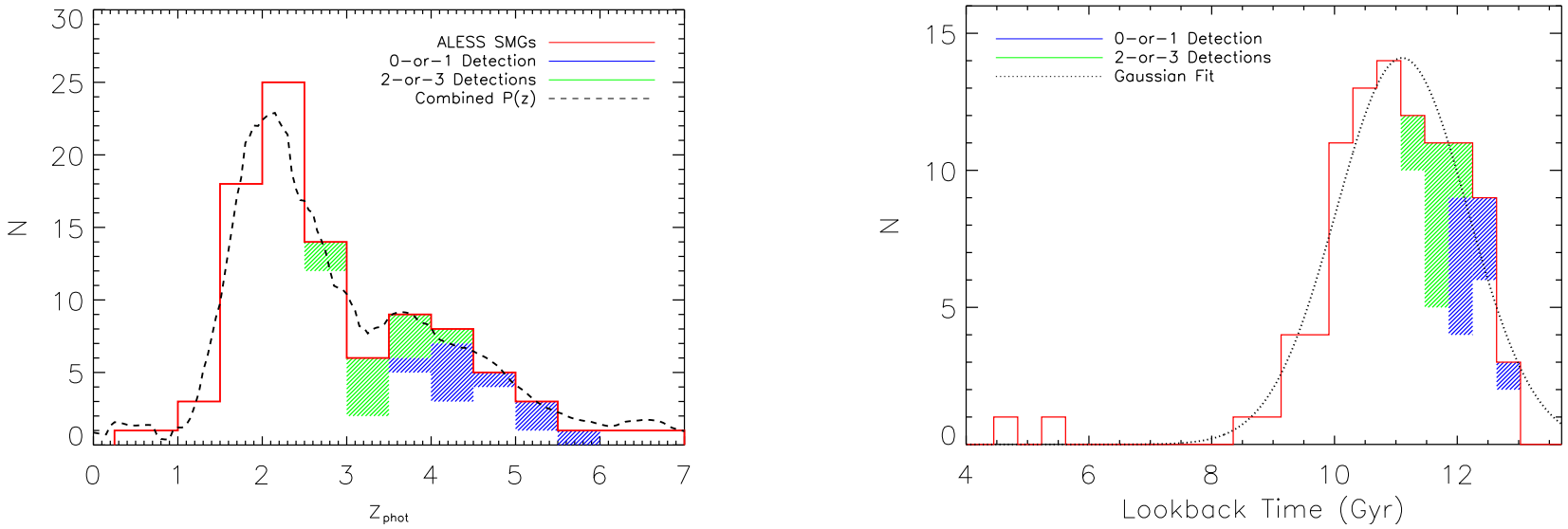

Figure 2.12: *Top Left:* The complete redshift distribution of the ALESS SMGs. We assign redshifts to SMGs detected in 0-or-1 and 2-or-3 wavebands by completing the H-band absolute magnitude distribution at $z > 2.5$, as described in § 2.5.2.3. We combine the probability distribution for the photometric redshift of each SMG, and overlay this as a dashed line. The combined probability distribution is in close agreement with the shape of the redshift distribution, indicating that the distribution is not sensitive to the uncertainties on individual photometric redshifts, or secondary redshift solutions. *Top Right:* The complete distribution of ALESS SMGs as a function of time. We find the distribution is well-described by a Gaussian centered at 11.10 ± 0.05 Gyr (equivalent to $z = 2.6 \pm 0.1$), with a width of 1.07 ± 0.05 Gyr.

(SPT). Given the large beam size ($\sim 1'$) of the SPT the sources were also required to be detected at 870 μm with LABOCA. Weiß et al. (2013) obtain secure redshifts for 20 SMGs in their sample and provide tentative redshifts, derived from single line identification, for five sources (three sources are not detected in emission). Considering the lower estimates for the tentative redshifts the sample has a median redshift of $z = 3.4 \pm 0.5$, and for the upper limits on the tentative redshifts $z = 3.8 \pm 0.4$, with the true median likely lying between the two values.

The median redshift for the SPT sources is higher than that of the ALESS SMGs, although the two are formally in agreement at the ~ 2–σ confidence level. However, the most noticeable discrepancy between the samples lies in the shape of the distributions. Firstly, there are no robust spectroscopic redshift SPT sources at $z < 2$, whereas ~ 25 per cent of the ALESS SMGs lie at $z_{phot} < 2$, of which 7 are spectroscopically confirmed to lie at $z < 2$ (see Figure 2.3; Danielson et al. in prep). Secondly, the ALESS photometric redshift distribution has a tail to high redshift ($z_{phot} \sim 6$), however the distribution declines steadily between $z_{phot} = 2$–6. In contrast the SPT distribution is relatively flat between $z = 2$–6. As stated by Weiß et al. (2013), their bright 1.4mm flux selection criteria, $S_{1.4\mathrm{mm}} > 20$ mJy ensures they only select lensed sources. This potentially introduces two biases into the redshift distribution: 1) The lensing probability is a function of redshift; for example, from $z = 1.5$ (where there are no SPT sources) to $z = 6$ the probability of strong gravitational lensing ($\mu \sim 10$) increases from $P(z) = 0.6 \times 10^{-4}$ to 3×10^{-4} (i.e. a factor of 5 increase; see Figure 6 from Weiß et al. 2013). In Figure 2.13 we show the redshift distribution for the SPT sample, corrected by the lensing probability function given in Weiß et al. (2013; see also Hezaveh et al. 2012). We note this has a significant effect on the shape of the distribution, bringing it into closer agreement with the ALESS sample at $z > 2.0$. The weighted median of the corrected Weiß et al. (2013) sample is $z \sim 3.1 \pm 0.3$, which is in agreement with the median redshift of the $z > 2.0$ ALESS SMGs of $z_{phot} = 3.0 \pm 0.4$. 2) Evolution in the source size with redshift will affect the lensing magnification, as increasingly compact sources are more highly amplified (Hezaveh et al. 2012, but see discussion in Weiß et al. 2013)

Given the different selection wavelengths between the ALESS SMGs and the SPT sample, and the potentially uncertain effects of lensing, we caution against drawing far-reaching conclusions between these two redshift distributions. To resolve any tension between these two samples, we require spectroscopic redshifts for an unlensed sample of

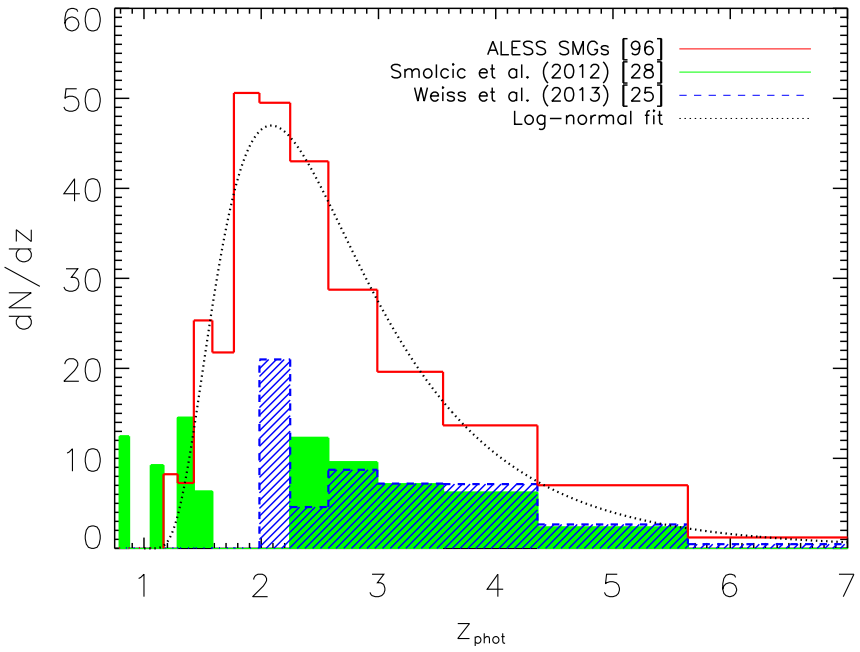

Figure 2.13: The redshift distribution of the ALESS SMGs, binned uniformly in time, and normalized by the width of each bin. We find the redshift distribution is well-represented by a log-normal distribution (see Eqn 2) with $\mu = 1.53 \pm 0.02$ and $\sigma_z = 0.59 \pm 0.01$. For comparison we show the redshift distribution from Smolčić et al. (2012), an interferometric study of 28 millimetre-selected SMGs, containing spectroscopic and photometric redshifts. We also show the spectroscopic redshift distribution from a similar interferometric study of 25 millimetre-selected *lensed* SMGs from Weiß et al. (2013; hatched), choosing the robust or best-guess redshifts from their analysis. We note that we have included the lensing probability as function of redshift, given in Weiß et al. (2013), in the distribution. The SMG samples presented here have selection functions that are difficult to quantify (especially the lensed sample of Weiß et al. (2013)), and hence do not have a well defined survey area. As such, we present the redshift distributions in terms of raw number counts but provide the number of sources in each sample in the legend in the top right. In contrast to these previous studies, the redshift distribution of the ALESS SMGs does not show evidence of a flat distribution between $z \sim 2$–6, and displays a clear peak in the distribution at $z = 2$.

SMGs, selected at both 870 μm and 1.4 mm, however given the optical properties of these sources this will only be feasible using a blind redshift search of molecular emission lines, similar to that employed by Weiß et al. (2013).

2.6.2 Pairs & Multi-component SMGs

At least 35 per cent of the LESS sub-mm sources fragment into multiple SMGs. Using our photometric redshifts we can now test whether these multiple SMGs are physically associated or simply due to projection effects. In total we derive photometric redshifts for 18 SMG pairs, of which the photometric redshifts of all but one agree at a 3-σ confidence level. However, as the median combined uncertainty on the photometric redshift of each pair is $\sigma_z = 0.3$, this simply highlights these large uncertainties. Furthermore this uncertainty on each pair is similar to the width of the redshift distribution of the whole population and so we expect SMGs to appear as pairs, irrespective of whether they are associated.

A more sensitive method to test for small scale clustering of SMGs is to investigate if there is a significant excess of ALESS SMGs, at similar redshifts, and in the same ALMA map, compared to pairs of SMGs drawn from different ALMA maps. To test for any excess we initially create random pairs of SMGs, drawn from different ALMA maps, and measure $\Delta z = z_1^{phot} - z_2^{phot}$. We then compare this to the distribution of Δz we measure between SMGs in the same ALMA map. To take into account the errors on each photometric redshift we Monte Carlo the redshift for each SMG within the associated error bar, and repeat the entire procedure 1000 times. We identify a tentative excess of 2.8 ± 1.5 pairs, from the sample of 18, at $0 < \Delta z < 0.5$ in the ALMA maps containing multiple sources. However this is not a significant result [8].

The strongest candidates for an associated pair of SMGs are ALESS 55.1 and 55.5. These SMGs are separated by $\sim 2''$, have merged 870 μm emission and straddle a single optical – near-infrared counterpart; the photometric redshift of this source indicates it is not a lensing system. We note that the photometry for these SMGs is drawn from the same optical – near-infrared source. A further two LABOCA sources, LESS 67 and LESS 116, fragment into multiple ALESS SMGs with similarly small on-sky separations ($< 3''$) however we cannot verify if they are physically associated.

[8] We note that including sources from the Supplementary ALESS catalogue in this analysis does not increase the significance of the result.

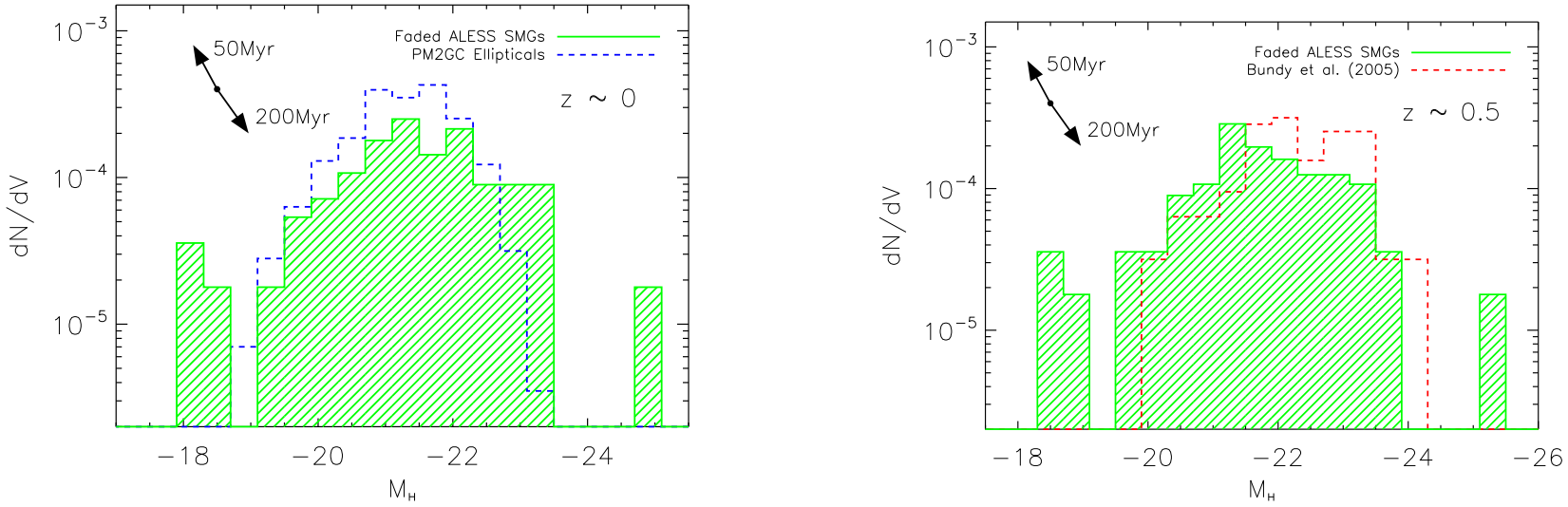

Figure 2.14: *Left:* The absolute H-band magnitude distribution of the ALESS SMGs, faded to the present day assuming a 100 Myr burst duration SFH. We adopt the SMG number counts from Karim et al. (2013) to extrapolate the ALESS SMG sample to 1 mJy, and duty-cycle correct the volume density. In the upper left, vectors indicate the effect of adopting either a 50 Myr or 200 Myr burst. In comparison we show the absolute H-band magnitude distribution of a morphologically classified, volume-limited sample, of elliptical galaxies over the redshift range 0.03–0.1 (PM2GC; Calvi et al. 2011, 2013). We conclude good agreement in both typical luminosity range, and space density, of faded SMGs to local ellipticals. *Right:* We again show the ALESS SMGs, faded to $z = 0.5$. We compare this to an absolute H-band magnitude distribution for a morphologically classified sample of elliptical galaxies at $z \sim 0.5$ (Bundy et al., 2005). We find the number density of the SMGs and intermediate redshift ellipticals are in agreement, however the ALESS SMGs are on average ~ 0.5 magnitudes fainter.

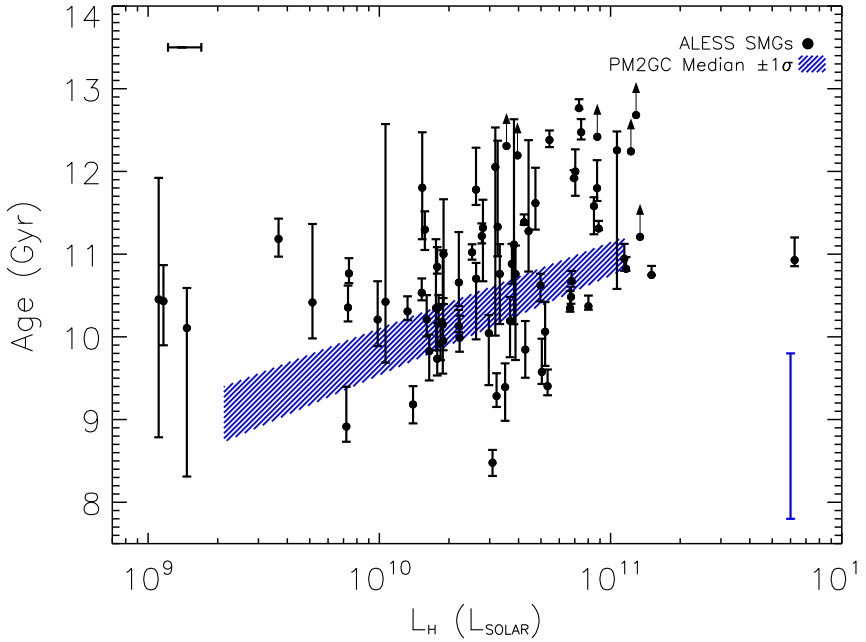

Figure 2.15: A comparison of the mass-weighted ages of the PM2GC sample of elliptical galaxies to the current look-back age of the ALESS SMGs. The error bar in the bottom right of the figure shows the typical MW-age error at these old ages, as derived from the spectrophotometric modelling (Poggianti et al., 2013). Despite the large systematic uncertainty, the PM2GC ellipticals have mass-weighted ages which are in broad agreement with the ALESS SMGs. This is consistent with a simple evolutionary model where SMGs are the progenitors of local elliptical galaxies. The typical error in L_H for the ALESS SMGs is shown in the upper left of the figure.

2.6.3 Stellar Masses

We estimate stellar masses for the ALESS SMGs from their absolute H-band magnitudes, which we note are calculated from the best-fit SED and take into account the effects of the K-correction. We select this waveband as a compromise between limiting the effects of dust extinction (the correction decreases with increasing wavelength), and the potential contribution of thermally pulsating asymptotic giant branch (TP-AGB) stars (which increases at longer wavelengths [Henriques et al. 2011]).

The median absolute H-band magnitude for the 77 ALESS SMGs detected in > 4 wavebands is -24.56 ± 0.15. As discussed in § 2.5, by assuming the ALESS SMGs detected in < 4 wavebands are missed due to our photometric selection limits, we can complete the $M_{\rm H}$ distribution by enforcing the condition that the distribution is not bimodal. Using the complete $M_{\rm H}$ distribution we measure a median absolute H-band magnitude for the ALESS SMGs of -24.33 ± 0.15. The median value of $M_{\rm H}$ for the ALESS SMGs is in

agreement with previous work by Hainline et al. (2011), who measure a median $M_{\rm H} = -24.45 \pm 0.20$ for the stellar emission from a sample of 65 spectroscopically confirmed, radio-identified, SMGs from the Chapman et al. (2005) sample.

To convert these absolute H-band magnitudes to stellar masses we must next adopt a mass-to-light ratio. As we discussed in § 2.5 the SFHs for the ALESS SMGs are highly degenerate, and it is not possible to accurately distinguish between the model SFHs. To determine a mass-to-light ratio we therefore consider the range spanned by the best-fit Burst and Constant SFHs (the two extremes of SFH we consider). We use the Bruzual & Charlot (2003) Simple Stellar Populations (SSPs) to construct an evolved spectrum from the best-fit constant and burst SFHs for each SMG, and measure the absolute H-band magnitude [9]. We then define the stellar mass as the total mass in stars and stellar remnants, using STARBURST99 to determine the mass lost due to winds and supernovae (Leitherer et al., 1999; Vázquez & Leitherer, 2005; Leitherer et al., 2010).

The median mass-to-light ratio for the ALESS SMGs is $M\,/\,L_H = 0.08 \pm 0.02$ for the burst SFH, and $M\,/\,L_H = 0.25 \pm 0.05$ for the constant SFH, however we caution the mass-to-light ratios between the burst and the constant SFH solutions for individual SMGs vary by $> 3\times$ for $\sim$40 per cent of the sample. Nevertheless, we apply the best fit mass-to-light ratios for each of the 77 ALESS SMGs detected in > 3 wavebands to their dust-corrected absolute H-band magnitudes, and determine median stellar masses of $M_\star = (7.4 \pm 1.0) \times 10^{10}\,{\rm M}_\odot$ for the Burst SFH, $M_\star = (9.2 \pm 0.8) \times 10^{10}\,{\rm M}_\odot$ for the Constant SFH, and $M_\star = (8.9 \pm 1.4) \times 10^{10}\,{\rm M}_\odot$ if we take the average of the mass estimates for each SMG. For the 19 SMGs detected in < 4 wavebands we do not have sufficient information on the SFH to determine a mass-to-light ratio. If we adopt the median mass-to light ratio for the detected SMGs, the stellar mass of the non-detected SMGs is $M_\star = (2.9 \pm 0.4) \times 10^{10}\,{\rm M}_\odot$ for the Burst SFH, $M_\star = (8.5 \pm 1.3) \times 10^{10}\,{\rm M}_\odot$ for the Constant SFH, and $M_\star = (5.7 \pm 0.8) \times 10^{10}\,{\rm M}_\odot$ for the average of the mass estimates. Combining the samples we derive a median stellar mass for the 96 ALESS SMGs of $M_\star = (8 \pm 1) \times 10^{10}\,{\rm M}_\odot$, when taking the mass as the average of the the Burst and Constant values. We note that all the stellar masses quoted here are for a Salpeter Initial Mass Function (IMF), and the median mass-to-light ratio is $M\,/\,L_H = 0.15 \pm 0.01$ [10] (the average mass-to-light ratio

[9] We enforce the condition that the age of the star-formation event is $20\,{\rm Myr} \leq t_{\rm age} \leq 1\,{\rm Gyr}$.

[10] The mass-to-light ratio for the instantaneous burst SFH is sensitive to changes on the order $\sim 10\,{\rm Myr}$, and over the range $10-40\,{\rm Myr}$ varies from $M\,/\,L_H \sim 0.02$–0.1. However, when considering the range 10 –

between a 100 Myr Burst and Constant SFH is $M\,/\,L_H = 0.14$).

The median stellar mass for the ALESS SMGs is lower than that found for the C05 sample of SMGs by Hainline et al. (2011; $M_\star = 1.6 \pm 0.3 \times 10^{11}\,\mathrm{M}_\odot$) [see also Michalowski et al. 2010; $M_\star = 3.5 \times 10^{11}\,\mathrm{M}_\odot$]. Given the uncertainty surrounding stellar mass estimates it is more informative to compare the absolute H-band magnitudes of the ALESS SMGs to the C05 sample. As stated earlier these are in agreement, and so any difference in the median stellar mass is due to differences in the mass-to-light ratios adopted. We note that the C05 sample of SMGs have significant contamination in M_H due to AGN activity (Hainline et al., 2011), which we do not see for the ALESS SMGs. However, the median M_H and masses for the C05 SMGs quoted here are corrected for that AGN contamination.

Although we highlight that the stellar masses for the ALESS SMGs are highly uncertain, we can crudely test their accuracy by comparing them to the dynamical masses, and CO-derived gas masses, of similar SMGs. Bothwell et al. (2013) recently obtained observations of ^{12}CO emission from 32 SMGs, drawn from the C05 sample. These SMGs have typical single-dish derived 870 μm fluxes of 4–20 mJy, and were found to have a median gas mass of $M_{gas} = (3.5 \pm 1.1) \times 10^{10}\,\mathrm{M}_\odot$. We note that Swinbank et al. (2014) used the dust masses of the ALESS SMGs to derive a median gas mass of $M_{gas} = 4.2 \pm 0.4 \times 10^{10}\,\mathrm{M}_\odot$, comparable to the result from Bothwell et al. (2013). Combining the median gas mass from Bothwell et al. (2013) with the median stellar mass of the ALESS SMGs, and assuming a dark matter contribution of $\sim$25 per cent, suggests that SMGs have typical dynamical masses of $\sim$1–2 $\times 10^{11}\,M_\odot$. Crucially our estimate of the dynamical mass is consistent with spectroscopic studies of resolved Hα or ^{12}CO emission lines, which demonstrate that SMGs typically have dynamical masses of 1–2 $\times 10^{11}\,M_\odot$ (Swinbank et al. 2004; Alaghband-Zadeh et al. 2012; Bothwell et al. 2013), inside a 5 kpc radius.

2.6.4 Evolution of SMGs: z=0

We now investigate the possible properties of the descendants of the ALESS SMGs at the present day by modelling how much their H-band luminosity will fade between their observed redshift and the present redshift. First we must make assumptions about the future evolution of the ALESS SMGs, the most crucial of which is the duration of the

40 Myr the median stellar mass remains stable at $M_\star \sim (8 \pm 1) \times 10^{10}\,\mathrm{M}_\odot$.

SMG phase. As stated in § 2.6.3, based on existing CO studies of SMGs the ALESS SMGs are likely to have a median gas mass of $M_{gas} \sim (4 \pm 1) \times 10^{10}\,\mathrm{M}_{\odot}$, and from Swinbank et al. (2014) they have a median SFR of $840 \pm 120\,\mathrm{M}_{\odot}\mathrm{yr}^{-1}$ for a Salpeter IMF. If the SFR remains constant, and all the gas is converted into stars, this suggests that the SMG phase has a maximum duration on the order of 100 Myr (see also Swinbank et al. 2006; Hainline et al. 2011; Hickox et al. 2012).

To measure the change in H-band luminosity of the ALESS SMGs we use the Bruzual & Charlot (2003) SSPs to model the SED evolution. On average we are seeing each SMG midway through its burst and so, for a SMG duration of 100 Myr, we calculate the fading in L_H between 50 Myr into the burst, and the required age at the present day. We note that this assumes that the contribution to the fading from a pre-burst stellar population is negligible and that each SMG undergoes only a single burst.

The ALESS SMGs represent a complete survey over 0.25 degree^2 and so we can also calculate their co-moving space density. We first extrapolate the ALESS sample to $S_{870} \geq 1$ mJy, using the ALESS SMG number counts from Karim et al. (2013), noting that we again make the assumption there is no dependence of M_H on S_{870}. We also apply a factor of two correction to the number counts to account for the under-density of SMGs in the ECDFS (see Weiß et al. 2009). As the SMG phase has a finite duration we duty-cycle correct the number density following:

$$\phi_{\mathrm{D}} = \rho_{\mathrm{SMG}}(t_{\mathrm{obs}}/t_{\mathrm{burst}}), \tag{2.6.3}$$

where ϕ_{D} is the comoving space density of SMG descendants, ρ_{SMG} is the observed space density of ALESS SMG, t_{obs} is the duration of the epoch that we observe the SMGs over and t_{burst} is the duration of the SMG phase. We estimate t_{obs} from the 10–90th percentiles of the redshift distribution, $1.6 < z < 4.5$, and as stated earlier we assume the SMG phase has a duration of 100 Myr. Taking these corrections into account we estimate the volume density of the descendants of $S_{870} \geq 1$ mJy SMG is $\sim (1.4 \pm 0.4) \times 10^{-3}\,\mathrm{Mpc}^{-3}$.

It has been suggested that SMGs may be the progenitors of local elliptical galaxies (e.g. Lilly et al. 1999; Genzel et al. 2003; Blain et al. 2004; Swinbank et al. 2006; Tacconi et al. 2008; Swinbank et al. 2010a). We now test the relation of the descendants of the ALESS SMGs to local ellipticals using a morphologically classified sample of ellipticals galaxies, taken from the Padova Millennium Galaxy and Group catalogue (PM2GC; Calvi et al. 2011, 2013). This catalogue represents a volume-limited survey ($z = 0.03$–0.1) over

38 degrees^2, with morphologies determined by an automatic tool that mimics a visual classification (Calvi et al. 2012, see also Fasano et al. 2012). These galaxies were observed in the $Y-, H-$ and K-bands by the UKIDSS Large Area Survey (Lawrence et al., 2007) and we derive absolute H-band magnitudes from the recent data release (Lawrence et al., 2012). This comparison sample of local elliptical galaxies, has a median redshift of $z = 0.08$, median absolute H-band magnitude of $M_H = -21.1 \pm 0.1$ and a space density of $(2.0 \pm 0.1) \times 10^{-3}\,\mathrm{Mpc}^{-3}$.

Using the observed redshift of the SMGs, and our adopted SFH, we individually fade each ALESS SMG to $z = 0.08$, and estimate a median faded absolute H-band magnitude of $M_H = -21.2 \pm 0.2$. We show the "faded" distribution in Figure 2.14, where we see very good agreement with absolute H-band magnitude distribution of the PM2GC ellipticals. As stated earlier, we estimate the space density of the descendants of ALESS SMGs is $(1.4 \pm 0.4) \times 10^{-3}\,\mathrm{Mpc}^{-3}$, similar to the PM2GC ellipticals, $(2.0 \pm 0.1) \times 10^{-3}\,\mathrm{Mpc}^{-3}$. We note that both the fading correction in M_H, and the number density, of the SMGs are dependent on the duration of the SMG phase. If we instead adopt a burst of 50 or 200 Myr duration then the median absolute H-band magnitude is $M_H = -20.9 \pm 0.2$ or $M_H = -21.7 \pm 0.2$, and the number density is (3 ± 1) or (0.7 ± 0.2) $\times 10^{-3}\,\mathrm{Mpc}^{-3}$, respectively, and these changes are shown by vectors in Figure 2.14

We note that if the burst duration is indeed $\gtrsim 200$ Myr then > 10 per cent of the SMG descendants would have a H-band absolute magnitude brighter than the brightest elliptical in the PM2GC sample. This excess of bright galaxies assumes SMGs undergo no future interactions, i.e. minor mergers, or subsequent star formation, which would only act to increase the total absolute H-band magnitude, and so make the discrepancy larger. We suggest that this makes burst durations of > 200 Myr unlikely. For our estimated burst duration of 100 Myr the space density of SMGs is lower than local ellipticals, indicating the SMG phase could be < 100 Myr. A burst duration shorter than 100 Myr would make the descendants of the ALESS SMGs fainter than the $z = 0$ elliptical sample, but have a larger space density. If we consider a burst duration of 50 Myr then a dry-merger fraction of two-thirds would bring the number density into agreement with the PM2GC ellipticals, and the resulting median M_H of the SMGs to $M_H = 21.4 \pm 0.1$.

We now consider two further tests of this evolutionary model. First, we consider the mass-weighted stellar ages of the PM2GC ellipticals, calculated with a spectrophotometric model that finds the combination of SSP synthetic spectra that best-fits the observed

spectroscopic and photometric features of each galaxy (Poggianti et al., 2013). As can be seen in Figure 2.15 these appear broadly consistent with the ages of the ALESS SMGs. The PM2GC ellipticals have a mass-weighted stellar age of $\sim 10\,\mathrm{Gyr}$ ($z \sim 2$) but with a systematic uncertainty of $\pm 2\,\mathrm{Gyr}$ (Poggianti et al., 2013), compared to the median age of the ALESS SMGs of $11.1 \pm 0.1\,\mathrm{Gyr}$. This might indicate that the bulk of stellar mass in the ellipticals formed later than the current redshift of the ALESS SMGs, however given the systematic uncertainties and the difficulty in age-dating very old stellar populations we find the similarity in the ages striking.

As a second comparison, we consider the the mass of the dark matter halos that the PM2GC ellipticals reside in. We use the halo mass catalogues from Yang et al. (2005), and find that these ellipticals have a typical halo mass of $0.5 \times 10^{13}\,\mathrm{M}_{\odot}$ with a 1-σ range of $0.1\text{–}8 \times 10^{13}\,\mathrm{M}_{\odot}$. This is consistent with the typical halo masses of SMGs descendants ($3 \times 10^{13}\,\mathrm{M}_{\odot}$ with a 1–σ range of $0.9\text{–}7 \times 10^{13}\,\mathrm{M}_{\odot}$; Hickox et al. 2012), although there is clearly a large amount of scatter.

We conclude that by assuming a simple scenario where an SMG undergoes a star formation event with a duration of 100 Myr, at a constant SFR, and then evolves passively, we determine that the median absolute H-band magnitude and number density of the ALESS SMGs are in good agreement with those of $z \sim 0$ ellipticals. We also find that the shape of the absolute H-band distribution (Figure 2.14), the mass-weighted stellar ages and the halo masses of local ellipticals are in good agreement with those predicted for the descendants of SMGs, suggesting that within this simple model SMGs are sufficient to explain the formation of most local elliptical galaxies brighter than $M_H \sim -18.5$.

2.6.5 Evolution of SMGs: Intermediate redshift tests

We now consider whether intermediate redshift populations agree with the toy model proposed here. We use a catalogue from Bundy et al. (2005), which provides morphological classifications for $z < 22.5\,\mathrm{mag}$ galaxies in the GOODS-South field. These galaxies are covered by the photometry employed in § 2.4 and so we can derive a photometric redshift and measure an absolute H-band magnitude for each source from SED fitting in the same manner as the ALESS SMGs. We select galaxies from the catalogue that are visually classified as ellipticals, and with a photometric redshift $0.4 < z_{phot} < 0.6$ (the mid-point in time of evolution from an SMG phase, to the local Universe). The final sample has a median absolute H-band magnitude of $M_H = -22.0 \pm 0.2$ and a

number density of $(1.6 \pm 0.2) \times 10^{-3}\,\mathrm{Mpc}^{-3}$. The number density of the ALESS SMGs, $(1.4 \pm 0.4) \times 10^{-3}\,\mathrm{Mpc}^{-3}$, is in agreement with the intermediate population of elliptical galaxies, however fading the absolute H-band magnitudes of the ALESS SMGs to $z \sim 0.5$, we find that they are marginally fainter at $M_H = -21.5 \pm 0.2$ (see Figure 2.14). Given the difficulty in morphological classification at $z \sim 0.5$, and the small number of sources in each sample, we caution against drawing strong conclusions from this result. However it does indicate the ALESS SMGs are broadly consistent with $z \sim 0.5$ elliptical galaxies.

Recently, near-infrared spectroscopy with the Wide-Field Camera 3 (WFC3) on the *Hubble Space Telescope (HST)* has been used to estimate the age of the stellar populations in quiescent spheroidal galaxies at $1.5 < z < 2$, the likely progenitors of local ellipticals. In particular, Whitaker et al. (2013) recently used this technique to estimate stellar ages for a sample of 171 quiescent galaxies at $1.4 < z < 2.2$, with stellar masses $M_\star \gtrsim 5 \times 10^{10}\,\mathrm{M}_\odot$ (similar to the ALESS SMGs). Whitaker et al. (2013) divide their quiescent sample into blue (34) and red (137) subsets, based on U, V and J-band colours, and fit absorption line models to the stacked spectra of each subset, deriving median stellar ages of $0.9^{+0.2}_{-0.1}$ and $1.6^{+0.5}_{-0.4}\,\mathrm{Gyr}$ for the blue and red subsets respectively. We use a weighted average of the number of galaxies in each subset, to determine that the complete sample has a median stellar age of $\sim 1.4\,\mathrm{Gyr}$, at a median redshift of $z \sim 1.7$ (see Figure 4; Whitaker et al. 2013). Combining the median stellar age and redshift of these post-starburst galaxies suggests that they formed at $z \sim 2.6$ (see also Bedregal et al. 2013) This is consistent with the toy model proposed earlier where the ALESS SMGs, with a median redshift of $z_{phot} = 2.5 \pm 0.2$, form the majority of their stellar mass in a single burst at $z \sim 2.5$, and do not undergo subsequent periods of significant star formation.

2.6.6 Evolution of SMGs: Black Hole Masses

Finally, given the apparent link between SMGs and elliptical galaxies at $z \sim 0$ we now investigate whether their black hole masses are consistent with our toy evolutionary model. To estimate black hole masses for the ALESS SMGs we use their X-ray properties, presented in Wang et al. (2013). However, only ten ALESS SMGs are detected at X-ray energies and so we must first consider whether these SMGs are representative of the entire sample.

In our approach we will assume the black hole masses of the X-ray detected SMGs are related to the total stellar mass of the galaxy; however in our initial analysis we

will use the H-band luminosity as a proxy for stellar mass. To account for the positive K-correction in the X-ray band we only consider SMGs in the redshift range $z = 0$–2.5, which includes seven X-ray detected SMGs. These SMGs have a median H-band luminosity of $L_H = (1.1 \pm 0.3) \times 10^{12}\,\mathrm{L}_\odot$, which is brighter than for the population as a whole [$L_H = (0.5 \pm 0.1) \times 10^{12}\,\mathrm{L}_\odot$; Figure 2.9]; a two-sided KS test returns a 3 per cent probability they are drawn from the same parent distribution. If we instead split the ALESS SMG sample at the median H-band luminosity, $L_H = 0.5 \times 10^{12}\,\mathrm{L}_\odot$, then the X-ray non-detected SMGs at $L_H > 0.5 \times 10^{12}\,\mathrm{L}_\odot$ have a median H-band luminosity of $L_H = (1.0 \pm 0.2) \times 10^{12}\,\mathrm{L}_\odot$ and a two-sided KS test returns a probability of 85 per cent that the X-ray detected and non-detected SMGs with $L_H > 0.5 \times 10^{12}\,\mathrm{L}_\odot$ are drawn from the same parent distribution (see also Wang et al. 2013).

A possible explanation for the higher H-band luminosities of the X-ray detected SMGs is that they suffer contamination in L_H from an AGN power-law component (see Hainline et al. 2011). However, to bring the H-band luminosity of the X-ray detected SMGs into agreement with the complete sample requires a power-law fraction of ~ 50 per cent which is not seen in the SEDs of the ALESS SMGs (see Figure 2.16).

We now investigate whether these X-ray detected SMGs are preferentially detected in X-ray emission due to higher star formation rates. Using the far-infrared derived SFRs for the ALESS SMGs from Swinbank et al. (2014), we find the X-ray detected SMGs have a median star formation rate of $\mathrm{SFR_{FIR}} = 570 \pm 140\,\mathrm{M_\odot yr^{-1}}$, which is consistent with the X-ray non-detected, $L_H > 0.5 \times 10^{12}\,\mathrm{L}_\odot$, SMGs which have a median $\mathrm{SFR_{FIR}}$ of $590 \pm 130\,\mathrm{M_\odot yr^{-1}}$. We note that the median $\mathrm{SFR_{FIR}}$ of the $L_H < 0.5 \times 10^{12}\,\mathrm{L}_\odot$ SMGs is $220 \pm 40\,\mathrm{M_\odot yr^{-1}}$, a factor of $\sim 2.5\times$ lower. This suggests that the potential X-ray emission from star formation is similar for the X-ray detected and non-detected SMGs with $L_H > 0.5 \times 10^{12}\,\mathrm{L}_\odot$, and is consistent with the results from Wang et al. (2013), who argue for dominant AGN contributions to the X-ray emission of the X-ray detected SMGs.

These results suggest that the X-ray detected SMGs have H-band luminosities and SFRs comparable to the $L_H > 0.5 \times 10^{12}\,\mathrm{L}_\odot$ SMGs. As we demonstrated in § 2.5.2.2 the X-ray detected SMGs are also indistinguishable from the X-ray non-detected SMGs in terms of IRAC flux ratios, and so combining all these results we conclude that other than in X-ray emission, the X-ray detected SMGs are not distinguishable from average $L_H > 0.5 \times 10^{12}\,\mathrm{L}_\odot$ SMGs. Instead we propose that SMGs with $L_H \lesssim 0.5 \times 10^{12}\,\mathrm{L}_\odot$ are not detected at X-ray energies due to the selection limits on the X-ray data. As the median

H-band luminosity of the ALESS SMGs with $L_H < 0.5 \times 10^{12}\,\mathrm{L}_\odot$ is a factor of 3.5× lower than the brighter half of the sample then, under the simple assumption that L_X and L_H represent $M_{\rm BH}$ and $M_\star$, this suggests that X-ray data a factor of $\sim$3.5× deeper is required to detect these SMGs down to the same Eddington ratio as the X-ray detected SMGs.

Although the X-ray detected SMGs only appear representative of the ALESS SMGs above $L_H > 0.5 \times 10^{12}\,\mathrm{L}_\odot$, we can still estimate their black hole masses, and hence their relation to the black hole masses of local ellipticals. The ten ALESS SMGs detected at X-ray energies have a median absorption corrected X-ray luminosity of $\log L_{0.5-8\,\mathrm{keV,corr}} = 43.3 \pm 0.4\,\mathrm{erg\,s^{-1}}$. We initially convert the luminosity from 0.5–8 keV to 2–10 keV, dividing through by a conversion factor of 1.21, and estimate a bolometric luminosity following $L_{bol} = 35 \times L_{2-10}$ (Alexander et al., 2008). We adopt an Eddington ratio of $\eta = 0.2$, which was calculated for a small number of SMGs with direct black hole mass measurements (Alexander et al., 2008), and from this estimate we calculate a median black hole mass of $M_{\rm BH} \sim (3^{+3}_{-1}) \times 10^7\,\mathrm{M}_\odot$. We note that our uncertainty does not include any error in the Eddington ratio or the bolometric luminosity conversion, and assumes that the average Eddington ratio for these SMGs is consistent with the SMGs in Alexander et al. (2008).

Using the black hole masses and stellar masses of the X-ray detected ALESS SMGs, we can estimate the growth required to match the black holes in local ellipticals. The X-ray detected SMGs have $M_{\rm BH}\,/\,M_\star = 0.2^{+0.2}_{-0.1} \times 10^{-3}$, and require $\sim$9× growth of their black hole masses, at fixed stellar mass, to match the local relation ($M_{\rm BH}\,/\,M_\star = 1.7 \pm 0.4 \times 10^{-3}$ at these masses; Häring & Rix 2004). If we assume the SMG lifetime is $\sim$100 Myr, and that we are seeing each SMG on average half-way through the burst, then following Eqn 10 from Alexander & Hickox (2012), and assuming $\eta = 0.2$, the SMBH will have grown by $\sim$20 per cent at the end of the SMG phase. However, a further factor of $\sim$7× growth is still required to match the local $\mathrm{M}_\star$–$\mathrm{M}_{\rm BH}$ relation. It has been speculated that this growth may come in the form of a QSO phase (e.g. Sanders et al. 1988; Coppin et al. 2008; Simpson et al. 2012), during which the SMBH would grow at approximately the Eddington limit. If we assume all of the remaining SMBH growth occurs in a QSO phase, then the duration of this phase must be $\sim$100 Myr.

A lifetime of 100 Myr for a QSO phase is high but not unreasonable (Martini & Weinberg, 2001), however it is highly unlikely that the accretion is Eddington limited for the entirety of this period (McLure & Dunlop, 2004; Kelly et al., 2010). If the accretion is

not Eddington limited during this phase, then this analysis suggests that we have either under-estimated the black hole masses or over-estimated the stellar masses in these SMGs. Indeed, when estimating black holes masses for the X-ray detected SMGs we have made assumptions on the current Eddington ratio, η, and the conversion from X-ray luminosity to a bolometric luminosity, both of which have significant uncertainties. The black hole masses we estimate are inversely proportional to the initial Eddington ratio, and it is feasible that this is lower than the value we adopted ($\eta = 0.2$; Alexander et al. 2008). Due to the uncertainties surrounding our estimate of the median black hole mass, we simply conclude that the SMBHs in these SMGs are likely to require an extended period of black hole growth after the SMG phase, and that this is most likely to occur during a high accretion rate QSO-phase.

2.7 Summary & Conclusions

In this chapter we have presented a multi-wavelength study of the first large sample of 870 μm-selected SMGs with unambiguous identifications based on ALMA interferometry. Crucially, these precise identifications, at the same wavelength as used for the original single-dish survey, mean that our analysis is free from the mis-identification and incompleteness associated with the use of radio–mid-infrared proxies to locate the counterparts of single-dish identified sub-mm sources (see discussion in Hodge et al. 2013b). The main conclusions from our work are:

- We measure aperture photometry in 19 wavebands for 96 ALESS SMGs (Hodge et al., 2013b). From this initial sample 77 SMGs are detected in ≥ 4 wavebands and have sufficient photometry to derive photometric redshifts from SED fitting. These 77 SMGs have a median redshift of $z_{phot} = 2.3 \pm 0.2$, with a 1-σ spread of $z_{phot} = 1.8$–3.5.

- Nineteen SMGs in our sample have insufficient photometry to derive photometric redshifts. We initially divide these sources into subsets detected in 0-or-1 and 2-or-3 wavebands and test whether they are real or spurious by stacking their emission in other wavebands. Detections at 250, 350 and 500 μm for both subsets confirm that these are typically far-infrared bright sources on average.

- We use the distribution of absolute H-band magnitudes at $z < 2.5$ to measure the incompleteness in the distribution at $z > 2.5$, and use this to estimate redshifts

for the 19 ALESS SMGs detected in < 4 wavebands. We estimate the median redshifts for the SMGs detected in 2-or-3 and 0-or-1 wavebands as $z \sim 3.5$ and $z \sim 4.5$ respectively.

- The redshift distribution for the complete sample of 96 ALESS SMGs has a median redshift of $z_{phot} = 2.5 \pm 0.2$ with 35 ± 5 per cent of SMGs lying at $z > 3$. In terms of their look-back age, the distribution is well-fit by a Gaussian distribution centered at 11.1 ± 0.1 Gyr, and with a 1-σ width of 1.1 ± 0.1 Gyr.

- We compare the redshift distribution of the ALESS SMGs to recent interferometric observations of smaller samples of millimetre-selected SMGs from Smolčić et al. (2012) and Weiß et al. (2013). The median redshift of the SMGs presented in Smolčić et al. (2012) is $z = 2.6 \pm 0.4$, in agreement with the ALESS SMGs, however the median redshift millimetre-selected, lensed, SMGs in Weiß et al. (2013) is considerably higher, $z \sim 3.6 \pm 0.4$, although correcting for lensing effects reduces this to $z \sim 3.1 \pm 0.3$. Due to differences in the selection wavelength and the difficulties in accurately constraining the lensing selection function we caution against strong conclusions drawn from the discrepancy in the median redshifts of the ALESS SMGs and the SMGs presented in Weiß et al. (2013). We note that in contrast to both of these previous studies, which have suggested the redshift distribution of SMGs is flat above $z \sim 3$, the ALESS redshift distribution peaks at $z \sim 2.5$, and declines steadily towards high redshift ($z > 4$).

- Nineteen of the 86 ALMA maps employed in our analysis do not contain an SMG with an 870-μm flux density > 1.4 mJy. Karim et al. (2013) and Hodge et al. (2013b) propose this is due to the original LABOCA sub-mm source fragmenting into a number of faint SMGs, and so we measure the number density and redshift distribution of 3.6 μm sources in these "blank" maps and compare it to the redshift distribution in the field. We identify an excess of sources at $z \sim 1$–3 indicating that, on average, these "blank" maps contain multiple SMGs below our detection threshold. We stack the ALMA 870 μm maps at the position of these 3.6 μm sources and measure an average flux of 0.36 ± 0.09 mJy per source, and a total contribution per map of 0.76 ± 0.19 mJy. Although this is not sufficient to explain the difference in total flux measured by LABOCA and ALMA in these regions, it suggests that there are faint SMGs in these "blank" maps, which lie at a similar redshift to the

S_{870} brighter ALESS SMGs.

- Using the complete M_H distribution for our sample we derive a median stellar mass of $(8 \pm 1) \times 10^{10}\,\mathrm{M}_{\odot}$ for the ALESS SMGs, but caution that due to the unconstrained SFHs, and hence mass-to-light ratios, this is subject to significant systematic uncertainties (at least $\sim 5\times$).

- We investigate the possible properties of the descendants of the ALESS SMGs at the present day. Fading the H-band luminosities of the ALESS SMGs, assuming a SFH consisting of a 100 Myr burst with constant SFR, we show the present day descendants will have an absolute H-band magnitude of $M_H \sim -21.2 \pm 0.2$, and a space density of $(1.4 \pm 0.4) \times 10^{-3}\,\mathrm{Mpc}^{-3}$. These properties are in good agreement with those of local elliptical galaxies, derived from the volume-limited PM2GC survey, which have a median absolute H-band magnitude of $M_H = -21.1 \pm 0.1$ and a space density of $(2.0 \pm 0.1) \times 10^{-3}\,\mathrm{Mpc}^{-3}$. We show that the mass-weighted stellar ages of the PM2GC ellipticals (~ 10 Gyr, but with a systematic uncertainty of ± 2 Gyr) are in broad agreement with the lookback times to the ALESS SMGs, providing support for our simple evolutionary model.

- We test our simple evolutionary model against intermediate- and high-redshift populations of quiescent spheroidal galaxies. We find that a morphologically classified sample of ellipticals at $z \sim 0.5$ shows broad agreement in shape, and number density to the "faded" ALESS SMGs at this epoch, but are typically $\sim 0.5 \pm 0.3$ magnitudes fainter. In addition, recent near-infrared spectroscopy of quiescent, red, spheroids at $z = 1.5$–2, the likely descendants of SMGs, indicates their stellar populations formed at $z \sim 2.6$, consistent with the median redshift of the ALESS SMGs, $z_{phot} = 2.5 \pm 0.2$.

- Finally, we show that the X-ray detected SMGs (Wang et al., 2013) are indistinguishable in terms of H-band luminosities, SFRs and IRAC flux ratios to the ALESS SMGs brighter than $L_H > 0.5 \times 10^{12}\,\mathrm{L}_{\odot}$. We use the X-ray properties of these SMGs to estimate a median black hole mass of $M_{\mathrm{BH}} \sim (3^{+3}_{-1}) \times 10^{7}\,\mathrm{M}_{\odot}$, which combined with stellar mass estimates, indicates the black holes in these SMGs are required to grow by approximately an order of magnitude to match the local black hole–spheroid mass relation.

We have presented the redshift distribution of a large sample of 870 μm-selected SMGs with precise interferometrically-determined positions from ALMA. Crucially, the redshift distribution of the ALESS SMGs declines steadily from $z \sim 2.5$ and does not plateau at high redshift ($z > 3$), as has been suggested by smaller samples of millimetre-selected SMGs. Furthermore, we present a simple evolutionary scenario where SMGs undergo a period of intense star-formation, before passively evolving into local elliptical galaxies. We compare the number density and "faded" H-band luminosity of the ALESS SMGs to local and intermediate-redshift samples of elliptical galaxies, and find that both are in agreement with our simple evolutionary model. Our toy model is consistent with an evolutionary scenario where most of the stars in the majority of local luminous elliptical galaxies are formed through a single starburst SMG event at high redshift.

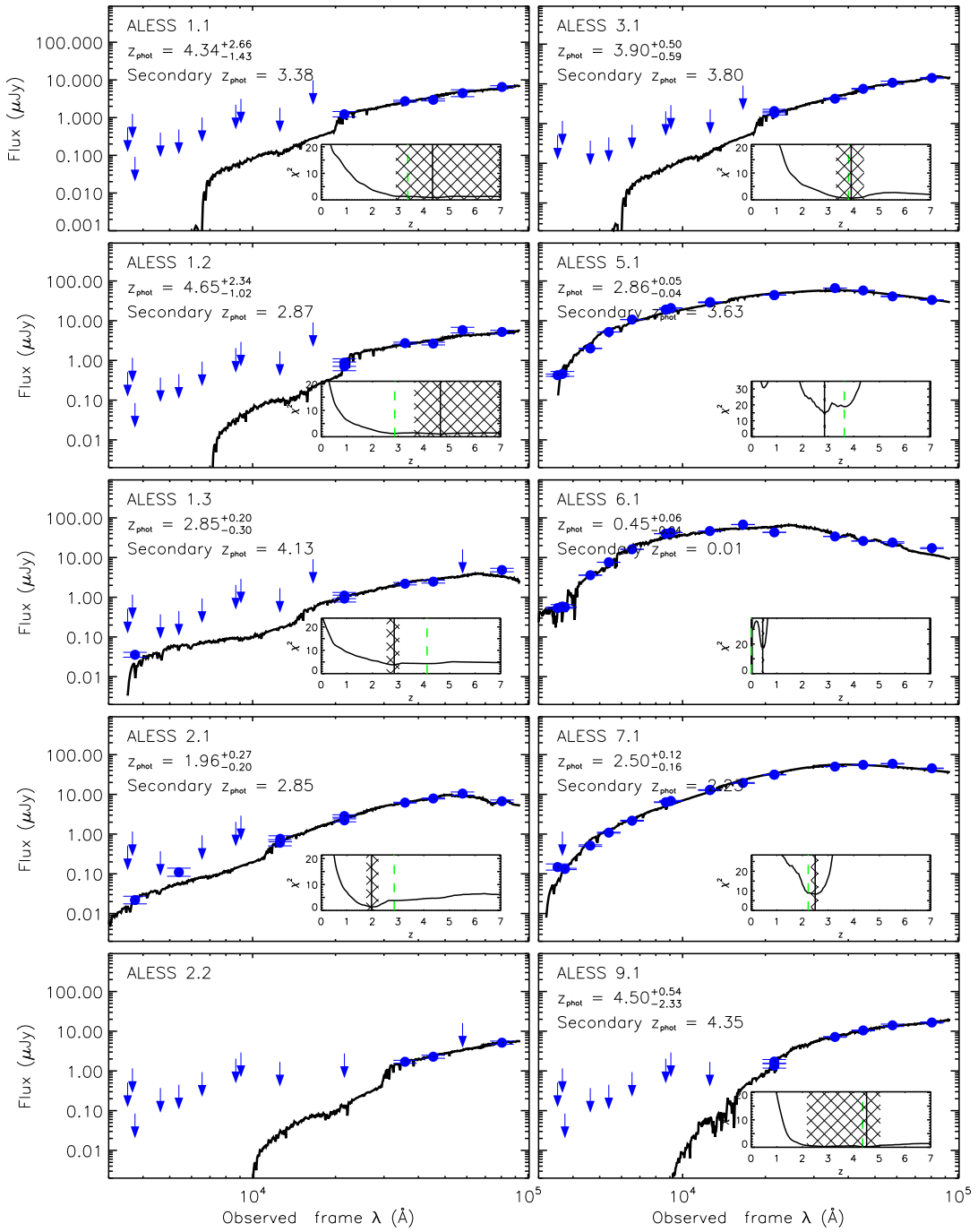

Figure 2.16: The photometry and best fit spectral energy distribution for all 96 ALESS SMGs we consider in this study. Data points and errors are observed photometry, and arrows indicate $3\,\sigma$ detection limits. Although we present the photometry for all sources, only redshifts derived from ≥ 4 photometric detections are considered in our results. In the inset panel in each plot we show the χ^2 distribution as a function of redshift, and indicate the best-fit photometric redshift with a solid line. The hatched region shows the uncertainty on the derived redshift. Secondary redshifts are returned by HYPERZ when a secondary minima has a > 10 per cent probability of being true, based on the reduced χ^2, and where appropriate these are indicated with a green dashed line. We find the majority of our SMGs are well-fit by the best-fit SED template, and only six SMGs display evidence of an $8\,\mu$m excess above the best-fit SED.

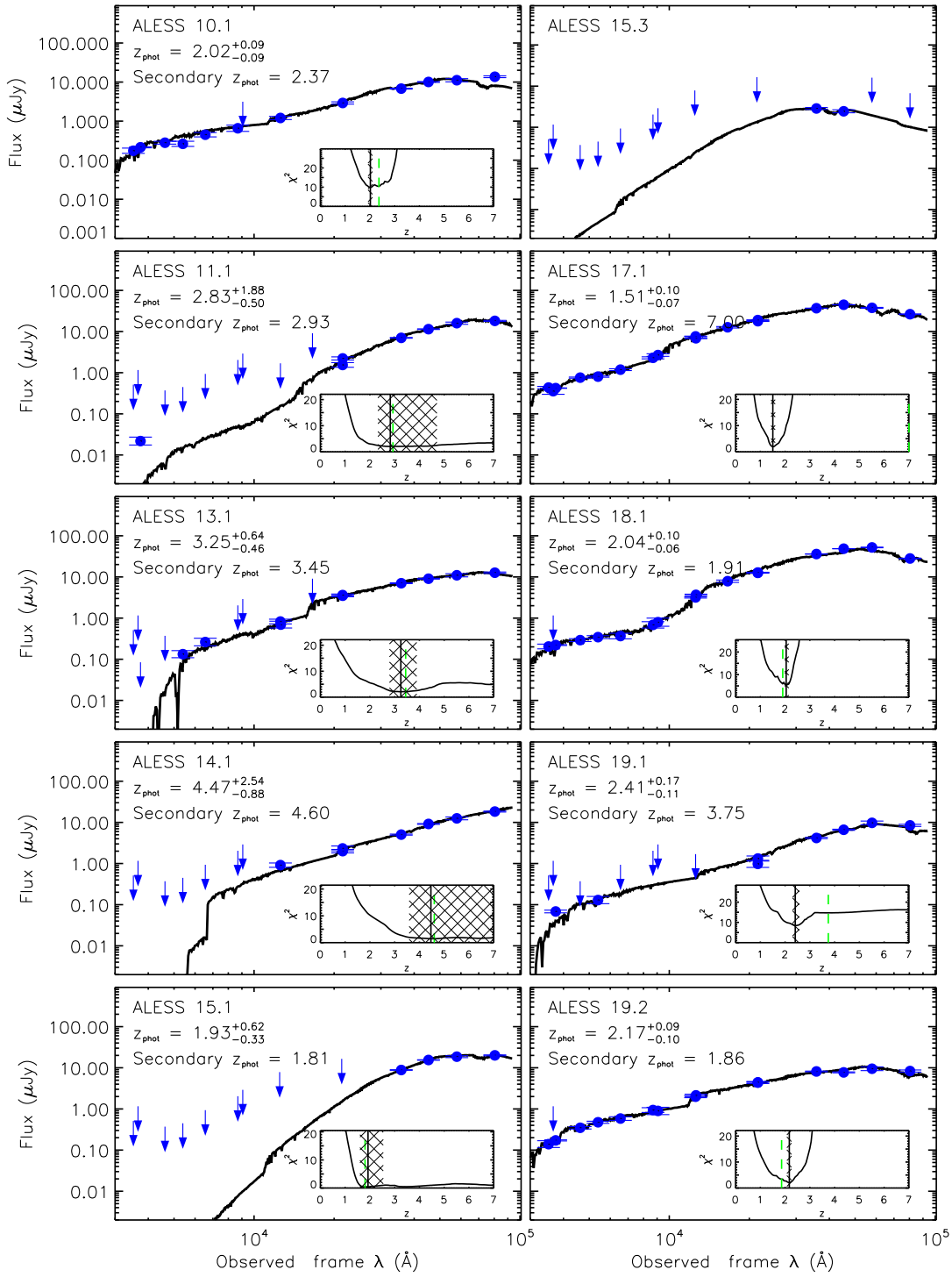

Figure 2.16: continued

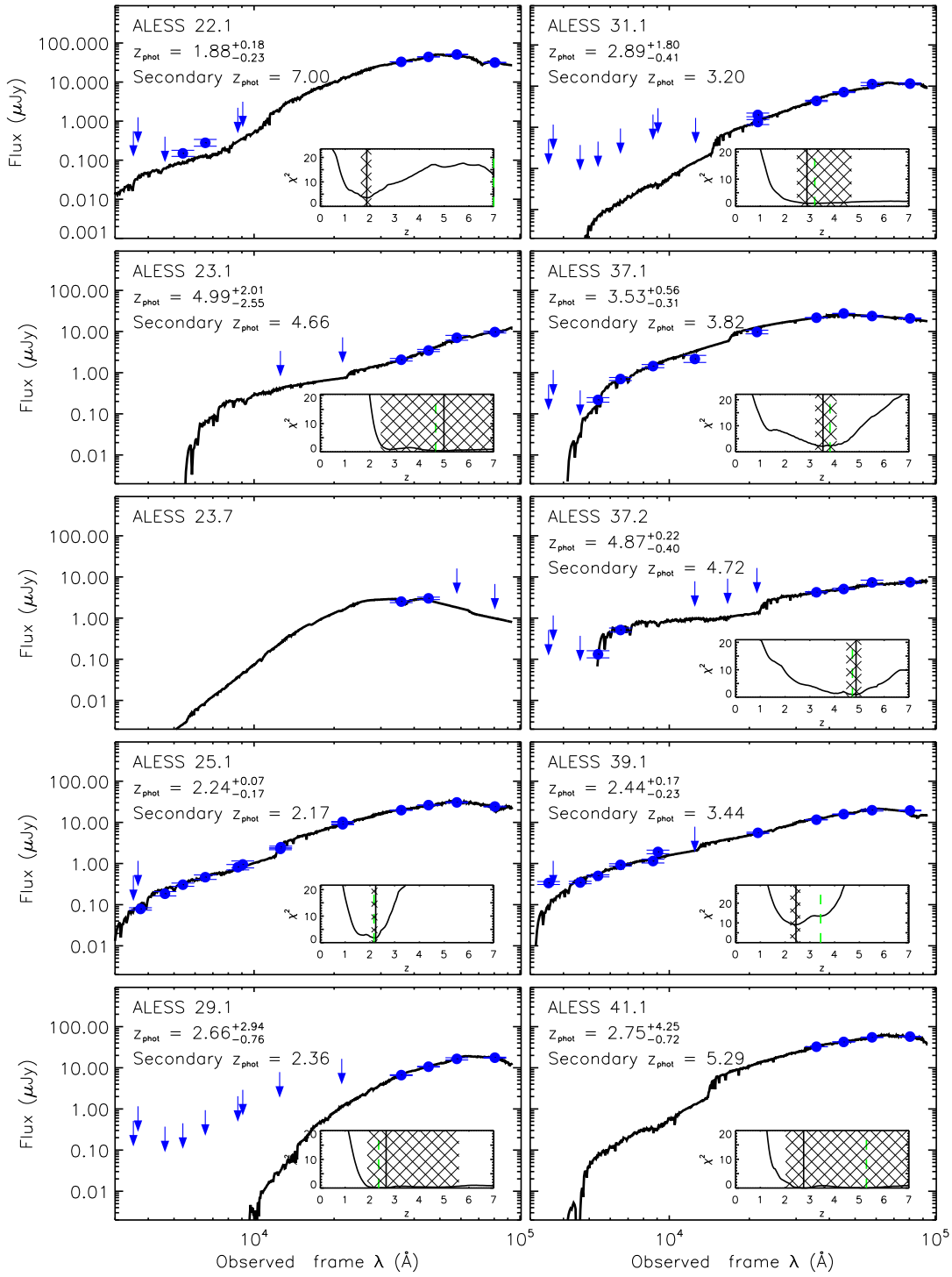

Figure 2.16: continued

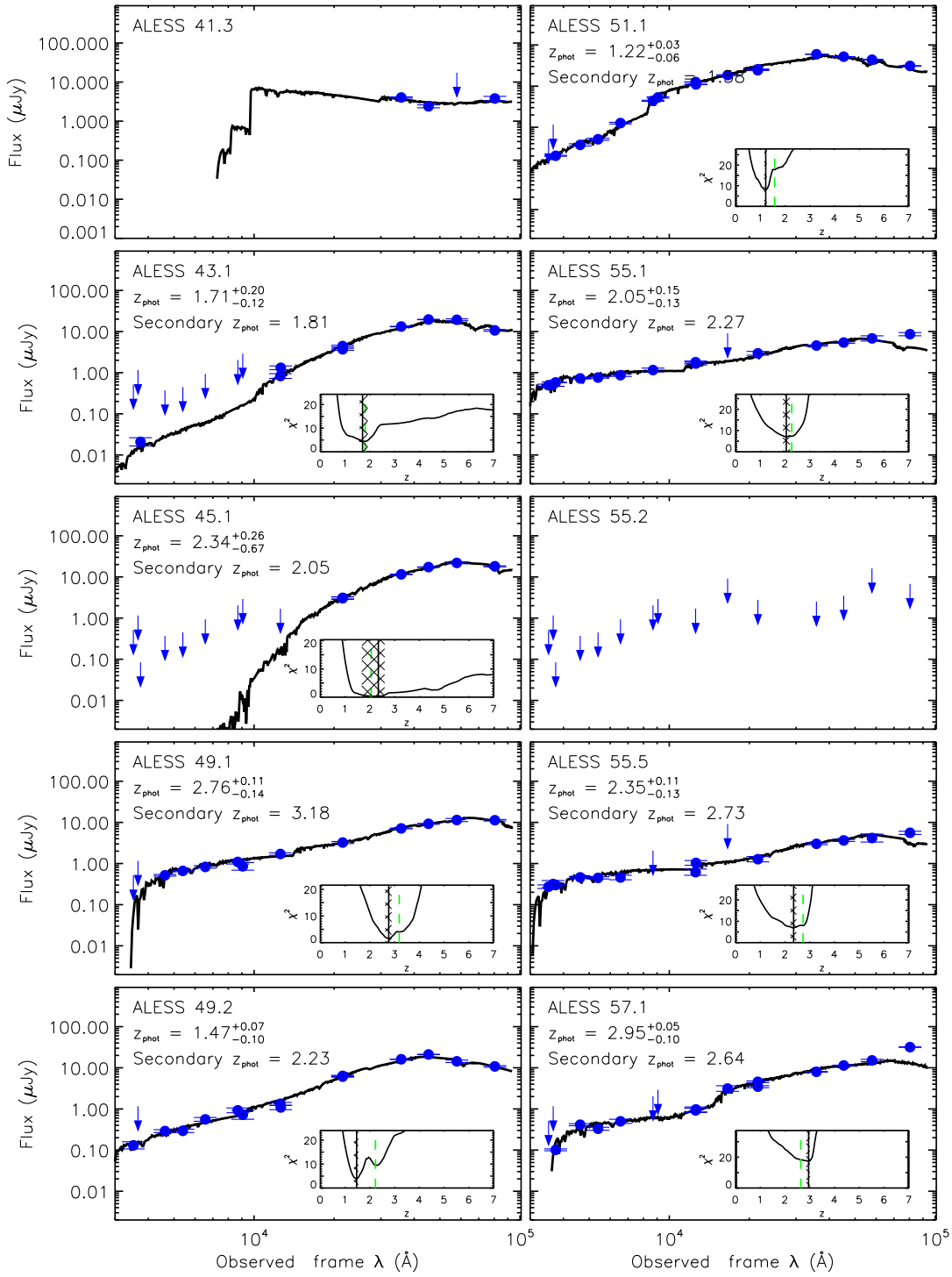

Figure 2.16: continued

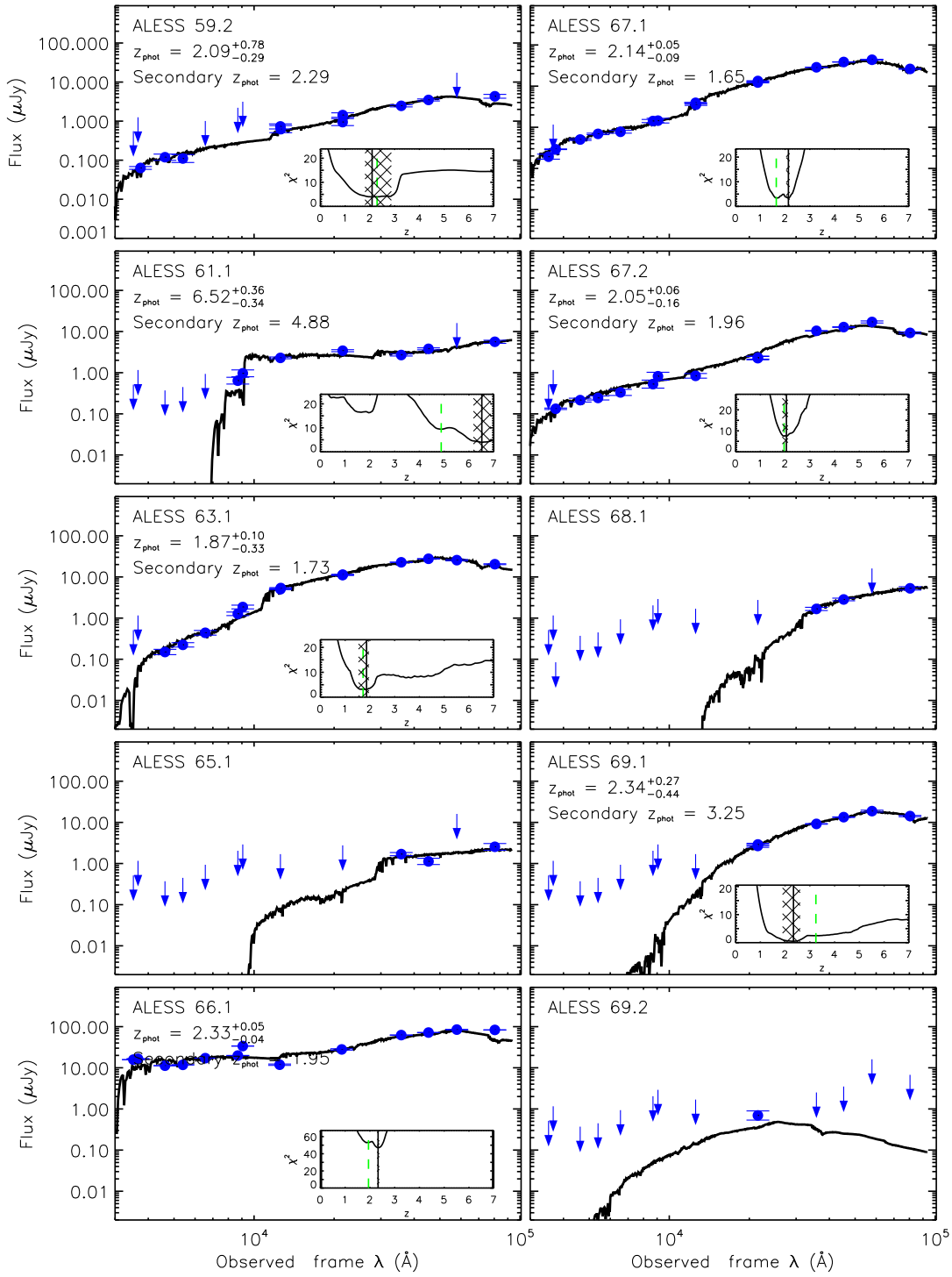

Figure 2.16: continued

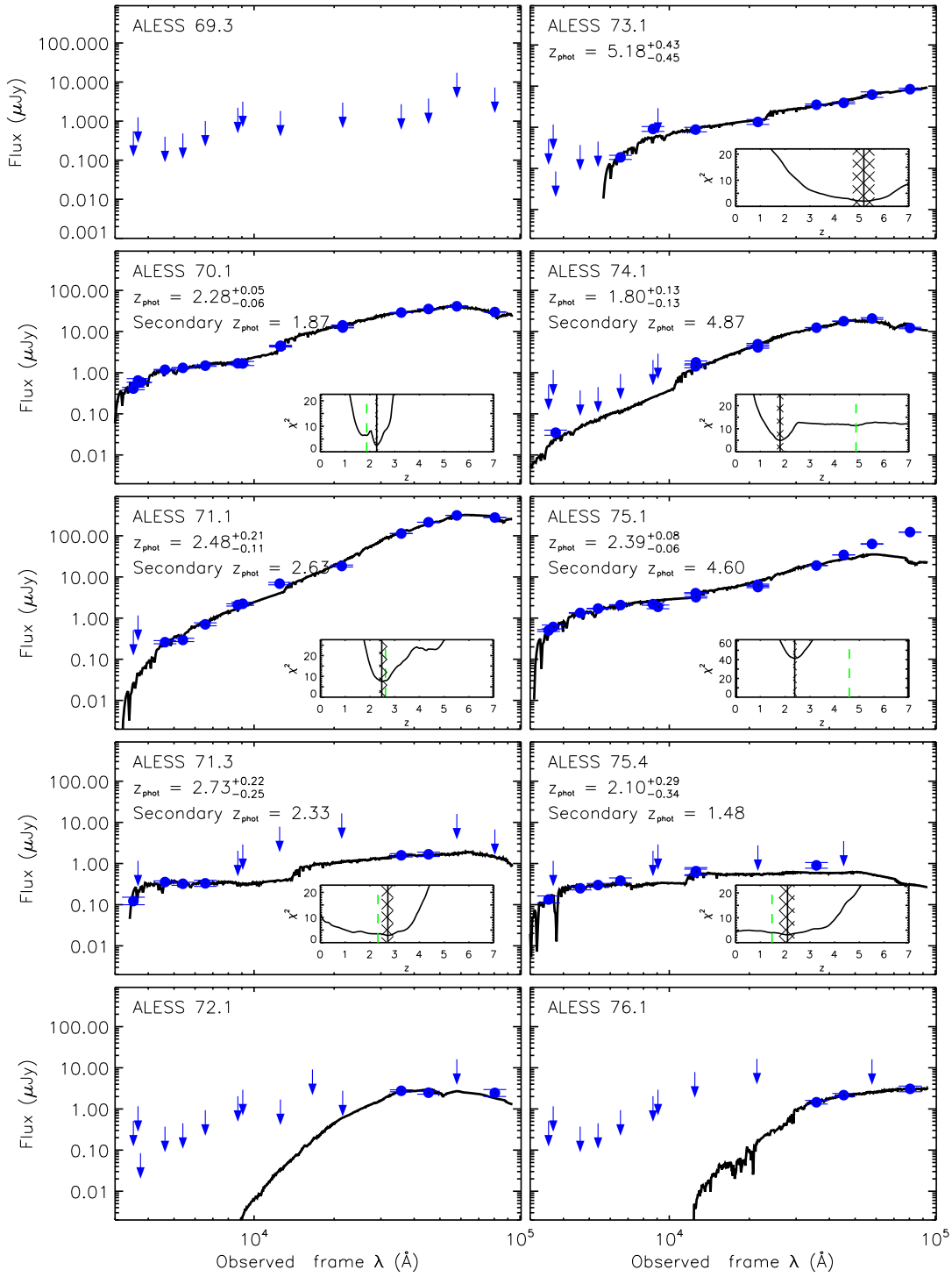

Figure 2.16: continued

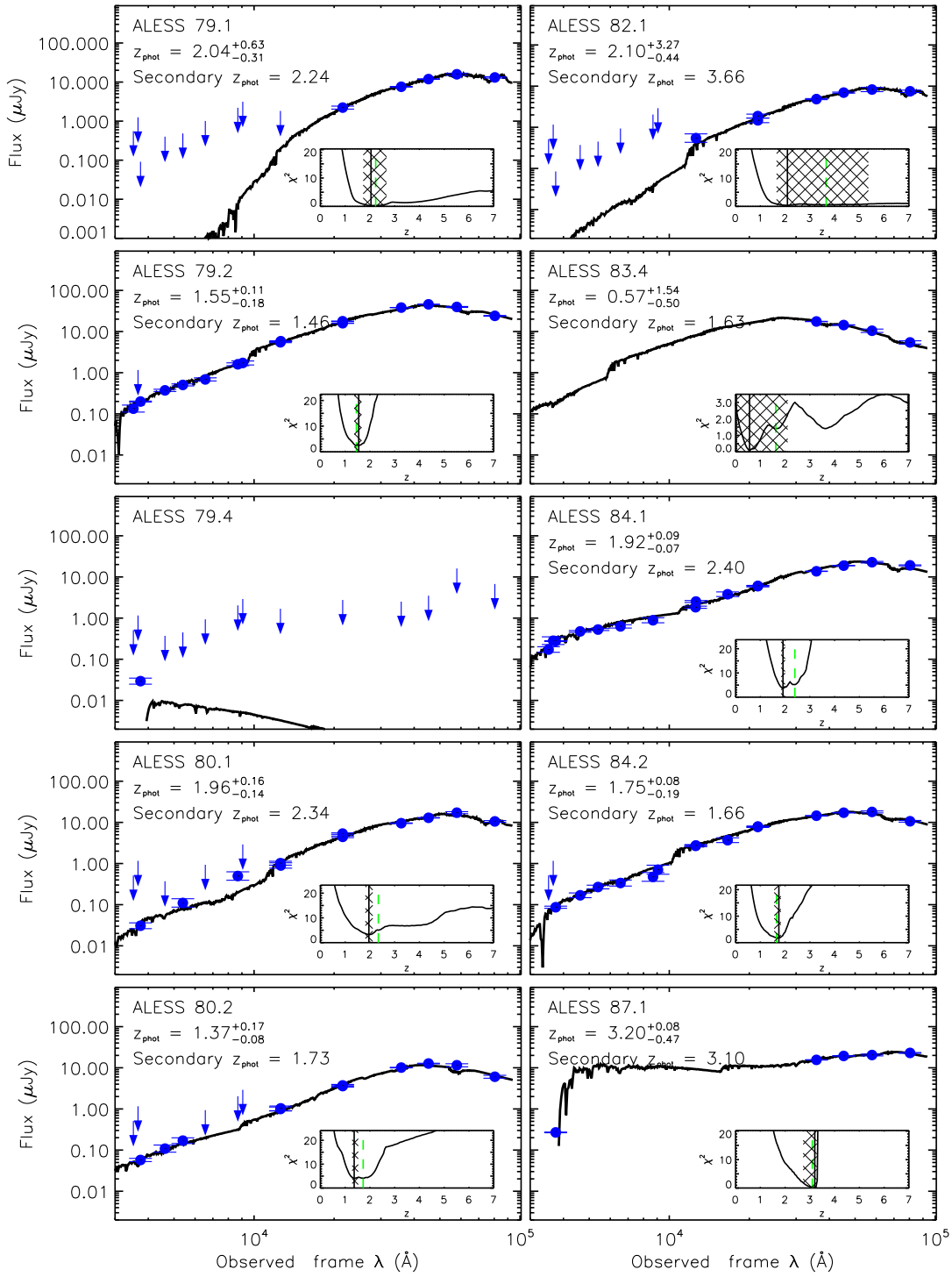

Figure 2.16: continued

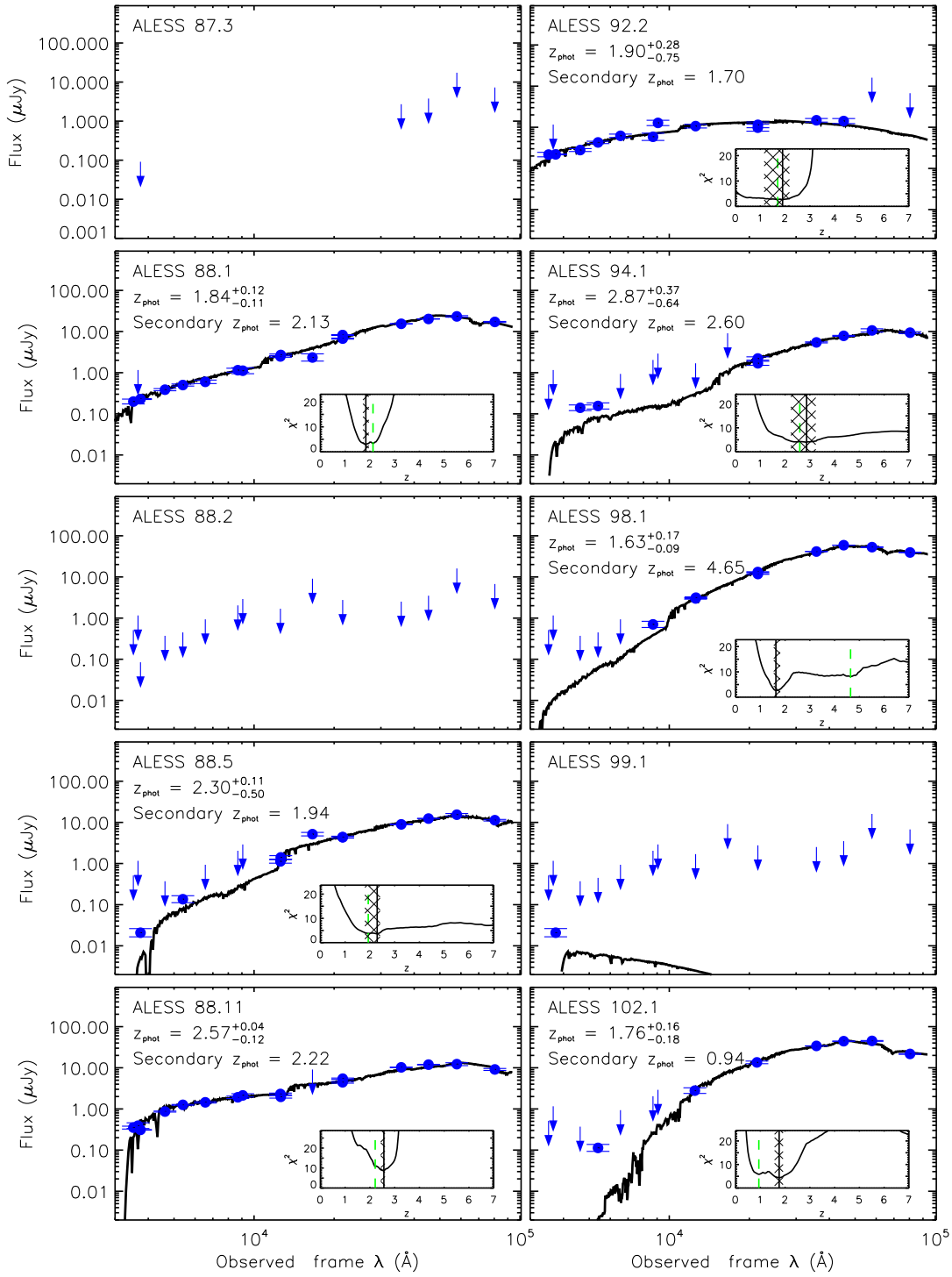

Figure 2.16: continued

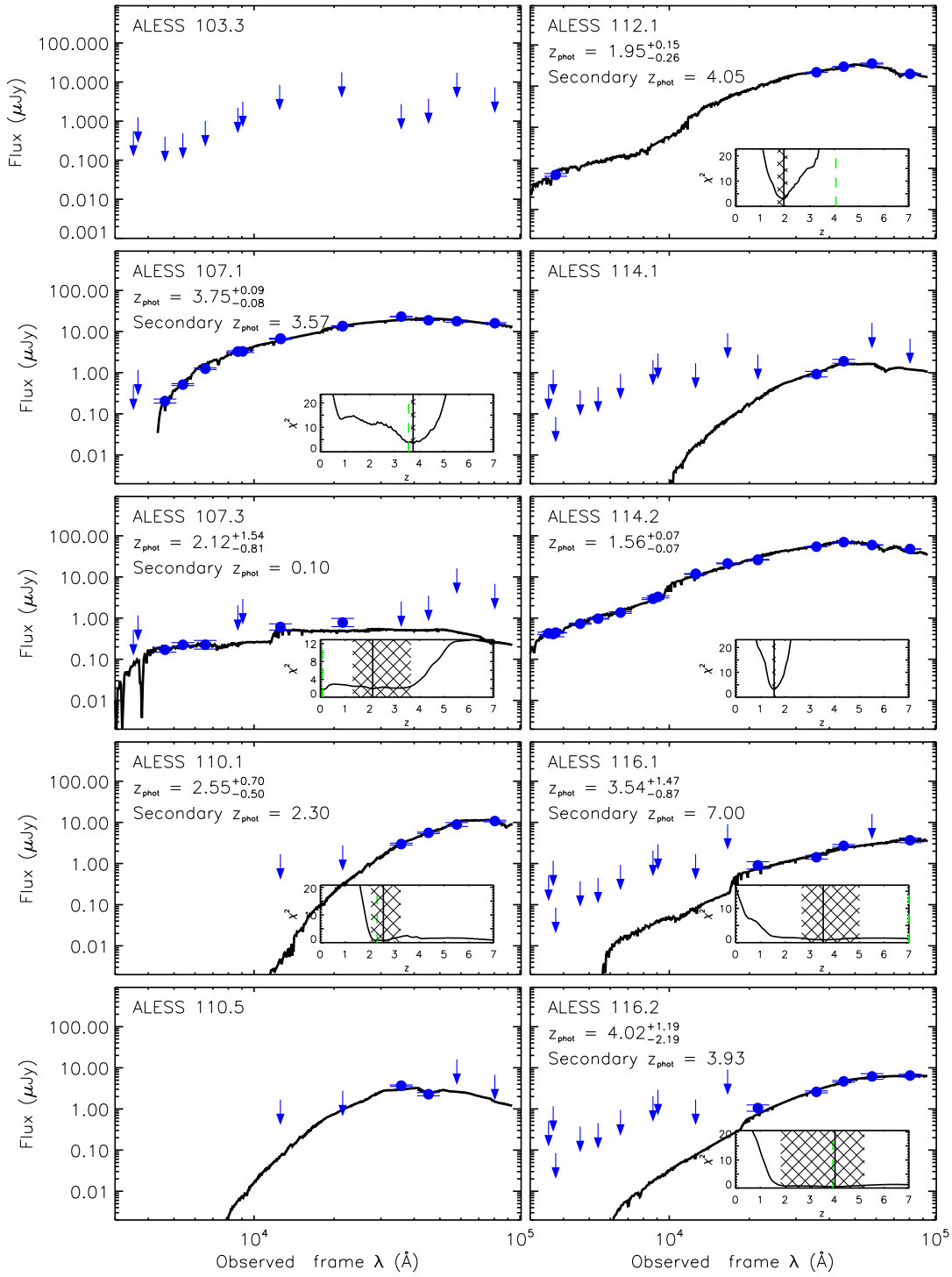

Figure 2.16: continued

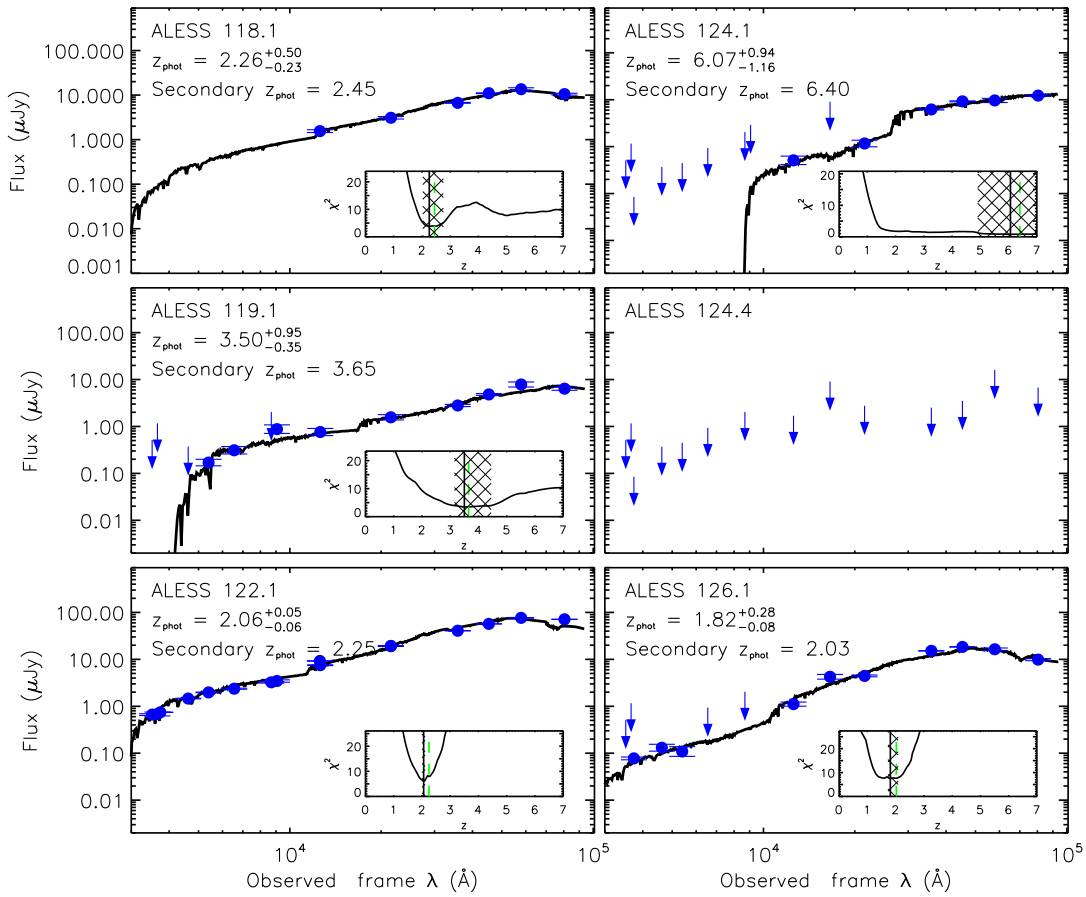

Figure 2.16: continued

Figure 2.17: Here we show $8'' \times 8''$ BIK_s (left) and $3.6\,\mu m$, $4.5\,\mu m$ and $8.0\,\mu m$ (right) colour images for each ALESS SMG. Contours indicate $870\,\mu m$ detections at 3, 5, 7.... $\times\sigma$. The ALESS SMGs are typically aligned with a near-infrared counterpart, and where detected appear red in the optical BIK_s images. A red circle represents the aperture used to measure the photometry of each SMG.

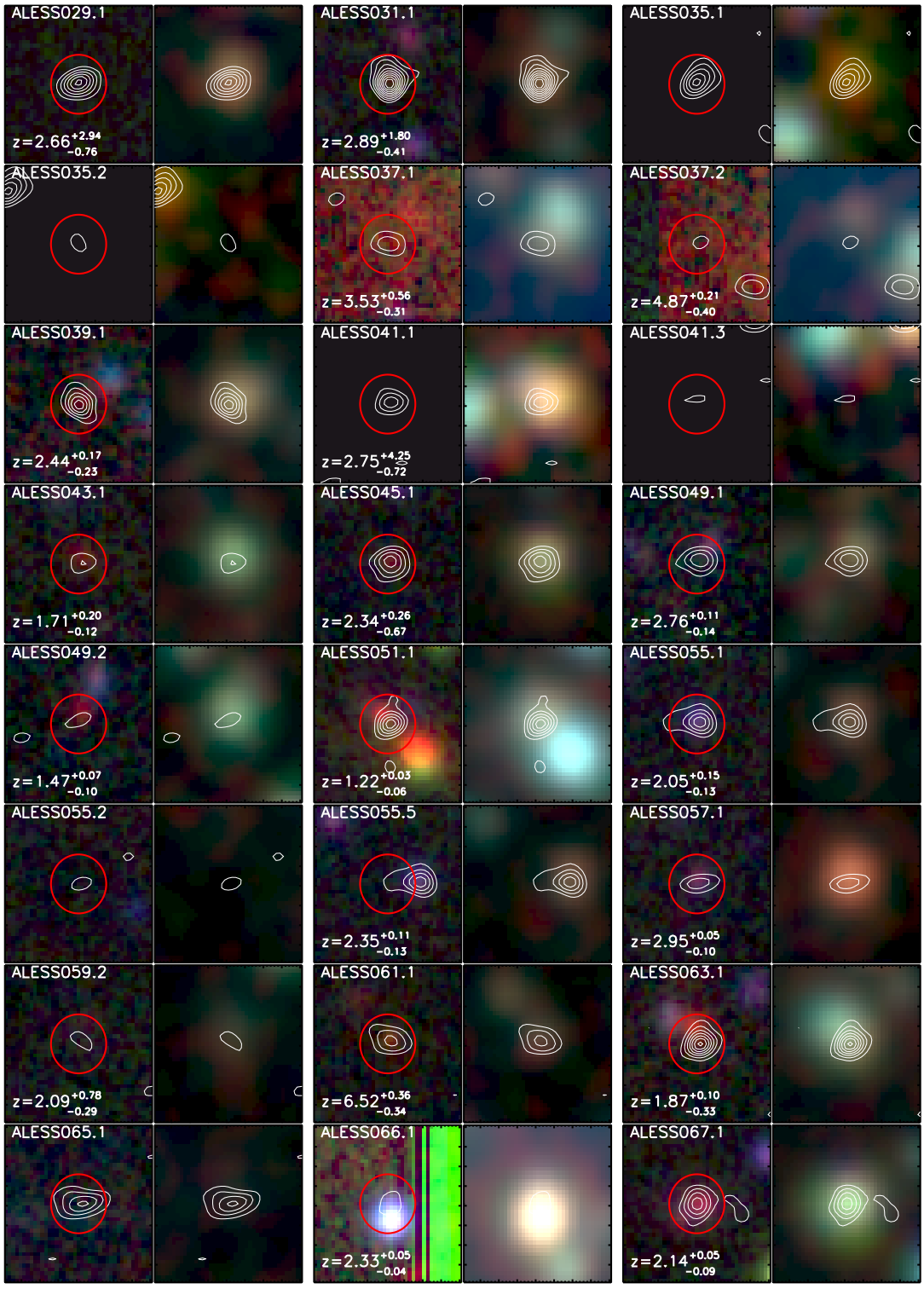

Figure 2.17: continued

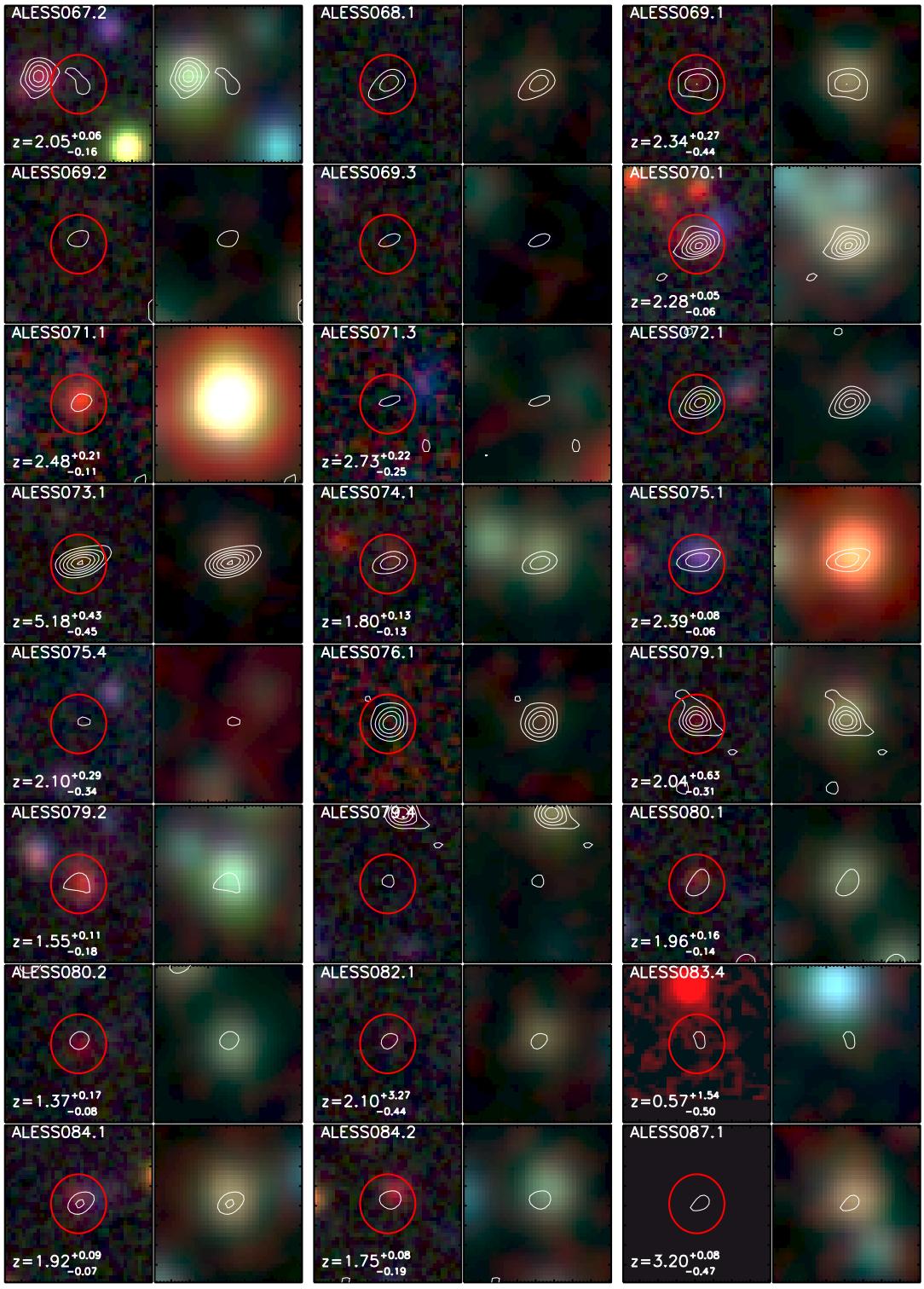

Figure 2.17: continued

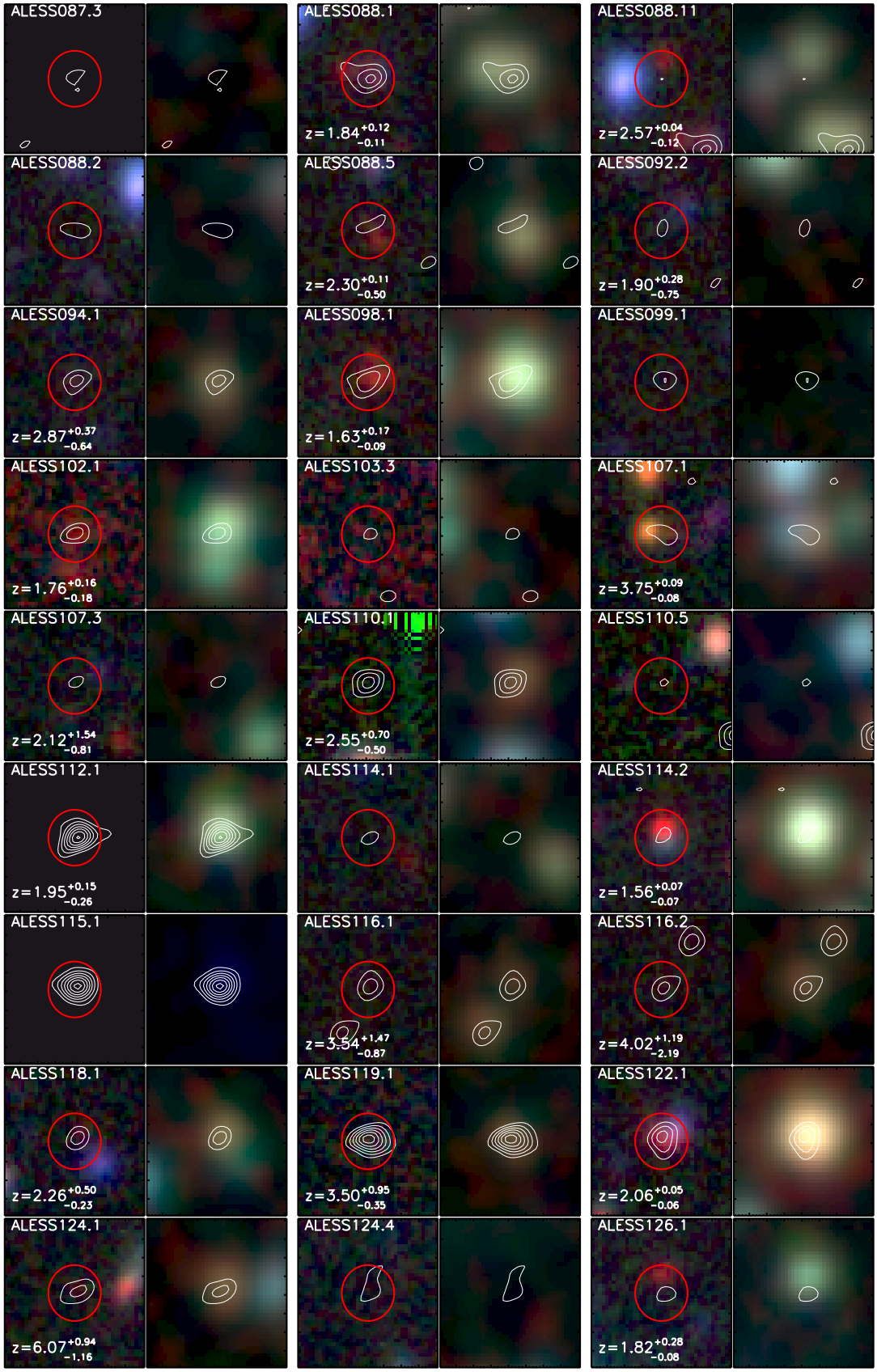

Figure 2.17: continued

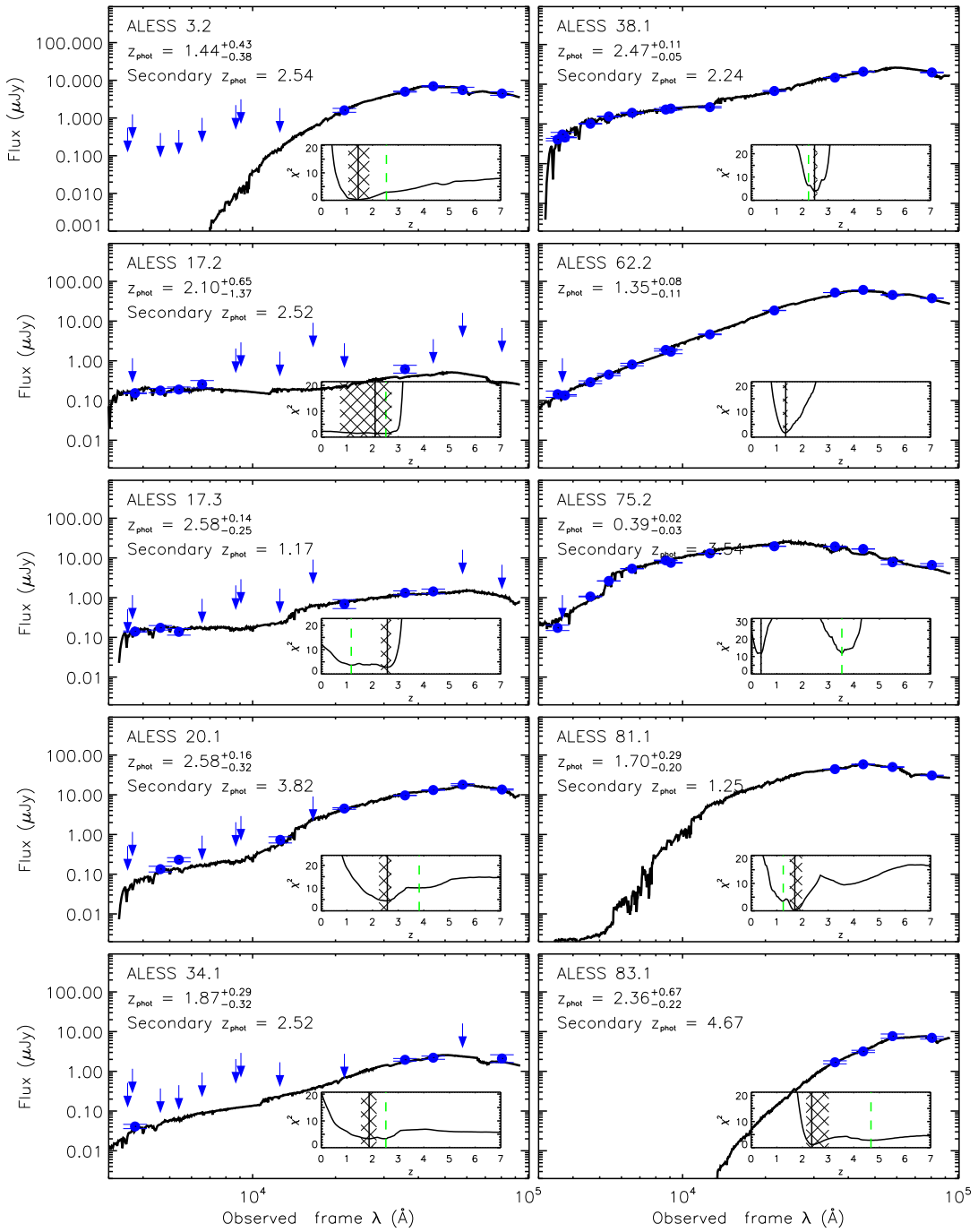

Figure 2.18: The photometry and best fit spectral energy distribution for 14 SMGs from the ALESS supplementary catalogue (Hodge et al., 2013b). Data points and errors are observed photometry, and arrows indicate $3\,\sigma$ detection limits. In the inset panel in each plot we show the χ^2 distribution as a function of redshift, indicating the best-fit photometric redshift with a solid line, and where appropriate the secondary solution with a green dashed line. The hatched region shows the uncertainty on the derived redshift.

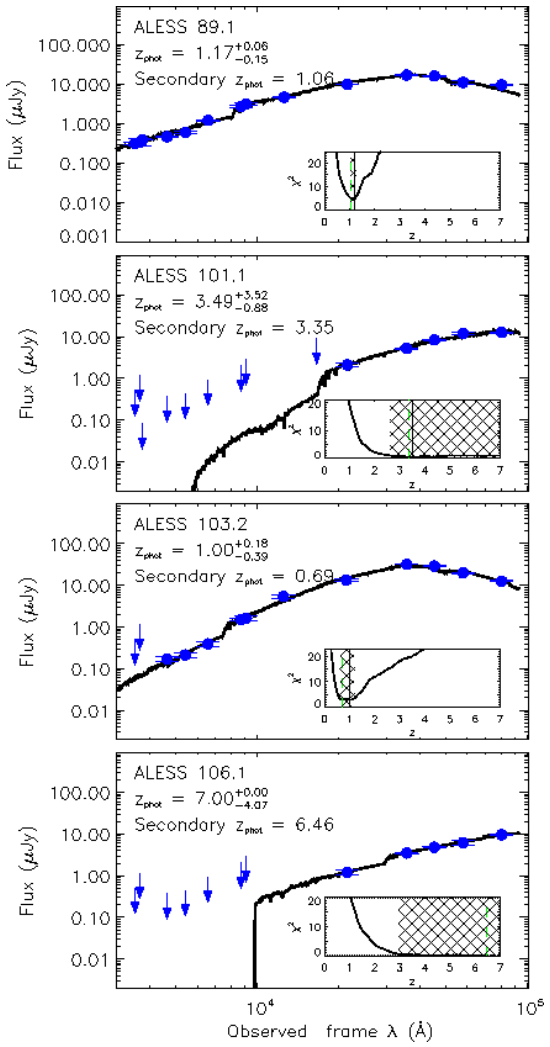

Figure 2.18: continued

ID	MUSYC U	MUSYC U_{38}	VIMOS U	B	V	R	I	z	J^a	H	K^a	3.6 μm	4.5 μm	5.8 μm	8.0 μm
ALESS 3.2	>26.18	>25.29	...	>26.53	>26.32	>25.53	>24.68	>24.29	>24.88	...	23.39 ± 0.12	22.15 ± 0.03	21.79 ± 0.03	22.05 ± 0.16	22.27 ± 0.08
ALESS 17.2	...	>25.29	25.94 ± 0.04	25.77 ± 0.14	25.71 ± 0.16	25.38 ± 0.24	>24.68	>24.29	>24.88	>23.06	>24.35	24.43 ± 0.24	>24.09	>22.44	>23.38
ALESS 17.3	>26.18	>25.29	26.04 ± 0.04	25.80 ± 0.14	26.05 ± 0.21	>25.53	>24.68	>24.29	>24.88	>23.06	24.30 ± 0.26	23.60 ± 0.12	23.51 ± 0.15	>22.44	>23.38
ALESS 20.1	>26.18	>25.29	...	26.08 ± 0.18	25.49 ± 0.13	>25.53	>24.68	>24.29	$24.24 \pm 0.20^*$	>23.06	$22.27 \pm 0.06^*$	21.44 ± 0.02	21.10 ± 0.02	20.76 ± 0.05	21.07 ± 0.03
ALESS 34.1	>26.18	>25.29	27.37 ± 0.14	>26.53	>26.32	>25.53	>24.68	>24.29	>24.88	...	>24.35	23.17 ± 0.08	23.04 ± 0.10	>22.44	23.09 ± 0.17
ALESS 38.1	24.88 ± 0.09	24.56 ± 0.14	24.76 ± 0.01	23.89 ± 0.03	23.43 ± 0.02	23.20 ± 0.03	22.99 ± 0.06	22.93 ± 0.08	22.84 ± 0.05	...	21.83 ± 0.03	20.98 ± 0.01	20.61 ± 0.01	...	20.66 ± 0.02
ALESS 62.2	26.00 ± 0.23	>25.29	26.08 ± 0.04	25.25 ± 0.09	24.77 ± 0.07	24.13 ± 0.08	23.21 ± 0.08	23.33 ± 0.12	22.24 ± 0.03	...	20.73 ± 0.01	19.61 ± 0.00	19.43 ± 0.00	19.76 ± 0.02	19.96 ± 0.01
ALESS 75.2	25.80 ± 0.19	>25.29	...	23.83 ± 0.02	22.85 ± 0.01	22.08 ± 0.01	21.55 ± 0.02	21.71 ± 0.03	21.12 ± 0.01	...	20.67 ± 0.01	20.68 ± 0.01	20.83 ± 0.01	21.67 ± 0.11	21.84 ± 0.06
ALESS 81.1	...	...	...	...	...	...	...	...	...	...	...	19.79 ± 0.00	19.48 ± 0.00	19.65 ± 0.02	20.18 ± 0.01
ALESS 83.1	...	...	...	...	...	...	...	...	...	...	...	23.33 ± 0.09	22.64 ± 0.07	21.68 ± 0.11	21.79 ± 0.05
ALESS 89.1	25.17 ± 0.11	25.08 ± 0.22	24.93 ± 0.02	24.73 ± 0.06	24.46 ± 0.05	23.71 ± 0.06	22.82 ± 0.05	22.67 ± 0.07	22.23 ± 0.03	...	21.44 ± 0.02	20.84 ± 0.01	20.90 ± 0.01	21.30 ± 0.08	21.47 ± 0.04
ALESS 101.1	>26.18	>25.29	>28.14	>26.53	>26.32	>25.53	>24.68	>24.29	...	>23.06	23.08 ± 0.09	22.10 ± 0.03	21.59 ± 0.03	21.21 ± 0.08	21.15 ± 0.03
ALESS 103.2	>26.18	>25.29	...	25.84 ± 0.15	25.57 ± 0.14	24.91 ± 0.16	23.45 ± 0.09	23.37 ± 0.12	$22.07 \pm 0.10^{**}$	...	$21.08 \pm 0.09^{**}$	20.14 ± 0.01	20.24 ± 0.01	20.66 ± 0.05	21.15 ± 0.03
ALESS 106.1	>26.18	>25.29	...	>26.53	>26.32	>25.53	>24.68	>24.29	...	...	23.71 ± 0.16	22.55 ± 0.05	22.19 ± 0.05	21.91 ± 0.14	21.45 ± 0.04

Table 2.6: $3\,\sigma$ upper limits are presented for non-detections, and photometry is left blank where a source is not covered by available imaging. ^{a} We measure J and K photometry from three imaging surveys, but quote a single value, in order of $3\,\sigma$ detection limit. * Photometry measured from HAWK-I imaging. ** Photometry measured from MUSYC imaging.

ID	RA (J2000)	Dec (J2000)	z_{phot}	χ^2_{red}	Filters (Det [Obs])	M_H (AB)	$M\,/\,L_H$ ($M_\odot L_\odot^{-1}$)
ALESS 003.2	03:33:22.19	−27:55:20.9	$1.44^{+0.43}_{-0.38}$	0.23	5 [13]	−22.34	0.36
ALESS 017.2	03:32:08.26	−27:51:19.7	$2.10^{+0.65}_{-1.37}$	1.43	5 [14]	−20.76	0.15
ALESS 017.3	03:32:07.37	−27:51:33.9	$2.58^{+0.14}_{-0.25}$	2.79	6 [15]	−21.97	0.15
ALESS 020.1	03:33:16.76	−28:00:16.0	$2.58^{+0.16}_{-0.32}$	4.38	8 [14]	−24.74	0.18
ALESS 034.1	03:32:17.96	−27:52:33.3	$1.87^{+0.29}_{-0.32}$	3.32	4 [14]	−21.70	0.15
ALESS 038.1	03:33:10.84	−27:56:40.2	$2.47^{+0.11}_{-0.05}$	3.79	13 [13]	−24.88	0.05
ALESS 062.2	03:32:36.58	−27:34:53.8	$1.35^{+0.08}_{-0.11}$	1.68	13 [14]	−24.59	0.05
ALESS 075.2	03:31:27.67	−27:55:59.2	$0.39^{+0.02}_{-0.03}$	11.44	12 [13]	−20.84	0.18
ALESS 081.1	03:31:27.55	−27:44:39.6	$1.70^{+0.29}_{-0.20}$	0.23	4 [4]	−25.04	0.36
ALESS 083.1	03:33:09.42	−28:05:30.6	$2.36^{+0.67}_{-0.22}$	1.22	4 [4]	−23.59	0.36
ALESS 089.1	03:32:48.69	−28:00:21.9	$1.17^{+0.06}_{-0.15}$	4.64	14 [14]	−22.88	0.17
ALESS 101.1	03:31:51.60	−27:45:53.0	$3.49^{+3.52}_{-0.88}$	0.59	5 [14]	−25.15	0.18
ALESS 103.2	03:33:25.82	−27:34:09.9	$1.00^{+0.18}_{-0.39}$	2.91	11 [13]	−23.24	0.08
ALESS 106.1	03:31:39.64	−27:56:39.2	$7.00^{+0.00}_{-4.07}$	0.02	5 [12]	−26.31	0.11

Table 2.8: The derived properties of the supplementary ALESS SMGs detected in ≥ 4 Optical-to-NIR wavebands.

Chapter 3

The SCUBA-2 Cosmology Legacy Survey: ALMA Resolves the Bright-end of the Sub-millimetre Number Counts

3.1 Motivation

In Section 1.4 of this thesis I discussed the importance of obscured star formation in the history of the Universe, and the role that SMGs play in both tracing and contributing to this activity. SMGs are thus an important component in galaxy formation models and the number counts of SMGs is one of the most fundamental properties of the sub-mm Universe that these models must reproduce. Historically, hierarchical models of galaxy formation have either struggled to match the observed number counts of SMGs (e.g. Blain et al. 1999a; Devriendt & Guiderdoni 2000; Granato et al. 2000), or required controversial changes, such as the adoption of a top heavy IMF (Baugh et al., 2005). The impact of sub-mm observations upon on these models highlights the importance of the SMG population in our understanding of galaxy formation, however it emphasises the importance of accurately constrained observational properties.

In the past decade a number of studies have used bolometer cameras at single-dish facilities (e.g SCUBA, LABOCA, MAMBO, AzTEC) to conduct wide-field surveys aimed at detecting extragalactic sub-mm sources (e.g. Coppin et al. 2006; Weiß et al. 2009;

Austermann et al. 2010; Lindner et al. 2011; Aretxaga et al. 2011). These surveys have provided estimates of the number counts of sub-mm sources and have been used as a constraint on galaxy formation models. However, these single-dish surveys are limited by the coarse resolution provided by single-dish facilities (typically ∼15–20″). This coarse resolution, combined with a negative K-correction that provides significant path length for associations, means that there is a significant possibility that multiple individual SMGs appear blended into a single sub-mm source. Fundamentally, this source blending will distort the shape of the sub-mm number counts and produce a false tail of bright sources.

In the previous chapter I discussed the ALMA Cycle-0 follow-up observations of sub-mm sources detected in the LABOCA survey of the Extended *Chandra* Deep Field South (ALESS). These 1.5″ resolution ALMA observations directly pinpointed the SMGs that contribute to each of the single-dish sub-mm sources, and showed that at least 35 % of the LABOCA sources are comprised of ≥ 2 individual SMGs. One key result from the ALMA survey is that no SMGs were detected above 9 mJy, despite the LABOCA sample containing 12 sources above this limit. The absence of bright sources led Karim et al. (2013) to conclude that the bright-end of the sub-mm number counts had been significantly over-estimated, due to source multiplicity. In the following chapter I use ALMA observations of a sample of 30 bright sub-mm sources, selected from deep, wide-field, imaging with SCUBA-2, to constrain the bright-end of the sub-mm number counts. The following chapter was accepted for publication in the Astrophysical Journal in May 2015.

3.2 Abstract

We present high-resolution 870 μm continuum maps obtained with the Atacama Large Millimetre / sub-millimetre Array (ALMA) of 30 bright sub-millimetre sources in the UKIDSS Ultra Deep Survey (UDS) field. The sub-millimetre sources are selected from deep, panoramic 850-μm imaging with the SCUBA-2 bolometer camera on the James Clerk Maxwell Telescope as part of the SCUBA-2 Cosmology Legacy Survey, and are representative of the brightest sources in the field (median $S_{\rm SCUBA\text{-}2} = 8.7 \pm 0.4$ mJy). The ALMA maps have a resolution of $0.35'' \times 0.25''$, but to ensure that we do not resolve-out flux in detected sources we construct a catalogue from tapered images with a resolution of $0.80'' \times 0.65''$ and a median noise of 0.26 mJy beam^{-1}. We detect 52 sub-millimetre galaxies (SMGs) at $> 4\,\sigma$ significance in our 30 ALMA maps, with flux densities of 1.3–12.9 mJy.

In 61^{+19}_{-15} % of the ALMA maps the single-dish source is comprised of a blend of ≥ 2 SMGs, where the secondary SMGs are Ultra-Luminous Infrared Galaxies (ULIRGs) with $L_{\rm IR} \gtrsim 10^{12}\,{\rm L}_{\odot}$. Across all of our ALMA maps the brightest SMG contributes on average 80^{+6}_{-2} % of the single-dish flux density, and in the ALMA maps containing ≥ 2 SMGs the secondary SMG contributes on average 25^{+1}_{-5} % of the integrated ALMA flux. We construct the bright-end of the sub-millimetre number counts and show that multiplicity boosts the apparent single-dish cumulative counts by 20 % at a flux density of $S_{870} > 7.5\,{\rm mJy}$, and by 60 % at $S_{870} > 12\,{\rm mJy}$. We combine our sample with previous ALMA studies of fainter SMGs and show that the counts are well-described by a double power-law with a break at $8.5 \pm 0.6\,{\rm mJy}$. The break corresponds to a luminosity of $\sim 6 \times 10^{12}\,{\rm L}_{\odot}$ (star formation rate of $\sim 10^{3}\,{\rm M}_{\odot}{\rm yr}^{-1}$) that for the typical sub-millimetre sizes of these SMGs, which are resolved in our ALMA data with $R_{\rm e} = 1.2 \pm 0.1\,{\rm kpc}$, corresponds to a SFR density of $\sim 100\,{\rm M}_{\odot}\,{\rm yr}^{-1}\,{\rm kpc}^{-2}$. Finally, the number density of $S_{870} \gtrsim 2\,{\rm mJy}$ SMGs in the maps of the brightest SMGs in our sample is 80 ± 30 times higher than that derived from blank-field counts. An over-abundance of faint SMGs is inconsistent with line-of-sight projections dominating multiplicity in the brightest SMGs, and indicates that a significant proportion of these pairs of high-redshift ULIRGs must be physically associated.

3.3 Introduction

The population of dusty galaxies that is detected at sub-millimetre (sub-mm) wavelengths, SMGs, represent some of the most intense sites of star formation in the Universe. Sub-mm sources were first uncovered in surveys with SCUBA at the James Clerk Maxwell Telescope (JCMT; e.g. Smail et al. 1997; Hughes et al. 1998; Barger et al. 1998; Eales et al. 1999; Pope et al. 2005; Coppin et al. 2006), but subsequently studied at various facilities (e.g. Greve et al. 2004, 2008; Laurent et al. 2005; Scott et al. 2006; Bertoldi et al. 2007; Weiß et al. 2009; Austermann et al. 2010; Lindner et al. 2011; Aretxaga et al. 2011), and the radio-identified subset of the population has been shown to lie at a median redshift of $z \sim 2.3$ (Chapman et al., 2005). At these redshifts the typical flux densities of the sources ($S_{\nu} \sim 5$–$15\,{\rm mJy}$) correspond to total infrared luminosities of $\sim 10^{13}\,{\rm L}_{\odot}$ (star formation rate $\sim 10^{3}\,{\rm M}_{\odot}{\rm yr}^{-1}$; see Magnelli et al. 2012; Swinbank et al. 2014), comparable to local Ultra-Luminous Infrared Galaxies (ULIRGs). The importance of such prodigious star formation rates (SFRs), and thus rapid growth in stellar mass at high-redshift has led a number of authors to suggest that sub-mm sources represent a high-redshift phase

in the evolution of local elliptical galaxies (e.g. Lilly et al. 1999; Genzel et al. 2003; Blain et al. 2004; Swinbank et al. 2006; Tacconi et al. 2008; Hainline et al. 2011; Hickox et al. 2012; Toft et al. 2014; Simpson et al. 2014), highlighting their importance for models of galaxy formation.

Despite surveys with sub-mm / mm cameras such as SCUBA-2, LABOCA, AzTEC, or SPIRE on board *Herschel*, uncovering large numbers of sources, follow-up studies have been hampered by the coarse resolution delivered by these single-dish facilities (typically 15″–30″ FWHM). At this resolution, identifying the optical / near-infrared counterparts to the sub-mm emission (i.e. resolving the sub-mm source into its constituent SMGs) is challenging, a problem that is compounded by the expectation that these heavily dust-obscured galaxies are faint at optical wavelengths. One route to identifying the SMGs contributing to each sub-mm source has been to exploit the correlation between radio flux density and far-infrared emission in local galaxies, since 1.4 GHz imaging with the Very Large Array (VLA) provides the sub-arcsecond resolution required to pinpoint individual SMGs (e.g. Ivison et al. 1998, 2002, 2004, 2007; Smail et al. 2000; Bertoldi et al. 2007; Biggs et al. 2011; Lindner et al. 2011). Studies employing this method have successfully constrained the properties of $\sim 50\,\%$ of the SMG population (Hodge et al., 2013b), but they do have limitations: this approach involves significant assumptions about the multi-wavelength properties of SMGs, and it is typically biased towards sources at lower redshift ($z \lesssim 2.5$) due to the positive K-correction at radio frequencies.

A further complication to the multi-wavelength identification procedure is caused by the potential blending of multiple individual SMGs into a single sub-mm source. Such source blending, or multiplicity, is somewhat expected given the coarse resolution of single-dish surveys, but is exacerbated by two further effects. Firstly, the negative K-correction means that a sub-mm selection probes a large redshift range ($z \sim 1$–8), providing a significant path length for projection. Secondly, a number of studies have suggested that the intense star formation in SMGs is predominantly triggered by merger activity (e.g. Tacconi et al. 2008; Engel et al. 2010; Swinbank et al. 2010a; Alaghband-Zadeh et al. 2012; Menéndez-Delmestre et al. 2013; Chen et al. 2015) and that the SMG population is strongly clustered (Blain et al. 2004; Scott et al. 2006; Weiß et al. 2009; Hickox et al. 2012, but see also Adelberger 2005; Williams et al. 2011). If SMGs are interacting, or reside in over-densities, then we may also expect to resolve sub-mm sources into physically associated (potentially interacting) pairs of SMGs. Indeed, studies of sub-mm sources that employ

radio identifications often identify multiple *robust* counterparts to a single sub-mm source (e.g. Ivison et al. 2007), providing the first indication that multiplicity is a non-negligible effect.

Prior to the Atacama Large Millimetre / sub-millimetre Array (ALMA), sub-mm interferometry with facilities such as the Plateau de Bure Interferometer (PdbI) or Sub-Millimetre Array (SMA) offered the only definitive route to identify the SMGs contributing to single-dish detected sub-mm sources. However, while these facilities provide the ~ 1–$2''$ resolution necessary to locate SMGs, their sensitivity meant that follow-up observations were typically only possible for a handful of the brightest sub-mm sources (e.g. Gear et al. 2000; Iono et al. 2006; Wang et al. 2007; Younger et al. 2007, 2009; Dannerbauer et al. 2008; Cowie et al. 2009; Aravena et al. 2010; Wang et al. 2011; Barger et al. 2012; Smolčić et al. 2012; Chen et al. 2013; Ivison et al. 2013), and often at different wavelengths to the initial single-dish selection. The first conclusive evidence of multiplicity in sub-mm sources was presented by Wang et al. (2011), who used observations with the SMA to show that two bright sub-mm sources were comprised of blends of two-or-three individual SMGs, with flux densities of $S_{850} = 3$–$5\,\mathrm{mJy}$, and thought to be at different redshifts.

Building upon this result, Barger et al. (2012) used the SMA to observe 16 SCUBA-detected sources in the GOODS-N field, at $\sim 2''$ resolution. The observations resolve three of the sub-mm sources into multiple SMGs, leading the authors to conclude that $\sim 40\,\%$ of SMGs brighter than 7 mJy may be blends of multiple SMGs. However, the SMA observations have a typical depth of $\sigma_{860} \sim 0.6$–$1\,\mathrm{mJy}$, hence only being sensitive to secondary SMGs brighter than 3–4 mJy, and the small number of sources in the sample leads to significant uncertainties on the multiplicity fraction. In a similar study, Smolčić et al. (2012) showed that 6 / 28 LABOCA 870-μm sources are comprised of blends of SMG in 1.3-mm follow-up observations with the PdBI, with a further 9 sources not detected. While this again hints at significant multiplicity, the results are complicated by the different selection wavelengths of the single-dish and interferometric follow-up observations.

The commissioning of ALMA promises a revolution in our understanding of the SMG population. Indeed, even with the limited capabilities available in Cycle-0, Hodge et al. (2013b) obtained robust observations of 88 single-dish sources detected at 870 μm in the LABOCA survey of the Extended *Chandra* Deep Field South (LESS). These ALMA, $1.5''$ resolution, "snapshot" observations pinpointed the SMGs contributing to the LABOCA sources and showed that at least $35\,\%$ of the sources are comprised of ≥ 2 SMGs. Fur-

thermore, to recover the LABOCA flux density, Hodge et al. (2013b) also showed that it is necessary to include flux in faint sources below their nominal detection threshold, indicating that a significant proportion of the ALMA maps contain additional faint 1–2 mJy SMGs.

One key result from this ALMA-LESS (ALESS) survey is that despite the sample containing 12 LABOCA sources above 9 mJy, only one ALMA-detected SMG is brighter than this limit. As a result, Karim et al. (2013) conclude that due to multiplicity the bright-end of the sub-mm number counts may have been significantly overestimated in single-dish surveys, suggesting a cut-off in the SFR in the most luminous starbursts corresponding to a potential Eddington limit at 9 mJy (equivalent to a SFR of $\sim 10^3\,\mathrm{M_{\odot}yr^{-1}}$), although a number of SMGs above this threshold have been detected in previous interferometric surveys (e.g. Younger et al. 2007, 2009; Barger et al. 2012; Chen et al. 2013).

To improve the statistics of multiplicity in the brightest sub-mm sources we have obtained ALMA 870 μm follow-up observations of 30 bright sub-mm sources in the UKIDSS Ultra Deep Survey (UDS) field (Lawrence et al., 2007). These single-dish targets were selected from deep, wide-field observations taken as part of the SCUBA-2 Cosmology Legacy Survey (S2CLS; e.g. Geach et al. 2013) at the JCMT (14.5″ resolution), and are representative of the brightest sources in the field (Geach et al. in prep.). We use the data to measure the multiplicity in the single-dish population, probe the bright-end of the number counts and investigate the number density of secondary SMGs.

The chapter is structured as follows. In § 3.4 we discuss our sample selection, the ALMA observations, and our data reduction. In § 3.5 we describe the construction of our source catalogue and provide a comparison between the ALMA and SCUBA-2 detections. In § 3.6 we discuss the fraction of the single-dish sources that fragment into multiple SMGs and present the *resolved* number counts. Our conclusions are given in § 3.7. We adopt a cosmology with $H_0 = 71\,\mathrm{km\,s^{-1}\,Mpc^{-1}}$, $\Omega_{\Lambda} = 0.73$, and $\Omega_{\mathrm{m}} = 0.27$. Throughout this work error estimates are from a bootstrap analysis, unless otherwise stated.

3.4 Observations & Data Reduction

3.4.1 Sample Selection

The sub-mm sources in this chapter were selected from observations taken as part of the S2CLS programme at the JCMT. The latest S2CLS map of the UDS field (as of 2014

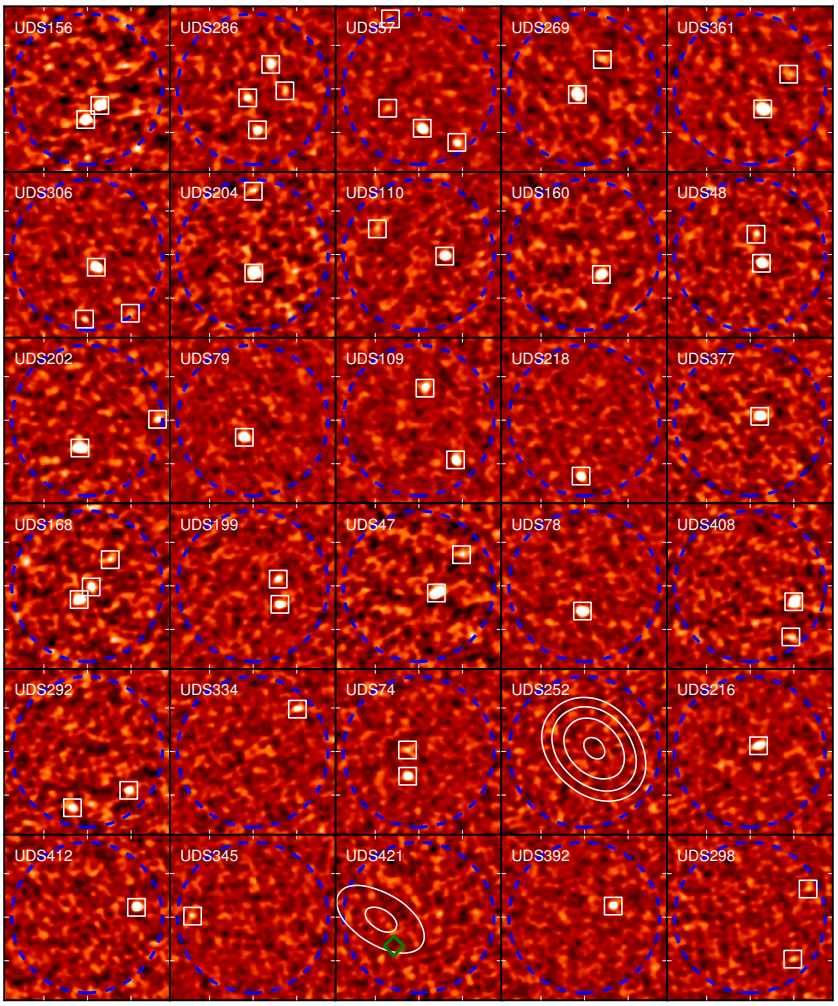

Figure 3.1: ALMA 870-μm continuum maps, at 0.8″ resolution, of 30 bright sub-mm sources in the UDS field. These sources are selected to be representative of the brightest sources detected in the S2CLS survey of this $\sim 0.8\,\mathrm{deg}^2$ field. The $18'' \times 18''$ non-primary-beam-corrected maps (roughly 150 kpc$\times$ 150 kpc at the typical SMG redshift, $z = 2.5$) are ordered by decreasing single-dish flux density and have a median 1-σ rms of $0.26\,\mathrm{mJy\,beam}^{-1}$. The dashed circle on each thumbnail represents the primary beam (FWHM) of ALMA at 870-μm. We detect 52 SMGs at $> 4\,\sigma$ (marked by a squares) in the 30 ALMA maps, with 870-μm flux densities of 1.3–12.9 mJy. In 18 / 30 ALMA maps the single-dish sub-mm source fragments into two or more individual SMGs. In particular, we highlight UDS 57, 168, 286 and 306, where the ALMA observations demonstrate that the single-dish source is comprised of three-or-four SMGs. In two ALMA maps, UDS 252 and 421, we do not detect any SMGs, but note that both SCUBA-2 sources are detected in *Herschel* / SPIRE imaging. We plot contours representing the single-dish SCUBA-2 emission at 3, 3.5, 4.0, 4.5 $\times\sigma$ for these sources, note that UDS 421 has a potential VLA / 1.4 GHz counterpart (diamond; Arumugan et al. submitted) that is not detected in our ALMA maps.

August) reaches a uniform depth of $\sigma_{850} = 1.3\,\mathrm{mJy}$ across $0.78\,\mathrm{deg}^2$. However, our initial sample selection for the Cycle-1 deadline in early 2013 was made from the first version of these observations (2013 February), which reached a 1-σ_{850} depth of 2.0 mJy. From these earlier observations we selected 31 sources detected at $> 4\,\sigma$, and hence having observed 850-μm flux densities of > 8mJy. We removed one source from our sample that is a bright, lensed, SMG with previous interferometric follow-up observations (Ikarashi et al. 2011), leaving a sample of 30 targets.

In Figure 3.2 we show the flux density distribution for the 30 sources in our sample, measured from the deeper 2014 August S2CLS map of the UDS field ($\sigma_{850} = 1.3\,\mathrm{mJy}$). In the deeper imaging 12 / 30 of the sub-millimetre sources scatter to lower flux densities ($S_{850} < 8\,\mathrm{mJy}$), with two sources not detected above our $3.5\,\sigma$ detection threshold (although both ALMA maps contain SMGs). While we present the ALMA observations of these two "sources" (UDS 298 and 392), we note that formally 28 of the sources in our sample are now single-dish-detected. Overall our sample consists of 850 μm-bright sub-mm sources, with a median flux density of $(8.7 \pm 0.4)\,\mathrm{mJy}$. The completeness of our sample relative to the new, deeper catalogue is $> 50\,\%$ at $S_{850} > 8\,\mathrm{mJy}$, and $100\,\%$ at $S_{850} > 11\,\mathrm{mJy}$ over this $0.8\,\mathrm{deg}^2$ field.

3.4.2 Data Reduction

We obtained ALMA 870 μm (Band 7) continuum imaging of all 30 targets from our sample on 2013 November 1, as part of the Cycle-1 project 2012.1.00090.S. All targets were observed using 7.5-GHz of bandwidth centered at 344 GHz (870 μm), chosen to match the frequency of the original SCUBA-2 observations. We used a "single continuum" correlator setup with four basebands of 128 dual-polarization channels each. The FWHM primary beam of ALMA is 17.3″ at our observing frequency, and we centred the observations at the position of the sub-mm sources in the 2013 February SCUBA-2 map. Importantly, the ALMA primary beam (FWHM) is larger than the SCUBA-2 beam (FWHM = 14.5″) and hence our observations are able to detect all SMGs that contribute significantly to the single-dish source.

The observations were conducted using 26 12-m antennae with a range of baselines from 20 to 1250 m, and a median baseline of 200 m. The array configuration yields a synthesized beam of $0.35'' \times 0.25''$ using Briggs weighting (robust parameter = 0.5), at a P.A. of ~ 55 deg for our observations. The observing strategy involved our 30 targets being

observed in two measurement sets, each containing 15 unique targets. Each measurement set contains seven or eight sub-blocks, consisting of 30 s observations of ten targets. In total each target was observed five times (total integration time of 150 s), with each repeat distributed randomly within these sub-blocks. Calibration observations were taken between each sub-block, with 90 s phase calibration observations (J 0217+014) and 30 s atmospheric calibrations. The absolute flux scale for each measurement set was derived from observations of J 0238+166, and either J 0423−0120 or J 0006−0623 was used for bandpass calibration.

The calibration and imaging of our science targets, and calibrators, was performed using the Common Astronomy Software Application (casa version 4.2.1).[1] To image each target we first Fourier transform the *uv*-data to create a "dirty" map, using Briggs weighting (robust parameter = 0.5). Following Hodge et al. (2013b) we determine the amount of cleaning required based on the presence of strong sources in the maps. We first estimate the RMS in each dirty map and clean the map to $3\,\sigma$. We then measure the RMS in the cleaned map and identify any sources above $5\,\sigma$. If a source is detected at $> 5\,\sigma$ then we repeat the cleaning process but place a tight clean box around each $> 5\,\sigma$ source and clean the dirty map to $1.5\,\sigma$. If a map does not contain any $> 5\,\sigma$ sources then the map cleaned to $3\,\sigma$ is considered the final map. The final maps have a range of 1-σ_{870} depths from 0.19–0.24 mJy beam^{-1} (median $\sigma_{870} = 0.21$ mJy beam^{-1}).

Long wavelength studies to resolve SMGs, either in the sub-mm, radio, or molecular line emission (i.e. ^{12}CO), suggest that we may risk resolving the SMGs in our high-resolution ALMA maps (see Chapman et al. 2004; Tacconi et al. 2006; Biggs & Ivison 2008; Younger et al. 2010; Engel et al. 2010; Bothwell et al. 2010; Simpson et al. 2015). Hence, to ensure that any extended flux from the SMGs is not resolved-out, and that we detect low surface-brightness, extended, sources, we repeated the imaging process using natural weighting, and applied a 0.6″ Gaussian taper in the *uv*-plane; using a Gaussian taper down-weights visibilities on long baselines, and yields a larger synthesized beam at the cost of increased noise. The maps were then imaged, and cleaned, using the same procedure described above to create a set of low-resolution "detection" maps. These low-resolution "detection" maps have a median rms of $\sigma_{870} = 0.26$ mJy beam^{-1} and a median synthesized beam of $0.8'' \times 0.65''$. Both the "detection" and higher resolution maps have

[1] We repeated the data reduction using the most recent version of casa (4.2.2) and found it had no effect on our final maps or source catalogue.

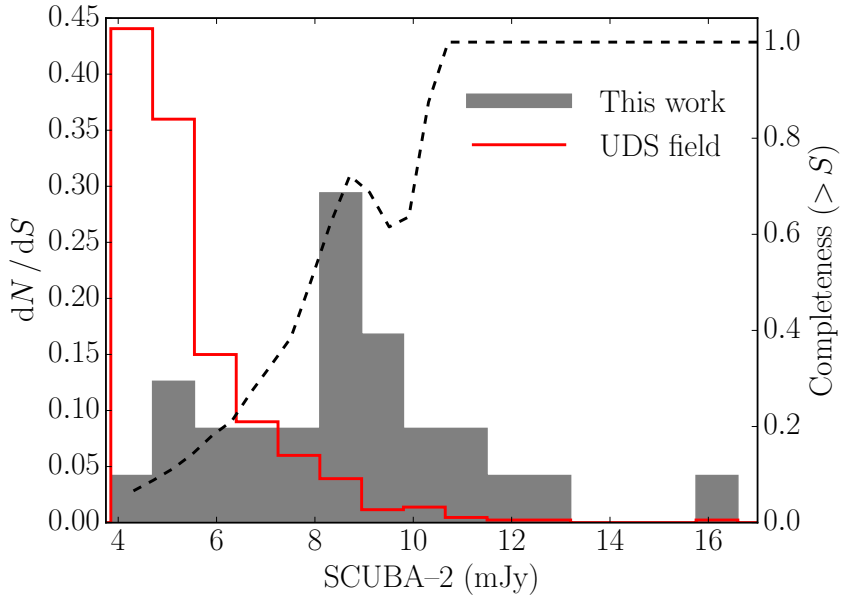

Figure 3.2: The 850-μm flux distribution of the single-dish-identified sub-mm sources targeted with ALMA (shaded histogram) compared to the flux distribution of sub-mm sources in the UDS field (open histogram). Both distributions are normalised by the total number of sources in each sample. A dashed line shows the completeness of our sample, relative to the latest single-dish catalogue (right-hand axis). While our observations do not represent a flux-limited sample in the new S2CLS map, we note that they are clearly weighted to the bright-end of the sub-mm population. The ALMA sample is >50 % complete for single-dish sources brighter than 8 mJy, and 100 % complete at > 11 mJy.

a size of $36'' \times 36''$, and a pixel scale of $0.04''$.

3.5 Source Extraction

To construct a source catalogue from our ALMA maps we use the source extraction package SExtractor (v2.8.6; Bertin & Arnouts 1996). We search the low-resolution $0.8''$ "detection" maps and identify all $> 3\,\sigma$ "peaks" in the non-primary-beam corrected maps. At the position of each $> 3\,\sigma$ detection we measure both the peak flux density and the integrated flux density in a $0.8''$ radius aperture. We also measure integrated flux densities in the higher resolution maps, at the position of all the detected sources in the $0.8''$ resolution maps. The fluxes measured in both sets of maps are primary-beam corrected using the model of the primary beam response output by CASA. The integrated flux densities of the calibrators, in the $0.8''$ radius aperture, are 4 % lower than the total flux densities, and we apply this correction to the integrated flux densities of the SMGs.

Although we extract sources above $3\,\sigma$, we expect a catalogue at this SNR-limit to contain some spurious detections. To estimate the level of contamination we invert the $0.8''$ resolution "detection" maps and repeat the source extraction. Within the FWHM primary beam the number of negative detections is lower than positive sources at $> 3.5\,\sigma$, but the contamination is 50 % at 3.5–4.0 σ. The number of sources detected across all 30 inverted maps is ≤ 1 at $> 4\,\sigma$ (corresponding to 2 % of our catalogue) and we therefore adopt this as the detection threshold for our source catalogue. Applying a $4\,\sigma$ cut to our source catalogue yields 52 SMGs, within the FWHM primary beam of the 30 ALMA maps. A search for sources outside the ALMA primary beam does not identify any statistically significant detections. We detect no SMGs in two ALMA maps (UDS 252 and 421) and a single SMG in a further ten maps. However, in most of the ALMA maps we detect multiple SMGs and 14, 2, and 2 of the maps contain 2, 3, or 4 SMGs, respectively.

We perform a number of tests to investigate whether the sources are resolved in the ALMA imaging. These are detailed in Simpson et al. (2015), but we give a summary here. First, we measure the ratio of the peak flux in the $0.3''$ and $0.8''$ resolution maps. The peak flux of the SMGs is lower in the $0.3''$ resolution maps, with a median ratio of $S^{0.3}_{\rm pk} \,/\, S^{0.8}_{\rm pk} = 0.65 \pm 0.02$, indicating that the sources are resolved in the higher resolution imaging. Secondly, we investigate the ratio of the integrated-to-peak flux density in the $0.8''$ maps; if the sources are unresolved the peak flux density will equal the integrated flux density. The median ratio of peak-to-total flux in the $0.8''$ imaging is 0.82 ± 0.03, again indicating that the sources are marginally resolved at $0.8''$ resolution. Finally, we fit point-source and extended models to the sub-mm emission at both resolutions and find that a point-source model results in significant residuals, and is insufficient to describe the emission from these sources. We also show that the sizes derived from the model fitting are consistent with the properties of the SMGs in the *uv*-plane (Simpson et al., 2015). We therefore take the flux density of each SMG to be the integrated flux measured in the $0.8''$ maps, unless it is lower than the peak flux density.

3.5.1 Completeness & Reliability

To test the completeness and reliability of our source extraction we create 2×10^4 simulated ALMA maps. However, to ensure that we have realistic noise properties we start with one pair (i.e. at $0.3''$ and $0.8''$ resolution) of our source-subtracted ALMA maps. To these we then add a model source at the same, but random, position in both resolution maps. The

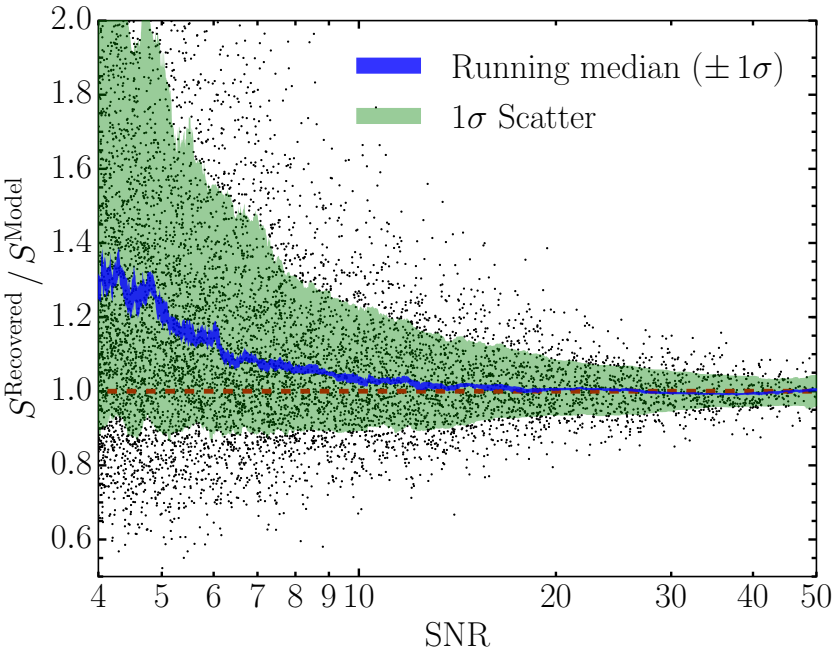

Figure 3.3: The results of simulations involving injecting fake sources into our source-subtracted ALMA maps to test the reliability of our source extraction procedure. Here we show the ratio of the recovered to input source flux density as a function of output source SNR, where the flux density of each model source is drawn from a steeply declining power-law distribution (with an index of -2). We show the running median and associated 1-σ bootstrap uncertainty, along with the 1-σ scatter. At our detection threshold of $4\,\sigma$ the flux of individual sources is on average boosted by 30 %, falling to $<10\%$ at $>6\,\sigma$ and $<1\%$ at $>15\,\sigma$.

flux densities of the model sources are drawn randomly from a steeply declining power-law distribution (with an index of -2; consistent with Karim et al. 2013), and have peak SNR values of 2–50 σ. The intrinsic FWHM size of each model source is drawn from a uniform distribution from 0–0.5″, and we convolve each model source with the ALMA synthesized beam. To simulate realistic noise, we add the convolved source to a random position in one pair (i.e. at 0.3″ and 0.8″ resolution) of our source-subtracted ALMA maps.

We perform the source extraction procedure described above on each simulated map and consider a source recovered if it is detected within 0.8″ of the injected position. The completeness is 93 % at $>4\,\sigma$, rising to about 100 % at $5.5\,\sigma$, consistent with the results of similar studies (e.g. Karim et al. 2013; Ono et al. 2014).

In Figure 3.3 we show the ratio of output-to-input flux density for our simulated sources. The flux densities of sources in a signal-to-noise limited catalogue are known to be boosted if the sources are drawn from a non-uniform flux distribution. The effect,

known as flux-boosting, arises due to more sources scattering upwards in flux density, because of random noise fluctuations, than scatter down as a result of the steeply rising source counts (see also Hogg & Turner 1998; Scott et al. 2002; Coppin et al. 2006; Weiß et al. 2009). On average a $4\,\sigma$ detection in our ALMA maps is boosted in flux by 30 %, with the boost falling to $<10\,\%$ at $>6\,\sigma$ and $<1\,\%$ at $>15\,\sigma$. This flux boosting is sensitive to the slope of the power-law that defines the flux distribution of the sources, and we note that varying the slope within the 1-σ uncertainties presented by Karim et al. (2013) changes the correction by $\pm\,10\%$ at a detection limit of $4\,\sigma$. We also measure the peak and integrated flux densities of the simulated sources at both resolutions and find that the flux boosting correction does not affect our conclusion that the SMGs in our sample are resolved in the high-resolution imaging.

To correct the measured flux densities of the 52 SMGs detected in our ALMA imaging for flux boosting we calculate the median ratio of output-to-input flux for the simulated sources in bins of $0.25\,\sigma$. We fit a spline to the median of each bin, and correct the flux densities in our catalogue based on the SNR of each source and the spline fit (Figure 3.3). Our final source catalogue thus consists of 52 SMGs, with a range of deboosted 870-μm flux densities of 1.3–12.9 mJy beam^{-1}, detected in 30 ALMA maps targeting the brighter single-dish sub-mm sources from the 0.8 deg^2 S2CLS UDS field.

3.5.2 Astrometry and Flux Recovery

We first compare the flux integrated across all sources in our maps to that seen by SCUBA-2, to test if our catalogue is missing large numbers of faint sources or if we are missing very extended sub-mm emission. We also use our catalogue to test the astrometry of the SCUBA-2 map. For each ALMA map we create a model of the detected SMGs using their primary-beam-corrected flux densities and convolve each ALMA model map with a model of the SCUBA-2 beam. The model beam is consistent with a beam created by stacking of bright SMGs in the UDS field, and with calibrator observations. These convolved ALMA maps do not take into account the contribution to the SCUBA-2 detection from sources either below the ALMA detection threshold, or outside the primary beam. It also neglects any effect due to the different bandwidth of the SCUBA-2 (35 GHz half-power bandwidth) and ALMA (2×4 GHz) observations. However, it provides a reasonable test of the effect of a $20\times$ improvement in resolution that our ALMA observations provide, relative to SCUBA-2.

ID	R.A. (J2000)	Dec. (J2000)	$\sigma_{\rm ALMA}$ (mJy beam^{-1})	$S_{\rm obs}^{\rm SCUBA\text{-}2}$ (mJy)	S/N$_{\rm peak}^{\rm ALMA}$	$S_{\rm obs}^{\rm ALMA}$ (mJy)	Deboosting^b correction	FWHM^c ($''$)
UDS156.0	2:18:24.14	−5:22:55.3	0.34	16.1±1.2	24.5	9.7±0.7	1.00	0.25±0.02
UDS156.1	2:18:24.24	−5:22:56.9	0.34	16.1±1.2	20.0	8.5±0.7	1.00	0.24±0.03
UDS286.0	2:17:25.73	−5:25:41.2	0.30	12.4±1.2	13.3	5.2±0.7	0.98	0.29±0.04
UDS286.1	2:17:25.63	−5:25:33.7	0.30	12.4±1.2	12.9	5.1±0.6	0.98	0.26±0.07
UDS286.2	2:17:25.80	−5:25:37.5	0.30	12.4±1.2	8.6	2.7±0.6	0.95	...
UDS286.3	2:17:25.52	−5:25:36.7	0.30	12.4±1.2	4.6	1.7±0.6	0.80	...
UDS57.0	2:19:21.14	−4:56:51.3	0.26	12.1±1.2	26.3	9.5±0.6	1.00	0.34±0.02
UDS57.1	2:19:20.88	−4:56:52.9	0.26	12.1±1.2	10.5	6.0±0.9	0.97	0.26±0.05
UDS57.2	2:19:21.41	−4:56:49.0	0.26	12.1±1.2	4.9	1.8±0.6	0.82	...
UDS57.3	2:19:21.39	−4:56:38.8	0.26	12.1±1.2	4.2	2.7±1.0	0.78	...
UDS269.0	2:17:30.44	−5:19:22.4	0.29	11.4±1.2	33.8	12.9±0.6	1.00	0.48±0.01
UDS269.1	2:17:30.25	−5:19:18.4	0.29	11.4±1.2	4.5	2.6±0.7	0.79	...
UDS361.0	2:16:47.92	−5:01:29.8	0.27	11.4±1.2	25.8	11.8±0.6	1.00	0.62±0.02
UDS361.1	2:16:47.73	−5:01:25.8	0.27	11.4±1.2	4.2	2.6±0.7	0.77	...
UDS306.0	2:17:17.07	−5:33:26.6	0.24	10.5±1.3	28.7	8.3±0.5	1.00	0.30±0.02
UDS306.1	2:17:17.16	−5:33:32.5	0.24	10.5±1.3	6.6	2.6±0.4	0.90	...
UDS306.2	2:17:16.81	−5:33:31.8	0.24	10.5±1.3	4.0	3.0±0.9	0.76	...
UDS204.0	2:18:03.01	−5:28:41.9	0.31	10.4±1.2	27.6	11.6±0.6	1.00	0.58±0.02
UDS204.1	2:18:03.01	−5:28:32.5	0.31	10.4±1.2	4.1	2.9±0.9	0.77	...
UDS110.0	2:18:48.24	−5:18:05.2	0.30	9.5±1.2	22.5	7.7±0.6	1.00	0.28±0.02
UDS110.1	2:18:48.76	−5:18:02.1	0.30	9.5±1.2	4.3	2.5±0.8	0.78	...
UDS160.0	2:18:23.73	−5:11:38.5	0.30	9.5±1.2	20.8	7.9±0.6	1.00	0.41±0.03
UDS48.0	2:19:24.57	−4:53:00.2	0.24	9.4±1.1	28.4	7.5±0.5	1.00	0.28±0.02
UDS48.1	2:19:24.62	−4:52:56.9	0.24	9.4±1.1	5.6	1.6±0.5	0.86	...
UDS202.0	2:18:05.65	−5:10:49.6	0.25	9.3±1.2	27.7	10.5±0.5	1.00	0.36±0.02
UDS202.1	2:18:05.05	−5:10:46.3	0.25	9.3±1.2	6.5	3.9±0.9	0.90	...
UDS79.0	2:19:09.94	−5:00:08.6	0.24	8.9±1.2	23.8	7.7±0.5	1.00	0.43±0.02
UDS109.0	2:18:50.07	−5:27:25.5	0.26	8.8±1.2	16.0	7.7±0.7	0.99	0.48±0.03
UDS109.1	2:18:50.30	−5:27:17.2	0.26	8.8±1.2	9.6	4.3±0.6	0.97	...
UDS218.0	2:17:54.80	−5:23:23.0	0.23	8.7±1.2	17.0	6.6±0.7	1.00	0.37±0.04
UDS377.0	2:16:41.11	−5:03:51.4	0.26	8.7±1.2	28.5	8.1±0.5	1.00	0.16±0.02

Table 3.2: ^{a} Source is not detected by SCUBA-2; ^{b} The intrinsic flux densities of the ALMA SMGs are obtained by multiplying $S_{\rm obs}^{\rm ALMA}$ with the deboosting correction; ^{c} Intrinsic source size, corrected for synthesised beam (see Simpson et al. 2015). Sizes are only measured for SMGs detected at $> 4\,\sigma$.

ID	R.A. (J2000)	Dec. (J2000)	$\sigma_{\rm ALMA}$ (mJy beam^{-1})	$S^{\rm SCUBA\text{-}2}_{\rm obs}$ (mJy)	S/N$^{\rm ALMA}_{\rm peak}$	$S^{\rm ALMA}_{\rm obs}$ (mJy)	Deboosting[b] correction	FWHM[c] ($''$)
UDS168.0	2:18:20.40	−5:31:43.2	0.30	8.7±1.2	17.3	6.7±0.6	1.00	0.42±0.03
UDS168.1	2:18:20.31	−5:31:41.7	0.30	8.7±1.2	7.0	3.0±0.6	0.92	...
UDS168.2	2:18:20.17	−5:31:38.6	0.30	8.7±1.2	4.2	2.0±0.7	0.78	...
UDS199.0	2:18:07.18	−4:44:13.8	0.26	8.6±1.2	13.4	4.3±0.6	0.98	0.28±0.06
UDS199.1	2:18:07.19	−4:44:10.9	0.26	8.6±1.2	8.7	2.5±0.5	0.96	...
UDS47.0	2:19:24.84	−5:09:20.7	0.31	8.4±1.2	21.7	8.7±0.6	1.00	0.28±0.03
UDS47.1	2:19:24.64	−5:09:16.3	0.31	8.4±1.2	4.0	2.7±0.8	0.76	...
UDS78.0	2:19:09.74	−5:15:30.6	0.25	7.6±1.2	22.9	8.2±0.5	1.00	0.35±0.03
UDS408.0	2:16:22.26	−5:11:07.8	0.28	7.6±1.2	17.9	9.1±0.7	1.00	0.66±0.04
UDS408.1	2:16:22.28	−5:11:11.9	0.28	7.6±1.2	4.5	2.7±0.9	0.79	...
UDS292.0	2:17:21.53	−5:19:07.8	0.28	6.7±1.2	9.7	4.2±0.8	0.97	...
UDS292.1	2:17:21.96	−5:19:09.8	0.28	6.7±1.2	6.9	3.9±0.8	0.91	...
UDS334.0	2:17:02.47	−4:57:20.0	0.27	6.7±1.2	7.5	3.8±0.8	0.93	...
UDS74.0	2:19:13.19	−4:47:08.0	0.24	6.0±1.2	15.2	4.6±0.5	0.98	0.38±0.04
UDS74.1	2:19:13.19	−4:47:05.0	0.24	6.0±1.2	4.8	1.8±0.5	0.81	...
UDS216.0	2:17:56.74	−4:52:38.9	0.28	5.2±1.2	14.5	5.3±0.5	0.98	0.70±0.04
UDS412.0	2:16:20.13	−5:17:26.2	0.25	5.1±1.2	17.2	6.6±0.7	1.00	0.30±0.07
UDS345.0	2:16:57.61	−5:20:38.6	0.24	4.8±1.2	5.3	2.3±0.7	0.84	...
UDS392.0[a]	2:16:33.29	−5:11:59.0	0.23	<4.1	13.3	3.8±0.5	0.98	<0.18
UDS298.0[a]	2:17:19.57	−5:09:41.2	0.24	<4.1	4.4	1.6±0.4	0.79	...
UDS298.1[a]	2:17:19.46	−5:09:33.2	0.24	<4.1	4.2	2.1±0.8	0.78	...

Table 3.2: continued

We measure a small, systematic, offset in both R.A. and Dec. of $-0.6^{+0.3}_{-0.3}''$ and $-1.1^{+0.2}_{-0.5}''$, respectively (in the sense ALMA−SCUBA-2), amounting to less than the fiducial pixel size of the SCUBA-2 map ($2''$). As expected, the separation between the SCUBA-2 source and the convolved ALMA map centroid is a function of the SNR of the single-dish detection (Figure 3.4). Importantly, the measured separations are consistent with the expected single-dish positional uncertainties: 70 % of the separations are smaller than the predicted 1-σ uncertainty on the single-dish position given by Equation B22 from Ivison et al. (2007). These offsets are between the SCUBA-2 and convolved ALMA peak positions, and hence only represent the expected search radius for a single, isolated, counterpart to the single-dish emission (i.e. an ALMA map with a single detected SMG). However, the median separation between the brightest SMG in each map and the SCUBA-2 detection is $1.7^{+0.6}_{-0.2}''$, which is consistent with (although with a marginally increased scatter) the median separation of the convolved ALMA map centroids and the SCUBA-2 positions

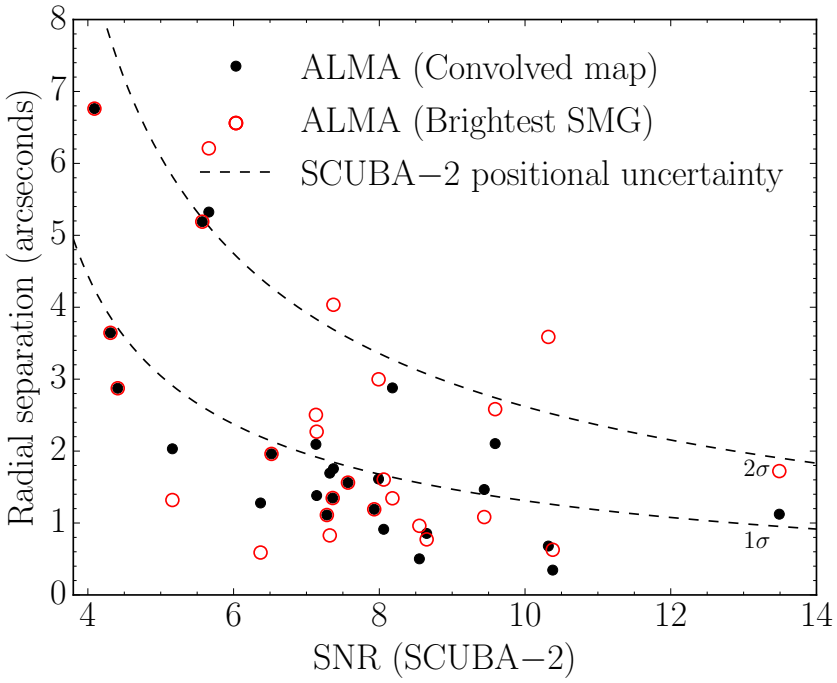

Figure 3.4: We convolve the SMGs detected in each ALMA map with the SCUBA-2 beam and measure the positional offset between the flux centroid in the convolved map and the original single-dish-detected sub-millimetre source. The offset between the individual ALMA SMGs in each map and the single-dish source is also shown. The offsets between the ALMA convolved sources and the SCUBA-2 sources are consistent with the predicted uncertainty on the SCUBA-2 positions (see Ivison et al. 2007).

($1.6^{+0.2}_{-0.2}$″). These results indicate that the offset to the brightest SMG is consistent with the SNR-based search radius used to identify counterparts to a sub-mm source, prior to interferometric observations in the sub-mm (e.g. Ivison et al. 2007).

To confirm the relative flux scales, and also to test that the observations have not resolved-out flux or missed large numbers of faint SMGs, we compare the peak flux density of the convolved ALMA maps to the SCUBA-2 detections (see Figure 3.5). The median ratio of the ALMA-to-SCUBA-2 flux is $S^{\rm ALMA}\,/\,S^{\rm SCUBA\text{-}2} = 0.99^{+0.10}_{-0.04}$, including upper limits for a source at the edge of the primary beam in the ALMA "blank" maps. The result indicates good agreement between flux scales, and suggests that all of the SMGs that contribute significantly to the single-dish flux density are recovered, although we caution that the systematic uncertainties on the absolute flux calibration of both SCUBA-2 and ALMA are expected to be 5–10 % (Dempsey et al., 2013).

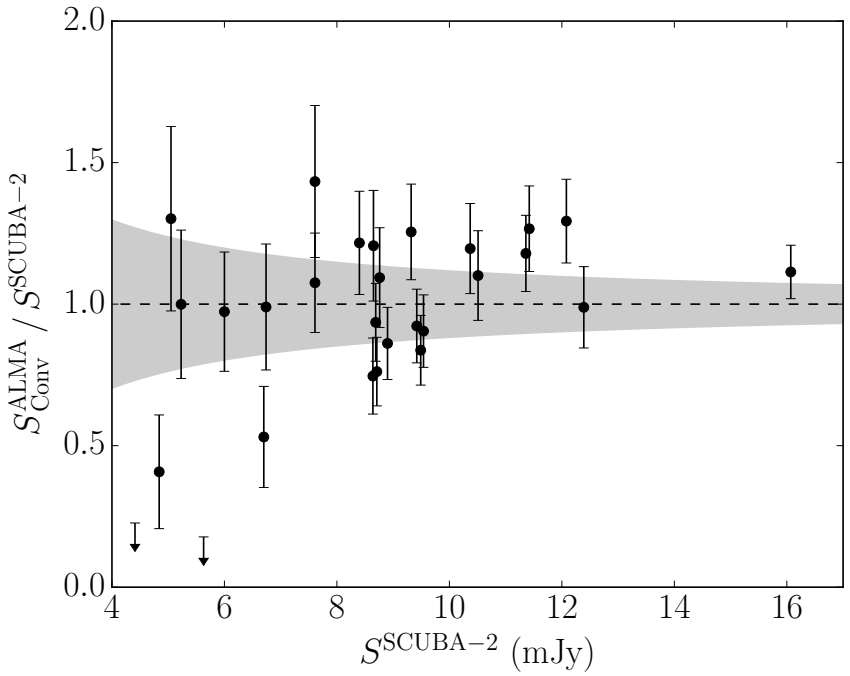

Figure 3.5: A comparison of the peak sub-mm emission from the SMGs detected in each ALMA map, convolved with the SCUBA-2 beam, and the SCUBA-2 flux density. The typical uncertainty on the SCUBA-2 flux densities is represented by the grey shaded region. We find good agreement between the SCUBA-2 and ALMA flux densities, with a median ratio of $S^{\rm ALMA}\,/\,S^{\rm SCUBA\text{-}2} = 0.99^{+0.10}_{-0.04}$. We do not detect any SMGs in two ALMA maps, but note that in both cases the SCUBA-2 single dish source is detected in *Herschel* / SPIRE imaging at 250, 350, and 500 μm indicating that these sources are real but potentially faint or multiple SMGs.

3.6 Discussion

3.6.1 Multiplicity

Previous interferometric follow-up studies of sub-mm sources have hinted that a fraction of the sources may be comprised of multiple individual SMGs, which appear blended in the $\gtrsim 15''$ resolution single-dish imaging (e.g. Tacconi et al. 2006; Ivison et al. 2007; Wang et al. 2011; Barger et al. 2012; Smolčić et al. 2012; Hodge et al. 2013b). Such an effect is expected, given the low resolution of single-dish sub-mm maps, but prior to ALMA the effect has been challenging to quantify due to the small sample sizes, mixed wavelength of observations and the limited sensitivity of follow-up studies.

It is evident from the ALMA maps presented in Figure 3.1 that a significant proportion of the single-dish sub-mm sources in our sample are comprised of multiple, $S_{870} > 1$ mJy, SMGs. Indeed, 17 of the 28 SCUBA-2 detected sources fragment into > 1 SMGs, a

multiple fraction of 61^{+19}_{-15} % if we consider any secondary component, and assuming poisson uncertainties. In particular we highlight UDS 57, 168, 286 and 306 where the single-dish sub-mm sources are a blend of three-or-four SMGs. Hence, each of these maps contains multiple ULIRGs ($S_{870} \gtrsim 1$ mJy) with a star formation rate [2] of $\gtrsim 150\,\mathrm{M_\odot\,yr^{-1}}$.

Defining multiplicity by the number of companions is clearly dependent on the sensitivity limit for these secondary components. However, adopting a limit of $S_{870} > 1$ mJy measures the number of ULIRGs that contribute to each single-dish sub-mm source, is reasonably well-matched to the depth of our maps and is sufficiently bright that we would expect to detect < 1 SMG by chance in our 30 survey fields based on the blank field counts (see Figure 3.9). As we show in § 3.6.4 the number density of these secondary SMGs appears to be higher than that expected in random fields or from simple selection biases, indicating that a fraction of these multiples are likely to be physically associated.

It is interesting to note that two of our ALMA maps are blank, i.e. we do not detect any SMGs at $> 4\,\sigma$. Although the sub-mm sources targeted in these maps (UDS 252 and 421) are two of the fainter SCUBA-2 sources in our sample (4.4 mJy and 5.6 mJy) they are detected in both the 2013 February and 2014 August SCUBA-2 maps, as well as in 250, 350, and 500 μm *Herschel* / SPIRE imaging (50 mJy and 26 mJy at 250 μm, respectively), indicating that they are not simply spurious SCUBA-2 detections. A simple explanation (given that 17 of our ALMA maps contain multiple SMGs) is that in these maps the single-dish source is comprised of multiple SMGs below our detection threshold. In this case, two-or-three SMGs marginally below the detection threshold at the edge of the FWHM primary beam ($S_{870} < 2$ mJy) would be sufficient to explain the missing flux in these maps, and we note that this would increase the fraction of multiples in our sample to about 70 %.

While the presence of a ULIRG companion to the majority of the brightest SMGs is clearly significant, it is important to investigate the relative brightness of the secondary components, and the contribution they make to the flux density of the original SCUBA-2 detections. In Figure 3.6 we show the fraction of the integrated flux density in an ALMA map that is emitted by each SMG. We stress that the integrated flux density is the sum of the primary beam corrected flux densities of the SMGs in each ALMA map, and that this calculation does not take into account the effect of the SCUBA-2 beam. Where secondary components (i.e. fainter SMGs) are detected in an ALMA map, the ratio between brightest

[2] Assuming a typical conversion between 870-μm flux density and FIR-luminosity (e.g. Swinbank et al. 2014), and a Salpeter Initial Mass Function

and secondary component is on average 25^{+1}_{-5} %, falling to 16 % and 9 % for the third and fourth components, respectively.

Next, we investigate the ratio of the brightest component in each ALMA map to the original SCUBA-2 detection. We measure a median ratio of $S^{\rm ALMA}_{\rm Brightest}$ / $S^{\rm SCUBA\text{-}2} = 0.80^{+0.06}_{-0.02}$, and do not find a significant trend in this ratio with single-dish flux (Figure 3.7). This result has important implications for studies that identify a single counterpart to the sub-mm emission from a single-dish source using emission at different wavelengths (e.g. 1.4 GHz); it suggests that even if the probabilistic identification is correct (see Hodge et al. 2013b) the true flux density of the SMG is on average 20 % lower than the single-dish flux. Within the associated errors this is broadly consistent with the results of Cowley et al. (2015), who create simulated single-dish and interferometric follow-up observations using the semi-analytic model GALFORM.

We now compare our results to samples of interferometrically identified SMGs in the literature. Barger et al. (2012) present 860-μm SMA observations for a sample of 16 850-μm SCUBA-detected sources and find that three of the sources are comprised of multiple SMGs. As stated by these authors, the number of sources in the sample is small, and as the SMA maps reach a depth $\sigma_{860} \sim 0.7$–1 mJy, they are only sensitive to secondary SMGs brighter than 3–4 mJy (at the phase centre). Similarly, Smolčić et al. (2012) found that six out of 28 LABOCA sources (870 μm selected) fragment into multiple components in 1.3-mm observations with the PdBI; in nine of the PdBI maps no SMGs are detected. While this study again hints at multiplicity, it is more challenging to interpret as the single-dish selection and interferometric follow-up observations were conducted at different wavelengths.

Recently, Hodge et al. (2013b) presented the results of an 870-μm ALMA survey of 122 single-dish sources detected in the 870-μm LABOCA survey of the Extended *Chandra* Deep Field South (LESS). The reader should note that the single-dish sub-mm sources studied by Hodge et al. (2013b) are on average 30 % fainter than the sources presented here. From the 88 best quality ALESS maps, Hodge et al. (2013b) extract a sample of 117 SMGs. In 32 of the maps the single-dish detected sub-mm source fragments into multiple SMGs. While this indicates that the fraction of sub-mm sources that are blends of multiple SMGs is 35 %, there are two caveats. First, 17 of the ALMA maps are blank, with the most likely reason being that the sub-mm source has fragmented into > 2 SMGs below the detection threshold (Hodge et al., 2013b). Secondly, Hodge et al. (2013b) show that

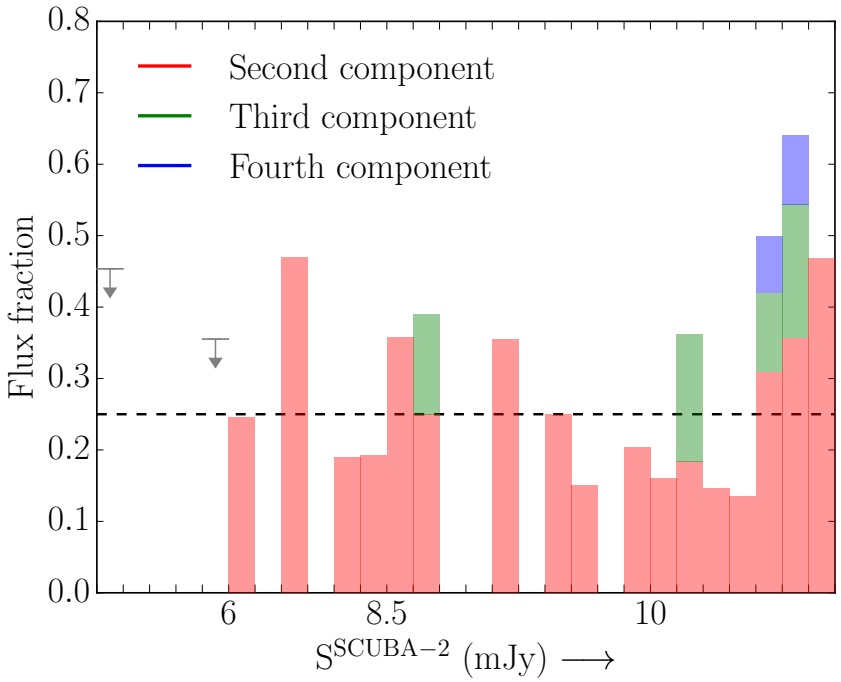

Figure 3.6: In 61^{+19}_{-15} % of our ALMA maps the single-dish source targeted comprises of a blend of ≥2 SMGs. Here we show the fraction of the total integrated flux in a map that is emitted by each individual SMG. Each interval on the abscissa represents an individual ALMA map, and the maps are ordered by increasing single dish flux density. Where an ALMA map contains >1 SMG the second component contributes on average 25^{+1}_{-5} % of the total flux (dashed line), with the third and fourth components contributing 16 % and 9 %, respectively. The two ALMA blank maps in our sample are represented by upper limits, placed at the maximum that a $4\,\sigma$ source at the edge of the ALMA primary beam could contribute to the SCUBA-2 flux density.

to recover the LABOCA flux density in the ALMA maps it is necessary to account for flux from sources below their detection threshold, indicating that a significant proportion of their ALMA maps contain faint 1–2 mJy SMGs, even though sources in this flux range should be rare in random patches of sky. Support for this conclusion comes from a stacking analysis of individually undetected IRAC galaxies in the ALMA maps, which shows that these galaxies are brighter in the sub-mm than expected for typical IRAC galaxies (Decarli et al., 2014).

To perform an accurate comparison between our sample and ALESS we remove the SMGs from our sample that lie below the ALESS detection threshold and repeat the multiplicity calculation. In total 13 SMGs are fainter than the ALESS threshold and are removed from our sample, resulting in an additional "blank" ALMA map (3 / 30). Of the 17 maps in our sample that contain multiple SMGs, seven would have been classed as single

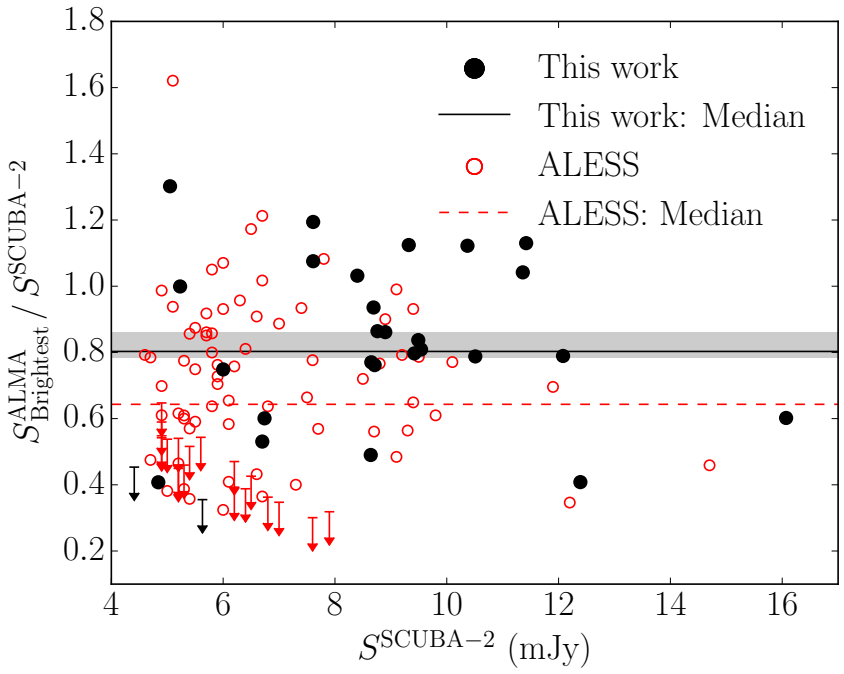

Figure 3.7: The fraction of the SCUBA-2 flux density emitted by the brightest SMG in each ALMA map, as a function of single-dish flux density. The median ratio for our sample is $S^{\rm ALMA}_{\rm Brightest} \,/\, S^{\rm SCUBA} = 0.80^{+0.06}_{-0.02}$ and we do not see a significant trend with single-dish flux density. Upper limits correspond to "blank" ALMA maps, and are the maximum contribution from a $< 4\,\sigma$ source located at the edge of the ALMA primary beam. For comparison we show the results from the ALESS survey (Hodge et al., 2013b), which found that 88 ALMA-identified LABOCA sub-mm sources have a median $S_{\rm Brightest} \,/\, S^{\rm LABOCA} = 0.64^{+0.06}_{-0.03}$. The lower fraction of flux density in the brightest component for the ALESS sample may be due to the combination of multiplicity and the larger beam size of LABOCA (19.2″), relative to SCUBA-2 (14.5″).

identifications in the ALESS survey and ten as multiples, yielding a multiplicity fraction of 37^{+15}_{-11} %. Hence, the fraction of single-dish sources classed as single identifications in our survey and ALESS are in close agreement.

To investigate any further differences between the samples we next compare the fraction of the single-dish flux density in the brightest component in each ALMA map. The median ratio of the observed flux densities in the ALESS sample is $S^{\rm ALMA}_{\rm Brightest} \,/\, S^{\rm LABOCA} = 0.64^{+0.06}_{-0.03}$, which is lower than our sample at a $2\,\sigma$ significance level ($S^{\rm ALMA}_{\rm Brightest} \,/\, S^{\rm SCUBA\text{-}2} = 0.80^{+0.06}_{-0.02}$). However, the larger beam of LABOCA (FWHM $= 19.2''$) compared to SCUBA-2 (FWHM $= 14.5''$) means that secondary components contribute more to the single-dish detection. To test the effect of the beam size on the single-dish flux density we convolve a model of the SMGs in each ALMA map with the SCUBA-2 and LABOCA beams. We find that on average the LABOCA flux density is 2 % higher than the SCUBA-2 detection, but stress that this is heavily weighted by the maps containing a single SMG (where the flux densities are identical) and that individual sources can be up to 13 % brighter in the LABOCA observations. While this is clearly a small effect it does not account for sources fainter than the ALMA detection threshold or outside the ALMA FWHM primary beam. Given all of the results above, we conclude that the sample presented here and by Hodge et al. (2013b) are broadly consistent.

3.6.2 Number Counts

The number counts of SMGs provide one of the most basic "observables", which galaxy formation models of the far-infrared Universe must match. Recently, it has been suggested that the number of the brightest sub-mm sources ($S_{870} \gtrsim 9\,$mJy) may have been overestimated in single-dish studies (e.g. Karim et al. 2013) due to multiplicity. The single-dish sources in our sample are selected from the central $0.78\,{\rm deg}^2$ of the S2CLS wide-field map of the UDS and have a median flux density of $(8.7 \pm 0.4)\,$mJy. The sample is thus ideally suited to investigate the effects of multiplicity, and measure the intrinsic form of the bright-end of the number counts.

As discussed earlier our ALMA sample is increasingly incomplete for faint SCUBA-2 sources and so we choose to construct the number counts from our ALMA source catalogue at $S_{870} > 7.5\,$mJy.[3] To account for the incompleteness in our sample we first construct

[3]The sensitivity of our ALMA maps drops to 50 % at the FWHM of the primary beam. However, the SMGs used to construct the number counts are detected at $> 15\,\sigma$, and all of the sources would have been

the counts from the ALMA observations assuming the selection is complete. For each ALMA-detected SMG we then correct the area surveyed based on the fraction of sources targeted in the flux bin of the parent single-dish sub-mm source.

In Figures 3.8 & 3.9 we show the differential and cumulative counts constructed from both our ALMA observations, and the parent SCUBA-2 sample (the uncertainty on the number counts are derived from Poisson statistics; see Gehrels 1986). As expected the ALMA number counts show a decrease relative to the single-dish counts; the intrinsic cumulative counts are 20 % lower than the single-dish SCUBA-2 counts at $S_{870} > 7.5$ mJy, and 60 % lower at $S_{870} > 12$ mJy.

Before discussing the shape and parametrization of the number counts, we first note that there is a difference between the bright-end of the number counts presented here, and the ALMA 870-μm counts derived from the ALESS survey (Karim et al., 2013). Our ALMA observations targeted eleven single-dish sources with flux densities > 9 mJy and detect seven SMGs above this threshold. In contrast, Karim et al. (2013) target 12 single-dish sources brighter than 9 mJy, but detect only one ALMA source above this threshold. The difference between these results may be due to multiplicity and the difference in the beam sizes of LABOCA and SCUBA-2 (see § 3.6.1). However, it is important to note that the samples are small and are still dominated by small number statistics.

We now combine our sample with the ALESS survey (Karim et al., 2013), with the aim of providing a single parametrization of the intrinsic sub-mm number counts (Figure 3.9). To extend the range of the number counts to lower flux densities we also include two studies that have used serendipitous detections of sources in deep targeted ALMA observations to measure the number counts of faint SMGs at 1.2 and 1.3 mm from Ono et al. (2014) & Hatsukade et al. (2013), respectively. Although such studies are sensitive to clustering between the sources detected serendipitously and the original targets (which were not selected to be sub-mm sources), they do provide a crude estimate of the likely number counts of faint sources. We convert these counts to 870 μm using the composite SMG spectral energy distribution (SED) from the ALESS survey (see Swinbank et al. 2014), redshifted to $z = 2.5$ (flux conversion factors are 2.4 $\times$ and 3.1 $\times$, at 1.2 mm and 1.3 mm, respectively). Although these converted faint number counts are sensitive to the shape of the adopted SED, they do appear to be in reasonable agreement with the cumulative

detected even at the edge of the primary beam.

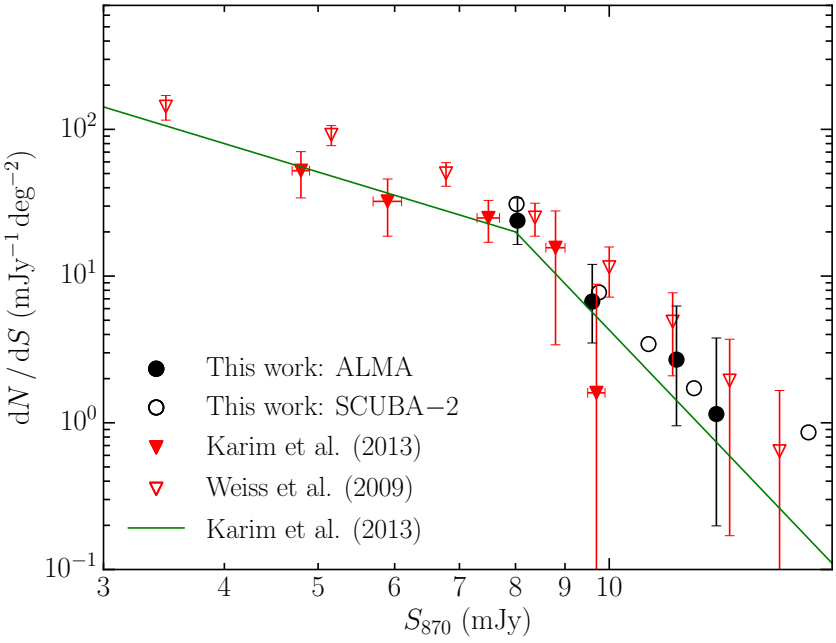

Figure 3.8: The 870 μm differential counts constructed from our ALMA observations, compared to the parent single-dish SCUBA-2 sample. We also show the counts derived from the LABOCA, single-dish survey LESS (Weiß et al. 2009), and the counts from the follow-up ALMA survey ALESS (Karim et al. 2013). The counts derived from our survey are in agreement with the ALESS sample at $S_{870} \lesssim 9$ mJy and are well-described by a double-power law (see § 3.6.2). We detect seven SMGs with $S_{870} > 9$ mJy, compared to one SMG in ALESS, and do not see a sharp cut-off in the counts, relative to the single-dish observations.

counts from both this study, and ALESS (see Figure 3.9).

Since the number counts decline steeply at the bright-end we choose to model the counts with a double-power law of the form

$$N(>S) = \frac{N_0}{S_0}\left[\left(\frac{S}{S_0}\right)^{\alpha} + \left(\frac{S}{S_0}\right)^{\beta}\right]^{-1}, \tag{3.6.1}$$

where N_0 , S_0, α and β describe the normalisation, break, and slope of the power laws, respectively. The best-fit parameters of the model are $N_0 = 390^{+110}_{-80}$ deg^{-2}, $S_0 = 8.4^{+0.6}_{-0.6}$ mJy, $\alpha = 1.9^{+0.2}_{-0.2}$ and $\beta = 10.5^{+3.0}_{-3.2}$, and as can be seen in Figure 3.9 the parametrization provides an adequate representation of the cumulative counts. However we caution that the number of sources at both the bright and faint end of the counts remains low (26 and 20 at $S_{870} < 2$ mJy and $S_{870} > 8$ mJy, respectively) and this is reflected in the uncertainties on the best-fit parameters.

When constructing the observed sub-mm number counts we have included three SMGs from our sample that we identify as potential gravitationally lensed sources (UDS 109.0,

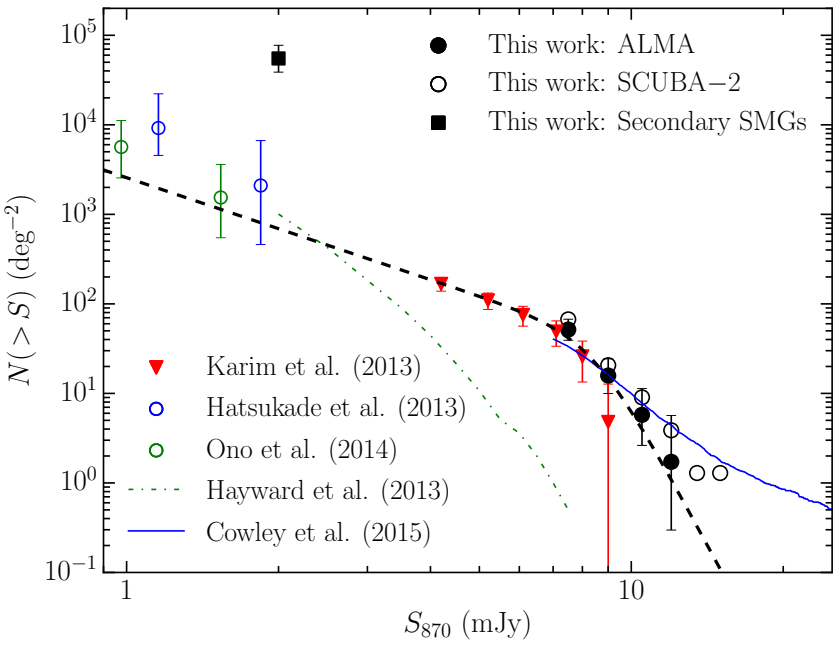

Figure 3.9: Similar to Figure 3.8, but instead showing the cumulative counts from the 870 μm surveys. The effect of multiplicity is more obvious in the cumulative counts and at $S_{870} > 7.5$ mJy the intrinsic counts from our ALMA survey are 20 % lower than the counts from the parent single-dish sample, falling to 60 % lower at $S_{870} > 12$ mJy. The cumulative counts from ALMA serendipitous detections at 1–1.3 mm, converted to 870 μm, are broadly in agreement with the sample presented here and from ALESS. We plot the best-fit double power-law function to all of the ALMA samples, which has a break at a characteristic flux density of $8.5^{+0.6}_{-0.6}$ mJy (dashed line). The theoretical predictions from Cowley et al. (2015) appear well-matched to the counts presented here. However, the counts presented by Hayward et al. (2013a) are least an order of magnitude lower than the observed counts at $S_{870} > 5$ mJy, which is attributed to the absence of "starbursts" in the model. The number density of secondary sources in ALMA maps with a primary SMG > 8 mJy (black square) is a factor of 80 ± 30 higher than the blank-field counts, which is inconsistent with these SMGs representing a line-of-sight population, and suggests that a significant fraction of these SMGs are physically associated.

UDS 160.0, and UDS 269.0). All three of these SMGs appear to be close to, but spatially offset from, galaxies at $z \lesssim 1$ (see Simpson et al. 2015). Although there are no indications that these SMGs are strongly lensed (i.e. no multiple images), even a modest magnification of $\mu \geq 1.7$ is sufficient to push the intrinsic flux density of these sources below our threshold for constructing the number counts. If we remove these three SMGs then the cumulative number counts decrease by 18 % at $S_{870} > 7.5\,\mathrm{mJy}$ and the parameters of the best-fit double power-law, for all of the ALMA samples, change by less than their associated 1-σ uncertainties.

It has been suggested that an absence of bright SMGs ($S_{870} \gtrsim 9\,\mathrm{mJy}$) may indicate a physical limit to the intense starbursts that are occurring in these sources (see Karim et al. 2013). We detect bright SMGs in our survey and do not find evidence for a sharp cut-off in the counts. However, we do find that number counts decline strongly towards the bright-end with a distinct break at a flux density of $S_0 = 8.4^{+0.6}_{-0.6}\,\mathrm{mJy}$, which may suggest a typical threshold to the SFR. If we adopt the relationship between S_{870} and L_{FIR} for the ALESS SMGs (Swinbank et al., 2014), and the SMGs presented here (Ma. et al. in prep.), then this break corresponds to a luminosity of $\sim 6 \times 10^{12}\,\mathrm{L}_{\odot}$, or a SFR of $\sim 10^3\,\mathrm{M}_{\odot}\mathrm{yr}^{-1}$ (for a Salpeter IMF). The SMGs in our sample are resolved in our ALMA imaging, and the brightest SMGs have a median half-light radius of $1.2 \pm 0.1\,\mathrm{kpc}$ (Simpson et al., 2015). Given the sizes of the SMGs, the break in the number counts corresponds to a typical threshold to the star formation rate density in these starbursts of $\sim 100\,\mathrm{M}_{\odot}\,\mathrm{yr}^{-1}\,\mathrm{kpc}^{-2}$. The star formation rate density of a typical SMG at the break in the number counts is an order of magnitude lower than the expected Eddington limit for these sources (see Andrews & Thompson 2011; Simpson et al. 2015). However, we stress that the star formation rates are integrated across the whole star-forming region. If the star formation in these SMGs is occurring in individual "clumps" (e.g. Swinbank et al. 2011; Danielson et al. 2011, 2013 then these individual regions may be Eddington-limited, while the overall star-forming region appears sub-Eddington.

3.6.3 Comparison to galaxy formation models

We now compare our results to recent theoretical predictions for sub-mm number counts, which attempt to simulate the effects of blending in single-dish surveys. Hayward et al. (2013a) construct single-dish and intrinsic sub-mm number counts, based on a hybrid numerical model. By construction, the single-dish counts from the model are in broad

agreement with single-dish observations at $S_{870} \sim 5\,\mathrm{mJy}$ but, as shown in Figure 3.9, the intrinsic cumulative number counts under-predict the observed counts by over an order of magnitude at $S_{870} > 5\,\mathrm{mJy}$. As stated by Hayward et al. (2013a) the deficit is likely due to the absence of merger-driven "starbursts" in the model that act to elevate the star formation in these systems. We note that a previous model that includes "starbursts" is in closer agreement with the observed counts (see Hayward et al. 2013b). However, that model has a limited treatment of source blending and as shown in Hayward et al. (2013a) multiplicity has an order of magnitude effect on their predictions, which is not seen in our data.

In Figure 3.9 we also show the cumulative sub-mm counts from the semi-analytic model GALFORM (Lacey et al. in prep.) constructed using the simulations of single-dish and ALMA follow-up observations presented by Cowley et al. (2015). The current version of the model adopts an Initial Mass Function (IMF) in starbursts that is top-heavy, but is closer to Salpeter and less extreme than the IMF adopted in previous versions of the model (e.g. Baugh et al. 2005). In this new model the intense starbursts in SMGs are predominantly triggered by instabilities in gas-rich discs. To ensure a fair comparison to the counts presented here, we repeat the simulations presented in Cowley et al. (2015) but adopt the SCUBA-2 beam size and select sources with a flux density $\geq 7.5\,\mathrm{mJy}$. As can be seen in Figure 3.9 the predicted follow-up counts from the model are in broad agreement with the counts presented here.

3.6.4 Origin of Multiplicity

A number of studies have investigated the environments of SMGs and concluded that the population are strongly clustered (Blain et al., 2004; Scott et al., 2006; Weiß et al., 2009; Hickox et al., 2012), although studies have questioned the robustness of these results (Adelberger, 2005; Williams et al., 2011). Similarly, a small number of single-dish sources have been *resolved* into pairs of SMGs that have been spectroscopically confirmed to lie at the same redshift (e.g. Tacconi et al. 2006; Hodge et al. 2013a; Ivison et al. 2013). Such small scale over-densities of SMGs are unsurprising if these sources represent a population of massive galaxies, potentially undergoing merger induced star formation. Source multiplicity in SMGs thus offers one route to investigate the environments of these sources on scales up to 140 kpc (the FWHM primary beam of ALMA at $z \sim 2.5$).

The origin of multiplicity in SMGs can be conclusively tested through spectroscopic

follow-up of the SMGs detected in each ALMA map. However, as we do not currently have spectroscopic redshifts for any of the SMGs in our sample we instead use the number density of sources fainter than the primary SMG in each ALMA map to assess their likely association. If these secondary SMGs are simply line-of-sight projections, then, in the absence of any bias, the number density of sources should be equivalent to the background counts. However, we must take into account the effect of blending on our initial sample selection, which will enhance the number of SMGs with companions in our target sample. Hence in the following analysis we *only* consider ALMA maps in our sample that contain an SMG brighter than 8 mJy. In doing so we ensure that we only consider the maps that would have been observed, regardless of whether blending with the detected companion boosts the flux density of the single-dish source into our sample.

There are eleven ALMA maps in our sample that contain an SMG brighter than 8 mJy, and we detect a total of twelve secondary SMGs in these maps. To derive the surface density we must adopt a flux limit for the sample. As the noise in the primary-beam corrected maps increases with distance from the phase centre, and to ensure that we have uniform coverage, we first remove one secondary SMG with $S_{870} < 2$ mJy that would not have been detected at the edge of the ALMA primary beam. We calculate the area surveyed by the ALMA primary beam in these maps and measure that the cumulative number density of secondary SMGs brighter than 2 mJy is $(5.5^{+2.2}_{-1.6}) \times 10^4\,\mathrm{deg}^{-2}$ and we show this point in on Figure 3.9. In these eleven maps we expect to detect 0.14 SMGs at $S_{870} > 2$ mJy (adopting the blank field counts in Figure 3.9) but identify eleven SMGs. Therefore, the number density of the secondary sources in our maps is a factor of 80 ± 30 times higher than the blank field number counts, indicating that the brightest SMGs appear to reside in over-dense regions.

There is a small bias towards multiplicity in the selection of our single-dish sources that arises from observations of > 8 mJy SMGs that, due to random noise fluctuations, scatter to lower values in the SCUBA-2 map. In such a scenario, an 8 mJy SMG is more likely to scatter back into our catalogue if it has a companion SMG that boosts the single-dish flux density above our selection threshold. To determine the magnitude of this effect we use a simulation of single-dish observations of SMGs, presented by Cowley et al. (2015). To remove any intrinsic clustering in the simulation we randomise the positions of all of the input SMGs and then apply the sample selection described above. The resulting cumulative number density of secondary SMGs is a factor of 1.75 ± 0.75 times higher than

the blank-field number counts. While this analysis confirms that our sample has a small bias due to noise, which increases the number of secondary SMGs, it is clearly insufficient to explain the magnitude of the observed offset.

Clearly, to conclusively confirm these physical associations requires spectroscopic redshifts. We do not have spectroscopic redshifts for any of the SMGs in our sample, and as shown by Simpson et al. (2014) the photometric redshifts of SMGs have considerable uncertainties, ruling out the ability to perform this test with photometric redshifts alone. Moreover, only 35 % of the secondary SMGs we have considered have a K-band counterpart ($5\,\sigma$ detection limit 25.0 mag; see Ma et al. in prep.). The only way to conclusively test if these sources are associated is through atomic or molecular emission spectroscopy (i.e. [CII], ^{12}CO) with sub-mm interferometry (see Weiß et al. 2013).

3.7 Conclusion

We have presented ALMA observations of 30 sub-mm bright single-dish sources in the UDS field. These sources were selected from 0.8 deg^2 14.5″ resolution observations with SCUBA-2 at the JCMT as part of the SCUBA-2 Cosmology Legacy Survey. The main conclusions from our study are:

- The 30 ALMA maps in our sample have a resolution of $0.35'' \times 0.25''$, and median noise of 0.21 mJy beam^{-1}. Using tapered versions of these maps (median resolution $0.8'' \times 0.65''$, $\sigma_{870} = 0.26$ mJy beam^{-1}) as detection images, we detect 52 SMGs at $> 4\,\sigma$.

- A comparison of the peak-to-integrated flux of the SMGs demonstrates that the sources are resolved in both the "detection" and "high-resolution" maps. As shown in Simpson et al. (2015) the brightest SMGs in our sample have a median intrinsic size of FWHM $= 0.30 \pm 0.04''$, physical size of (2.4 ± 0.2) kpc, and we do not find any evolution in the size of the rest-frame far-infrared emission with either redshift or 870 μm flux density.

- We find that 61^{+19}_{-15} % of the single-dish sub-mm sources in our sample are comprised of a blend of ≥ 2 SMGs brighter than $\gtrsim 1$ mJy (i.e. multiple ULIRGs). On average the brightest SMG in each ALMA map comprises 80^{+6}_{-2} % of the single-dish flux density, and where a secondary SMG is detected it contributes 25^{+1}_{-5} % to the total

integrated flux density in the ALMA map. In two of our maps we do not detect any SMGs, and in ten maps we detect a single SMG. The remaining maps contain multiple SMGs, with 2, 3, or 4 SMGs detected in 14, 2 and 2 maps, respectively.

- We compare our observations to the Cycle-0 ALMA survey of single-dish sources, ALESS. After accounting for the relative depths of both surveys we show that the fraction of sub-mm sources that are comprised of a blend of multiple individual SMGs is consistent, at $\gtrsim 35\,\%$. However, in ALESS the brightest SMG in each ALMA map contains on average $65\,\%$ of the single-dish flux density, compared to $80\,\%$ for our sample. We show that this may be driven in part by the difference between the beam size of the initial single-dish selection for ALESS (LABOCA; $19.2''$) and our survey (SCUBA-2; $14.5''$).

- We construct the differential and cumulative sub-mm counts of SMGs from our ALMA observations. The multiplicity bias in single-dish sources means that the intrinsic cumulative number counts are $20\,\%$ lower at $S_{870} > 7.5\,\mathrm{mJy}$ than the single-dish SCUBA-2 survey, and $60\,\%$ lower at $S_{870} > 12\,\mathrm{mJy}$. We compare the counts derived from our survey to the theoretical models and demonstrate that the counts from the most recent GALFORM semi-analytic model (Cowley et al., 2015) are consistent with our results, at the flux density limit of our survey.

- The number density of secondary SMGs ($S_{870} > 2\,\mathrm{mJy}$) around the brightest sources in our sample is 80 ± 30 times higher than expected from blank-field number counts. We caution that this result is still dominated by small number statistics, but we show that even after accounting for selection biases a significant fraction of these SMGs are likely to be physically associated. This suggests that the brightest SMGs reside in over-dense regions of SMGs

Chapter 4

The SCUBA-2 Cosmology Legacy Survey: ALMA Resolves the Rest-frame Far-infrared Emission of Sub-millimetre Galaxies

4.1 Motivation

Identifying the progenitors of local elliptical galaxies represents one of the key stages in our understanding of galaxy formation. In the previous chapter I discussed the observational evidence that elliptical galaxies formed the majority of their stellar mass in a relatively short-lived phase, early in the history of the Universe ($z \gtrsim 2$). Recently, near-IR imaging has been used to identify a population of similarly massive, quiescent galaxies at moderately high redshift ($z \sim 2$) and it has been suggested that these galaxies represent one stage in the evolution of an elliptical galaxy. A key feature of both local ellipticals and high-redshift quiescent galaxies is that they formed the bulk of their stellar mass in an intense starburst at high redshift, leading to speculation that SMGs are the progenitors of both populations.

Perhaps one of the most surprising features of high-redshift quiescent galaxies is that they have been found to be extremely compact. The morphologies of SMGs thus provide a powerful tool to probe the suggested evolutionary scenario. Studies of the resolved stellar emission from SMGs can probe the size of the pre-existing population. However, the

prodigious star formation rates of SMGs means that understanding the spatial distribution of the ongoing star formation is crucial to understanding the stellar distribution of the post starburst galaxy. Prior to the work presented in this thesis, the sub-mm emission from SMGs had been resolved in only a handful of cases. In the previous chapter I presented a sample of 52 SMGs, detected in 870 μm ALMA imaging of 30 SCUBA-2-detected sub-mm sources. In this chapter I investigate the sub-mm morphologies of a subset of 23 of these SMGs that are spatially resolved in the 0.3″ resolution ALMA imaging. The following chapter was presented in part in Simpson et al. (2015), ApJ, 799, 81.

4.2 Abstract

We present high-resolution (0.3″) ALMA 870 μm imaging of 52 sub-millimetre galaxies (SMGs) in the Ultra Deep Survey (UDS) field and investigate the size and morphology of the sub-millimetre (sub-mm) emission on 2–10 kpc scales. We derive a median intrinsic angular size of FWHM $= 0.30 \pm 0.04$″ for the 23 SMGs in the sample detected at a signal-to-noise ratio (SNR) > 10. Using the photometric redshifts of the SMGs we show that this corresponds to a median physical half-light diameter of 2.4 ± 0.2 kpc. A stacking analysis of the SMGs detected at an SNR < 10 shows they have sizes consistent with the 870 μm-bright SMGs in the sample. We compare our results to the sizes of SMGs derived from other multi-wavelength studies, and show that the rest-frame ~ 250 μm sizes of SMGs are consistent with studies of resolved ^{12}CO ($J = 3$–2 to 7–6) emission lines, but that sizes derived from 1.4 GHz imaging appear to be approximately two times larger on average, which we attribute to cosmic ray diffusion. The rest-frame optical sizes of SMGs are around four times larger than the sub-millimetre sizes, indicating that the star formation in these galaxies is compact relative to the pre-existing stellar distribution. The size of the starburst region in SMGs is consistent with the majority of the star formation occurring in a central region, a few kpc in extent, with a median star formation rate surface density of $90 \pm 30\,\mathrm{M_\odot\,yr^{-1}\,kpc^{-2}}$, which may suggest that we are witnessing an intense period of bulge growth in these galaxies.

4.3 Introduction

Nearly twenty years after their discovery, there is still debate about the nature of the population of luminous, but highly dust-obscured sources detected at high redshifts in

sub-millimetre and millimetre surveys. The observational data suggest that the 850 μm-detected sub-millimetre galaxies (SMGs) lie at a median redshift $z = 2.5 \pm 0.2$ (Simpson et al. 2014, see also Chapman et al. 2005; Wardlow et al. 2011; Yun et al. 2012; Smolčić et al. 2012; Weiß et al. 2013) and are powered by bursts of star formation in relatively massive, gas-rich galaxies (stellar masses of $\sim 10^{11}\,\mathrm{M}_{\odot}$ and gas masses of $\sim 0.5 \times 10^{11}\,\mathrm{M}_{\odot}$, e.g. Hainline et al. 2011; Michałowski et al. 2012; Bothwell et al. 2013) with space densities of $\sim 10^{-5}\,\mathrm{Mpc}^{-3}$. A modest proportion of SMGs have been shown to host an accreting super-massive black hole (e.g. Alexander et al. 2008; Pope et al. 2008; Wang et al. 2013) and many appear disturbed or irregular in high-resolution rest-frame optical imaging from *HST*, albeit predominantly with a low Sérsic index (e.g. Conselice et al. 2003; Chapman et al. 2003; Swinbank et al. 2010a; Targett et al. 2013; Wiklind et al. 2014; Chen et al. 2015). SMGs thus share some of the traits of local Ultraluminous Infrared Galaxies (ULIRGs), although they are $\sim 10^3$ times more abundant at a fixed far-infrared luminosity (e.g. Chapman et al. 2005; Lindner et al. 2011; Magnelli et al. 2012; Yun et al. 2012; Swinbank et al. 2014) and appear to be more massive than these proposed analogues (e.g. Tacconi et al. 2002).

In the past decade, near-infrared (NIR) spectroscopy has also identified a population of quiescent, red, galaxies at $z = 1.5$–3, which have been proposed as the potential descendants of high redshift starbursts (SMGs). The stellar populations in these high-redshift quiescent galaxies follow a fairly tight "red-sequence", indicating that the stellar population was formed rapidly in an intense starburst phase (e.g. Kriek et al. 2008a). The high star formation rates of SMGs ($300\,\mathrm{M}_{\odot}\,\mathrm{yr}^{-1}$; Magnelli et al. 2012; Swinbank et al. 2014), combined with large molecular gas reservoirs, indicate that they have the potential to form a stellar component of 10^{10}–$10^{11}\,\mathrm{M}_{\odot}$ in 100 Myrs. Such rapid stellar mass growth, at high redshift, has led to speculation that SMGs may be the progenitors of both these high-redshift quiescent galaxies, and local elliptical galaxies (Lilly et al., 1999; Genzel et al., 2003; Blain et al., 2004; Swinbank et al., 2006; Tacconi et al., 2008; Hainline et al., 2011; Hickox et al., 2012; Toft et al., 2014; Simpson et al., 2014).

Studies investigating this proposed evolutionary scenario typically compare properties such as the stellar mass, spatial clustering and space densities of the population and the proposed descendants. However, each of these methods has significant associated uncertainties. In particular, the stellar masses of SMGs have been shown to be highly dependent on the assumed star formation history, with systematic uncertainties of a factor

of around five on individual measurements (see Hainline et al. 2011; Michałowski et al. 2012). Studies of resolved Hα and ^{12}CO emission lines indicate SMGs have dynamical masses of (1–2) $\times 10^{11}\,\mathrm{M}_{\odot}$ (Swinbank et al. 2006; Alaghband-Zadeh et al. 2012; Bothwell et al. 2013), placing an upper limit on the stellar masses, but the number of SMGs with measured dynamical masses is small and the samples inhomogeneous. The spatial clustering of single-dish detected sub-mm sources has been shown to match that expected for the progenitors of local ellipticals (Hickox et al., 2012). However, these results are complicated by source blending in the coarse (19″) resolution single-dish sub-mm imaging (Hodge et al., 2013b), whereby the detected sub-mm source comprises of multiple individual SMGs. Finally, while the space densities of SMGs and ellipticals are in agreement, the analysis is highly dependent on the assumed duty cycle of the SMG population (e.g. Simpson et al. 2014).

The morphologies of SMGs provide an alternative, and potentially powerful, tool for testing any evolutionary connection, since the population of quiescent galaxies at high redshift appear extremely compact in rest-frame optical imaging (half-light radius [R_{e}] $\sim 1\,\mathrm{kpc}$; e.g. Daddi et al. 2005; Zirm et al. 2007; Toft et al. 2007; Buitrago et al. 2008; van Dokkum et al. 2008; Newman et al. 2012; Patel et al. 2013; Krogager et al. 2013). Recently, Chen et al. (2015) presented Wide Field Camera 3 (WFC3)/*HST* imaging of 48 SMGs, finding a median half-light radius of $R_{\mathrm{e}} = 4.4^{+1.1}_{-0.5}\,\mathrm{kpc}$, considerably larger than the quiescent population (see also Targett et al. 2013; Wiklind et al. 2014). However, as discussed by Chen et al. (2015), the SMGs in their sample are predominantly disturbed systems, with indications that the intense star formation is triggered by merger activity (see also Frayer et al. 1999; Greve et al. 2005; Tacconi et al. 2006; Engel et al. 2010; Ivison et al. 2013). The sizes presented by Chen et al. (2015) are thus likely to over-estimate the size of the system at post-coalescence. In addition, the high star formation rates of SMGs, combined with large molecular gas reservoirs, means that they have the potential to at least double their stellar mass during the starburst phase. As such, understanding the spatial distribution of the ongoing star formation is crucial to understanding the stellar distribution of the post starburst galaxy.

In the local Universe ULIRGs, the proposed analogues of SMGs, appear to be compact (1–2 kpc diameter) using resolved ^{12}CO/dust/mid-infrared/radio emission (Condon et al. 1991b; Downes & Solomon 1998; Soifer et al. 1999; Sakamoto et al. 2008; Rujopakarn et al. 2011; Ueda et al. 2014). At the typical redshift of SMGs ($z = 2.5$) it has only been

possible to resolve the dust emission in a small number of the brightest sources. Younger et al. (2010) present observations of two bright SMGs ($S_{870} = 13\,\mathrm{mJy}$ & $18\,\mathrm{mJy}$) using the Sub-millimetre Array (SMA). Both of these SMGs appear resolved in the SMA data and have a FWHM of $0.6 \pm 0.2''$; at the typical redshifts of SMGs this corresponds to a physical size of 4–5 kpc. More recently Hodge et al. (2013b) obtained interferometric follow-up observations, with the Atacama Large Millimetre Array (ALMA), of single-dish identified sub-mm sources. Hodge et al. (2013b) identified 99 SMGs in the $1.6''$ resolution ALMA maps, but found that only one SMG is resolved with a FWHM of 9 kpc. The remaining SMGs are unresolved, with sizes $< 10\,\mathrm{kpc}$ (Hodge et al., 2013b).

Limited studies in the radio and CO also hint that SMGs have sizes of a few kpc in diameter (see Menéndez-Delmestre et al. (2009) for a discussion of the mid-infrared sizes of SMGs). However these studies suffer from two limitations. In ^{12}CO the resolution achieved using facilities such as the Plateau de Bure Interferometer (PdBI) or SMA is barely sufficient to resolve the emission to $\lesssim$ 3–4 kpc, and studies indicate the SMGs are either unresolved or marginally resolved at this resolution (e.g. Tacconi et al. 2006; Engel et al. 2010). These ^{12}CO observations are also typically carried out in the higher-J transitions, which trace the denser and warmer gas, not necessarily reflecting the full extent of the gas reservoir, or star formation activity. Indeed there is evidence from spatially-resolved ^{12}CO ($J = 1$–0) observations of a small sample of SMGs that the cool gas extents of these systems are considerably larger than claimed from high-J observations (e.g. Ivison et al. 2011; Riechers et al. 2011b; Hodge et al. 2013a). In contrast to studies of ^{12}CO emission, radio observations provide the resolution required to resolve SMGs at 1.4 GHz with eMERLIN (e.g. Biggs & Ivison 2008) or at higher frequencies with the Karl G. Jansky Very Large Array (VLA). However, such studies in the radio typically rely on the far-infrared radio correlation to identify the sub-mm sources. The identification procedure is inherently probabilistic, and as shown by Hodge et al. (2013b) the reliability and completeness of the identifications is 80 % and 50 pc respectively. In addition, the form of the spatially-resolved far-infrared radio correlation is still debated in the local Universe, owing to the potential diffusion/leakage of the cosmic rays and the influence of magnetic fields on the resulting emission (Bicay & Helou, 1990; Murphy et al., 2006, 2008). Hence translating radio sizes into star formation extents is uncertain, especially when extrapolating the results of local studies to SMGs at $z \gtrsim 2$.

In this chapter we present the results of ALMA 870 μm observations of 30 bright sub-

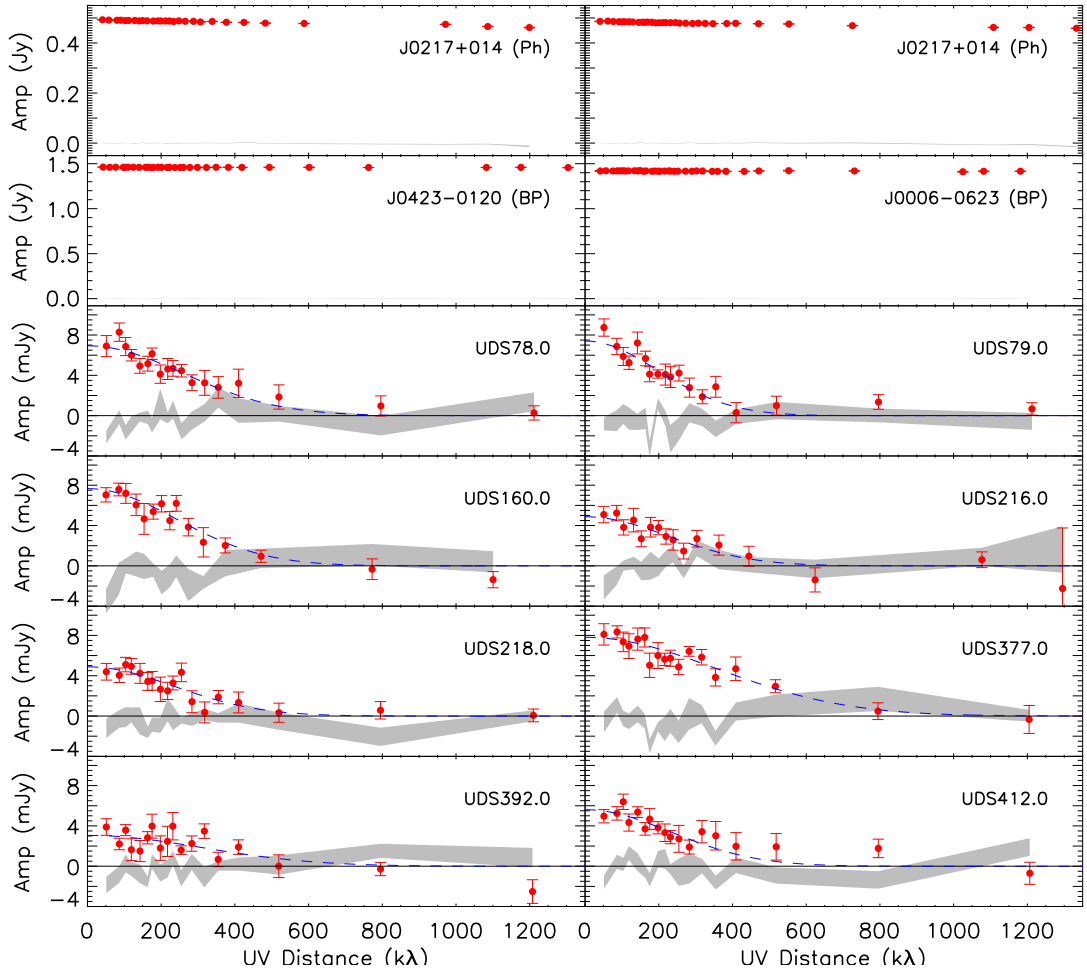

Figure 4.1: Components of the complex visibility versus *uv*-distance for the phase (Ph) and bandpass (BP) calibrators from both measurement sets (top), and an example eight SMGs from our sample (lower panels). The real components of the complex visibilities are plotted as data points, while the 1-σ range of the imaginary components is shown as a grey shaded region. Both the real and imaginary components are plotted on the same scale on the left axis. The amplitudes of both sets of calibrators are relatively flat with *uv*-distance, indicating that they are unresolved point sources, although we note a marginal drop in the flux of the phase calibrator, which suggests it is weakly resolved. In contrast the amplitudes for seven of the SMGs decline strongly with *uv*-distance, confirming our conclusion that these sources are resolved in the sub-mm imaging at 0.3″ resolution. We plot on each SMG a dashed line representing the best-fitting Gaussian to the amplitudes. We note that our measurements of the size and flux density of these SMGs in the image plane are consistent with the Gaussian fits to the amplitudes (the median ratio in size is $\mathrm{FWHM^{uv}}\,/\,\mathrm{FWHM^{image}} = 0.9 \pm 0.2$).

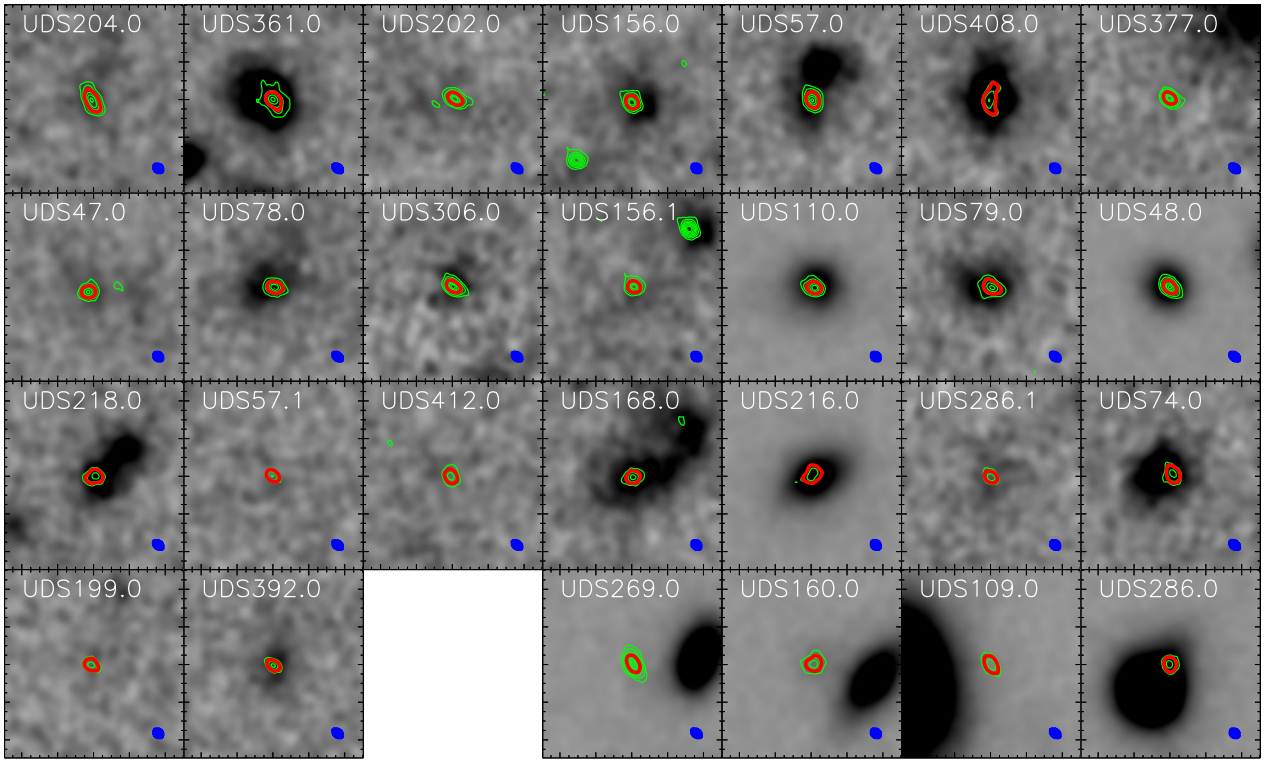

Figure 4.2: Grayscale K-band images of the 27 bright (SNR $> 10\,\sigma$) ALMA-identified SMGs in our sample. The images are in order of decreasing 870 μm flux density, except for the final four panels, which are classed as potentially lensed SMGs (images are separated by a blank panel). Each panel is $5'' \times 5''$ and we contour the ALMA maps over the images of the galaxies. The green contours on each image represent ALMA 870 μm emission at 4, 8, 12, ... $\times\sigma$, and a single red contour represents where the ALMA 870 μm surface brightness is 50 % of the peak value; for an ideal point source this contour should be identical to the size of the ALMA beam FWHM (bottom right of each panel). We note that the red contour appears more extended than the beam, indicating that these SMGs are resolved in the $0.3''$ resolution ALMA data. Overall, 15 % of the SMGs are not detected in the K-band imaging ($5\,\sigma$ detection limit 25.0 mag).

millimetre sources. These SMGs are selected at 850-μm from the SCUBA-2 (Holland et al., 2013) Cosmology Legacy Survey of the UKIDSS Ultra Deep Survey (UDS) field, and were mapped at an angular resolution of 0.3″ FWHM using ALMA. In this work we focus on the sizes and morphologies of these SMGs; the catalogue and number counts were presented in Chapter 3. We discuss in § 4.4 our sample selection, and the ALMA 870 μm observations and their reduction. In § 4.5 we present the sizes of the resolved dust emission in the SMGs, and in § 4.6 we present a comparison of these typical SMGs to similar high-redshift sources and to local U/LIRGs. We give our conclusions in § 4.7. Throughout the chapter, we adopt a cosmology with $\Omega_\Lambda = 0.73$, $\Omega_\mathrm{m} = 0.27$, and $H_0 = 71\,\mathrm{km\,s^{-1}\,Mpc^{-1}}$, in which an angular size of 1″ corresponds to 8.5–7.5 kpc at $z \sim 1.5$–3.5. Unless otherwise stated, error estimates are from a bootstrap analysis.

4.4 Observations and Analysis

The observations discussed here targeted 30 870 μm sources lying in the UKIDSS UDS field. These sources were selected from wide-field 850 μm observations of the UDS field taken as part of the SCUBA-2 Cosmology Legacy Survey (S2CLS) program with the SCUBA-2 camera on the James Clerk Maxwell Telescope (JCMT). The current SCUBA-2 observations reach a typical depth of $\sigma_{850} = 1.2$ mJy across a $0.8 \times 0.8\,\mathrm{degree}^2$ field, and have an angular resolution of 14.8″ FWHM. From an early version of these observations, with $\sigma_{850} = 2$ mJy, we selected a sample of 30 of the brightest sub-millimetre sources in the field, detected at $> 4\sigma$ significance and hence having 850μm flux densities of 8 mJy–16 mJy.

4.4.1 ALMA data

The data reduction and source extraction from our ALMA data was described in detail in Chapter 3. Here we give a brief description. The ALMA data were taken on 2013 November 1, as part of the Cycle-1 project 2012.1.00090.S. We observed all 30 sub-millimetre sources with ALMA, using 7.5-GHz of bandwidth centered at 344 GHz (870 μm; Band 7); the same frequency as the original SCUBA-2 observations. We used a "single continuum" correlator setup with four basebands of 128 dual-polarization channels each.

The phase centers for the ALMA pointings are the centroid position of the sub-millimetre source from the early SCUBA-2 map. The ALMA primary beam at this frequency is 17.3″ FWHM, larger than the 14.8″ FWHM of the SCUBA-2 beam and

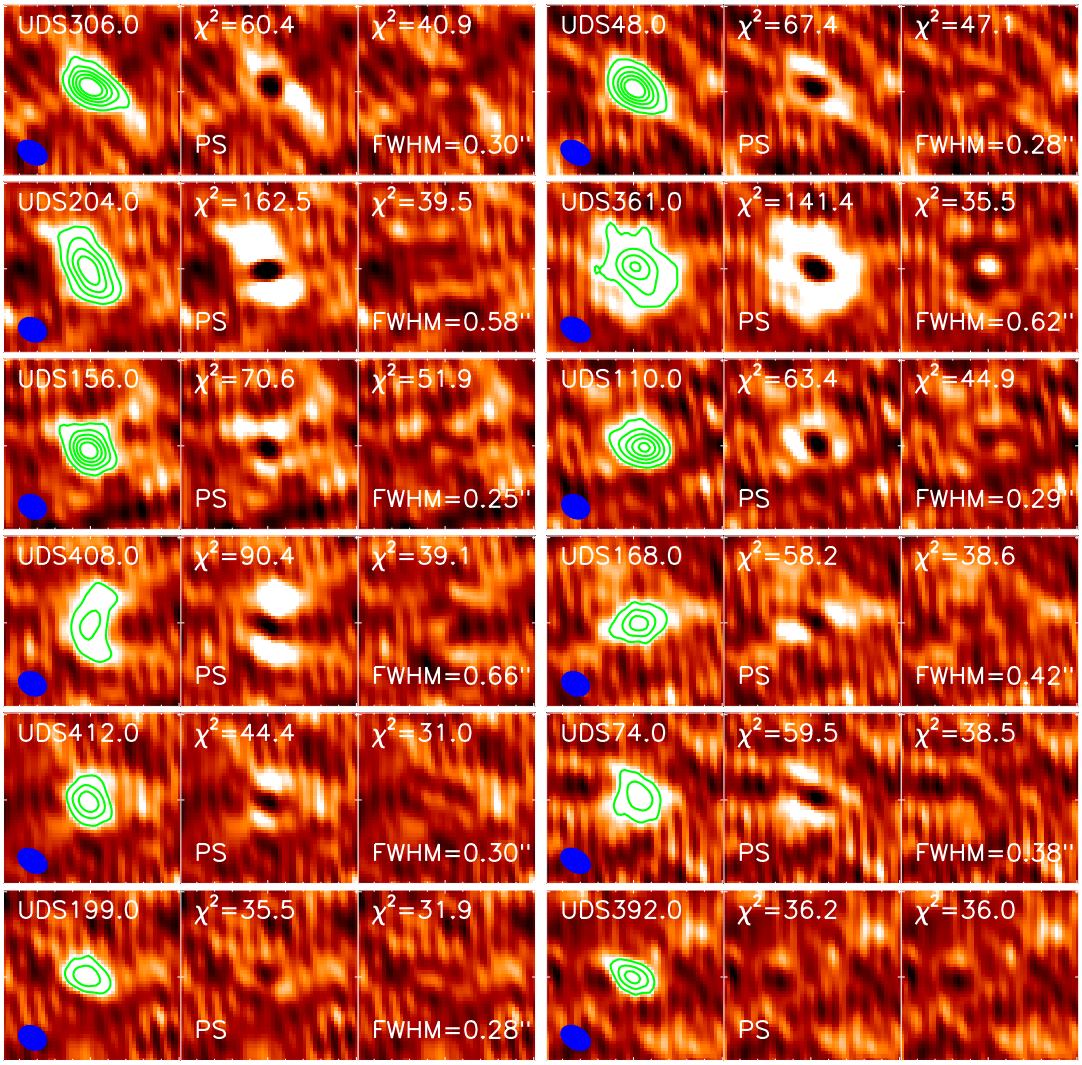

Figure 4.3: Examples showing $2'' \times 2''$ images of our high resolution 870 μm maps ($0.3''$; left) alongside the residuals from fitting a point source model (PS; middle of each set of three panels) and an elliptical Gaussian model (resolved; right) for 12 example SMGs in our sample. The green contours represent 870 μm emission at 4, 8, 12, ... $\times\sigma$, and the colour-scale in each image is clipped at $\pm 3\,\sigma$. The ALMA beam is shown in the bottom left of the left-hand column. The SMGs presented here are chosen such that they span the full range in detection significance for the sample, and are a fair representation of the data quality of our ALMA maps. In eleven of these images there are significant residuals when fitting a point source model to the 870 μm emission, indicating that these sources are resolved in our ALMA maps. In contrast we highlight UDS392.0, which is well-described by a point source model and is classed as unresolved in our analysis. For the full sample of 23 SMGs the median difference in χ^2 between the best-fit extended and point-source model is $\Delta\,\chi^2 = 20 \pm 2$. We find that 22 / 23 SMGs are resolved in our $0.3''$ resolution imaging, and derive a median angular size for the sample of $0.30 \pm 0.04''$ (deconvolved FWHM of the major axis).

so is sufficient to recover all of the SMGs contributing to the single-dish sub-millimetre emission. The array configuration for our observations was such that the 26 ALMA 12-m antennae employed had a maximum baseline of 1250 m, and a median baseline of 200 m. This is in fact more extended than our requested compact C32-1 configuration and as a result yields a synthesized beam of $0.35'' \times 0.25''$ using Briggs weighting (robust parameter = 0.5). The maximum angular scale that our observations are sensitive to is $5''$, which as we show in § 4.5.1 is an order of magnitude larger than the FWHM of the sources in our sample.

The observations of our 30 targets were split into two 15-target blocks. Each block comprises seven or eight sub-blocks of 30 s observations of 10 targets, with the targets each observed five times. The targets were randomly assigned to different sub-blocks; i.e. one source might be observed in sub-blocks 1,3,5,6,7, and another in 1,2,3,4,6. Each block has a full set of calibration observations and each 5-min sub-block is separated by a 90 s phase calibration observation and a 30 s atmospheric calibration (taken on the phase calibrator). Hence, for each map we obtained a 150 s integration. Absolute flux calibration was derived from J 0238 + 166 and we used observations of the secondary phase calibrator J 0217 + 014, for phase referencing. The total integration time for the project was 2.6 hrs.

The data were imaged using the Common Astronomy Software Application (casa version 4.2.1). As detailed in Chapter 3 the *uv*-data were Fourier transformed to create a "dirty" image. We then applied the same procedure adopted by Hodge et al. (2013): a tight clean box was placed around all $> 5\,\sigma$ emission in each map and these were cleaned down to a depth of $1.5\,\sigma$. The final cleaned maps have a median angular resolution of $0.35'' \times 0.25''$ (P.A. ~ 55 deg), using Briggs weighting (robust parameter = 0.5), and a median rms of $\sigma_{870} = 0.21$ mJy beam^{-1} (with a range from 0.19–0.24 mJy beam^{-1}). We inspect our maps and find that we do not detect any sources at sufficiently high SNR to reliably self-calibrate.

To construct the master catalogue, and ensure that the extended flux from the SMGs is recovered, we repeated the imaging procedure described above, but using natural weighting, and applying a Gaussian taper to the data in the *uv*-plane. Applying a Gaussian taper means that a lower weighting is given to visibilities at large distances in the *uv*-plane, producing a map with a larger synthesized beam, hence with less emission resolved out, at the expense of higher noise. The resulting maps have a median angular resolution of $0.8'' \times 0.65''$, and median rms of $\sigma_{870} = 0.26$ mJy beam^{-1}. Hence two sets of maps were

created; "detection" maps with a synthesised beam of $\sim 0.8''$ FWHM and "high-resolution" maps at $\sim 0.3''$ FWHM.

To construct our catalogue, we identify sources within the ALMA primary beam FWHM that are detected at $> 4\,\sigma$ in the $0.8''$ FWHM "detection" maps, and extract both the peak flux density and the total flux density in a $0.8''$ radius aperture for each SMG. We search for sources outside the ALMA primary beam FWHM, but do not find any statistically significant detections (see Chapter 3). In total we identify 52 SMGs above $4\,\sigma$ in the 30 ALMA maps, at $0.8''$ FWHM resolution. These SMGs have a range of 870 μm flux density of 1–14 mJy and we recover the single-dish SCUBA-2 with a median ratio of $S^{\rm SCUBA2}\,/\,S^{\rm ALMA} = 1.04 \pm 0.05$. As the analysis presented in this chapter is focused on the size distribution of SMGs, we cut our SMG sample at a higher significance limit to provide sufficiently high signal-to-noise ratios (SNR) for the SMGs to reliably measure their sizes. As we show below, this corresponds to SNR ≥ 10 ($S_{870} \gtrsim 4$ mJy) at $0.8''$ resolution, which reduces our sample to 27 SMGs. In order to check the measured fluxes of these sources we also used the IMFIT routine in CASA to model each SMG and find good agreement between the model and aperture derived flux densities ($S^{\rm Model}\,/\,S^{\rm Aperture} = 1.02 \pm 0.01$). Where appropriate in the following analysis, we will also use the average properties of the remaining 25 SMGs with $S_{870} \lesssim 4$ mJy to test for trends with flux density across the whole sample.

Given the relatively bright $\gtrsim 8$ mJy flux limit used to select our target sample, we need to be aware of the potential influence of gravitational lensing (e.g. Blain 1996; Chapman et al. 2002) [1]. Indeed, we identify four examples of potential gravitationally-lensed sources in our bright SMG sample: UDS 109.0, UDS 160.0, UDS 269.0, and UDS 286.0. All of these sources appear to be close to, but spatially offset from, galaxies at $z \lesssim 1$ (Figure 4.2). If these sources are lensed then their apparent sizes need to be corrected for lens amplification. However, they all appear singly-imaged (with no sign of multiple images at our sensitive limits) and as we have no precise estimates of their redshifts or the masses of the foreground lenses, it is impossible to reliably determine this correction. We therefore

[1] Lensing models predict that our sample contains 1–2 SMGs that are lensed with an amplification factor > 2 (e.g. Paciga et al. 2009). However we note that the prediction is based on the Chapman et al. (2005) redshift distribution for SMGs, which does not contain the high-redshift tail of sources seen in other SMG redshift distributions (e.g. Yun et al. 2012; Smolčić et al. 2012; Weiß et al. 2013; Simpson et al. 2014). Hence the prediction for the number density of lensed sources is likely to be a lower limit.

highlight these four SMGs in Figure 4.2, and note that the derived sizes for these sources are likely to be over-estimated. When discussing the properties of our sample we do not include the potentially lensed sources in the analysis, and so our final sample consists of 23 SMGs detected at SNR $> 10\,\sigma$.

4.4.2 Robustness of imaging

As we show in § 4.5.1 most of the SMGs in our sample are resolved in the $0.3''$ resolution ALMA maps. However, we now perform two tests to ensure that an error in the calibration of the raw data does not drive our conclusion that the sources are resolved.

The observing strategy for our targets was such that each SMG was observed five separate times through the observing block, with phase calibration observations between each repeat observation. First, we test for variations in the source size as a function of time, as might be expected if the phase solution applied to the data does not correctly model fluctuations. To do so, we separately image each repeat observation of UDS 204.0, the brightest SMG in our sample (the integration time is sufficient to detect the source at 8–$10\,\sigma$ in an individual scan). The SMG appears resolved in all five images, with an intrinsic source size in the range $0.52''$–$0.63''$, and all sizes consistent within the associated 1–σ uncertainties ($\sim 0.05''$).

Secondly, we re-classify an observation of the phase calibrator as a science target observation in the observing sequence and repeat the calibration of the data set. If an error in the calibration of the raw data, due to phase variations, is causing the SMGs in our sample to appear resolved then the phase calibrator will also appear resolved in this scan. We image this phase calibrator scan in the same manner as the SMG observations and model the emission using the IMFIT routine. In the individual scan the phase calibrator has an intrinsic size of FWHM $= 0.06 \pm 0.01''$, which is marginally higher that the intrinsic size measured in an image combining all scans (FWHM $= 0.03 \pm 0.01''$). However, by removing a phase calibrator scan we have introduced a ten minute gap in our calibration observations, which is double that used throughout the observations. Hence any difference in the size of the phase calibrator should be classed as an upper limit on the uncertainty due to errors in the phase calibration of the data. Taken together these tests indicate that the SMGs in our sample do not appear resolved due to errors in the calibration of the raw data.

In our analysis in § 4.5.1 we use the IMFIT routine in CASA to fit an elliptical Gaussian

model (convolved with the synthesised beam) for the 870 μm emission from each SMG. However, before applying this approach to the bright SMGs in our sample, we now test the reliability of the fits as a function of SNR using simple simulated galaxies. To do so, we create 20,000 elliptical Gaussian model sources with a uniform distribution of peak SNR from 4 to 30 (covering the range of SMGs in our full sample) and a major-axis size distribution that is uniform from 0 to 1″. The model sources are distributed uniformly in SNR at 0.8″ resolution, reflecting the selection function of our full SMG catalogue. In order to use realistic noise maps we add these models to a randomly-chosen position in one of the residual (source-subtracted) ALMA maps.

We use CASA to fit an elliptical Gaussian to each injected model source and derive the best-fit size for each. We note that the IMFIT routine can return a point source solution if this is the best model. For each model parameter we calculate the fractional offset between the input model value and the recovered value. As expected we find that the precision of the recovered parameters is a function of SNR. To ensure that the sizes we derive for the SMGs are reliable we define a selection limit that the 1-σ spread in $(\mathrm{FWHM}^{\mathrm{Model}} - \mathrm{FWHM}^{\mathrm{True}}) / \mathrm{FWHM}^{\mathrm{True}} < 0.3$, i.e. 68% of the model sources are recovered with a fractional error less than 30%. We find that this requirement is met for sources that are detected at a SNR ≥ 10, which is the justification for our use of this limit to define the bright SMG sample analysed in this chapter.

These simulations also indicate a small bias in the recovered size for sources with SNR between 10 to 30 σ of $(\mathrm{FWHM}^{\mathrm{Model}} - \mathrm{FWHM}^{\mathrm{True}}) / \mathrm{FWHM}^{\mathrm{True}} = 0.018 \pm 0.002$ (1-σ spread of ± 0.14), which we have not corrected for in the following analysis. The simulations also allow us to investigate the resolution limit of our maps, by determining the true size of a model source for which the IMFIT routine returns a point source best-fit solution. For SMGs with SNR = 10–30 we find that 90% of the model sources that are best fit by point source models using IMFIT actually have a "true" size $\leq 0.18''$ (i.e. smaller than half the size of the beam major axis). Hence, we can be confident that any SMGs that have a point source best-fit model have a size $\leq 0.18''$, and we adopt this as an upper limit for the size of the unresolved SMGs.

4.4.3 Multi-wavelength properties

During our analysis we use archival multi-wavelength information on this well-studied field. An extensive analysis of the multi-wavelength properties of the SMG sample will be

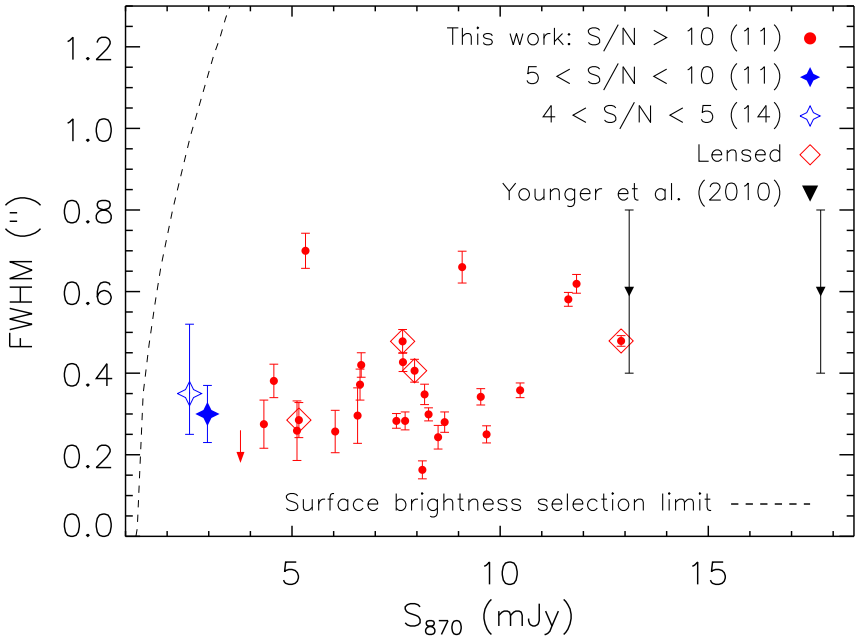

Figure 4.4: Angular size distribution of the 870 μm emission from SMGs as a function of their 870-μm flux density. A dashed line represents our surface brightness selection limit. The 23 SMGs detected at $\geq 10\,\sigma$, have a median intrinsic size of $0.30 \pm 0.04''$ (deconvolved FWHM of the major axis). We stack the 870 μm emission from SMGs detected at 5–10 σ and 4–5 σ, and show the size derived from each stack. We find that these 870 μm-faint SMGs have sizes that are on average consistent with the brighter SMG distribution. We highlight four SMGs that are potentially lensed sources, but note that these are not included in our analysis. For comparison we show the sizes of two bright SMGs measured from observations with the SMA (Younger et al., 2010).

presented in Ma et al. (in prep), but for the purposes of this chapter we use two pieces of information from that work: constraints on the likely redshifts of the SMGs using photometric redshifts; and estimates of their far-infrared luminosities.

First, we use the photometric redshift catalogue of this field produced by the UKIDSS UDS team, which is based on a K-band selected sample of sources. To briefly summarise, photometric redshifts are determined for each field source by fitting template spectral energy distributions (SEDs) to the observed $UBVRi'z'JHK$ and IRAC 3.6 and 4.5 μm photometry, using the public SED fitting code EAZY (Brammer et al., 2008). Excellent agreement is found between the photometric and spectroscopic redshifts for 2146 sources in the field, with a median dispersion of $(z_{\rm phot} - z_{\rm spec}) / (1 + z_{\rm spec}) = 0.03$ (see Hartley et al. 2013; Mortlock et al. 2013).

Matching the SMG catalogue to the photometric redshift sample we find 19 matches within $1''$ of the 23 bright SMGs, which leaves four of the SMGs without redshift infor-

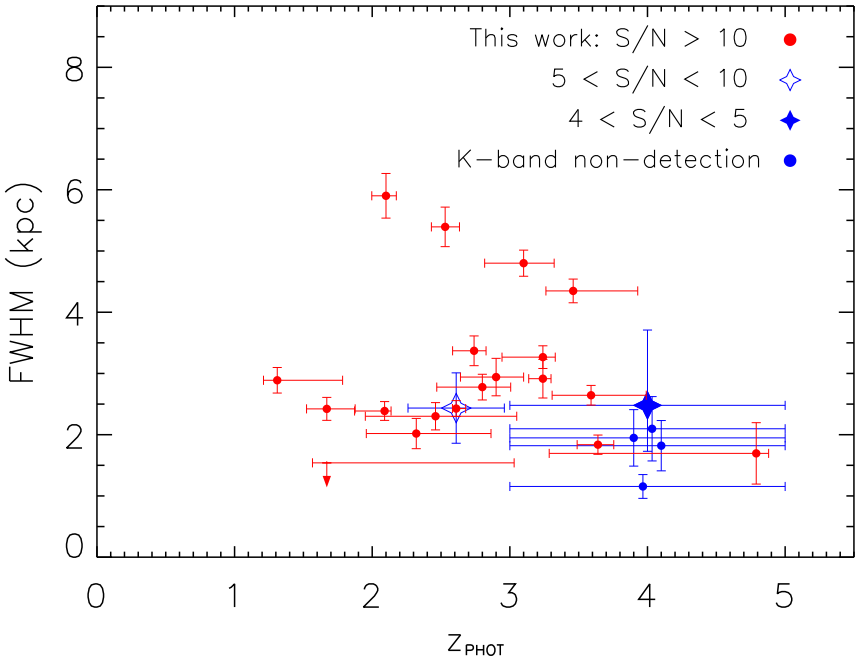

Figure 4.5: Physical size of SMGs as function of redshift. Four SMGs in our sample do not have a photometric redshift, and we fix the redshift of these sources at $z = 4 \pm 1$ (the redshifts are offset in the plot). The potentially lensed SMGs are not shown on this figure. The median physical size of the 23 SMGs in the sample is FWHM $= 2.4 \pm 0.2$ kpc, and we do not find a trend in the physical size with redshift. From our stacking analysis we measure an average physical size for the SMGs detected at SNR $= 5$–$10\,\sigma$ of 2.4 ± 0.6 kpc, consistent with our results for the 870 μm-brighter SMGs. We also show the results of stacking the 14 SMGs detected at SNR $= 4$–$5\,\sigma$, but note that 8/14 sources in the stack do not have a photometric redshift.

mation. We also searched for IRAC counterparts for the four SMGs without photometric redshifts and find that three have detections in the IRAC imaging; however, the limited number of photometric bands available for all of these sources mean it is impossible to derive precise photometric redshifts. Simpson et al. (2014) argue that these NIR-faint SMGs typically lie at higher redshifts than the optical/NIR-brighter SMGs, and so we adopt their approach and assign these sources a redshift of $z = 4 \pm 1$.

To derive the FIR luminosities of the SMGs we exploit the *Herschel* SPIRE imaging (Pilbratt et al., 2010; Griffin et al., 2010) of the field at 250, 350 and 500 μm, along with the precise position of the ALMA source to deblend and extract flux densities for the SMGs. Following the approach of Swinbank et al. (2014), they use a prior catalogue of sources detected at 24 μm or 1.4 GHz, along with the ALMA source positions, to model the sources contributing to the map flux in the vicinity of each SMG. Having extracted flux densities or limits in the three SPIRE bands, along with the ALMA 870 μm flux density,

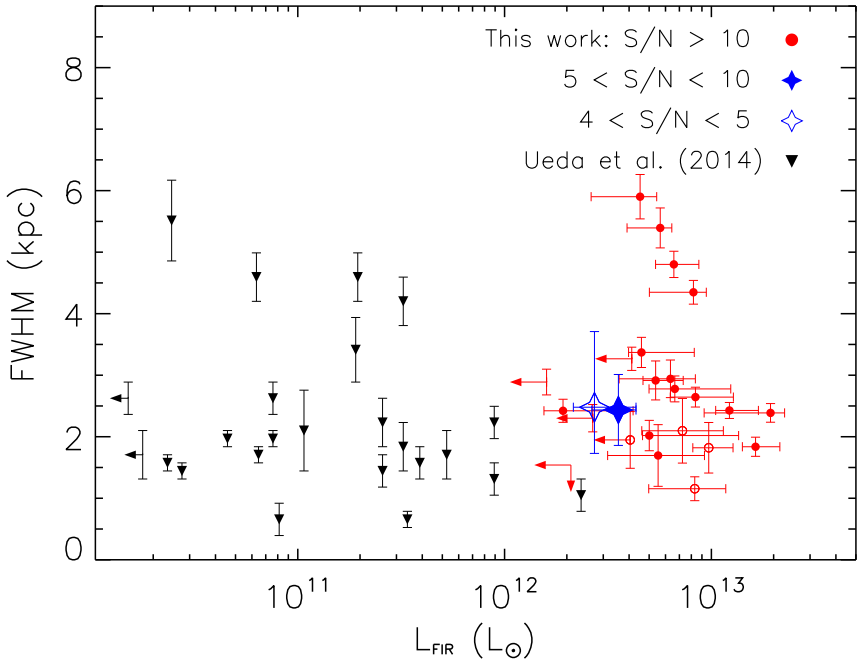

Figure 4.6: Physical size of the SMGs in our sample as a function of FIR-luminosity. The 23 SMGs shown have a median FIR luminosity of $L_{\rm FIR} = (5.7 \pm 0.7) \times 10^{12}\,{\rm L}_{\odot}$, and a median physical size of FWHM $= 2.4 \pm 0.2$ kpc. We do not find a trend between $L_{\rm FIR}$ and the physical size of the SMGs. For comparison we also show the sizes of local "merger-remnants" measured from interferometric observations of the ^{12}CO ($J = 1$–0 / 2–1 / 3–2) molecular emission line. These local galaxies have a median size of 1.9 ± 0.2 kpc, and are marginally smaller than the SMGs presented here. As the "low"-J ^{12}CO typically exceeds the size of the star-forming region, the star formation in SMGs appears to be considerably more extended than in local U/LIRGs.

they fit a library of model spectral energy distribution (SED) templates (see Swinbank et al. 2014), to the FIR-photometry and determine the best-fit template. We integrate the best-fit SED from 8 to 1000 μm to derive the total far-infrared luminosity of each SMG. If an SMG is undetected in the *Herschel* 250, 350 and 500 μm imaging then the far-infrared luminosity is treated as an upper limit. We measure a median far-infrared luminosity for the 23 SMGs in our sample of $L_{\rm FIR} = (5.7 \pm\ 0.7) \times 10^{12}\,{\rm L}_{\odot}$, and a median dust temperature of $T_{\rm d} = 32 \pm 3$ K. We find that $5\,/\,11$ and $10\,/\,14$ SMGs detected at SNR $= 5$–$10\,\sigma$ and SNR $= 4$–$5\,\sigma$, respectively, are undetected in the *Herschel* 250, 350 and 500 μm imaging. We stack the *Herschel* SPIRE maps for these subsets and derive an average $L_{\rm FIR} = 3.6^{+0.8}_{-0.9} \times 10^{12}\,{\rm L}_{\odot}$ and $L_{\rm FIR} = 2.7^{+1.6}_{-0.6} \times 10^{12}\,{\rm L}_{\odot}$ for the SNR $= 5$–$10\,\sigma$ and SNR $= 4$–$5\,\sigma$ subsets, respectively.

4.5 Results

4.5.1 Resolved dust emission

We show the ALMA maps with a 0.3″ FWHM resolution synthesized beam for the 27 SNR ≥ 10 SMGs in Figure 4.2. These are presented as contours overlaid on K-band grayscale images, to allow the reader to make a qualitative comparison of the size and shape of the contour corresponding to the half-peak-flux level and the corresponding size for the synthesized beam. We see evidence in a majority of the SMGs that the sub-millimetre emission appears to be more extended than would be expected for an unresolved source with the same peak flux, with several examples also showing structure on smaller scales (e.g. UDS 74.0, UDS 216.0, UDS 218.0, UDS 361.0, UDS 408.0).

To quantitatively test if the SMGs are resolved in our data we initially perform two non-parametric tests. First we compare the peak flux of each source in the 0.8″ FWHM observations to the higher resolution 0.3″ FWHM imaging (note that the maps are calibrated in Jy beam^{-1}). The peak flux of the SMGs is lower in the 0.3″ resolution maps, with a median ratio of $S^{0.3}_{\rm pk} / S^{0.8}_{\rm pk} = 0.65 \pm 0.02$, and a 1-$\sigma$ range of ± 0.04. A drop in the peak flux density between the sources imaged at different resolutions indicates that flux from each SMG is indeed more resolved in the higher-resolution imaging. We note that a 40% reduction in the peak flux between the 0.3″ and 0.8″ resolution imaging corresponds to an intrinsic source size of $\sim 0.3''$.

As a second test we compare the total flux density in an aperture for each source to the peak flux density at both 0.3″ and 0.8″ FWHM resolution. We convert each map into units of Jy pixel^{-1} and measure the "total" flux density in an 0.8″ radius aperture. The ratio of the peak-to-total flux density is 0.50 ± 0.03 at 0.3″ FWHM resolution, compared to 0.83 ± 0.03 at 0.8″ FWHM. This supports the conclusion that the bulk of the bright SMGs are resolved by ALMA at 870 μm with a 0.3″ FWHM synthesised beam, and suggests that the average angular size of the population is 0.3–0.4″. We note that the aperture fluxes of the SMGs measured in the 0.3″ and 0.8″ imaging are in good agreement, with a median ratio of $S^{0.3}_{\rm Aper} / S^{0.8}_{\rm Aper} = 1.02 \pm 0.03$.

We next investigate whether the SMGs appear resolved in the uv-plane, rather than in the image plane, compared to the calibrator sources used for our observations (which are expected to be unresolved). For each source we align the phase centre of the map to the position of the SMG or calibrator source, and extract the amplitudes for each source

as a function of *uv*-distance. The amplitudes represent the observed flux of the source on different angular scales in the image plane, with the longest baseline providing information on the smallest angular scales that our observations are sensitive to. For an ideal point source the amplitudes should be constant with *uv*-distance. As Figure 4.1 demonstrates we do indeed recover an effectively flat distribution for both the phase and bandpass calibrators.

In Figure 4.1 the amplitudes as a function of *uv*-distance for the eight SMGs which are the sole sources detected in their respective ALMA maps (restricting the sample in this way removes any complications due to modelling and subtracting other sources in the primary beam). The amplitudes of seven of the SMGs clearly decrease with increasing *uv*-distance. A single SMG, UDS 392.0, appears to be only marginally resolved on the longest baselines (our analysis in the image plane identifies this SMG as unresolved, see Fig 2 and 3). We fit the amplitudes for each SMG with a single Gaussian component and determine the equivalent size in the *uv*-plane. The model fits in the *uv* and image planes are consistent, and give a median size ratio between the image- and *uv*-derived sizes of $\mathrm{FWHM^{uv}} / \mathrm{FWHM^{image}} = 0.9 \pm 0.2$ and a median flux density ratio $S^{\mathrm{image}} / S^{uv} = 1.1 \pm 0.1$. In 2–3 of the SMGs the flux density does not fall to zero on baselines $\gtrsim 600\,\mathrm{k}\lambda$, indicating that there is unresolved flux in these sources on an angular scale of $\lesssim 0.3''$, but this unresolved component comprises $\lesssim 10\,\%$ of the total flux density.

Given that our non-parametric tests indicate that the SMGs are resolved in our $0.3''$ imaging, we now chose to fit a more complex model to the sources. Using the IMFIT routine we determine the best-fit elliptical Gaussian model for the 23 SMGs in our bright sample ($\mathrm{SNR} > 10\,\sigma$). The free parameters of the model are position; peak flux density; major and minor axis; and position angle. The median intrinsic size of the 23 SMGs is $0.30 \pm 0.04''$ (deconvolved FWHM of the major axis), and one SMG is modelled as a point source; as the intrinsic sizes of the sources are comparable to the beam we choose to focus our analysis on the FWHM of the major axis. The median χ^2 for the elliptical Gaussian fit is 38.3 ± 1.4, and the number of degrees of freedom of the fit is 33 (we define beam to be the size of the resolution element). If we fit each SMG with a point source model then the median difference in χ^2 between the best-fit extended and point-source model is $\Delta\,\chi^2 = 20 \pm 2$ (see Figure 4.3) [2].

[2] We also determined the best-fit Gaussian model for the SMGs in the $0.8''$ imaging but find that 65 % are unresolved, consistent with our results from the higher resolution ($0.3''$) imaging. The re-

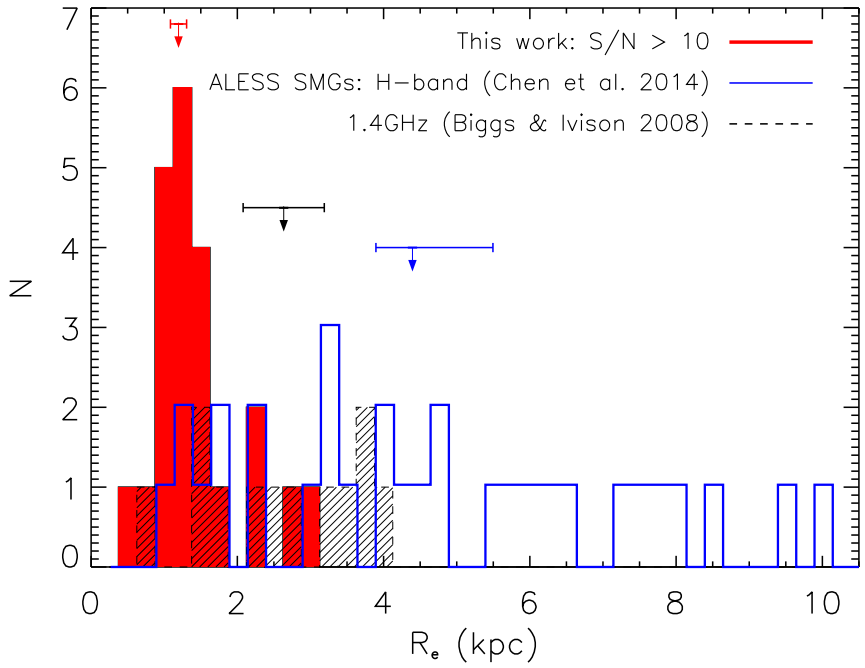

Figure 4.7: Comparison of the 870 μm sizes of the SMGs in our sample, to the sizes of SMGs measured in 1.4 GHz / VLA imaging (Biggs & Ivison, 2008) and H-band/*HST* imaging (Chen et al., 2015). To allow a fair comparison between the samples we present all of the sizes in terms of an effective radius. The median size of the 12 SMGs identified in the 1.4 GHz imaging is $R_{\rm e} = 2.6 \pm 0.6$ kpc, approximately double the median 870 μm size of SMGs, $R_{\rm e} = 1.2 \pm 0.1$ kpc. Convolving the 870 μm emission with a kernel of scale length 1–2 kpc, which is appropriate for modelling cosmic ray diffusion in star-forming galaxies at low redshift (Murphy et al., 2008), increases the median size of the SMGs to 3.8–5.2 kpc. Chen et al. (2015) measure a median size of $R_{\rm e} = 4.4^{+1.1}_{-0.5}$ kpc from rest-frame optical *HST* imaging of 17 interferometrically-identified SMGs at $z = 1$–3. The H-band sizes of these SMGs are on average 3 times larger than the 870 μm sizes presented here, indicating that the obscured star-forming region in SMGs is compact relative to the stellar emission.

Figure 4.4 shows the sizes of the SMGs as a function of their 870 μm flux density. The dispersion of the 870 μm sizes is small and there is no clear trend in the size of the dust emission region with 870 μm flux density. We note however that the two SMG with $S_{870} \sim 12$ mJy in the sample are around two times larger than the median of the sample. While this may be interpreted as a weak trend in the size of SMGs with 870-μm flux density we caution against a strong conclusion, given the limited sample size at these fluxes. We also show the sizes of two bright SMGs ($S_{870} = 13$ mJy and 18 mJy) presented by Younger et al. (2010). These SMGs were observed with the SMA and both appear marginally resolved in the uv-plane, with sizes of $0.6 \pm 0.2''$ (deconvolved FWHM). While the size measurements for these sources have large associated uncertainties, they are consistent with the sizes presented here.

To search for trends in our sample over a larger dynamical range we have also used the fainter SMGs detected in our ALMA maps. While the individual sizes measured for these galaxies have significant uncertainties, we can attempt to derive a typical size for samples of faint SMGs via stacking (this is reasonable as the synthesised beam does not vary significantly between observations; the beam major and minor axes vary by at most $0.03''$ and $0.02''$, respectively across the full sample). We split the fainter 25 SMGs into roughly equal sub-samples detected at SNR = 5–10 σ (median $S_{870} = 3.1 \pm 0.5$ mJy) and SNR = 4–5 σ (median $S_{870} = 2.6 \pm 0.3$ mJy), containing 11 and 14 SMGs, respectively. We stack the $0.3''$ FWHM maps of these sub-samples and use IMFIT to measure the size of the stacked profile. We derive sizes of $0.30 \pm 0.07''$ and $0.35^{+0.17}_{-0.10}''$ for the two sub-samples respectively. The errors on the measured size of each subset are derived by bootstrapping the maps included in the stacks and repeating the analysis. These results indicate that at least on average the 1–4 mJy SMGs in our full sample have the same size distribution as those with observed 870 μm flux densities of 4–15 mJy sources (see Figure 4.4).

solved sources in the $0.8''$ imaging have a median FWHM ratio between the two sets of imaging of $\mathrm{FWHM}^{0.8} / \mathrm{FWHM}^{0.3} = 1.2 \pm 0.1$, however we strongly caution that we have not included upper limits in this calculation and hence the ratio will be biased towards higher values.

4.6 Discussion

4.6.1 Physical size of SMGs

The 23 SMGs detected at $> 10\,\sigma$ in our sample have a median angular FWHM of $0.30 \pm 0.04''$. For each SMG we use the photometric redshift to convert the measured angular diameter into an intrinsic physical scale, and derive that the median physical size of the SMGs is 2.4 ± 0.2 kpc (FWHM of the major axis). As shown in Figure 4.7, the distribution has a narrow interquartile range of 1.8–3.2 kpc, indicating that the dispersion in the intrinsic size of our sample of SMGs is small. We use the results of our stacking analysis to derive an average physical size of 2.4 ± 0.6 kpc and $2.5^{+1.2}_{-0.7}$ kpc, at a median redshift of $z = 2.6 \pm 0.4$ and $z = 4 \pm 1$, for the SNR = 5–10 σ and SNR = 4–5 σ subsets, respectively, indicating no trend in the size of SMGs with redshift (see Figure 4.5). An important caveat of this result is that only one SMG in our sample has a photometric redshift of $z \gtrsim 3.5$. Four SMGs do not have a photometric redshift and it is likely that these sources lie at $z \sim 4$ (see Simpson et al. 2014); however the uncertainties on these redshifts are large. At $z = 4$ these SMGs have a distribution of physical FWHM from < 1.3–2.1 kpc, and are consistent with the lower redshift SMGs in the sample. However, if they instead lie at $z = 6$, then the range of FWHM is < 1.1–1.7 kpc, and these sources would be smaller than all but one $z < 4$ SMG.

Recently Weiß et al. (2013) discussed that evolution in the size of SMGs with redshift is a possible explanation for the discrepancy between the redshift distribution of lensed and unlensed SMGs. As 60% of the SMGs presented by Weiß et al. (2013) lie at $z > 3.5$ we cannot investigate this claim further. However, we note that for the *unlensed* SMGs presented here, we do not find any evolution in the sizes of the 870 μm emitting region at $z < 3.5$.

4.6.1.1 Comparison of the multi-wavelength sizes of SMGs

We now compare the 870 μm sizes presented here to the sizes of SMGs measured from observations at different wavelengths. First, we compare our results to a sample of 12 SMGs (median $S_{850} = 6.8 \pm 0.6$ mJy) with deconvolved sizes measured from $0.5''$ resolution 1.4 GHz/VLA imaging (Biggs & Ivison, 2008). In their analysis Biggs & Ivison (2008) fit an elliptical Gaussian model to the 1.4 GHz emission from each SMG, deriving a median angular size of FWHM $= 0.64 \pm 0.14''$. At the redshifts of these SMGs this angular size

corresponds to a median physical size of FWHM = 5.3 ± 1.1 kpc. Four SMGs in their sample do not have a redshift and we set these to the median redshift of the sample ($z = 2$; consistent with the radio-detected SMGs in Simpson et al. 2014). Hence the 1.4 GHz sizes for the SMGs presented by Biggs & Ivison (2008) are about two times larger than the 870 μm sizes presented here.

It is important to initially note that the radio counterparts to the sub-mm emission presented in Biggs & Ivison (2008) were identified via a probabilistic approach using the far-infrared radio correlation. As shown by Hodge et al. (2013b) these identifications are 80 % reliable, and so we might expect that 2-or-3 of the radio sources presented in Biggs & Ivison (2008) are not the true counterpart to the sub-mm emission. However, we do not know if such mis-identifications are likely to be biased towards galaxies with larger, or smaller, sizes at 1.4 GHz.

Another possible explanation for the discrepancy between the radio and far-infrared sizes of SMGs is that the diffusion length of cosmic rays ($\sim$ 1–2 kpc) is expected to be larger than the diffusion length of far-infrared photons ($\sim$ 100 pc), due to magnetic fields efficiently transporting cosmic rays through the host galaxy. Murphy et al. (2008) present a study of 18 local star-forming galaxies with resolved imaging at 70 μm and 1.4 GHz. They show that the radio emission from these galaxies can be modelled as the convolution of the far-infrared emission with an exponentially declining kernel, with an e-folding length of the kernel of 1–2 kpc (see also Bicay & Helou 1990; Murphy et al. 2006). We convolve the median 870 μm size of the SMGs with this exponential kernel and find that the FWHM of the convolved profile is 3.8–5.2 kpc, showing that the radio sizes of Biggs & Ivison (2008) are likely consistent with our 870 μm sizes.

The galaxies presented by Murphy et al. (2008) are "normal" star-forming galaxies, with star formation rates three orders of magnitude lower than the SMGs presented here. The e-folding length of the kernel has been shown to depend on both star formation rate density and morphology, with high star formation rate densities and irregular galaxies having lower e-folding lengths (Murphy et al., 2008). In both of these situations ordered magnetic fields are disrupted, allowing cosmic ray electrons to stream more freely out of the galaxy, resulting in a shorter scale length. As such, we caution that a scale length of 1–2 kpc might be an over-estimate of the appropriate scale length for the radio emission from SMGs.

Next we compare the 870 μm sizes of SMGs to the sizes of SMGs measured from ^{12}CO

emission lines. Engel et al. (2010) present a compilation (including new observations) of the sizes of SMGs measured from resolved ^{12}CO ($J = 3$–2 / 4–3 / 6–5 / 7–6) emission lines (see also Tacconi et al. 2006, 2008). Deriving a median size for the sample is challenging, as the upper limits on the size of unresolved SMGs are typically similar to the sizes of the resolved sources. Treating the unresolved sources as point sources, the median size of the sample is FWHM $= 2.3 \pm 1.1$ kpc, but this rises to 3.7 ± 0.6 kpc if upper limits are taken as the "true" source size. In our analysis we have not included the sizes taken from Bothwell et al. (2010), as it is not clear that these sizes have been deconvolved for the beam.

In the study by Engel et al. (2010) the ^{12}CO-emission lines are often either unresolved, or marginally resolved, with sizes constrained at only 1–2 σ. The sizes are also measured from ^{12}CO emission lines across a range of rotational transitions, from $J = 2$–1 to 7–6, and we note that there is ongoing debate over whether emission from different transitions traces the same molecular gas (Weiß et al. 2007; Panuzzo et al. 2010; Bothwell et al. 2013; Narayanan & Krumholz 2014). Due to these issues we simply note that the sizes derived from *moderate-J* transitions of ^{12}CO are broadly consistent with the median 870 μm size of the SMGs in our sample.

Finally, we compare our results to the sizes of SMGs derived from high-resolution, *HST*, near-infrared imaging. Chen et al. (2015) recently presented H-band/*HST* imaging (rest-frame optical imaging) of 48 SMGs. These SMGs were drawn from the ALESS sample (Hodge et al., 2013b), and have precise $\lesssim 0.3''$ identifications from ALMA 870 μm observations. Chen et al. (2015) fit a Sérsic profile to the H-band emission, deriving a median half-light radius of $R_{\rm e} = 4.4^{+1.1}_{-0.5}$ kpc (see also Targett et al. 2013; Wiklind et al. 2014). As recommended by Chen et al. (2015), we have restricted their sample to the 17 SMGs with an apparent H-band magnitude < 24 mag and a photometric redshift between $z_{\rm phot} = 1$–3, which ensures that the size distribution is complete (median $S_{850} = 4.0 \pm 0.6$ mJy). The Sérsic profiles fitted by Chen et al. (2015) are more complicated than the Gaussian profiles used in our analysis, but we note that a Gaussian profile corresponds to a Sérsic profile with Sérsic index $n = 0.5$. If we convert our 870 μm sizes to a half-light radius we find that the SMGs have a median $R_{\rm e} = 1.2 \pm 0.1$ kpc in the sub-millimetre. As we show in § 4.6.3.1 the half-light radius of the best-fit Sérsic profile to the stacked 870 μm emission from the SMGs is consistent with the median size from the elliptical Gaussian fit. The optical sizes of the SMGs are about four times larger than the 870 μm dust emitting region, and as can be seen in Figure 4.7 the distribution of near-infrared sizes has considerably

more dispersion than the 870 μm sizes. The compact nature of the star formation means that it is plausible we are observing bulge growth in the form of obscured star formation. However, to test this hypothesis requires high-resolution dust and optical imaging of the same sample of SMGs to pinpoint the location of the star formation within the host galaxy.

4.6.1.2 Comparison to local U/LIRGs

We now compare the sizes of the SMGs in our sample to the sizes of local infrared-bright galaxies. Recently Ueda et al. (2014) presented a compilation of < 1 kpc resolution interferometric imaging (new and archival) of ^{12}CO ($J = 1$–0; 2–1; 3–2) emission from 30 local star-forming galaxies classified as "merger remnants". We select galaxies from their sample with far-infrared luminosities $> 1 \times 10^{10}$ L$_\odot$ (SFR $\gtrsim 1$ M$_\odot$ yr^{-1}), resulting in a sample of 24 galaxies with a median $L_{\rm FIR} = (1.4 \pm 0.1) \times 10^{11}$ L$_\odot$. The sample contains one ULIRG ($L_{\rm FIR} > 10^{12}$ L$_\odot$) and 12 LIRGs ($L_{\rm FIR} > 10^{11}$ L$_\odot$). Ueda et al. (2014) measure the size of each galaxy as the radius containing 80 % (R_{80}) of the total ^{12}CO flux. To ensure a fair comparison with the results presented here, we derive the correction between FWHM and R_{80}, and apply this correction to the sizes presented by Ueda et al. (2014). The sample of 24 local galaxies has a median diameter of 1.9 ± 0.2 kpc, with a $1\,\sigma$ dispersion of 1.3–3.4 kpc (consistent with Downes & Solomon 1998).

We caution that Ueda et al. (2014) present a sample of optically selected "merger-remnants" and although these "merger-remnants" are FIR-bright, the selection is not well-matched to the FIR-selected sample of SMGs presented here. Ueda et al. (2014) also measure the size of the sources in their sample from *low-J* transitions of ^{12}CO: 12 sources are observed in ^{12}CO ($J = 1$–0) emission, ten in ^{12}CO ($J = 2$–1), and two in ^{12}CO ($J = 3$–2). The lowest J transitions trace cold molecular gas, and are expected to reflect the size of the total gas reservoir, rather than the star-forming region. Indeed, studies of Arp 220, the closest ULIRG, find that the size of the rest-frame 860 μm emission is 50–80 pc, which is approximately two to four times smaller than the extent of the ^{12}CO ($J = 1$–0) emission (Downes & Solomon, 1998; Sakamoto et al., 2008).

The sizes of local U/LIRGs measured from *low-J* transitions of ^{12}CO appear marginally smaller than the 870 μm sizes of the SMGs presented here, although the two samples are consistent within the associated uncertainties. However, as we have discussed, sizes measured from the $J = 1$–0 transition of ^{12}CO are likely to be an upper limit on size of the star-forming region. In the absence of a sample of local ULIRGs with sizes measured

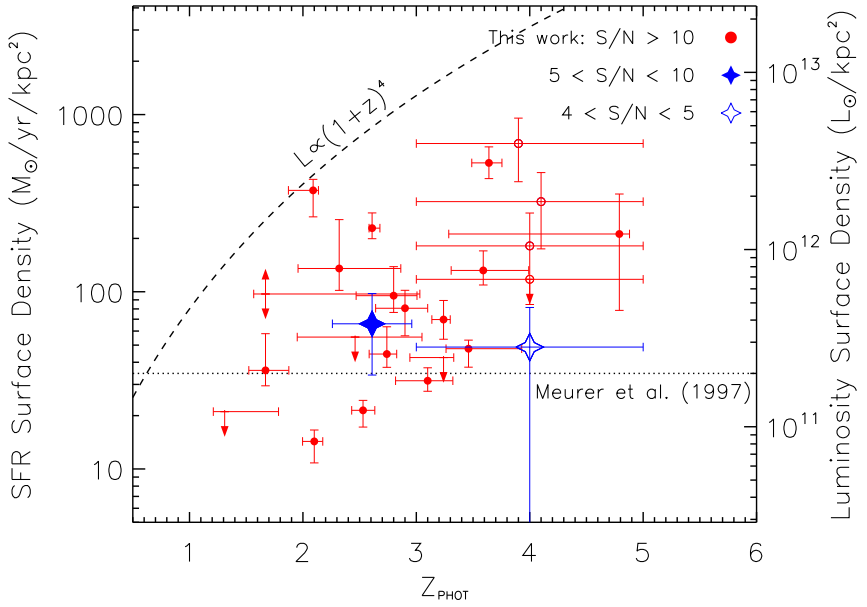

Figure 4.8: Star formation rate surface density of the SMGs in our sample as a function of redshift. The dashed line represents luminosity evolution $L_{\rm IR} \propto (1+z)^4$. A dotted line shows the 90^{th} percentile luminosity surface density for a sample of ultraviolet-selected sources (Meurer et al., 1997). The SMGs have a median star formation rate density of $90 \pm 30\,{\rm M}_\odot\,{\rm yr}^{-1}\,{\rm kpc}^{-2}$, and we note that no SMGs exceed the Eddington limit for a radiation pressure supported starburst ($\sim 1000\,{\rm M}_\odot\,{\rm yr}^{-1}\,{\rm kpc}^{-2}$; Andrews & Thompson 2011)

at approximately the same wavelength as the SMGs in this chapter, we simply note that the star-forming regions in SMGs may be significantly larger than local U/LIRGs.

4.6.2 Are SMGs Eddington Limited Starbursts?

The high star formation rates of SMGs means that they could host regions with an extreme star formation density, which could result in very different star formation conditions to other galaxy populations. In an isolated star-forming region the radiation pressure from massive stars may provide sufficient feedback to regulate the further collapse of the giant molecular cloud. Andrews & Thompson (2011) show via the balance of radiation pressure from star formation with self-gravitation, that the maximum star formation rate surface density, assuming optically thick dust emission ($\tau > 1$)[3], and in the absence of nuclear

[3]Andrews & Thompson (2011) state that a starburst should be treated as optically thick if the gas is above a critical surface density,

$$\Sigma_{\rm g} \gtrsim 1200\,{\rm M}_\odot\,{\rm kpc}^{-2}\,. \qquad (4.6.1)$$

heating via an active galactic nucleus (AGN), is

$$\mathrm{SFR}_{\mathrm{max}} \gtrsim 11 f_{\mathrm{gas}}^{-0.5} f_{\mathrm{dg}}^{-1} \ \mathrm{M}_{\odot}\ \mathrm{yr}^{-1}\mathrm{kpc}^{-2}\,, \tag{4.6.2}$$

where f_{gas} is the gas fraction in the star-forming region, and f_{dg} is the dust-to-gas ratio (see also Murray et al. 2005; Thompson et al. 2005; Murray et al. 2010). We adopt a dust-to-gas ratio of $f_{\mathrm{dg}} = 1/90$ (Magnelli et al., 2012; Swinbank et al., 2014), but note that $f_{\mathrm{dg}} = 1/50$ has also been suggested for star-forming galaxies (Kovács et al., 2006). Estimates of the dynamical masses (Swinbank et al., 2006; Alaghband-Zadeh et al., 2012), stellar masses (Hainline et al., 2011; Simpson et al., 2014) and gas masses (Bothwell et al., 2013) indicate that SMGs have typical gas fractions of $\sim 40\,\%$; however, this is a global property of the galaxy. As the size of the rest-frame optical emitting region in SMGs is around four times larger than the size of the star-forming region (Figure 4.7), it is likely that the gas fraction is considerably higher in the star-forming region. In our analysis we adopt a gas fraction of unity, i.e. gas is the dominant component, as this sets a lower limit on the maximum star formation rate surface density. If we adopt a gas fraction of $40\,\%$ then the maximum star formation rate surface density would rise by $60\,\%$. Adopting these values the maximum star formation rate surface density predicted by Andrews & Thompson (2011) is $\sim 1000\,\mathrm{M}_{\odot}\,\mathrm{yr}^{-1}\,\mathrm{kpc}^{-2}$.

The 23 SMGs in our sample have a median far-infrared luminosity of $(5.7 \pm 0.7) \times 10^{12}\,\mathrm{L}_{\odot}$, which corresponds to a median $\mathrm{SFR} = 990 \pm 120\,\mathrm{M}_{\odot}\,\mathrm{yr}^{-1}$ (for a Salpeter IMF). To derive the star formation rate surface density for our sample we initially divide the SFR of each SMG by a factor of two (the measured size of each SMG corresponds to the half-light radius of the profile). We show our sample in Figure 4.8, and assuming a uniform disc profile for the gas and cool dust distribution the median star formation rate surface density of the SMGs is $90 \pm 30\,\mathrm{M}_{\odot}\,\mathrm{yr}^{-1}\,\mathrm{kpc}^{-2}$. Only two SMGs have a star formation rate surface density above $500\,\mathrm{M}_{\odot}\,\mathrm{yr}^{-1}\,\mathrm{kpc}^{-2}$, and no SMGs exceed the maximum value predicted by Andrews & Thompson (2011).

The SMGs in our sample are forming stars at surface rate densities an order of magnitude lower than the estimated Eddington limit. However, we stress that these surface rate densities are integrated across the star-forming region (see Meurer et al. 1997). In

---

Here we have adopted a Rosseland mean dust opacity of $5\,\mathrm{cm}^{-2}\,\mathrm{g}^{-1}$ and a dust-to-gas ratio of $f_{\mathrm{dg}} = 90$ (see Andrews & Thompson 2011; Swinbank et al. 2014). Assuming the typical gas mass of SMGs, $4 \times 10^{10}\,\mathrm{M}_{\odot}$ (Swinbank et al., 2014), then the typical gas density of SMGs is $\Sigma_{\mathrm{g}} = 4000\,\mathrm{M}_{\odot}\,\mathrm{kpc}^{-2}$.

the well-studied lensed SMG SMM J2135-0102 (Swinbank et al., 2010b) it has been shown that the star formation is in four distinct "clumps" (FWHM = 100–300 pc), located within a gas disc with a half light radius ~ 1 kpc (Swinbank et al., 2011; Danielson et al., 2011, 2013). If the star formation in the SMGs in our sample is "clumpy", then individual regions in the gas disc may be Eddington limited, but the integrated star formation rate surface density will appear sub-Eddington.

Meurer et al. (1997) show that a sample of ultraviolet-selected sources (at $z = 0$–3) have a 90$^{\rm th}$ percentile global luminosity surface density of $2 \times 10^{11}\,{\rm L}_{\odot}\,{\rm kpc}^{-2}$ (with an associated uncertainty of a factor of three), which they interpret as an upper limit on the global luminosity surface density of a starburst. The SMGs presented here have a median global luminosity surface density of $(5.2 \pm 1.7) \times 10^{11}\,{\rm L}_{\odot}\,{\rm kpc}^{-2}$, a factor of three times higher than the value found by Meurer et al. (1997) (see Figure 4.8). A possible explanation for this discrepancy is that Meurer et al. (1997) measure half-light radii for the galaxies in their sample from ultraviolet imaging, and assume that dust attenuation is uniform across the galaxy. As discussed in § 4.6.1.1 we find that the rest-frame optical half-light radii of SMGs are a factor of four larger than the 870-μm dust half-light radius. The discrepancy in the optical sizes and dust sizes of SMGs indicates that their is significant differential reddening in these sources. If the ultraviolet-selected sources in (Meurer et al., 1997) suffer from similar differential reddening then the half-light radii measured in the ultra-violet are likely to overestimate the true extent of the star formation.

4.6.3 Are SMGs the progenitors of compact quiescent galaxies at $z \sim 2$?

It has been suggested that an evolutionary sequence exists whereby SMGs transition into local elliptical galaxies via a quiescent galaxy phase at redshift $z \sim 2$ (e.g. Lilly et al. 1999; Genzel et al. 2003; Blain et al. 2004; Swinbank et al. 2006; Tacconi et al. 2008; Swinbank et al. 2010a; Hickox et al. 2012; Toft et al. 2014; Simpson et al. 2014; Chen et al. 2015). This evolutionary scenario has been investigated by comparing properties, such as the stellar masses, spatial clustering, and space densities of SMGs, to the properties of the proposed descendants. However, each of these methods has significant uncertainties: the stellar masses of SMGs have been shown to be highly dependent on the assumed star formation history; the number of SMGs with measured dynamical masses is small and the samples are inhomogeneous; and the spatial clustering strength of single-dish identified sub-mm sources is biased by source blending.

Here we use sizes to test this evolutionary link, since a distinctive feature of the population of quiescent galaxies at redshift $z = 1$–3 is that they are extremely compact, with half-light sizes of $\sim 1\,\mathrm{kpc}$ [4] (e.g. Daddi et al. 2005; Zirm et al. 2007; Toft et al. 2007; Buitrago et al. 2008; van Dokkum et al. 2008; Newman et al. 2012; Patel et al. 2013; Krogager et al. 2013). A morphological analysis of SMGs thus provides an alternative route to investigating the proposed evolutionary sequence.

We construct a sample of spectroscopically confirmed quiescent galaxies at $z \sim 2$, to compare to SMGs, by combining the samples presented by van Dokkum et al. (2008) and Krogager et al. (2013). The galaxies in these samples have spectroscopically confirmed 4000Å / Balmer breaks, indicative of an old ($\gtrsim 0.5$–$1\,\mathrm{Gyr}$) stellar population, assuming no age-dependent dust reddening. Both studies use the code GALFIT to fit a Sérsic profile to the H-band emission from each galaxy. The combined sample of 24 quiescent galaxies has a median half-light radius of $R_\mathrm{e} = 1.5 \pm 0.2\,\mathrm{kpc}$ and a median Sérsic index of $n = 3.3 \pm 0.7$. The stellar masses of these galaxies are estimated to be $\gtrsim 10^{11}\,\mathrm{M}_\odot$ and the median redshift of the sample is $z = 2.2 \pm 0.1$. The age of the stellar population in these quiescent galaxies (0.5–1 Gyr) means that their progenitors likely lie at $z = 2.5$–3 consistent with the redshift distribution of SMGs (Toft et al. 2014; Simpson et al. 2014). We note that the half-light radii of the spectroscopically confirmed quiescent galaxies in our comparison sample are consistent with the sizes measured for a large sample of colour-selected quiescent galaxies at a similar redshift ($z = 1.5$–2.5) (Patel et al., 2013).

As discussed in § 4.6.1.1, Chen et al. (2015) show that the unobscured rest-frame optical light in SMGs has a median half light size of $R_\mathrm{e} = 4.4^{+1.1}_{-0.5}\,\mathrm{kpc}$ and Sérsic index of $n = 1.2 \pm 0.3$. In contrast, the quiescent galaxies in our comparison sample have a median half-light radius of $R_\mathrm{e} = 1.5 \pm 0.2\,\mathrm{kpc}$, significantly smaller than the rest-frame optical half-light radius of SMGs. The median Sérsic index of the SMGs is also significantly lower than the quiescent galaxies, indicating that a significant transformation of the light profile (and potentially stellar mass distribution) of SMGs is required if they are indeed the progenitors of the quiescent galaxies in our comparison sample. A number of studies have suggested that the star formation in SMGs is triggered by merger activity: in H-band/*HST* imaging $(82 \pm 9)\,\%$ of SMGs have signatures of interactions and/or irregular morphologies (Chen

[4] We note that mass selected samples ($M_\star > 5 \times 10^{10}\,\mathrm{M}_\odot$) containing both star-forming and quiescent galaxies at $z = 1$–3, have an half-light radius (4 kpc) that is higher than, and a Sérsic index (1.5) which is lower than, our sample of quiescent galaxies (see Patel et al. 2013; Buitrago et al. 2013)

et al., 2015), and the low Sérsic index n measured for the population is consistent with merging systems (Kartaltepe et al., 2012); dynamical studies of resolved Hα emission from SMGs find strong evidence of kinematically distinct multiple components (Swinbank et al., 2006; Alaghband-Zadeh et al., 2012); and a study of molecular line emission from SMGs finds that 75 % of sources are ongoing mergers, with the remaining 25 % classed as either disc or late stage mergers (Engel et al., 2010).

It is well established that mergers can induce torques that are effective at removing angular momentum from the gas in the system, allowing the gas to fall into the inner regions and potentially resulting in a kpc-scale nuclear starburst (e.g. Barnes & Hernquist 1991; Mihos & Hernquist 1994). Recently, Hopkins et al. (2013) presented numerical simulations of two gas rich disc galaxies undergoing a major merger at high-redshift. Hopkins et al. (2013) show that the major merger triggers an intense central starburst, with 50% of the star formation activity concentrated within a diameter of ~ 2 kpc. The simulations also demonstrate that the starburst increases the stellar surface density within the central 2 kpc diameter by two orders of magnitude. The size of the star-forming region in the SMGs presented in this work are consistent with simulations of major-mergers. If the star formation in SMGs is indeed a centrally concentrated starburst then we expect a significant rise in the concentration of the stellar component, increasing the fraction of light contained in a de Vaucouleurs-like ($n = 4$) profile.

4.6.3.1 Sérsic index

We now investigate whether there is evidence that the star formation in SMGs is more highly concentrated than the stellar component. First, we test whether our data have sufficiently high SNR to recover a more complex Sérsic profile [5]. We create 4000 model sources with a half-light size fixed at the median size of the SMGs, a range of Sérsic index from $n = 0.5$–4 and an SNR distribution that is uniform from 10–30 σ. To simulate realistic noise we add these models to a randomly chosen position in one of the residual (source-subtracted) ALMA maps.

We fit a Sérsic profile to each model source using the code GALFIT (Peng et al., 2010),

[5]The test we perform is to investigate the required SNR, and does not test the effects of spatial filtering on our ALMA maps, due to the configuration of the array. However, we note that the maximum angular scale that our maps are sensitive to is 5″, which is an order of magnitude larger than the FWHM of the SMGs in our sample.

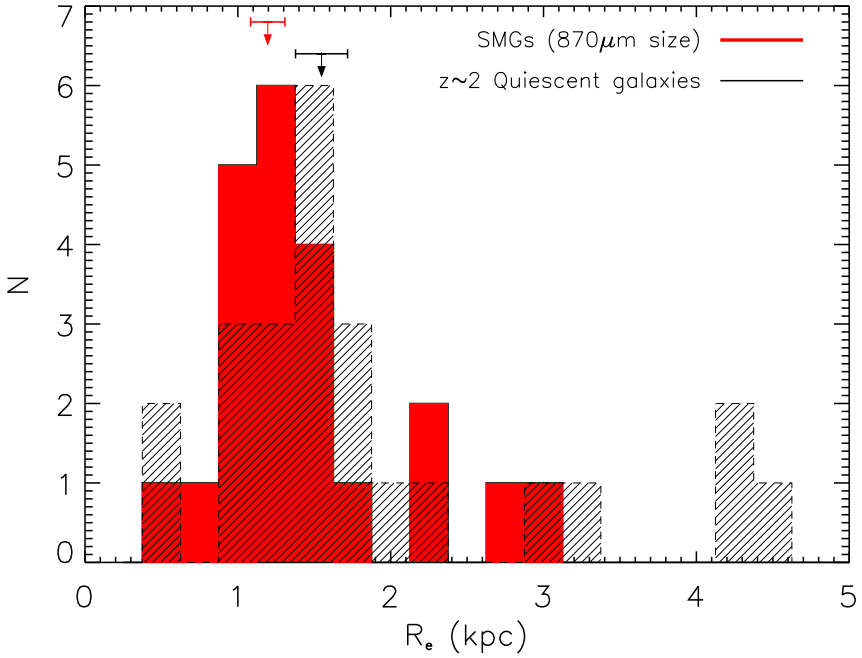

Figure 4.9: Comparison of the FWHM of the rest-frame FIR emission in SMGs to $z \sim 2$ quiescent galaxies, the proposed progenitors of local elliptical galaxies. The quiescent galaxies are selected to have strong 4000 Å / Balmer breaks, suggestive of an old stellar population, and are found to be compact in F160W/ *HST* imaging, with a median half light size of $R_{\rm e} = 1.5 \pm 0.2$, (van Dokkum et al., 2008; Krogager et al., 2013).

and find that the half-light size of the model sources is recovered accurately at all values of SNR and Sérsic index ($R_{\rm e}^{\rm rec} \,/\, R_{\rm e}^{\rm input} = 0.99 \pm 0.01$; 1-$\sigma$ dispersion ± 0.2). In contrast, although the Sérsic index is recovered correctly on average ($n^{\rm rec} \,/\, n^{\rm input} = 0.97 \pm 0.02$) the distribution has a 1-σ dispersion of 0.4–2.2, indicating that measurements for individual sources are highly uncertain [6]. Crucially, we find that the dispersion in the recovered Sérsic index is dependent on the SNR of the injected source; for SNR $> 20\,\sigma$ the 1-σ dispersion is 0.6–1.8. As such we do not attempt to fit a Sérsic profile on a source-by-source basis, but instead stack the 870 μm emission from the 23 SMGs detected at $> 10\,\sigma$ and use GALFIT to fit a Sérsic model to the stacked profile. The best-fit model to the stacked profile has a Sérsic index of $n = 2.5 \pm 0.4$ and a half-light radius of $R_{\rm e} = 0.17 \pm 0.03''$, where the errors are derived by bootstrapping the maps used in the stacking.

The median Sérsic index of the 870 μm emission from the SMGs is higher than the Sérsic index of the unobscured rest-frame optical light in SMGs (Chen et al. 2015, but

[6] If we re-fit our model sources, but force the Sérsic index to $n = 0.5$ the median recovered half-light size is $R_{\rm e}^{\rm rec} \,/\, R_{\rm e}^{\rm input} = 0.99 \pm 0.01$, with a 1-$\sigma$ dispersion ± 0.15

see also Targett et al. 2013), indicating that the ongoing star formation is more centrally concentrated. As we show in Figure 4.9, the half-light radius of the star formation in SMGs, median $R_{\rm e} = 1.2 \pm 0.1\,{\rm kpc}$, is comparable to the half-light radius of the quiescent galaxies in our comparison sample, $R_{\rm e} = 1.5 \pm 0.2\,{\rm kpc}$. If we combine the average Sérsic profile of the star formation and the pre-existing stellar population, under the simple assumption that the ongoing star-formation in SMGs doubles the luminosity of the stellar component, then the half-light radius of the resulting galaxy is $\sim 2\,{\rm kpc}$. This estimated half-light radius of the post-starburst SMGs is still marginally larger than median half-light radius of $z \sim 2$ quiescent galaxies. However, as shown by Chen et al. (2015) $(82 \pm 9)\,\%$ of SMGs have signs of either merger activity or disturbed morphologies, and it is likely that the size measured for the ongoing merger is larger than the size of the galaxy at post-coalescence. In addition, the contribution of the stars formed in the SMG phase to the luminosity of the post-starburst galaxy is highly dependent on the mass of stars formed and the relative ages of the stars formed in the starburst and the pre-existing stellar population. The half-light radius of the ongoing, extreme, star-formation in SMGs is comparable to the half-light radius of high-redshift compact quiescent galaxies, indicating that the ongoing star formation may explain the transformation required in the proposed evolutionary scenario from an intense starburst phase (SMG) to a local elliptical galaxies, via a compact quiescent galaxy at $z \sim 2$.

4.7 Conclusions

In this chapter we have presented high-resolution ($0.3''$) ALMA imaging of 52 SMGs in the UDS field. The main conclusions from our work are:

- We fit an elliptical Gaussian model to the 870 μm emission from 23 SMGs detected at ${\rm SNR} > 10\,\sigma$. The median diameter, deconvolved from the beam, of these 23 SMGs is ${\rm FWHM} = 0.30 \pm 0.04''$, and the distribution has a narrow interquartile range of 0.26–$0.42''$. Two SMGs in our sample (10 %) are best fit by a point source model, and have an upper limit on their size of $< 0.18''$. We stack the 870 μm emission from SMGs detected at ${\rm SNR} = 4$–$5\,\sigma$ and ${\rm SNR} = 5$–$10\,\sigma$, measuring an average size of $0.35^{+0.17}_{-0.10}''$ and $0.30 \pm 0.07''$ for each subset, respectively, consistent with the brighter examples.

- Using photometric redshifts we convert the angular diameter of each SMG to a physical scale. The median physical FWHM of the 23 SMGs detected at ${\rm SNR} > 10\,\sigma$

is 2.4 ± 0.2 kpc, and again the distribution has a narrow interquartile range of 1.8–3.2 kpc. We investigate the size of the rest-frame FIR-emission region in SMGs, but do not find a trend with either redshift or 870 μm flux density.

- We compare the 870 μm sizes of the SMG presented in this work to the sizes of SMGs measured at 1.4 GHz. The median FWHM of these SMGs is 5.1 ± 1.1 kpc, which is about two times larger than the median 870 μm size presented here. We convolve the median 870 μm profile of the SMGs with an exponentially declining kernel, with a scale length of 1–2 kpc, appropriate for modelling the radio and far-infrared emission in local star-forming galaxies (Murphy et al., 2008). The convolved profile has a FWHM = 3.8–5.2 kpc, showing that the radio sizes may be consistent with our sub-millimetre sizes. However, we caution that as stated by Murphy et al. (2008) the scale length of the convolution kernel may be sensitive to the star formation rate and morphology of the galaxy.

- We also compare the sizes we derive for the 870 μm emission region in SMGs to the sizes of SMGs measured from observations of resolved "moderate"-J ^{12}CO emission lines. Treating the upper limits in the CO studies as point sources, the median FWHM for the sample is 2.3 ± 1.1 kpc (rising to 3.7 ± 0.6 kpc if upper limits are taken as detections). Thus, the cool gas estimates of the sizes are consistent with the 870 μm sizes measured here.

- The pre-existing stellar population in SMGs has a half-light radius of $4.4^{+1.1}_{-0.5}$ kpc, as measured from rest-frame optical *HST* imaging (Chen et al., 2015), which is about four times larger than the extent of the ongoing star formation. The high dust content of SMGs means that the starburst component is likely to be missed in rest-frame optical imaging, while their prodigious star formation rates mean they have the potential to transform their stellar mass distribution. Hence, we expect the post-starburst galaxy to be compact, with a smaller half-light radius than the pre-existing stellar population.

- SMGs are slightly larger than local far-infrared bright galaxies (U/LIRGs), with low-J molecular gas sizes for the latter, median FWHM = 1.9 ± 0.2 kpc. However, these gas-derived sizes are likely to be larger than the far-infrared extents of the local galaxies, meaning the SMGs are probably physically larger systems.

- The 23 SMGs in our sample have a median star formation rate of SFR $= 1170 \pm 160\,\mathrm{M_\odot\,yr^{-1}}$ (for a Salpeter IMF), and a median star formation density of $90 \pm 30\,\mathrm{M_\odot\,yr^{-1}\,kpc^{-2}}$. The Eddington limit for a radiation pressure regulated starburst is $\sim 1000\,\mathrm{M_\odot\,yr^{-1}\,kpc^{-2}}$ (Andrews & Thompson, 2011). Hence, the SMGs in our sample have integrated star formation rate densities that are on average an order of magnitude lower than the Eddington limit. We suggest that this is due to the star formation occurring in "clumps", which may be Eddington limited, but appear sub-Eddington when integrated across the whole star formation region.

- The half-light radius of the ongoing star formation in SMGs is similar to the size of $z = 2.2 \pm 0.1$ quiescent galaxies, median $R_\mathrm{e} = 1.5 \pm 0.2$. The ongoing, compact, starburst in SMGs has the potential to at least double the pre-existing stellar mass, offering an explanation of the proposed transformation of SMGs into compact, quiescent galaxies at high-redshift, and thus how they fit into the evolutionary scenario proposed for local elliptical galaxies.

Chapter 5

Molecular gas in FIR-luminous QSOs at $z \sim 2.5$

5.1 Motivation

In section 1.6 of this thesis I discussed the proposed evolutionary pathway for a local elliptical galaxy. In this evolutionary scenario a high redshift merger of gas-rich galaxies results in a dust-obscured starburst phase (an SMG), which is followed by a period of intense AGN activity, or QSO phase. If such an evolutionary scenario exists then we expect to detect a small number of high redshift galaxies that are both far-infrared bright and are classified a QSO: sources that are transitioning between the star formation and AGN dominated phase. By observing the properties of such "transition" sources we can determine whether it is feasible that they are the descendents of SMGs. Prior to the work published in this thesis observations of far-infrared bright QSO had been presented in the literature (see Coppin et al. 2008) but, by selection, these QSO represent rare objects that correspond to an equally rare subset of the SMG population. The work presented in this chapter uses observations of molecular line emission with the PdBI to characterize two far-infrared bright QSO, selected to be representative of sources transitioning between the SMG and QSO phase. The following chapter is published, as written here, in Simpson et al. (2012), MNRAS, 426, 3201.

5.2 Abstract

We present IRAM Plateau de Bure Interferometer observations of the ^{12}CO (3–2) emission from two far-infrared luminous QSOs at $z \sim 2.5$ selected from the *Herschel*-ATLAS survey. These far-infrared bright QSOs were selected to have supermassive black holes (SMBHs) with masses similar to those thought to reside in sub-millimetre galaxies (SMGs) at $z \sim 2.5$; making them ideal candidates as systems in the potential transition from an ultraluminous infrared galaxy phase to a sub-mm faint, unobscured, QSO. We detect ^{12}CO (3–2) emission from both QSOs and we compare their baryonic, dynamical and SMBH masses to those of SMGs at the same epoch. We find that these far-infrared bright QSOs have similar dynamical but lower gas masses than SMGs. We combine our results with literature values and find that at a fixed $L_{\rm FIR}$, far-infrared bright QSOs have $\sim 50 \pm 30\%$ less warm/dense gas than SMGs. Taken together with previous results, which show QSOs lack the extended, cool reservoir of gas seen in SMGs, this suggests that far-infrared bright QSOs are at a different evolutionary stage. This is consistent with the hypothesis that far-infrared bright QSOs represent a short (~ 1 Myr) but ubiquitous phase in the transformation of dust-obscured, gas-rich, starburst-dominated SMGs into unobscured, gas-poor, QSOs.

5.3 Introduction

An evolutionary link between local ultraluminous infrared galaxies (ULIRGs, with far-infrared [FIR] luminosities of $L_{\rm FIR} \geq 10^{12}\,L_{\odot}$) and QSOs [1] was first suggested by Sanders et al. (1988) and considerable effort has been expended to test this connection in the local Universe (e.g. Tacconi et al. 2002; Veilleux et al. 2009). This hypothesis has been strengthened by the discovery of a relation between the mass of supermassive black holes (SMBHs) and the mass of their host spheroids (e.g. Magorrian et al. 1998; Gebhardt et al. 2000; Ferrarese & Merritt 2000), which suggests a physical connection between the growth of spheroids and their SMBHs. As shown by theoretical simulations, such a link can be formed through the suppression of star formation in a host galaxy by winds and outflows from an active galactic nucleus (AGN) at its centre (Di Matteo et al., 2005; Hopkins et al., 2005).

[1] QSO, quasi-stellar object, defined as having $M_{\rm B} \leq -22$ and one or more broad emission lines with a width $\geq 1000{\rm kms}^{-1}$

Both the ULIRG and QSO populations evolve very rapidly with redshift, and although subject to selection biases, intriguingly both populations appear to reach a broad peak in their activity at $z \sim 2.5$ (Shaver, 1988; Chapman et al., 2005; Wardlow et al., 2011). The high-redshift ULIRGs, which are typically bright at sub-millimetre wavelengths, and hence are called sub-millimetre galaxies (SMGs), are thought to represent the formation of massive stellar systems through an intense burst of star formation in the early Universe, potentially triggered by mergers of gas-rich progenitors (Frayer et al., 1998; Blain et al., 2002; Swinbank et al., 2006, 2010a; Tacconi et al., 2006, 2008; Engel et al., 2010) or cold accretion flows (Birnboim & Dekel, 2003; Dekel et al., 2009).

The similarity in the redshift distribution of the SMGs and QSOs may be indicating that the evolutionary link between these populations, which has been postulated locally, also holds at $z \sim 2$, when both populations were much more numerous, and significant in terms of stellar mass assembly. Indeed recent work on the clustering of $z \sim 2$ QSOs and SMGs has shown that both populations reside in parent halos of a similar mass, $M_{\rm halo} \sim 10^{13}\,{\rm M}_{\odot}$ (Hickox et al., 2012), adding another circumstantial connection between them. Moreover, this characteristic $M_{\rm halo}$ is similar to the mass at which galaxy populations transition from star-forming to passive systems (e.g. Brown et al. 2008; Coil et al. 2008; Hartley et al. 2010) which may be indirect evidence for the influence of QSO-feedback on star formation in galaxies (Granato et al., 2001; Lapi et al., 2006). One final circumstantial link between SMGs and QSOs comes from estimates of the masses of SMBHs in SMGs. Due to the dusty nature of SMGs these studies are inherently challenging, yielding results with more scatter than seen for optical quasars. However, they suggest that the SMBH masses are $\sim 10^{8}\,{\rm M}_{\odot}$, significantly lower than seen in comparably massive galaxies at the present-day (Alexander et al., 2008). This indicates the need for a subsequent phase of SMBH growth, which could be associated with a QSO phase.

One puzzling issue about the proposed evolutionary connection between high-redshift QSOs and SMGs is that only a small fraction of sub-millimetre detected galaxies ($s_{850} \gtrsim$ 5mJy), are identified as optically-luminous, $M_{\rm B} \leq -22$, $z \sim 1-3$ QSOs ($\sim 2\%$, Chapman et al. 2005; Wardlow et al. 2011), indicating that, if they are related, then the QSO and ULIRG phases do not overlap significantly. Taken together, these various results provide support for an evolutionary link between high-redshift ULIRGs (SMGs) and QSOs, with a fast transition ($\sim$ 1Myr) from the star-formation-dominated SMG-phase to the AGN-dominated QSO-phase (e.g. Page et al. 2012), where rapid SMBH growth can then

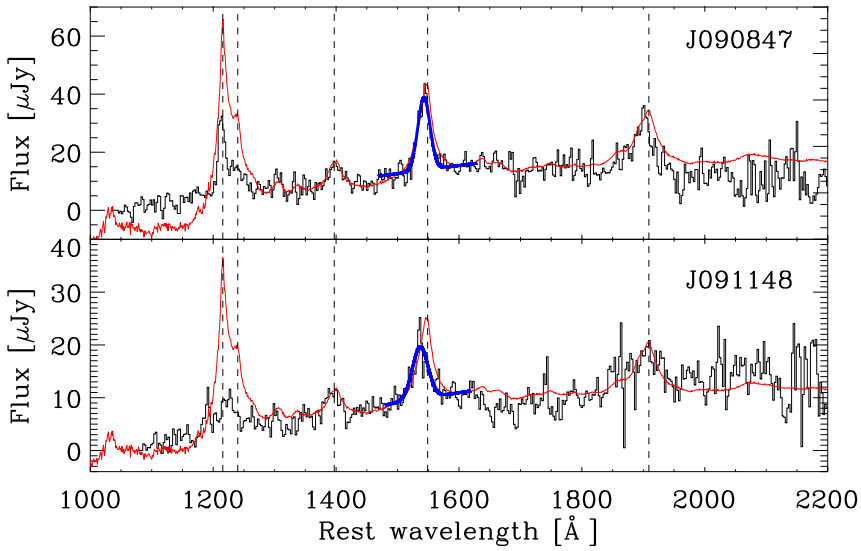

Figure 5.1: The 2SLAQ UV rest frame spectra for both QSOs in our sample from Croom et al. (2009), with the 2QZ composite QSO spectrum overlaid (red; Croom et al. 2002). From left-to-right, a dashed line indicates the rest wavelength of Lyα, NV, SiIV, CIV and CIII] emission. Both QSOs, but especially J0911+0027, have relatively weak Lyα 1215 emission when compared to CIV 1549, suggesting the presence of significant quantities of neutral gas in their vicinity (see also Omont et al. 1996). For each QSO we estimate the SMBH mass from the FWHM of the CIV 1549 line and the rest frame 1350Å luminosity (Vestergaard & Peterson, 2006). The FWHM of the CIV line is derived from the best fitting Gaussian and continuum model (shown in blue), which provides an adequate fit to the emission line in both cases: $\chi^2_{\rm r} = 1.4$ for J0908−0034 and $\chi^2_{\rm r} = 1.5$ for J0911+0027. The rest wavelength scale of the plots is based on the systemic redshifts derived from ^{12}CO (3–2), see § 5.5.

subsequently account for the present-day relation between spheroid and SMBH masses. In this scenario, when a QSO *is* detected in the far-infrared/sub-millimetre it will be in the transition phase from an SMG to an unobscured QSO, making its physical properties (e.g. gas mass, dynamics, etc.) a powerful probe of the proposed evolutionary cycle (e.g. Page et al. 2004, 2011; Stevens et al. 2005).

In this chapter we present a study with the IRAM Plateau de Bure interferometer (PdBI) of the cold molecular gas in two far-infrared-selected "transition" candidate QSOs from the *Herschel Space Observatory*[2] (Pilbratt et al., 2010) H-ATLAS survey (Eales et al., 2010). We detect ^{12}CO (3–2) in both far-infrared bright QSOs studied, and compare the gas and kinematic properties of these to other ^{12}CO-detected QSOs and SMGs to relate their evolution. Throughout we adopt cosmological parameters from Spergel et al. (2003) of: $\Omega_m = 0.27$, $\Omega_\Lambda = 0.73$ and $\mathrm{H}_0 = 71\,\mathrm{km\,s^{-1}\,Mpc^{-1}}$.

5.4 Observations & Data Reduction

5.4.1 Sample Selection

Our aim is to study the molecular gas and dynamical properties of far-infrared bright QSOs to test their evolutionary link to SMGs, for which larger samples are now available (Greve et al., 2005; Bothwell et al., 2013). We focus our study on potential transition (far-infrared bright) QSOs at the era when the activity in both the QSO and SMG populations peaked, $z \sim 2.5$. Previous ^{12}CO studies of unlensed far-infrared or sub-millimetre-bright QSOs (Coppin et al. 2008, including data from Beelen et al. 2004) have usually studied the most luminous QSOs, with SMBH masses 1–2 orders of magnitude larger than those seen in typical SMGs and correspondingly low space densities. Both of these factors make it hard to test an evolutionary link between these QSOs and typical SMGs (studies of lensed QSO samples, Riechers 2011, also suffer from the difficulty of determining the true space densities of the sources being studied). The limitations of these previous studies arose because of the lack of large samples of far-infrared/sub-millimetre detected QSOs; hence Coppin et al. (2008) selected a sample of luminous QSOs which were later found to be bright in the sub-mm. But with the advent of wide-field far-infrared/sub-millimetre surveys with *Herschel* we can now select samples of QSOs with redshifts, space densities,

[2] *Herschel* is an ESA space observatory with science instruments provided by European-led Principal Investigator consortia and with important participation from NASA

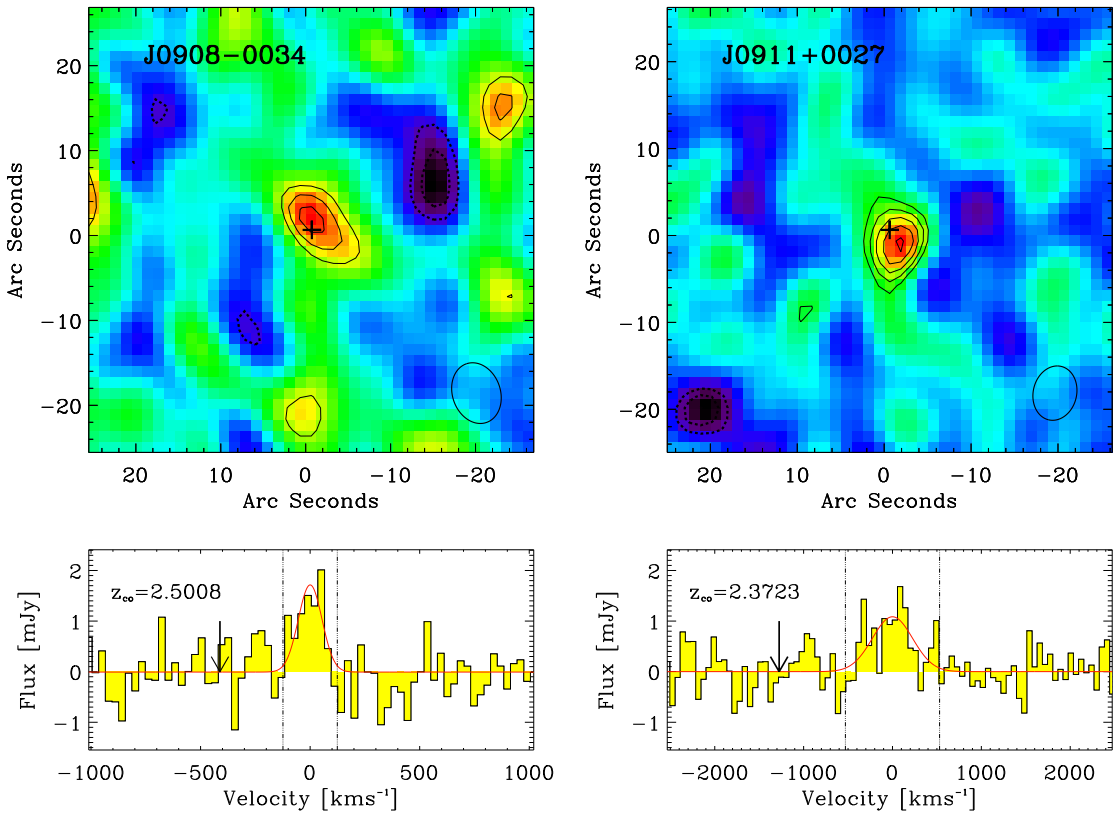

Figure 5.2: Top: The velocity-integrated ^{12}CO (3–2) emission for the two QSOs (summed over the regions marked in the spectra below). The contours represent signal-to-noise, and are spaced at $\pm 3, 4, 5, ... \times \sigma$ (dashed contours are negative). Significant ^{12}CO (3–2) emission is detected from both QSOs and is well-centered on the optical positions of the QSOs, indicated by a cross (offset by 1–2″, which is within the primary beam). Analysis of the channel maps shows both sources are unresolved with no evidence of velocity gradients, although the modest spatial resolution of our maps means that this is not a strong constraint. **Bottom**: Spectra showing the redshifted ^{12}CO (3–2) emission lines from both QSOs. The spectra were binned to a resolution of 10 MHz and 20 MHz respectively, and we overlay the best fitting Gaussian plus continuum model (the continuum emission in both QSOs is negligible). The redshift derived from ^{12}CO (3–2) as well as the line flux and line widths derived from the Gaussian fits are reported in Table 2. We note that the FWHM of the J0908−0034 emission line is relatively narrow, at $125 \pm 25\,\mathrm{km\,s^{-1}}$, compared to $530 \pm 100\,\mathrm{km\,s^{-1}}$ for J0911+0027. In each spectrum the predicted position of the ^{12}CO (3–2) emission line, from the 2SLAQ UV spectrum, is indicated by an arrow. The two dot-dashed lines correspond to ±FWHM, and show the region which was summed to produce the maps above.

QSO	$\alpha_{\rm CO}$ (J2000)	$\delta_{\rm CO}$ (J2000)	$S_{250\mu{\rm m}}$ [a] (mJy)	$S_{350\mu{\rm m}}$ [a] (mJy)	$S_{500\mu{\rm m}}$ [a] (mJy)	$S_{3{\rm mm}}$ (mJy)
J0908−0034	09 08 47.18	−00 34 16.6	9.0 ± 6.6	26.2 ± 8.1	15.0 ± 9.0	< 1.4
J0911+0027	09 11 48.30	+00 27 18.4	25.3 ± 5.8	14.7 ± 6.6	7.7 ± 7.8	< 1.0

Table 5.2: [a] J0908-0034 flux density values are after deblending sources. Fluxes extracted at the optical position of the QSO, before deblending, are 15.6 ± 6.4 mJy, 39.5 ± 7.1 mJy and 41.0 ± 8.5 mJy

far-infrared luminosities and most critically SMBH masses which are well-matched to those of the hypothesised descendents of typical SMGs.

For our analysis we have therefore used the sample of far-infrared observed QSOs from Bonfield et al. (2011) which are derived from the survey of the 9^h H-ATLAS field (Eales et al., 2010). Bonfield et al. (2011) extracted far-infrared fluxes from the SPIRE 250, 350 and 500-μm maps (Griffin et al., 2010; Pascale et al., 2011) at the optical position of 372 QSOs from either SDSS (Schneider et al., 2010) or 2SLAQ (Croom et al., 2009) surveys across the $\sim 16\,{\rm degree}^2$ field. A statistical background subtraction was performed on the measured fluxes for each QSO to account for confusion in the maps, see Bonfield et al. (2011). Of the 372 QSOs, $\sim 20\,\%$ are consistent with having $L_{\rm FIR} \geq 10^{12}\,L_{\odot}$, making them candidates for "transition" QSOs (e.g. between a far-infrared bright SMG and far-infrared faint unobscured QSO phase). Restricting the redshift range to $z = 2$–3 (to roughly match the redshift peak of SMGs, Chapman et al. 2005), gives 29 QSOs. We then estimated SMBH masses for these QSOs from the extrapolated rest frame 5100-Å luminosities (e.g. Wandel 1999) to select those with SMBH masses of $M_{\rm BH} \lesssim 3 \times 10^8\,{\rm M}_{\odot}$, comparable to SMGs (Alexander et al., 2008). These selection criteria resulted in nine targets and from this list we selected six QSOs for a project to determine their gas masses and dynamics through the detection of ^{12}CO (3–2) emission with PdBI. We estimated systemic redshifts for these QSOs using the measured wavelengths from Gaussian fits to the SiIV 1397, CIV 1549 and CIII] 1909 emission lines in their spectra (Fig. 5.1). We then adjust our estimates by the weighted mean velocity offsets of these lines from ^{12}CO (3–2), for the ^{12}CO-detected QSOs in Coppin et al. (2008) (we find SiIV 1397 provides the best estimate of the systemic redshifts). We note that, as previously seen by Omont et al. (1996), roughly $\sim 80\%$ of these far-infrared bright QSOs show very weak Lyα emission (Fig. 5.1). There may be a relation between far-infrared luminosity and weak Lyα, but

its physical origin is still unknown.

This chapter presents the PdBI observations of two QSOs from this sample: J0908−0034 (RA: 09 08 47.18, Dec: −00 34 17.9, J2000; $z_{\rm UV} = 2.5073$) and J0911+0027 (RA: 09 11 48.38, Dec: +00 27 19.7, J2000, $z_{\rm UV} = 2.3697$). Due to scheduling priorities the remaining four targets in the sample have not yet been completed. In this chapter we therefore combine our observations with literature values for ^{12}CO (3–2) detected FIR-bright QSOs, creating a sample from which we can study the population as a whole. As discussed earlier the limitations of previous studies means the literature values do not easily relate to the typical SMG, and due to their large SMBH masses are considered statistical outliers in the evolutionary scenario we propose. In § 5.6 we discuss our observations and their agreement with a simple evolutionary model linking SMGs and QSOs.

5.4.2 PdBI Observations

We used the six-element IRAM PdBI in compact (D) configuration to search for redshifted ^{12}CO (3–2) emission from the QSOs. We tuned the correlator WideX to the frequency of redshifted ^{12}CO (3–2) from the estimated redshifts derived from their UV emission lines (Fig. 5.1): 98.593GHz and 102.619GHz, for J0908−0034 and J0911+0027 respectively. The advantage of WideX is that its 3.6-GHz (dual polarisation) spectral coverage, at a fixed channel spacing of 1.95MHz, corresponds to a velocity range of $\sim$10,000 km s^{-1}, sufficient to identify the ^{12}CO (3–2) line even if the UV lines are significantly offset from the systemic redshift. We obtained a total on-source observing time of 6 hr for each QSO between 2010 April 26 and 2010 May 4. The overall flux density scale was calibrated to 3C 273, with observations of J0906+015 for phase and amplitude calibration. Receiver bandpass calibration was performed on 0923+392. The data were calibrated in the GILDAS software package and a naturally weighted data cube produced for each QSO. In this configuration the synthesised beam for natural weighting is $6.3'' \times 5.0''$ at a position angle (PA) of 166° for J0908−0034, and $7.3'' \times 5.6''$ at a PA of 19° for J0911+0027.

5.4.3 Far-infrared Luminosities and SMBH Masses

For our analysis we derive more accurate estimates of the far-infrared luminosities and SMBH masses of our QSOs. To estimate far-infrared luminosities of the QSOs in our sample, we exploit the *Herschel* SPIRE 250, 350 and 500-μm imaging. For each QSO, we deblend multiple sources in the vicinity, using the 250μm map to identify nearby sources.

Source	$z_{\rm CO}$	$S_{\rm CO}\Delta\nu$	FWHM$_{\rm CO}$	$L'_{\rm CO\,(3-2)}$	$L_{\rm FIR}$	$M_{\rm gas}$	$M_{\rm BH}$
		(Jy km s^{-1})	(km s^{-1})	(10^{10} K km s^{-1} pc^2)	($10^{12}\,L_\odot$)	($10^{10}\,{\rm M}_\odot$)	($10^8\,{\rm M}_\odot$)
J0908−0034	2.5008 ± 0.0002	0.23 ± 0.04	125 ± 25	0.77 ± 0.15	3.1 ± 0.8	0.77 ± 0.15	$1.6^{+0.3}_{-0.2}$
J0911+0027	2.3723 ± 0.0005	0.62 ± 0.10	530 ± 100	1.9 ± 0.3	3.5 ± 0.8	1.9 ± 0.3	$2.3^{+1.4}_{-0.9}$

Table 5.4: Physical properties of the FIR-bright QSOs in our sample.

For J0911+0027 there is a bright 250μm source centered at the optical position of the QSO which is clearly isolated, but J0908−0034 has significant (40%–60% at 250–500μm) contamination from a galaxy $\sim$30$''$ away. We report the final deblended photometry for each source in Table 5.1. To derive the far-infrared luminosity for each QSO, we fit a modified black body spectra to the SPIRE photometry, adopting a dust emissivity, $\beta = 1.6$ and fixing the temperature of the modified black body at $T_{\rm d} = 40\,K$, (the average dust temperature of $z \sim 2$–3 QSOs, Beelen et al. 2006) and calculate the far-infrared luminosity ($L_{\rm FIR}$) by integrating the best-fit SED between (rest-frame) 8–1000 μm. We note that if we instead allow the characteristic dust temperature to vary in the SED fit, we see at most a $\sim$45% change in $L_{\rm FIR}$, consistent within our error estimates. The modified black body fits confirm the $L_{\rm FIR}$ for both QSOs is $\sim (3-4\pm1)\times10^{12}\,L_\odot$ (Table 5.3). In comparison the median $L_{\rm FIR}$ for the QSO sample of Coppin et al. (2008) is $L_{\rm FIR} = (7.5\pm1.5)\times10^{12}\,L_\odot$, and the SMGs in Bothwell et al. (2012) is $L_{\rm FIR} = (4.8\pm0.6)\times10^{12}\,L_\odot$. The implied star-formation rates [3] (SFR) are 500–700 ${\rm M}_\odot\,{\rm yr}^{-1}$.

Similarly we calculated SMBH masses for both QSOs from the FWHM of their CIV 1549 emission lines and their rest frame 1350-Å continuum luminosities (L_{1350}), following Eq. 7 from Vestergaard & Peterson (2006). This relation is calibrated to the results of reverberation mapping, however the geometry of the broad line region (producing the emission lines) is poorly constrained and we caution it may bias virial mass estimates to low values (Jarvis & McLure, 2006; Fine et al., 2011). Nevertheless we derive the FWHM from a Gaussian fit to the CIV emission line in the 2SLAQ spectra (Fig. 5.1), measuring $4500\pm340\,{\rm km\,s}^{-1}$ and $5900^{+1600}_{-1300}\,{\rm km\,s}^{-1}$ for J0908−0034 and J0911+0027 respectively, and determine L_{1350} from the g-band SDSS magnitudes of $g = 21.41\pm0.05$ for J0908−0034 and $g = 21.64\pm0.05$ for J0911+0027. As we do not see strong evidence of reddening in the 2SLAQ spectrum of either QSO we do not consider the effects of dust extinction on

[3] SFR (${\rm M}_\odot{\rm yr}^{-1}$) $= 1.7\times10^{-10}\,L_{\rm FIR}$ ($L_\odot$) Kennicutt (1998), following a Salpeter IMF over a mass range 0.1–100${\rm M}_\odot$

our estimates of L_{1350} (Fig. 5.1). From these we estimate SMBH masses of $\sim 2 \times 10^8\,\mathrm{M}_\odot$ for both QSOs[4] (Table 5.3). We caution that estimates from the CIV emission line can overpredict the SMBH mass by a factor of 2–5, when compared to estimates from Hα (Ho et al., 2012). In the absence of a more robust mass estimator, we simply acknowledge that the SMBH masses of our sources may be overestimated.

5.5 Analysis & Results

We detect ^{12}CO emission near the optical position of each QSO (within $\lesssim$1–2″) and at frequencies close to those expected for redshifted ^{12}CO (3–2). For each QSO, we fit a combination of a Gaussian and a uniform continuum to the spectrum corresponding to the peak signal-to-noise, S/N, pixel in each map and report the resulting redshift, line width and line flux in Table 2, as well as overplotting the fit on Fig. 5.2. We detect no significant continuum emission at 3mm in either QSO (3-σ limits given in Table 5.1), which is consistent with no contribution from synchrotron emission to the far-infrared luminosities of these systems. The quoted errors were obtained from a bootstrap error analysis on the model fit to the data. The resulting values of χ^2 indicate good fits to both emission lines: $\chi^2_\mathrm{r} = 1.0$ for J0908−0034 and $\chi^2_\mathrm{r} = 1.1$ for J0911+0027. Previous results have found $\sim 25\%$ of SMGs display a double-peaked emission line, with a velocity difference between peaks $\gtrsim 500\,\mathrm{km\,s^{-1}}$ (Greve et al., 2005; Tacconi et al., 2006; Engel et al., 2010; Bothwell et al., 2013), indicating either a merger or disk-like kinematics. To test for this we attempt to fit a double Gaussian model to the spectra in Fig. 5.2. We find it produces a negligible improvement in χ^2, and conclude that single Gaussian fits are sufficient to describe the line profiles of both QSOs.

We collapse the spectral cube over the frequency range corresponding to $\pm$FWHM of the emission line to create the maps of the ^{12}CO (3–2) emission shown in Fig. 5.2. These maps are continuum subtracted, although as we noted above no significant continuum is detected in either source. We now discuss the ^{12}CO (3–2) emission line properties of each QSO in more detail.

J0908−0034 — The integrated ^{12}CO (3–2) emission is detected at a S/N of 5.5σ. The ^{12}CO emission line is relatively narrow and so we bin to a frequency resolution of 10 MHz

[4]We estimate errors by bootstrap resampling the 2SLAQ spectrum, with replacement, and re-fitting a Gaussian model.

($\sim 30\,\mathrm{km\,s^{-1}}$), as shown in Fig. 5.2. We find the ^{12}CO (3–2) emission line to be well fit by a single Gaussian with FWHM $= 125 \pm 25\,\mathrm{km\,s^{-1}}$, and a velocity-integrated flux of $S_{\rm CO}\Delta\nu = 0.23 \pm 0.05\,\mathrm{Jy\,km\,s^{-1}}$; see Table 2. From the peak of the Gaussian distribution, we determine a ^{12}CO redshift of $z = 2.5008 \pm 0.0002$. We compared $z_{\rm CO}$ with the wavelength of emission lines in the 2SLAQ spectrum of this QSO (Fig. 5.1). We found the UV lines to be blue-shifted by $\Delta v \sim 100$–$500\,\mathrm{km\,s^{-1}}$, relative to $z_{\rm CO}$, with Lyα and Nv emission lines having the largest offset. Systematic offsets of UV emission lines are not unusual, and are usually attributed to resonant scattering of the emission line, due to material in the line of sight to the AGN (Steidel et al., 2010). At the spatial resolution of our D-configuration PdBI observations we do not find any evidence for spatially resolved ^{12}CO (3–2) emission, and channel maps show no sign of a velocity gradient across the source.

J0911+0027 — The integrated ^{12}CO emission is detected at a significance of 7.2σ. The ^{12}CO (3–2) spectrum is binned to a frequency resolution of 20 MHz ($\sim 60\,\mathrm{km\,s^{-1}}$), as shown in Fig. 5.2. We find the ^{12}CO (3–2) emission line to be well fitted by a single Gaussian distribution with FWHM $= 530 \pm 100\,\mathrm{km\,s^{-1}}$, and a velocity integrated flux of $S_{\rm CO}\Delta\nu = 0.62 \pm 0.10\,\mathrm{Jy\,km\,s^{-1}}$; see Table 2. We determine a ^{12}CO redshift of $z = 2.3723 \pm 0.0005$ from the line fit. The rest frame UV emission lines in the 2SLAQ spectrum of this QSO are blue-shifted by $\Delta v \sim 500$–$1500\,\mathrm{km\,s^{-1}}$, relative to $z_{\rm CO}$ (Fig. 5.1). As with J0908−0034, Lyα and Nv emission lines display the largest offsets, but strong absorption in Lyα and Nv may affect the accuracy of the Gaussian fit to the emission lines. At the low spatial resolution of our D-configuration observations there is no evidence for spatially resolved ^{12}CO (3–2) emission, and again the channel maps do not show any indication of velocity gradients across the emission line.

We now compare our observations of these two far-infrared-luminous, but otherwise fairly typical, QSOs with the more luminous (and more massive) far-infrared bright QSOs previously studied, as well as with the SMG population. In particular, we investigate what the observed properties of our QSOs can tell us about their relationship to SMGs.

5.5.1 Gas Mass

The ^{12}CO (3–2) line emission from each QSO provides information about the molecular gas mass of the system (Solomon et al., 1997). We determine the ^{12}CO (3–2) line luminosity, $L'_{\rm CO\,(3-2)}$, following Eq. 3 from Solomon & Vanden Bout (2005), deriving

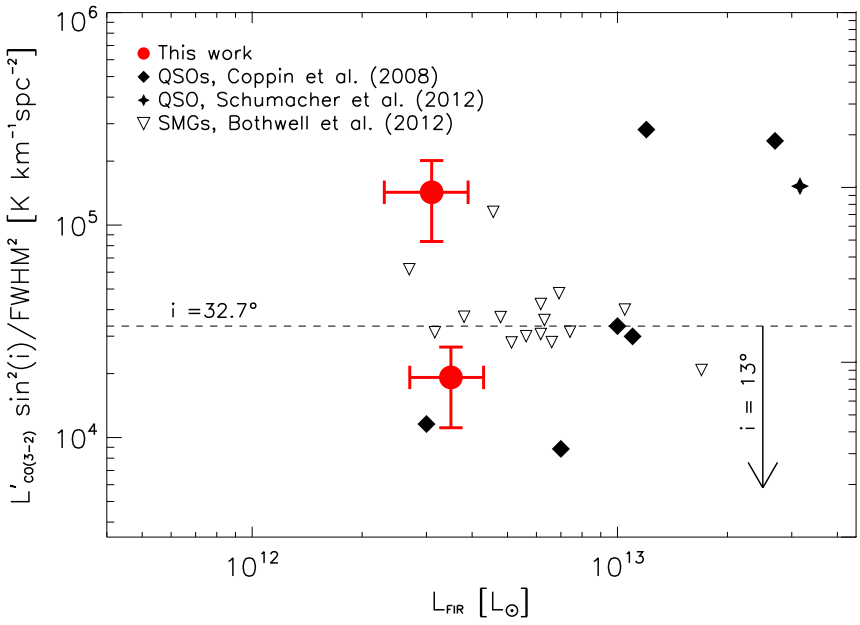

Figure 5.3: The variation in $L'_{\mathrm{CO}(3-2)} \sin^2 i/\mathrm{FWHM}^2$, a proxy for molecular gas-mass fraction, as a function of far-infrared luminosity, for high-redshift QSOs and SMGs. We adopt a mean inclination for both populations, of 32.7°, appropriate for randomly orientated discs. For each sample we determine the median, but given the similarity of the results, we show only the QSO value (dashed line). Our proxy for gas mass fraction assumes the gas reservoirs in QSOs and SMGs have the same geometry, physical radius and mean inclination on the sky. We do not expect SMGs to suffer an inclination bias, but this may not be true for the optically-identified QSOs we study here, as the identification is based on their broad line properties. We indicate with an arrow the effect of adopting a mean inclination of 13° for the QSO population, which may be more realistic, see § 5.5.2. One of our targets, J0908−0034, has an unusually narrow emission line, indicating the galaxy is observed close to face on. By adopting an average inclination we may be deriving a low dynamical mass, and hence a high gas fraction, for this source. Our proxy also assumes the population have the same line brightness ratio, see § 5.5.1. A value of $r_{31} = 0.52$ is more appropriate for SMGs, and would further increase the separation between the implied gas mass fractions of SMGs and QSOs, with the later having lower gas fractions, and hence appearing more evolved.

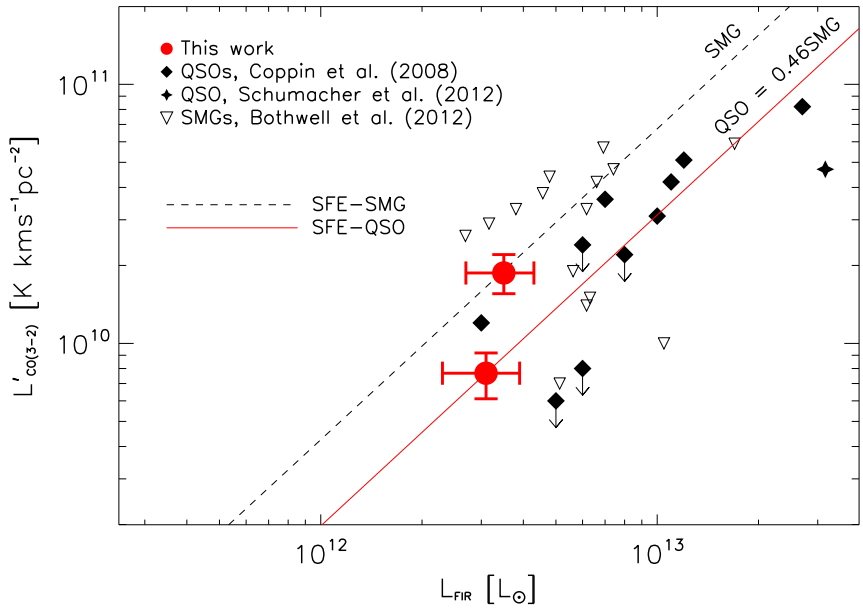

Figure 5.4: ^{12}CO (3–2) line luminosity ($L'_{\mathrm{CO\,(3-2)}}$) versus far-infrared luminosity (L_{FIR}) for far-infrared bright QSOs and ^{12}CO (3–2) detected SMGs. We plot the best-fit line to the SMG population and we fix the gradient of the fit to the QSOs to that measured for the SMGs, $\mathrm{dL'_{CO\,(3-2)}/dL_{FIR}} = 1.2 \pm 0.3$ (Bothwell et al., 2013). We treat upper limits in our QSOs sample as detections, and as such the fit is a conservative upper estimate. At a fixed L_{FIR} the QSOs have $L'_{\mathrm{CO\,(3-2)}}$ which is a factor of $\sim 50 \pm 30\%$ lower than the SMGs. A two-sided KS test indicates a 99.3% probability the $L'_{\mathrm{CO(3-2)}}/\,L_{\mathrm{FIR}}$ ratio for SMGs and QSOs are drawn from a different parent distribution. If we take into account the difference in the line brightness temperature ratios, r_{31}, for the two populations then this probability increases to 99.95%. The differences in the populations are in the sense that the far-infrared bright QSOs appear to have shorter gas consumption timescales, consistent with representing a subsequent evolutionary phase.

$L'_{\rm CO\,(3-2)} = (0.77\pm0.15)\times10^{10}\,{\rm K\,km\,s^{-1}\,pc^2}$ and $L'_{\rm CO\,(3-2)} = (1.9\pm0.3)\times10^{10}\,{\rm K\,km\,s^{-1}\,pc^2}$ for J0908−0034 and J0911+0027 respectively (Table 2).

To estimate the total masses of the gas reservoirs in these QSOs, we use the ^{12}CO (3–2) luminosity to determine the expected ^{12}CO (1–0) luminosity and from that derive the total gas mass. For the first step we must adopt a line brightness ratio, $r_{31} = L'_{\rm CO\,(3-2)}\,/\,L'_{\rm CO\,(1-0)}$, to convert the ^{12}CO (3–2) line luminosity to a ^{12}CO (1–0) luminosity. Bothwell et al. (2013) determine that for SMGs $r_{31} = 0.52 \pm 0.09$, which reflects the presence of an extended reservoir of cold gas. However, recent results indicate that such an extended reservoir is not present in QSOs, and as such we follow the results of Riechers et al. (2011a) and adopt a value of $r_{31} = 1.0$ (i.e. thermalised gas) in the conversion for both our QSOs, and the QSO sample of Coppin et al. (2008). We caution that this assumption has not been tested for our sample of QSOs, and in fact in AGN dominated systems super-thermal ratios, i.e. $r > 1$, are not uncommon (e.g. Papadopoulos et al. 2008; Ivison et al. 2012). We then adopt a CO-to-H_2 conversion factor of $\alpha = 1\,{\rm M_\odot}\,({\rm K\,km\,s^{-1}\,pc^2})^{-1}$ following Solomon & Vanden Bout (2005) to convert $L'_{\rm CO}$ (1–0) to a gas mass. Note that α is denoted as a conversion to H_2, but the resulting H_2 mass is defined as the total H_2+He gas mass. For ease of comparison we adopt the same value for α used in the SMG survey of Bothwell et al. (2013), and for consistency we scale the gas masses quoted in Coppin et al. (2008) to this value. In this manner we derive gas masses of $M_{\rm gas} = (0.77\pm0.15)\times10^{10}\,{\rm M_\odot}$ and $M_{\rm gas} = (1.9 \pm 0.3) \times 10^{10}\,{\rm M_\odot}$ for J0908−0034 and J0911+0027 respectively.

The gas masses of our far-infrared luminous QSOs are lower than the median gas mass of the typically more far-infrared luminous QSOs detected by Coppin et al. (2008), $M_{\rm gas} = (4.3 \pm 1.0) \times 10^{10}\,{\rm M_\odot}$, and they are also lower than the median gas mass of SMGs from Bothwell et al. (2013), $M_{\rm gas} = (5.3 \pm 1.0) \times 10^{10}\,{\rm M_\odot}$. We note that there is significant scatter around these averages. As we will discuss in § 5.6, the lower gas masses we derive for our far-infrared QSOs are consistent with them having recently evolved from a previous-SMG phase.

5.5.2 Gas Fraction

One rough measure of the evolutionary state of a system is the fractional contribution of molecular gas to its total mass. Hence, in the absence of significant replenishment of gas from external sources, we would expect the gas-mass fraction in SMGs to decline as they evolve, and thus in the evolutionary model we are testing, our QSOs ought to have lower

gas-mass fractions than SMGs.

In Fig. 5.3 we use a combination of observables which trace gas mass, $L'_{\mathrm{CO(3-2)}}$, and dynamical mass, $\mathrm{FWHM}^2/\sin^2 i$, as a proxy for gas-mass fraction, $L'_{\mathrm{CO(3-2)}}\sin^2 i/\mathrm{FWHM}^2$. In choosing this proxy we make two implicit assumptions: *(i)* that the conversion of $L'_{\mathrm{CO(3-2)}}$ to M_{gas} is the same for SMGs and QSOs, i.e. the populations have the same value of r_{31} and α; *(ii)* the physical extent, and orientation, of the reservoir is similar in both populations. Fig. 5.3 shows that the far-infrared bright QSOs have similar values of $L'_{\mathrm{CO(3-2)}}\sin^2 i/\mathrm{FWHM}^2$ on average to SMGs. To determine if this means that they have similar gas-mass fractions (potentially indicating they are not more evolved) we need to consider the two simplifying assumptions above.

It is believed that SMGs do not suffer from an inclination selection bias as their submillimetre emission is optically thin and so, if we are modelling their gas distributions as disc-like systems (Swinbank et al., 2011), we can adopt a mean inclination of 32.7°, appropriate for randomly orientated discs (Bothwell et al., 2013). Recent studies comparing ^{12}CO linewidths of QSOs and SMGs found no distinction between the populations, indicting that they have the same average inclination (Coppin et al., 2008). As such, in our analysis we adopt the same average inclination for QSOs and SMGs. However, optically-identified QSOs such as those studied here may have preferentially biased orientations, as to have identified them as QSOs we must be able to observe their broad-line regions. If we adopt a mean inclination of 13°, which has been previously suggested (Carilli & Wang, 2006), then the QSOs sample has an $\sim 85\%$ lower gas mass fraction, on average, than the SMGs. While the difference is significant at only 2.0σ, it is in the sense expected if QSOs are more evolved systems. We note that one of our targets, J0908−0034, has an unusually narrow line width for a high redshift galaxy, indicating we may be observing the system close to face on. By assuming an average inclination of 32.7° we may be deriving a low dynamical mass, and hence significantly overestimating the gas fraction for this source.

Our proxy for gas mass fraction also assumes the conversion from $L'_{\mathrm{CO(3-2)}}$ to gas mass is the same for both the QSO and SMG populations, which is a conservative assumption. If instead we were to include the differences in line brightness temperature ratio (r_{31}), expected for the two populations ($r_{31} = 1.0$ for QSOs, and $r_{31} = 0.52$ for SMGs), then the gas mass fraction is roughly doubled in SMGs, and as a result the offset between the populations in Fig. 5.3 becomes larger and the statistical significance of the difference increases to 3.6σ (including a bias in the QSO inclination). We conclude that although

the estimated gas mass fractions of far-infrared bright QSOs appear similar to typical SMGs, after adopting reasonable assumptions for the excitations and orientations of the two populations there is evidence of a difference in their gas fractions.

5.5.3 Gas Consumption Time Scales

A second important measure of the evolutionary state of SMGs and QSOs comes from their gas-consumption timescales: $M_{\rm gas}$/SFR (or the inverse of this: the star-formation efficiency). In our evolutionary scenario the gas reservoir in SMGs is depleted by star formation as they transform from dusty systems to unobscured QSOs. Our 'transition' FIR-bright QSOs are expected to represent a unique evolutionary phase, with prodigious star formation but lower gas masses, and thus shorter gas consumption timescales.

The ratio of the observables, ^{12}CO (3–2) line luminosity, $L'_{\rm CO(3-2)}$, and far-infrared luminosity, $L_{\rm FIR}$, can be used as a proxy for the gas consumption timescale of a galaxy. This ratio has the advantage that we do not make any assumptions in the conversion of ^{12}CO (3–2) measurement to ^{12}CO (1–0). We have therefore gathered samples of SMGs and FIR-bright QSOs which have been detected in ^{12}CO (3–2), allowing a direct comparison of observable quantities. We use literature values for the ^{12}CO (3–2) luminosities of QSOs (Beelen et al., 2004; Coppin et al., 2008; Schumacher et al., 2012) and ^{12}CO (3–2) detected SMGs (Bothwell et al., 2013). We plot our QSOs along with these comparison samples on Fig. 5.4, and overlay the best fit line to each sample. To test for a offset between the populations we fix the gradient of each line at 1.2 ± 0.3, which is the best fit value to ^{12}CO (3–2) SMGs (Bothwell et al., 2013). We also caution that when fitting a line to the sample upper limits are treated as detections. If any of these non-detections have significantly lower values of $L'_{\rm CO(3-2)}$ then the offset to the SMG population, seen in Fig. 5.4, will increase. We find that our observations follow a similar trend to the literature QSO values. Combining our results with the QSOs sample, we find $\sim 50 \pm 30\%$ [5] lower ratios of $L'_{\rm CO(3-2)}/\,L_{\rm FIR}$ than SMGs, potentially indicating shorter gas consumption timescales. To test if the SMGs and QSOs are also drawn from the same parent distribution we perform a two-sided Kolgomorov-Smirnov (KS) test on the ratio $L'_{\rm CO(3-2)}/\,L_{\rm FIR}$. The KS test returns a value of 0.7%, indicating a small probability that the populations are drawn from the same parent distribution, however we stress that this interpretation

[5] Error estimated by bootstrap resampling.

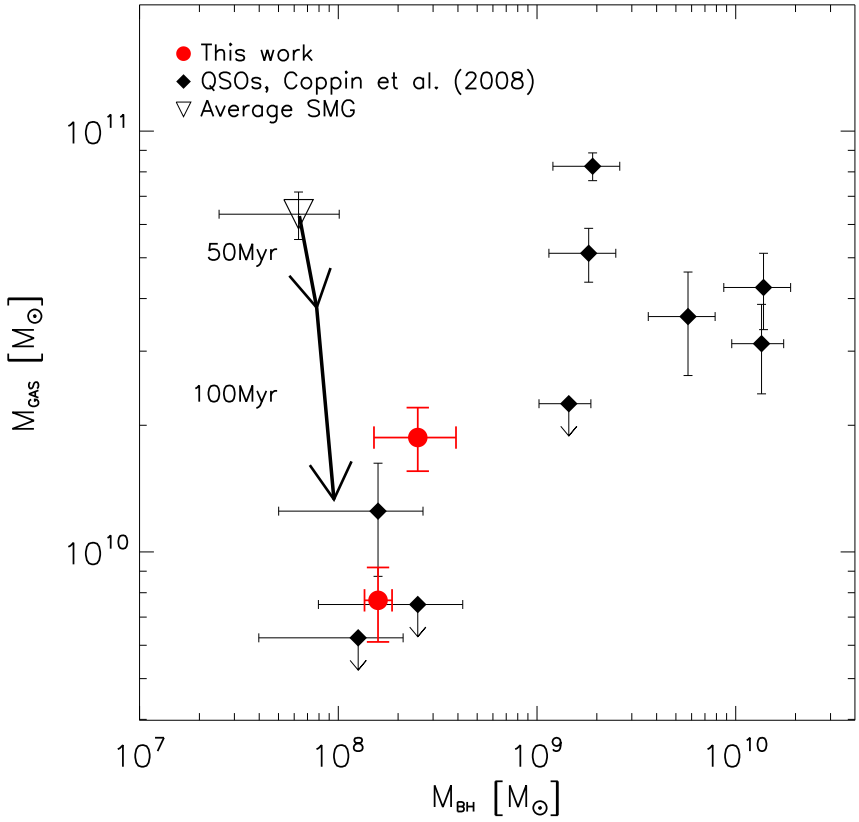

Figure 5.5: A comparison of gas and SMBH masses for far-infrared bright QSOs and SMGs which have been observed in ^{12}CO (3–2). The QSO points are taken from Coppin et al. (2008) (includes literature values from Beelen et al. (2004)) and the average SMG gas mass from Bothwell et al. (2013), and SMBH mass from Alexander et al. (2008). The gas masses are derived from the ^{12}CO (3–2) line luminosity, using the appropriate r_{31} for each population, see § 5.5.1. We show the predicted evolution of the gas mass and SMBH mass in a model SMG in which star formation and SMBH growth occur in tandem for a period of 50 or 100 Myrs. For the star formation we assume a constant rate of 500 $M_\odot yr^{-1}$ (Bothwell et al., 2013). The growth of the SMBH is calculated following Eq. 10 from Alexander & Hickox (2012), and we assume it is accreting with an Eddington ratio of $\eta = 0.2$ (Alexander et al., 2008). We conclude that the properties of the far-infrared bright QSOs in our sample, and the QSOs with $M_{\rm BH} < 10^9\,M_\odot$ from (Coppin et al., 2008), are consistent with their recent evolution from an earlier SMG-like phase. The far-infrared bright QSOs with $M_{\rm BH} > 10^9\,M_\odot$ are attributed as statistical outliers in this evolutionary scenario, as their SMBH masses are amongst the largest seen in the local universe.

implicitly assumes the same value for r_{31} in the two populations.

^{12}CO (3–2) emission traces warm and/or dense environments, hence to convert $L'_{\rm CO(3-2)}$ to a total gas mass we must make assumptions about the temperature distribution within the gas. In QSOs it is thought that the gas is close to thermal equilibrium, meaning that the ^{12}CO (3–2) transition traces the majority of the gas in the system (Riechers et al., 2011a). Bothwell et al. (2013) show that the ^{12}CO(J , $J-1$)$J \geq 2$ emission lines in SMGs are sub-thermally excited (see also Harris et al. 2010), which is interpreted as an indication for the presence of multiple temperature components: a warm component associated with the star-forming regions and a cooler component associated with extended, quiescent, gas (see also Danielson et al. 2011). If we use the proposed r_{31} value for QSOs, $r_{31} = 1.0$, and for SMGs, $r_{31} = 0.52$, the fixed offset between the two populations will increase, as the SMG gas masses roughly double relative to the QSOs. A two-sided KS test, including these values, returns a 0.05% probability that the SMG and QSO gas mass timescales are drawn from the same parent distribution. Thus it appears that the far-infrared bright QSOs not only lack the extended, cool reservoir of gas seen in SMGs (e.g. Ivison et al. 2010b, 2011) but also have less warm/dense gas than SMGs, suggesting that they are more evolved.

The lower ratios of $L'_{\rm CO(3-2)}/\,L_{\rm FIR}$ for our sample compared to SMGs disagrees with the results of Coppin et al. (2008), who do not find evidence for a fixed offset between their sample of extremely FIR-bright QSOs and the SMG sample of Greve et al. (2005). However, the reason for this discrepancy is likely due to the choice of SMG comparison samples used in the two analyses. For example, Coppin et al. (2008) compared their results to the Greve et al. (2005) sample which contains 18 SMGs, of which only 4 are unlensed ^{12}CO (3–2) detected sources (as such, in their analysis Coppin et al. (2008) create an SMG sample which contains 17 sources, observed in mix of CO transitions, and converted to a single CO transition by assuming the gas is thermalised). In contrast, we make use of the recent SMG survey of Bothwell et al. (2013), which contains 15 unlensed ^{12}CO (3–2) detected SMGs. Since we are now in a position to compare our QSOs to only ^{12}CO (3–2) detected, unlensed, SMGs this removes some of the uncertainty associated with combining samples observed in different transitions, and leads to a different conclusion.

5.6 Discussion

In order to study the link between QSOs and SMGs we have selected two far-infrared-detected QSOs at $z \sim 2.5$ (the epoch of peak activity in SMG and QSO populations) whose SMBH masses ($\sim 2 \times 10^8\,\mathrm{M}_\odot$) are comparable to the average SMBH mass for the SMG population (Alexander et al., 2008). In contrast the majority of previously ^{12}CO -detected (unlensed) far-infrared bright QSOs have $M_{\rm BH} \sim 10^9$–$10^{10}\,\mathrm{M}_\odot$ (Coppin et al., 2008), so much larger than the average SMG $M_{\rm BH}$ that they cannot have recently evolved from a typical SMG (as pointed out by Coppin et al. 2008). It is precisely this mismatch in SMBH masses which our study addresses. Given their FIR luminosities and SMBH masses our new sample is a more accurate representation of the typical far-infrared bright QSO population, and hence can be used to test an evolutionary link between SMGs and QSOs, through their gas and dynamical masses, as traced by their ^{12}CO (3–2) emission.

We show in Fig. 5.5 the distribution of estimated gas and SMBH masses for our two QSOs, as well as the average ^{12}CO (3–2) detected SMG from Bothwell et al. (2013) and the QSO sample from Coppin et al. (2008). We again note that gas masses are calculated by adopting $r_{31} = 1.0$ for QSOs, and $r_{31} = 0.52$ for SMGs, which are the appropriate values for each population. To investigate how galaxies might evolve with time we follow Coppin et al. (2008) and overlay a simple evolutionary model based on gas consumption and SMBH growth timescales. We take the average SFR of SMGs from Bothwell et al. (2013) as $500\,\mathrm{M}_\odot\,\mathrm{yr}^{-1}$ and use this to calculate the reduction in their gas mass with time. In this simple model we assume a constant SFR and do not include mass loss due to winds. By selection, our QSOs have SMBH masses similar to the average SMGs, but to estimate the growth of the central SMBH on the gas consumption timescale we follow Eq. 10 from Alexander & Hickox (2012). In line with the measured properties of SMGs, we limit the growth to an Eddington ratio, $\eta = 0.2$ [6], and an efficiency of 0.1 (Alexander et al., 2008), this then predicts the estimated growth in the SMBH mass in parallel to the depletion of the gas reservoir.

In Fig. 5.5 we plot tracks showing the evolution in the expected gas and SMBH masses for the descendents of SMGs after 50 and 100 Myrs. As can be seen, after 100 Myrs the SMGs in this model are expected to have almost completely depleted their gas reservoirs

[6] $\eta = 0.2$ indicates fast black hole growth. Within uncertainties it is feasible the growth is Eddington limited, $\eta = 1$.

and will have gas masses comparable to those we detect in the far-infrared luminous QSOs. At the same time their SMBHs will have grown by $\sim 50\%$, resulting in masses similar to those seen in our target QSOs. As can be seen from Fig. 5.5, the rate of growth of the SMBH and the depletion of the gas reservoir can link the properties of a typical SMG to those seen in our far-infrared bright QSOs around $\sim 100\,\mathrm{Myrs}$ later.

Are all SMGs likely to go through a QSO-phase? If these three $z \sim 2$–3 populations (i.e. $S_{850\mu\mathrm{m}} \gtrsim 5\,\mathrm{mJy}$ SMGs and QSOs with SMBH with masses of $\gtrsim 10^8\,\mathrm{M}_\odot$ that can be both far-infrared-bright and -faint) are uniquely related through a simple evolutionary cycle, then the product of their respective space densities and lifetimes should be similar. On average we expect the SMG lifetimes to be comparable to their gas depletion timescales (Fig. 5.5) or $\sim 10^8$ yrs (Swinbank et al., 2006; Hickox et al., 2012) and their volume density at $z \sim 2-3$ is $\sim 10^{-5}\,\mathrm{Mpc}^{-3}$ (e.g. Wardlow et al. 2011). In comparison, the QSO volume density at $z \sim 2-3$ (with SMBH masses above $\sim 10^8\,\mathrm{M}_\odot$) is $\sim 10^{-6}\,\mathrm{Mpc}^{-3}$ (Croom et al., 2009) and estimates of their lifetimes are $\gtrsim 10\,\mathrm{Myrs}$ (Martini & Weinberg, 2001; Hosokawa, 2002). As noted by a number of previous authors, the space densities and duty cycles of these populations are thus consistent with all SMGs subsequently transforming into a QSO.

If they transform through a far-infrared bright QSO phase how long can this be? From Chapman et al. (2005) and Wardlow et al. (2011) we estimate that far-infrared bright QSOs have a volume density at $z \sim 2-3$ of $\sim 10^{-7}\,\mathrm{Mpc}^{-3}$. By comparison to the SMG and QSO lifetimes this implies a duration for this transition phase of just $\sim 1\,\mathrm{Myr}$. Estimates of lifetimes and space densities for each population are uncertain at $>> 2\times$, and so a qualitative agreement is reasonable. If the QSO influences its host through winds and outflows with characteristic velocities of $\sim 1000\,\mathrm{km\,s}^{-1}$ (e.g. Harrison et al. 2012) then the estimated duration of the far-infrared bright phase would allow these winds to reach kpc scales, comparable to the likely extent of the gas reservoirs and star-formation activity within these systems (e.g. Tacconi et al. 2008; Ivison et al. 2011). This may help explain the short duration of the 'transition' phase, although it may be exhaustion of the gas reservoir by star formation which is allowing these winds to propagate freely.

5.7 Conclusions

The main conclusions from our study are:

- We have used IRAM PdBI to search for redshifted ^{12}CO (3–2) emission from two far-infrared bright QSOs at $z \sim 2.5$ selected from the H-ATLAS survey. These QSOs were selected to have SMBH masses of $M_{\rm BH} \leq 3 \times 10^8\,{\rm M}_\odot$, which are more comparable to typical SMGs than those in samples of high-redshift far-infrared luminous QSOs previously detected in ^{12}CO. Our observations detect ^{12}CO (3–2) emission from both QSOs and we derive line luminosities of $L'_{\rm CO(3-2)} = (0.77\pm0.15)\times 10^{10}\,{\rm K\,km\,s^{-1}\,pc^2}$ and $L'_{\rm CO(3-2)} = (1.9\pm0.3)\times10^{10}\,{\rm K\,km\,s^{-1}\,pc^2}$ for J0908−0034 and J0911+0027 respectively (Table 2).

- Comparing our FIR-bright QSOs (and similar systems from the literature) with SMGs, we find that the QSOs have similar values of $L'_{\rm CO(3-2)}\sin^2 i/{\rm FWHM}^2$, our proxy for gas mass fraction, to SMGs. However this is subject to a number of assumptions. If we consider that QSOs have a biased inclination angle of 13°, as has been suggested (Carilli & Wang, 2006), then the QSOs have an ∼85% lower gas mass fraction, at a significance of 2.0–σ. In the absence of gas replenishment this is consistent with QSOs being more evolved systems. Furthermore, adopting the appropriate line brightness ratios for each population roughly doubles the gas mass in SMGs, increasing this difference further, to a significance of 3.6–σ. So with plausible assumptions there appears to be evidence for evolution in the gas fraction, but we require spatially-resolved ^{12}CO (1–0) observations to test this conclusively.

- By comparing the gas consumption timescales, estimated from $L'_{\rm CO(3-2)}\,/\,L_{\rm FIR}$, for far-infrared bright QSOs with SMGs, we find that the QSOs have $\sim 50 \pm 30\%$ lower consumption timescales. A two-sided KS test returns a 0.7% probability that the populations are drawn from the same parent distribution, and adopting appropriate line brightness ratios, of $r_{31} = 1$ for QSO, and $r_{31} = 0.52$ for SMGs decreases this to 0.05%. We conclude that far-infrared bright QSOs appear to have a lower mass of warm/dense gas (probed directly through ^{12}CO (3–2)). Combined with previous results (Riechers et al., 2011a), showing that QSOs also lack an extended, cool reservoir of gas seen in SMGs, we interpret this as evidence that the far-infrared bright QSOs are at a different evolutionary stage than typical SMGs. In our evolutionary scenario this is consistent with far-infrared bright QSOs being in 'transition' from an SMG to a QSO.

- We show that the gas and the SMBH masses in QSOs and SMGs are consistent

with a model where SMGs transform into QSOs on a timescale of $\sim$ 100 Myrs. Furthermore, the relative volume densities and expected durations of the SMG and QSO phases are consistent with all SMGs passing through a subsequent QSO phase, and we estimate that the likely duration of the far-infrared bright QSO phase is just $\sim$ 1 Myr. We note that if necessary this duration is still sufficient to allow the QSO to influence the star formation and gas reservoirs across the full extent of the host galaxy through 1000-km s^{-1} winds and outflows. To rigorously test this connection we require ^{12}CO (1–0) observations, which would allow us to determine the gas reservoir masses of our QSOs, without making assumptions about the line brightness ratio, r_{31}.

The scale of this study is too small to single handedly prove or disprove an evolutionary link between SMGs and QSOs. However the data we have obtained provides further evidence supporting the idea originally proposed by Sanders et al. (1988) that these populations are linked by an evolutionary sequence. We have compared ^{12}CO (3–2) detected QSOs and SMGs through a number of observable quantities, and find the timescales for gas depletion, and SMBH growth, needed to link SMGs to these sources are consistent.

Chapter 6

Conclusions and Future Work

This thesis has investigated the properties of intensely star-forming galaxies at high-redshift. The following chapter summarises the key results from the work presented in this thesis, and discusses outstanding issues that are still to be addressed. Finally, I give a brief discussion of ongoing projects and the future direction of this work.

6.1 Summary of presented work

6.1.1 Multiwavelength properties of ALMA-identified SMGs

In chapter 2 I presented an analysis of the multiwavelength properties of a sample of 96 ALMA-identified SMGs. These SMGs were detected in 1.5″ resolution ALMA imaging of 88 LABOCA-detected sub-mm sources in the ECDFS (LESS; Weiß et al. 2009). The ALMA observations provide over an order of magnitude improvement in resolution relative to the LABOCA observations (FWHM = 19.2″), directly pin-pointing the individual SMGs that contribute to the single-dish sub-mm source and providing unambiguous identifications for their multiwavelength counterparts. Using the extensive multiwavelength imaging of the ECDFS I measured the optical-to-near-infrared photometry of all 96 ALMA-identified SMGs. By modelling the SEDs of the 77 SMGs that have 4–19 band photometry, I derive a median photometric redshift for this subset of $z_{phot} = 2.3 \pm 0.1$.

The remaining 19 SMGs have insufficient photometry to derive photometric redshifts, but by stacking *Herschel* observations at 250, 350 & 500 μm I confirm they are not spurious. Instead, these SMGs represent a population of optically faint, or completely undetected, sources. Assuming that these SMGs have an absolute H-band magnitude distribution comparable to that of a complete sample of $z \sim 1$–2 SMGs, I demonstrated that they

lie at higher redshifts, raising the median redshift for SMGs to $z_{phot} = 2.5 \pm 0.2$. In contrast to previous studies of the radio-detected subset of the SMG population, which are intrinsically biased towards lower redshift, it was shown that 35 ± 5 per cent of the total SMG population lie at $z \geq 3$.

Finally, I investigated the possible properties of the the descendants of SMGs. By assuming that the star formation activity in SMGs has a timescale of ~ 100 Myr it was shown that their descendants at $z \sim 0$ would have a space density and M_H distribution that are in good agreement with a volume limited sample of local ellipticals. The mass-weighted ages of the stellar populations of the local ellipticals are also shown to broadly agree with the look-back times of the SMG events. Taken together, these results are consistent with a simple model that identifies SMGs as events which form most of the stars seen in the majority of luminous elliptical galaxies at the present day.

6.1.2 The bright end of the 870 μm number counts

Chapter 3 presented ALMA 870 μm continuum imaging of 30 sub-mm sources in the UDS field. These sub-mm sources were selected from wide-field imaging with the SCUBA-2 instrument, taken as part of S2CLS, and are representative of the brightest sub-mm sources in the field. We detect 52 SMGs in the ALMA maps and find that 61^{+19}_{-15} % of the single-dish-detected sub-mm sources are comprised of a blend of multiple SMGs brighter than $\gtrsim 1$ mJy. The brightest SMGs in each ALMA map are shown to contribute on average 80^{+6}_{-2} % of the single-dish flux density, and in the ALMA maps containing ≥ 2 SMGs the secondary SMG contributes on average 25^{+1}_{-5} % of the integrated ALMA flux

From the ALMA observations I constructed the bright-end of the sub-mm number counts and demonstrated that multiplicity boosts the apparent single-dish number counts by 20 % at $S_{870} > 7.5$ mJy. By combining previous ALMA surveys I show that the sub-mm number counts are well-described by a double power-law with a break at 8.5 ± 0.6 mJy, corresponding to a star formation rate of $\sim 10^3\,\mathrm{M_\odot yr^{-1}}$. The steep decline in the sub-mm number counts at 8–9 mJy suggests a typical threshold to the star formation rate in SMG that, given the size of the star-forming region in these starbursts, corresponds to a star formation rate density of $\sim 100\,\mathrm{M_\odot yr^{-1}\,kpc^{-2}}$.

Finally, I investigate whether multiplicity of single-dish sources is driven by line-of-sight projections or physical associations between pairs of SMGs. Using the number density of secondary SMGs around the brightest sources I demonstrate that the secondary SMGs are

80 ± 30 times more numerous than expected from the blank field numbers counts. Even after accounting for selection biases this over-density of secondary SMGs is not consistent with these sources being line-of-sight projections, indicating that a significant proportion of these pairs of high-redshift starbursts must be physically associated. Such small scale over-densities of SMGs are unsurprising given that SMGs are massive galaxies, potentially undergoing merger-induced star formation.

6.1.3 Resolved sub-mm imaging of SMGs

Chapter 4 followed on from the work presented in chapter 3, and exploited $0.3''$ resolution ALMA 870 μm imaging to investigate the size and morphology of the sub-mm emission from SMGs. Sizes were measured individually for a subset of 23 SMGs detected at sufficiently high signal-to-noise ratio, and these sources were shown to have a median intrinsic angular size of FWHM $= 0.30 \pm 0.04''$. By combining the intrinsic angular sizes with the photometric redshifts of the SMGs we show that this corresponds to a median physical half-light diameter of 2.4 ± 0.2 kpc. Stacking the fainter SMGs in the sample shows that these sources have sizes consistent with the brighter SMG. The size of the star-forming region in SMGs does not have a significant trend with either redshift or sub-mm flux density.

The sub-mm sizes of the SMGs presented in this thesis are consistent with the sizes of other samples of SMGs measured from resolved ^{12}CO ($J = 3$–2 to 7–6) emission lines. However, the sizes of SMGs derived from 1.4 GHz imaging appear to be approximately two times larger on average, which was attributed to the larger diffusion length of cosmic rays.

The pre-existing stellar population in SMGs has a half-light radius, as measured from rest-frame optical imaging, that is about four times larger than the extent of the ongoing star formation (Chen et al., 2015). The high dust content of SMGs means that the starburst component is likely to be missed in this rest-frame optical imaging, while the prodigious star formation rates mean that the starburst has the potential to drastically alter the stellar mass distribution of the post-starburst galaxy.

SMGs have been suggested as the progenitors of a population of compact quiescent galaxies that are detected at high-redshift. However, an issue with this evolutionary scenario is that the size of the pre-existing stellar distribution in SMGs is significantly larger than their proposed descendants, indicating that a major transformation of the

stellar distribution is required. The size of the star-forming region in SMGs is comparable to the size of the stellar distribution in these compact quiescent galaxies. As the ongoing starburst in SMGs has the potential to at least double the pre-existing stellar mass the compact nature of the starburst offers an explanation for the transformation of the stellar mass distribution required if SMGs are indeed the progenitors of compact, quiescent galaxies.

6.1.4 The evolutionary connection between SMGs and FIR-bright QSOs

Finally, chapter 5 presented PdBI observations of molecular line emission from two far-infrared luminous QSOs at $z \sim 2.5$. An advantage of our work over previous studies is that the QSOs were selected to have supermassive black holes with masses similar to those thought to reside in SMGs at $z \sim 2.5$. The sample is thus well-suited to test a proposed evolutionary connection between SMGs and QSOs.

^{12}CO (3–2) emission is detected from both QSOs and we use the properties of the emission line to measure the gas and dynamical masses of both sources. A comparison between the gas and dynamical masses of far-infrared bright QSOs and SMGs at the same redshift, indicates that the QSOs are at a later evolutionary stage. In particular, far-infrared bright QSOs were shown to have $\sim 50 \pm 30\%$ less warm/dense gas than SMGs, at a fixed $L_{\rm FIR}$. A simple model for the expected evolution in the gas and black hole masses of SMGs was used to predict the properties of their descendents. Adopting a lifetime for the SMG phase of 100 Myrs, it was shown that the evolved properties are in good agreement with the far-infrared QSOs presented here. The agreement of the evolved properties is consistent with an evolutionary scenario where far-infrared bright QSOs represent a short phase in the transformation of starburst-dominated, dusty, SMGs into unobscured, gas-poor, QSOs.

6.2 Ongoing and Future Work

A number of outstanding questions have been addressed in this thesis regarding the properties, and evolution, of massive star-forming galaxies. I now discuss some of the work needed to further our understanding of these sources.

6.2.1 Spectroscopic redshifts of SMG

In chapter 2 I derived photometric redshifts for the ALESS SMGs. These photometric redshifts are a useful tool for constraining the overall redshift distribution for the population but they typically have associated uncertainties that are too large to facilitate detailed follow-up of individual sources. Instead, spectroscopic redshifts are required as these provide the precision required to measure properties such as the environments of SMGs or to conduct follow-up observations with instruments such as SINFONI to understand the dynamics of these sources. Danielson et al. (in prep) recently undertook an extensive optical-to-near-infrared spectroscopic programme to obtain redshifts for the ALESS SMGs. They obtain deep integrations using six different spectrographs, and determine the spectroscopic redshifts for 45 % of sample (Q=1,2,3), with a success rate of 50 %. Building on this project we were recently awarded time with XSHOOTER to determine redshifts for a subset of the ALMA-detected SMGs in the UDS field (see Chapter 3). The XSHOOTER instrument provides simultaneous coverage from 300–2500 nm, and is thus ideally suited to search for emission lines from sources with highly uncertain redshifts. A preliminary investigation of the spectra results in spectroscopic redshifts for a handful of SMGs, but with a similar success rate to Danielson et al. (in prep). A more thorough reduction and investigation of the spectra will hopefully yield more redshifts, but it is clear that this method is both expensive and only yields redshifts for a subset of the SMG population.

To fully characterize the SMGs population, free from selection biases, requires a sample with a high degree of spectroscopic completeness. The clearest route to obtaining such high completeness is to combine traditional optical-to-near-infrared spectroscopy for the optically-bright SMGs, with searches for atomic or molecular line emission for the remaining sources. By far the brightest of the far-infrared emission lines is the $^2P_{3/2}$–$^2P_{1/2}$ transition of singularly ionised carbon (traditionally referred to as [CII]), which can contribute up to 1 % of the total far-infrared luminosity. Utilising only the Band 7 capabilities of ALMA, the sheer strength of the [CII] emission line means it is feasible to perform a redshift search from $z \sim 4-7$; observations in other ALMA bands would widen this redshift range. In addition, although the rotational transitions of ^{12}CO are considerably fainter than the [CII] emission line, they are a viable target for projects to determine the redshifts of SMGs with millimetre and/or radio interferometers. Perhaps the most immediate impact of far-infrared spectroscopy will be to determine the redshifts of

the SMGs that are faint, or indeed undetected, at optical-to-near-infrared wavelengths. As discussed in chapters 2 and 3, these SMGs represent around 20–30 % of the >1 mJy 870 μm population, but the absence of optical-to-near-infrared counterparts to these sources means that their properties are largely unknown.

6.2.2 Gas Properties of SMGs

With an unbiased sample of spectroscopically confirmed SMGs we will be in a position to study, and constrain, the properties of the ISM in these sources. For instance, observations of low-J transitions of ^{12}CO can be used to investigate the properties of the cold and/or diffuse gas that provides a reservoir of fuel for further star formation, while observations of increasingly higher J transitions trace the warm and / or dense gas that is typically associated with the ongoing starburst. By studying the abundance of these different molecular transitions of ^{12}CO (complimented by studies of other atomic and molecular species) we can study the temperature and density structure of the gas in SMGs.

Typically, the gas properties of SMGs can only be constrained on a global scale. However, with ALMA in its most extended configuration it will be possible to resolve the emission from SMGs on scales of only ∼100 pc. Observations of the far-infrared emission from SMGs on such high angular scales may allow us to resolve individual star-forming "clumps" in these sources, something that in the past has only been possible in highly amplified, lensed systems (Swinbank et al., 2010b; Danielson et al., 2011, 2013). With observations on these scales we can decompose the kinematics of individual star-forming "clumps", and investigate the resolved Kennicutt-Schmidt (K-S) relation, which describes the efficiency of star formation, in SMGs. Currently, observations indicate that the global properties SMGs are broadly in agreement with the K-S relation for local ULIRGs. However, for SMGs the relation appears to break down on the scale of the individual star-forming "clumps", perhaps indicating that the physical processes that drive the star formation in these sources are different to those that govern local ULIRGs.

6.2.3 High Resolution Optical Morphologies & Kinematics

We are now in a situation where we have high-resolution *HST* imaging of the rest-frame optical emission from the ALESS SMGs, which locates the pre-existing stellar population, and high resolution ALMA imaging of the sub-mm emission from SMGs in the UDS field. It was discussed in chapter 4 that the optical emission from SMGs is extended

on scales of $\sim$4 kpc, whereas the ongoing star formation is significantly more compact ($\sim$1 kpc). Currently, we do not have any understanding of the location of this compact star formation within the host galaxy. Are we witnessing a significant period of bulge growth from a centrally concentrated starburst, which dramatically alters the stellar profile of these sources? Such a scenario would explain the transformation of Sérsic index that is required if SMGs transition into compact, quiescent galaxies. However, to answer this question we require high resolution imaging of the optical and far-infrared emission from the same sample of SMGs.

One of the key outstanding questions regarding SMGs is what triggers the intense starburst: is the high star formation linked to merger activity, or is it due to instabilities in a gas-rich disc. With a large sample of robustly identified SMGs we are now in a position to address this question. We have ongoing programs with SINFONI, an Integral Field Unit (IFU) spectrograph operating in the near-infrared, at the Very Large Telescope (VLT) that will provide us with resolved dynamics for a handful of SMGs, predominately from observations of the Hα emission line. From these observations we can then identify signatures of merger, or disc-like, activity. Theoretical predictions differ significantly on the triggering mechanism for SMGs and these observations will provide a distinct test of the various models. In particular, we can investigate predictions that the fraction of SMGs that are merger driven is strongly dependent on sub-mm flux density. Currently the IFU observations are restricted to a biased subset of SMGs that are both spectroscopically confirmed at optical-to-near-infrared wavelengths, and have bright Hα emission. To reliably answer the question of what triggers the intense starburst in SMGs requires dynamical information for an unbiased sample. Ideally, this could be achieved by combining near-infrared IFU emission line spectroscopy with observations of resolved molecular emission lines.

6.2.4 Properties of lower luminosity, obscured starbursts

Due to the sensitivity of the available instrumentation the work presented in this thesis has focused on $> 10^{12}\,\mathrm{L}_{\odot}$ ($\gtrsim 100\,\mathrm{M}_{\odot}\mathrm{yr}^{-1}$) high-redshift, obscured starbursts. With ALMA in full operations, as well as improvements to existing facilities (e.g. SMA, PdBI), it is now feasible to identify sources that are significantly fainter at sub-mm wavelengths. Observations with detection limits of 0.1–1 mJy (and even lower) are now feasible, and with these it will be possible to detect star-forming galaxies that have a level of obscured

activity that is similar to the unobscured activity typically seen in galaxies selected at shorter wavelengths (i.e. in H α emission). By comparing these populations we can gain a complete picture of the contribution of unobscured and obscured star formation to the cosmic star formation rate density, and hence a better understanding of the evolution of galaxies.

6.2.5 ALMA Identifications

The ALESS survey discussed in chapter 2 illustrated the importance of identifying single-dish sub-mm sources at their initial selection wavelength. Critically, the survey allowed us for the first time to study the properties of a large, flux limited sample of SMGs with unbiased identifications. However, while the area of the LESS survey is large ($0.25\,\mathrm{deg}^2$) it is not clear if it is sufficient to overcome the effect of cosmic variance (see Williams et al. 2011). In chapter 3 I presented successful ALMA follow-up of a 30 sub-mm sources detected in the S2CLS survey at the JCMT. The S2CLS programme has observed seven well-studied, extragalactic fields to 1–σ depths of 1–2 mJy. The observations reach a particularly exquisite depth in the $1\,\mathrm{deg}^2$ UDS field, and detect over 600 sub-mm sources with flux densities $\gtrsim$4 mJy. However, as demonstrated by ALESS the first step towards utilizing such a map is to obtain interferometric identifications at sub-mm wavelengths. ALMA is ideally suited to this task and even with its currently limited capabilities it can provide identifications for each of the S2CLS sources in the UDS field in only minute integrations. Observing all of the S2CLS sources in the UDS field would provide a statistically robust sample of >1000 LIRG/ULIRG-luminosity SMGs, allowing us to overcome the effects of cosmic variance and, along with detailed follow-up observations at other wavelengths, place stronger constraints on the properties of this important population of galaxies.

6.3 Final Remarks

Since their discovery $\sim$20 years ago, SMGs have been shown to represent an important stage in the evolution of galaxies. Successively larger surveys conducted at single-dish facilities have improved our understanding of the sub-mm Universe, but these studies have remained limited by the angular resolution achieved with bolometer cameras at single-dish facilities. The availability of new, as well as improved, sub-mm / mm interferometers means that we are no longer limited by this coarse resolution. However, although the sensitivity

and resolution of sub-mm / mm interferometers means they can rapidly identify sub-mm sources, the size of the half-power primary beam means that it remains prohibitively expensive to conduct large blank field surveys; even with full capabilities a $1\,\mathrm{deg}^2$ survey to detect $> 1\,\mathrm{mJy}$ SMGs with ALMA requires $\sim 1000\,\mathrm{hrs}$ of observing time. Instead, in the next few years, it will be exploitation of the synergy between wide-field imaging from single-dish facilities and sensitive, high-resolution, interferometric follow-up observations that proves most effective for studying the SMG population. Indeed, the S2CLS survey with SCUBA-2 at the JCMT is a perfect path-finder that will guide future ALMA observations. The S2CLS survey has already identified a sample of thousands of sub-mm sources and these are ideal targets for interferometric follow-up.

To fully characterize the SMG population we must combine observations of their emission across all wavelengths. Low frequency observations with radio interferometers offer one route to determining the extent of the cold gas reservoirs in SMGs, while far-infrared observations will determine the properties of the gas that is actively star-forming. Complimentary to these observations will be studies undertaken in the near-infrared. Observations with instrumentation such as SINFONI / KMOS at the VLT can determine the kinematics of SMGs, while the eagerly anticipated *James Webb Space Telescope* (*JWST*) will have unparalleled sensitivity and resolution across the wavelength range of both *HST* and *Spitzer*. Each of the facilities described offers a unique insight into the physics and chemistry of the starburst in SMGs, but it is the combination of all of these observations that will prove most enlightening.

Over the past 20 years the field of sub-mm astronomy has advanced at a staggering pace, moving rapidly onwards since the first detections of a handful of $850\,\mu$m-detected extragalactic sources. Advances in instrumentation means that we now have catalogues of many thousands of sources, selected across a range of wavelengths from $\sim$ 500–1200 μm. However, despite the vast improvement in the number of detected sources our understanding of the SMG population remains limited, with many fundamental questions still unanswered. Fortunately, we are now entering an era where ALMA will begin full operations. The immense capabilities of this facility will allow us observe SMG in unprecedented detail, and promises to revolutionise our understanding of the obscured activity in high-redshift, starburst galaxies.

Bibliography

Adelberger K. L., 2005, ApJ, 621, 574

Alaghband-Zadeh S. et al., 2012, MNRAS, 424, 2232

Alexander D. M., Brandt W. N., Smail I., Swinbank A. M., Bauer F. E., Blain A. W., Chapman S. C., Coppin et al., 2008, AJ, 135, 1968

Alexander D. M., Hickox R. C., 2012, New Astron. Rev., 56, 93

Alexander D. M., Smail I., Bauer F. E., Chapman S. C., Blain A. W., Brandt W. N., Ivison R. J., 2005, Nature, 434, 738

Andrews B. H., Thompson T. A., 2011, ApJ, 727, 97

Aravena M., Younger J. D., Fazio G. G., Gurwell M., Espada D., Bertoldi F., Capak P., Wilner D., 2010, ApJL, 719, L15

Aretxaga I., Hughes D. H., Coppin K., Mortier A. M. J., Wagg J., Dunlop J. S., Chapin E. L., Eales et al., 2007, MNRAS, 379, 1571

Aretxaga I. et al., 2011, MNRAS, 415, 3831

Austermann J. E. et al., 2010, MNRAS, 401, 160

Balestra I. et al., 2010, A&A, 512, A12

Barger A. J., Cowie L. L., Sanders D. B., Fulton E., Taniguchi Y., Sato Y., Kawara K., Okuda H., 1998, Nature, 394, 248

Barger A. J., Wang W.-H., Cowie L. L., Owen F. N., Chen C.-C., Williams J. P., 2012, ApJ, 761, 89

Barnes J. E., Hernquist L. E., 1991, ApJL, 370, L65

Baugh C. M., Lacey C. G., Frenk C. S., Granato G. L., Silva L., Bressan A., Benson A. J., Cole S., 2005, MNRAS, 356, 1191

Bedregal A. G. et al., 2013, ArXiv e-prints

Beelen A., Cox P., Benford D. J., Dowell C. D., Kovács A., Bertoldi F., Omont A., Carilli C. L., 2006, ApJ, 642, 694

Beelen A. et al., 2004, A&A, 423, 441

Bell E. F., McIntosh D. H., Katz N., Weinberg M. D., 2003, ApJS, 149, 289

Bertin E., Arnouts S., 1996, A&AS, 117, 393

Bertoldi F. et al., 2007, ApJS, 172, 132

Bicay M. D., Helou G., 1990, ApJ, 362, 59

Biggs A. D., Ivison R. J., 2008, MNRAS, 385, 893

Biggs A. D. et al., 2011, MNRAS, 413, 2314

Birnboim Y., Dekel A., 2003, MNRAS, 345, 349

Blain A. W., 1996, MNRAS, 283, 1340

Blain A. W., Chapman S. C., Smail I., Ivison R., 2004, ApJ, 611, 725

Blain A. W., Jameson A., Smail I., Longair M. S., Kneib J.-P., Ivison R. J., 1999a, MNRAS, 309, 715

Blain A. W., Smail I., Ivison R. J., Kneib J.-P., 1999b, MNRAS, 302, 632

Blain A. W., Smail I., Ivison R. J., Kneib J.-P., Frayer D. T., 2002, PhR, 369, 111

Blanton M. R. et al., 2003, ApJ, 594, 186

Bolzonella M., Miralles J.-M., Pelló R., 2000, A&A, 363, 476

Bonfield D. G. et al., 2011, MNRAS, 416, 13

Bonzini M. et al., 2012, ApJS, 203, 15

Bothwell M. S. et al., 2010, MNRAS, 405, 219

Bothwell M. S. et al., 2013, MNRAS, 429, 3047

Bower R. G., Lucey J. R., Ellis R. S., 1992, MNRAS, 254, 601

Brammer G. B., van Dokkum P. G., Coppi P., 2008, ApJ, 686, 1503

Brown M. J. I. et al., 2008, ApJ, 682, 937

Bruzual G., Charlot S., 2003, MNRAS, 344, 1000

Buitrago F., Trujillo I., Conselice C. J., Bouwens R. J., Dickinson M., Yan H., 2008, ApJL, 687, L61

Buitrago F., Trujillo I., Conselice C. J., Häußler B., 2013, MNRAS, 428, 1460

Bundy K., Ellis R. S., Conselice C. J., 2005, ApJ, 625, 621

Bunker A. J., Stanway E. R., Ellis R. S., McMahon R. G., McCarthy P. J., 2003, MNRAS, 342, L47

Calvi R., Poggianti B. M., Fasano G., Vulcani B., 2012, MNRAS, 419, L14

Calvi R., Poggianti B. M., Vulcani B., 2011, MNRAS, 416, 727

Calvi R., Poggianti B. M., Vulcani B., Fasano G., 2013, MNRAS, 432, 3141

Calzetti D., Armus L., Bohlin R. C., Kinney A. L., Koornneef J., Storchi-Bergmann T., 2000, ApJ, 533, 682

Carilli C. L. et al., 2010, ApJ, 714, 1407

Carilli C. L., Wang R., 2006, AJ, 131, 2763

Casey C. M., Chapman S. C., Smail I., Alaghband-Zadeh S., Bothwell M. S., Swinbank A. M., 2011, MNRAS, 411, 2739

Casey C. M. et al., 2013, MNRAS, 436, 1919

Casey C. M., Narayanan D., Cooray A., 2014, Physics Reports, 541, 45

Chakrabarti S., McKee C. F., 2008, ApJ, 683, 693

Chapin E. L. et al., 2009, MNRAS, 398, 1793

Chapman S. C., Blain A. W., Smail I., Ivison R. J., 2005, ApJ, 622, 772

Chapman S. C., Smail I., Ivison R. J., Blain A. W., 2002, MNRAS, 335, L17

Chapman S. C., Smail I., Windhorst R., Muxlow T., Ivison R. J., 2004, ApJ, 611, 732

Chapman S. C., Windhorst R., Odewahn S., Yan H., Conselice C., 2003, ApJ, 599, 92

Chary R., Elbaz D., 2001, ApJ, 556, 562

Chen C.-C., Cowie L. L., Barger A. J., Casey C. M., Lee N., Sanders D. B., Wang W.-H., Williams J. P., 2013, ApJ, 776, 131

Chen C.-C. et al., 2015, ApJ, 799, 194

Cimatti A. et al., 2002, A&A, 392, 395

Coil A. L. et al., 2008, ApJ, 672, 153

Condon J. J., 1992, ARAA, 30, 575

Condon J. J., Anderson M. L., Helou G., 1991a, ApJ, 376, 95

Condon J. J., Huang Z.-P., Yin Q. F., Thuan T. X., 1991b, ApJ, 378, 65

Connolly A. J., Szalay A. S., Dickinson M., SubbaRao M. U., Brunner R. J., 1997, ApJL, 486, L11

Conselice C. J., Chapman S. C., Windhorst R. A., 2003, ApJL, 596, L5

Cooper M. C. et al., 2012, MNRAS, 425, 2116

Coppin K., Chapin E. L., Mortier A. M. J., Scott S. E., Borys C., Dunlop J. S., Halpern M., Hughes et al., 2006, MNRAS, 372, 1621

Coppin K. E. K. et al., 2012, MNRAS, 427, 520

Coppin K. E. K. et al., 2009, MNRAS, 395, 1905

Coppin K. E. K. et al., 2008, MNRAS, 389, 45

Cowie L. L., Barger A. J., Wang W.-H., Williams J. P., 2009, ApJL, 697, L122

Cowley W. I., Lacey C. G., Baugh C. M., Cole S., 2015, MNRAS, 446, 1784

Cristiani S. et al., 2000, A&A, 359, 489

Croom S. M. et al., 2002, MNRAS, 337, 275

Croom S. M. et al., 2009, MNRAS, 392, 19

Croom S. M., Warren S. J., Glazebrook K., 2001, MNRAS, 328, 150

Daddi E. et al., 2005, ApJ, 626, 680

Dahlen T. et al., 2013, ApJ, 775, 93

Damen M. et al., 2011, ApJ, 727, 1

Danielson A. L. R. et al., 2013, MNRAS, 436, 2793

Danielson A. L. R., Swinbank A. M., Smail I., Cox P., Edge A. C., Weiss A., Harris A. I., Baker, , A. J. et al., 2011, MNRAS, 410, 1687

Dannerbauer H., Walter F., Morrison G., 2008, ApJL, 673, L127

Davé R., Finlator K., Oppenheimer B. D., Fardal M., Katz N., Kereš D., Weinberg D. H., 2010, MNRAS, 404, 1355

de Jong T., Klein U., Wielebinski R., Wunderlich E., 1985, A&A, 147, L6

Decarli R. et al., 2014, ApJ, 780, 115

Dekel A., Birnboim Y., Engel G., Freundlich J., Goerdt T., Mumcuoglu M., Neistein, Pichon, C et al., 2009, Nature, 457, 451

Dempsey J. T. et al., 2013, MNRAS, 430, 2534

Devriendt J. E. G., Guiderdoni B., 2000, A&A, 363, 851

Di Matteo T., Springel V., Hernquist L., 2005, Nature, 433, 604

Doherty M., Bunker A. J., Ellis R. S., McCarthy P. J., 2005, MNRAS, 361, 525

Dole H., Le Floc'h E., Pérez-González P. G., Papovich C., Egami E., Lagache G., Alonso-Herrero A., Engelbracht, C. W et al., 2004, ApJS, 154, 87

Downes D., Solomon P. M., 1998, ApJ, 507, 615

Dunne L., Eales S. A., 2001, MNRAS, 327, 697

Eales S. et al., 2010, PASP, 122, 499

Eales S., Lilly S., Gear W., Dunne L., Bond J. R., Hammer F., Le Fèvre O., Crampton D., 1999, ApJ, 515, 518

Engel H., Tacconi L. J., Davies R. I., Neri R., Smail I., Chapman S. C., Genzel R., Cox, P. et al., 2010, ApJ, 724, 233

Fasano G. et al., 2012, MNRAS, 420, 926

Ferrarese L., Merritt D., 2000, ApJL, 539, L9

Fine S., Jarvis M. J., Mauch T., 2011, MNRAS, 412, 213

Frayer D. T. et al., 1999, ApJL, 514, L13

Frayer D. T., Ivison R. J., Scoville N. Z., Yun M., Evans A. S., Smail I., Blain A. W., Kneib J.-P., 1998, ApJL, 506, L7

Gawiser E. et al., 2006, ApJS, 162, 1

Geach J. E. et al., 2013, MNRAS, 432, 53

Gear W. K., Lilly S. J., Stevens J. A., Clements D. L., Webb T. M., Eales S. A., Dunne L., 2000, MNRAS, 316, L51

Gebhardt K. et al., 2000, ApJL, 539, L13

Gehrels N., 1986, ApJ, 303, 336

Genzel R., Baker A. J., Tacconi L. J., Lutz D., Cox P., Guilloteau S., Omont A., 2003, ApJ, 584, 633

Granato G. L., De Zotti G., Silva L., Bressan A., Danese L., 2004, ApJ, 600, 580

Granato G. L., Lacey C. G., Silva L., Bressan A., Baugh C. M., Cole S., Frenk C. S., 2000, ApJ, 542, 710

Granato G. L., Silva L., Monaco P., Panuzzo P., Salucci P., De Zotti G., Danese L., 2001, MNRAS, 324, 757

Greve T. R., Bertoldi F., Smail I., Neri R., Chapman S. C., Blain A. W., Ivison R. J., Genzel et al., 2005, MNRAS, 359, 1165

Greve T. R., Ivison R. J., Bertoldi F., Stevens J. A., Dunlop J. S., Lutz D., Carilli C. L., 2004, MNRAS, 354, 779

Greve T. R., Pope A., Scott D., Ivison R. J., Borys C., Conselice C. J., Bertoldi F., 2008, ArXiv e-prints, 806

Griffin M. J. et al., 2010, A&A, 518, L3

Hainline L. J., Blain A. W., Smail I., Alexander D. M., Armus L., Chapman S. C., Ivison R. J., 2011, ApJ, 740, 96

Hainline L. J., Blain A. W., Smail I., Frayer D. T., Chapman S. C., Ivison R. J., Alexander D. M., 2009, ApJ, 699, 1610

Häring N., Rix H.-W., 2004, ApJL, 604, L89

Harris A. I., Baker A. J., Zonak S. G., Sharon C. E., Genzel R., Rauch K., Watts G., Creager R., 2010, ApJ, 723, 1139

Harrison C. M. et al., 2012, ArXiv e-prints, 1205.1801

Hartley W. G. et al., 2010, MNRAS, 407, 1212

Hartley W. G. et al., 2013, MNRAS, 431, 3045

Hatsukade B., Ohta K., Seko A., Yabe K., Akiyama M., 2013, ApJL, 769, L27

Hauser M. G., Dwek E., 2001, ARAA, 39, 249

Hayward C. C., Behroozi P. S., Somerville R. S., Primack J. R., Moreno J., Wechsler R. H., 2013a, MNRAS, 434, 2572

Hayward C. C., Narayanan D., Kereš D., Jonsson P., Hopkins P. F., Cox T. J., Hernquist L., 2013b, MNRAS, 428, 2529

Helou G., Soifer B. T., Rowan-Robinson M., 1985, ApJL, 298, L7

Henriques B., Maraston C., Monaco P., Fontanot F., Menci N., De Lucia G., Tonini C., 2011, MNRAS, 415, 3571

Hezaveh Y. D., Marrone D. P., Holder G. P., 2012, ApJ, 761, 20

Hickox R. C. et al., 2012, MNRAS, 2285

Ho L. C., Goldoni P., Dong X.-B., Greene J. E., Ponti G., 2012, ApJ, 754, 11

Hodge J. A., Carilli C. L., Walter F., Daddi E., Riechers D., 2013a, ApJ, 776, 22

Hodge J. A., Carilli C. L., Walter F., de Blok W. J. G., Riechers D., Daddi E., Lentati L., 2012, ApJ, 760, 11

Hodge J. A. et al., 2013b, ApJ, 768, 91

Hogg D. W., Turner E. L., 1998, PASP, 110, 727

Holland W. S. et al., 2013, MNRAS, 430, 2513

Hopkins P. F., Cox T. J., Hernquist L., Narayanan D., Hayward C. C., Murray N., 2013, MNRAS, 430, 1901

Hopkins P. F., Hernquist L., Cox T. J., Di Matteo T., Martini P., Robertson B., Springel V., 2005, ApJ, 630, 705

Hopkins P. F., Hernquist L., Cox T. J., Di Matteo T., Robertson B., Springel V., 2006, ApJS, 163, 1

Hopkins P. F., Hernquist L., Cox T. J., Kereš D., 2008, ApJS, 175, 356

Hosokawa T., 2002, ApJ, 576, 75

Hsieh B.-C., Wang W.-H., Hsieh C.-C., Lin L., Yan H., Lim J., Ho P. T. P., 2012, ApJS, 203, 23

Hubble E. P., 1926, ApJ, 64, 321

Hubble E. P., 1929, ApJ, 69, 103

Huggins W., 1864, Phil. Trans. R. Soc., 154, 437

Hughes D. H., Serjeant S., Dunlop J., Rowan-Robinson M., Blain A., Mann R. G., Ivison R., Peacock et al., 1998, Nature, 394, 241

Ikarashi S. et al., 2011, MNRAS, 415, 3081

Iono D. et al., 2006, ApJL, 640, L1

Ivison R. J., Greve T. R., Dunlop J. S., Peacock J. A., Egami E., Smail I., Ibar et al., 2007, MNRAS, 380, 199

Ivison R. J. et al., 2004, ApJS, 154, 124

Ivison R. J., Greve T. R., Smail I., Dunlop J. S., Roche N. D., Scott S. E., Page M. J., Stevens et al., 2002, MNRAS, 337, 1

Ivison R. J. et al., 2010a, A&A, 518, L31

Ivison R. J., Papadopoulos P. P., Smail I., Greve T. R., Thomson A. P., Xilouris E. M., Chapman S. C., 2011, MNRAS, 412, 1913

Ivison R. J. et al., 2012, MNRAS, 425, 1320

Ivison R. J., Smail I., Barger A. J., Kneib J.-P., Blain A. W., Owen F. N., Kerr T. H., Cowie L. L., 2000, MNRAS, 315, 209

Ivison R. J., Smail I., Le Borgne J.-F., Blain A. W., Kneib J.-P., Bezecourt J., Kerr T. H., Davies J. K., 1998, MNRAS, 298, 583

Ivison R. J., Smail I., Papadopoulos P. P., Wold I., Richard J., Swinbank A. M., Kneib J., Owen F. N., 2010b, MNRAS, 404, 198

Ivison R. J. et al., 2013, ApJ, 772, 137

Ivison R. J., Swinbank A. M., Swinyard B., Smail I., Pearson C. P., Rigopoulou D., Polehampton E., Baluteau, J.-P.. et al., 2010c, A&A, 518, L35

Jarvis M. J., McLure R. J., 2006, MNRAS, 369, 182

Karim A. et al., 2013, MNRAS, 432, 2

Kartaltepe J. S. et al., 2012, ApJ, 757, 23

Kelly B. C., Vestergaard M., Fan X., Hopkins P., Hernquist L., Siemiginowska A., 2010, ApJ, 719, 1315

Kennicutt R. C., 1998, ARA&A, 36, 189

Kovács A., Chapman S. C., Dowell C. D., Blain A. W., Ivison R. J., Smail I., Phillips T. G., 2006, ApJ, 650, 592

Kriek M., van der Wel A., van Dokkum P. G., Franx M., Illingworth G. D., 2008a, ApJ, 682, 896

Kriek M. et al., 2008b, ApJ, 677, 219

Krogager J.-K., Zirm A. W., Toft S., Man A., Brammer G., 2013, arxiv/1309.6316

Lagache G., Puget J.-L., Dole H., 2005, ARAA, 43, 727

Lapi A., Shankar F., Mao J., Granato G. L., Silva L., De Zotti G., Danese L., 2006, ApJ, 650, 42

Laurent G. T. et al., 2005, ApJ, 623, 742

Lawrence A. et al., 2007, MNRAS, 379, 1599

Lawrence A. et al., 2012, VizieR Online Data Catalog, 2314, 0

Le Fèvre O. et al., 2004, A&A, 428, 1043

LeFloc'h E., Aussel H., Ilbert O., Riguccini L., Frayer D. T., Salvato M., Arnouts S., Surace, J. et al., 2009, ApJ, 703, 222

Leitherer C., Ortiz Otálvaro P. A., Bresolin F., Kudritzki R.-P., Lo Faro B., Pauldrach A. W. A., Pettini M., Rix S. A., 2010, ApJS, 189, 309

Leitherer C. et al., 1999, ApJS, 123, 3

Lilly S. J., Eales S. A., Gear W. K. P., Hammer F., Le Fèvre O., Crampton D., Bond J. R., Dunne L., 1999, ApJ, 518, 641

Lilly S. J., Tresse L., Hammer F., Crampton D., Le Fevre O., 1995, ApJ, 455, 108

Lindner R. R. et al., 2011, ApJ, 737, 83

Lonsdale C. J., Persson S. E., Matthews K., 1984, ApJ, 287, 95

Luo B. et al., 2010, ApJS, 187, 560

Madau P., Dickinson M., 2014, ARAA, 52, 415

Madau P., Ferguson H. C., Dickinson M. E., Giavalisco M., Steidel C. C., Fruchter A., 1996, MNRAS, 283, 1388

Magnelli B. et al., 2012, A&A, 539, A155

Magorrian J. et al., 1998, AJ, 115, 2285

Martini P., Weinberg D. H., 2001, ApJ, 547, 12

McLure R. J., Dunlop J. S., 2004, MNRAS, 352, 1390

Menéndez-Delmestre K. et al., 2009, ApJ, 699, 667

Menéndez-Delmestre K., Blain A. W., Swinbank M., Smail I., Ivison R. J., Chapman S. C., Gonçalves T. S., 2013, ApJ, 767, 151

Meurer G. R., Heckman T. M., Lehnert M. D., Leitherer C., Lowenthal J., 1997, AJ, 114, 54

Michałowski M. J., Dunlop J. S., Cirasuolo M., Hjorth J., Hayward C. C., Watson D., 2012, A&A, 541, A85

Mignoli M. et al., 2005, A&A, 437, 883

Mihos J. C., Hernquist L., 1994, ApJL, 431, L9

Miller N. A. et al., 2013, ApJS, 205, 13

Miller N. A., Fomalont E. B., Kellermann K. I., Mainieri V., Norman C., Padovani P., Rosati P., Tozzi P., 2008, ApJS, 179, 114

Mortlock A. et al., 2013, MNRAS, 433, 1185

Murphy E. J. et al., 2006, ApJL, 651, L111

Murphy E. J., Helou G., Kenney J. D. P., Armus L., Braun R., 2008, ApJ, 678, 828

Murphy, Jr. T. W., Armus L., Matthews K., Soifer B. T., Mazzarella J. M., Shupe D. L., Strauss M. A., Neugebauer G., 1996, AJ, 111, 1025

Murray N., Quataert E., Thompson T. A., 2005, ApJ, 618, 569

Murray N., Quataert E., Thompson T. A., 2010, ApJ, 709, 191

Narayanan D., Hayward C. C., Cox T. J., Hernquist L., Jonsson P., Younger J. D., Groves B., 2010, MNRAS, 401, 1613

Narayanan D., Krumholz M. R., 2014, MNRAS, 442, 1411

Nelan J. E., Smith R. J., Hudson M. J., Wegner G. A., Lucey J. R., Moore S. A. W., Quinney S. J., Suntzeff N. B., 2005, ApJ, 632, 137

Newman A. B., Ellis R. S., Bundy K., Treu T., 2012, ApJ, 746, 162

Nonino M. et al., 2009, ApJS, 183, 244

Oliver S. J. et al., 2012, MNRAS, 424, 1614

Omont A., McMahon R. G., Cox P., Kreysa E., Bergeron J., Pajot F., Storrie-Lombardi L. J., 1996, A&A, 315, 1

Ono Y., Ouchi M., Kurono Y., Momose R., 2014, ApJ, 795, 5

Paciga G., Scott D., Chapin E. L., 2009, MNRAS, 395, 1153

Page M. J., Carrera F. J., Stevens J. A., Ebrero J., Blustin A. J., 2011, MNRAS, 416, 2792

Page M. J., Stevens J. A., Ivison R. J., Carrera F. J., 2004, ApJL, 611, L85

Page M. J. et al., 2012, Nature, 485, 213

Panuzzo P. et al., 2010, A&A, 518, L37

Papadopoulos P. P., Kovacs A., Evans A. S., Barthel P., 2008, A&A, 491, 483

Pascale E. et al., 2011, MNRAS, 415, 911

Pascarelle S. M., Lanzetta K. M., Fernández-Soto A., 1998, ApJL, 508, L1

Patel S. G. et al., 2013, ApJ, 766, 15

Peng C. Y., Ho L. C., Impey C. D., Rix H.-W., 2010, AJ, 139, 2097

Pilbratt G. L. et al., 2010, A&A, 518, L1

Poggianti B. M. et al., 2013, ApJ, 762, 77

Pope A., Borys C., Scott D., Conselice C., Dickinson M., Mobasher B., 2005, MNRAS, 358, 149

Pope A. et al., 2008, ApJ, 675, 1171

Popesso P. et al., 2009, A&A, 494, 443

Puget J.-L., Abergel A., Bernard J.-P., Boulanger F., Burton W. B., Desert F.-X., Hartmann D., 1996, A&A, 308, L5

Ravikumar C. D. et al., 2007, A&A, 465, 1099

Riechers D. A., 2011, ApJ, 730, 108

Riechers D. A. et al., 2010, ApJL, 720, L131

Riechers D. A. et al., 2011a, ApJL, 739, L32

Riechers D. A., Hodge J., Walter F., Carilli C. L., Bertoldi F., 2011b, ApJL, 739, L31

Rujopakarn W., Rieke G. H., Eisenstein D. J., Juneau S., 2011, ApJ, 726, 93

Sakamoto K., Wang J., Wiedner M. C., Wang Z., Peck A. B., Zhang Q., Petitpas G. R., Ho, L., et al., 2008, ApJ, 684, 957

Sandage A., Visvanathan N., 1978, ApJ, 225, 742

Sanders D. B., Soifer B. T., Elias J. H., Neugebauer G., Matthews K., 1988, ApJL, 328, L35

Scheiner J., 1899, ApJ, 9, 149

Schneider D. P. et al., 2010, AJ, 139, 2360

Schumacher H., Martínez-Sansigre A., Lacy M., Rawlings S., Schinnerer E., 2012, MNRAS, 423, 2132

Scott S. E., Dunlop J. S., Serjeant S., 2006, MNRAS, 370, 1057

Scott S. E., Fox M. J., Dunlop J. S., Serjeant S., Peacock J. A., Ivison R. J., Oliver S., Mann, R. et al, 2002, MNRAS, 331, 817

Shaver P. A., 1988, in Astronomical Society of the Pacific Conference Series, Vol. 2, Optical Surveys for Quasars, P. Osmer, M. M. Phillips, R. Green, & C. Foltz, ed., p. 265

Silverman J. D. et al., 2010, ApJS, 191, 124

Simpson J. M. et al., 2012, MNRAS, 426, 3201

Simpson J. M. et al., 2015, ApJ, 799, 81

Simpson J. M. et al., 2014, ApJ, 788, 125

Slipher V. M., 1914, Popular Astronomy, 22, 19

Smail I., Ivison R. J., Blain A. W., 1997, ApJL, 490, L5

Smail I., Ivison R. J., Blain A. W., Kneib J.-P., 2002, MNRAS, 331, 495

Smail I., Ivison R. J., Owen F. N., Blain A. W., Kneib J.-P., 2000, ApJ, 528, 612

Smolčić V. et al., 2012, A&A, 548, A4

Soifer B. T., Neugebauer G., 1991, AJ, 101, 354

Soifer B. T., Neugebauer G., Matthews K., Becklin E. E., Ressler M., Werner M. W., Weinberger A. J., Egami E., 1999, ApJ, 513, 207

Soifer B. T., Sanders D. B., Madore B. F., Neugebauer G., Danielson G. E., Elias J. H., Lonsdale C. J., Rice W. L., 1987, ApJ, 320, 238

Solomon P. M., Downes D., Radford S. J. E., Barrett J. W., 1997, ApJ, 478, 144

Solomon P. M., Vanden Bout P. A., 2005, ARAA, 43, 677

Spergel D. N., Verde L., Peiris H. V., Komatsu E., Nolta M. R., Bennett C. L., Halpern M., Hinshaw, G., et al., 2003, ApJS, 148, 175

Stanway E. R., Bunker A. J., McMahon R. G., Ellis R. S., Treu T., McCarthy P. J., 2004, ApJ, 607, 704

Steidel C. C., Adelberger K. L., Giavalisco M., Dickinson M., Pettini M., 1999, ApJ, 519, 1

Steidel C. C., Erb D. K., Shapley A. E., Pettini M., Reddy N., Bogosavljević M., Rudie G. C., Rakic O., 2010, ApJ, 717, 289

Steidel C. C., Giavalisco M., Pettini M., Dickinson M., Adelberger K. L., 1996, ApJL, 462, L17

Stevens J. A., Page M. J., Ivison R. J., Carrera F. J., Mittaz J. P. D., Smail I., McHardy I. M., 2005, MNRAS, 360, 610

Strolger L.-G. et al., 2004, ApJ, 613, 200

Surace J. A. et al., 2005, http://swire.ipac.caltech.edu/swire/astronomers/publications

Swinbank A. M., Chapman S. C., Smail I., Lindner C., Borys C., Blain A. W., Ivison R. J., Lewis G. F., 2006, MNRAS, 371, 465

Swinbank A. M. et al., 2012, MNRAS, 427, 1066

Swinbank A. M. et al., 2011, ApJ, 742, 11

Swinbank A. M. et al., 2014, MNRAS, 438, 1267

Swinbank A. M., Smail I., Chapman S. C., Blain A. W., Ivison R. J., Keel W. C., 2004, ApJ, 617, 64

Swinbank A. M. et al., 2010a, MNRAS, 405, 234

Swinbank A. M., Smail I., Longmore S., Harris A. I., Baker A. J., De Breuck C., Richard J., Edge, A. C. et al., 2010b, Nature, 464, 733

Szokoly G. P. et al., 2004, ApJS, 155, 271

Tacconi L. J., Genzel R., Lutz D., Rigopoulou D., Baker A. J., Iserlohe C., Tecza M., 2002, ApJ, 580, 73

Tacconi L. J., Genzel R., Smail I., Neri R., Chapman S. C., Ivison R. J., Blain A., Cox, P., et al., 2008, ApJ, 680, 246

Tacconi L. J., Neri R., Chapman S. C., Genzel R., Smail I., Ivison R. J., Bertoldi F., Blain et al., 2006, ApJ, 640, 228

Targett T. A. et al., 2013, MNRAS, 432, 2012

Taylor E. N. et al., 2009, ApJS, 183, 295

Teplitz H. I., Collins N. R., Gardner J. P., Hill R. S., Heap S. R., Lindler D. J., Rhodes J., Woodgate B. E., 2003, ApJS, 146, 209

Thomas D., Maraston C., Bender R., Mendes de Oliveira C., 2005, ApJ, 621, 673

Thompson T. A., Quataert E., Murray N., 2005, ApJ, 630, 167

Toft S. et al., 2014, ApJ, 782, 68

Toft S. et al., 2007, ApJ, 671, 285

Treister E. et al., 2009, ApJ, 693, 1713

Ueda J. et al., 2014, ArXiv: 1407.6873

van der Wel A., Franx M., van Dokkum P. G., Rix H.-W., Illingworth G. D., Rosati P., 2005, ApJ, 631, 145

van Dokkum P. G., Franx M., Förster Schreiber N. M., Illingworth G. D., Daddi E., Knudsen K. K., Labbé I., Moorwood et al., 2004, ApJ, 611, 703

van Dokkum P. G. et al., 2008, ApJL, 677, L5

Vanzella E. et al., 2008, A&A, 478, 83

Vázquez G. A., Leitherer C., 2005, ApJ, 621, 695

Veilleux S., Kim D.-C., Sanders D. B., 2002, ApJS, 143, 315

Veilleux S. et al., 2009, ApJS, 182, 628

Vestergaard M., Peterson B. M., 2006, ApJ, 641, 689

Vieira J. D. et al., 2013, Nature, 495, 344

Vlahakis C., Eales S., Dunne L., 2007, MNRAS, 379, 1042

Wandel A., 1999, ApJ, 527, 649

Wang S. X. et al., 2013, ApJ, 778, 179

Wang W.-H., Cowie L. L., Barger A. J., Williams J. P., 2011, ApJL, 726, L18

Wang W.-H., Cowie L. L., van Saders J., Barger A. J., Williams J. P., 2007, ApJL, 670, L89

Wardlow J. L. et al., 2011, MNRAS, 415, 1479

Weiß A. et al., 2013, ApJ, 767, 88

Weiß A., Downes D., Neri R., Walter F., Henkel C., Wilner D. J., Wagg J., Wiklind T., 2007, A&A, 467, 955

Weiß A. et al., 2009, ApJ, 707, 1201

Whitaker K. E. et al., 2013, ApJL, 770, L39

Wiklind T. et al., 2014, ApJ, 785, 111

Williams C. C. et al., 2011, ApJ, 733, 92

Yang X., Mo H. J., van den Bosch F. C., Jing Y. P., 2005, MNRAS, 356, 1293

Younger J. D. et al., 2010, MNRAS, 407, 1268

Younger J. D., Fazio G. G., Huang J.-S., Yun M. S., Wilson G. W., Ashby M. L. N., Gurwell M. A., Lai et al., 2007, ApJ, 671, 1531

Younger J. D. et al., 2009, ApJ, 704, 803

Yun M. S., Reddy N. A., Condon J. J., 2001, ApJ, 554, 803

Yun M. S. et al., 2012, MNRAS, 420, 957

Zheng W. et al., 2004, ApJS, 155, 73

Zirm A. W., van der Wel A., Franx M., Labbé I., Trujillo I., van Dokkum P., Toft S., Daddi et al., 2007, ApJ, 656, 66